CALIFORNIA ENERGY COMMISSION

California Energy Commission

CONSULTANT REPORT

Application of Surface Deformation and Induced Seismicity to Geothermal Operation and Exploration

Prepared for: **California Energy Commission**
Prepared by: **Imageair Inc.**

Imageair, Inc.

November 2023| CEC-300-2023-037

California Energy Commission

Primary Author:

Mariana Eneva

Imageair, Inc.

600 Greensburg Circle

Reno, NV 89509

(858) 361-8192

meneva@imageair-inc.com

Contract Number: GEO-16-003

Prepared for:

California Energy Commission

Erica Loza (former CAM Elizabeth DeJong)
Contract Manager

Elizabeth Giorgi (former Manager Gina Barkalow)
Branch Manager
Reliability, Renewable Energy & Decarbonization Incentives Division

Armand Angulo
Assistant Deputy Director
Reliability, Renewable Energy & Decarbonization Incentives Division

Deana Carrillo
Director
Reliability, Renewable Energy & Decarbonization Incentives Division

Drew Bohan
Executive Director

ACKNOWLEDGMENTS

PREFACE

The California Energy Commission's Geothermal Grant and Loan Program is funded by the Geothermal Resources Development Account and provides funding to local jurisdictions and private entities for a variety of geothermal projects.

Application of Surface Deformation and Induced Seismicity to Geothermal Operation and Exploration is the final report for the Geothermal Grant and Loan Program Agreement Number GEO-16-003 conducted by Imageair Inc. The information from this project contributes to the Geothermal Grant and Loan Program's overall goals to:

- Promote the use and development of California's vast geothermal energy resources.
- Address any adverse impacts caused by geothermal development.
- Help local jurisdictions offset the costs of providing public services necessitated by geothermal development.

For more information about the Geothermal Grant and Loan Program, please visit the Energy Commission's website on the [Geothermal Grant and Loan Program webpage](http://www.energy.ca.gov/programs-and-topics/programs/geothermal-grant-and-loan-program) (http://www.energy.ca.gov/programs-and-topics/programs/geothermal-grant-and-loan-program),

ABSTRACT

The project demonstrated that InSAR is a cost-effective method of monitoring surface deformation over space and time significantly exceeding the capabilities of ground-based surveys. The measurements provided for the four study geothermal fields can be used as a reference point for future monitoring activities. This can greatly help geothermal operators and regulators in reservoir management and is highly recommended to continue in the future, especially in view of plans for additional geothermal developments.

The project used satellite data to detect land changes (deformation) in four geothermal fields in California (Coso, Salton Sea, North Brawley, and Heber). The research took place between 2017 and 2020. The project team applied a method known as Interferometric Synthetic Aperture Radar (InSAR) to detect and measure changes over time, at thousands of individual points. These consisted of vertical movements of the ground surface (sinking or rising, also known as subsidence or uplift, respectively) and horizontal displacements in the west-east direction. The observations agreed with data from ground-based surveys. They were also compared with seismicity resulting from geothermal industrial processes (induced) and occurring naturally (tectonic). Deformation modeling allowed the project team to connect surface deformation and fluid depletion from the geothermal operations.

Changes in the spatial patterns of surface deformation were associated with variations in production and injection. Subsidence at Coso and North Brawley decreased with decreasing production. Subsidence persisted in Salton Sea areas with steady energy production, while a geothermal development in the northeastern part of the field showed differences between the pre- and post-production periods. Both subsidence and uplift took place at Heber, changing with production and injection.

In some cases, induced seismicity clustered in areas of subsidence and correlated with fluid extraction rates. Tectonic earthquakes at Salton Sea (M5.1 in 2005) and North Brawley (M5.4 in 2012), and near Coso (M7.1 in 2019) caused distinct deformation signatures in the fields.

TABLE OF CONTENTS

LIST OF FIGURES

LIST OF TABLES

EXECUTIVE SUMMARY

Background

Building on two earlier projects with the California Energy Commission, this project used satellite data to detect, monitor, and analyze land changes in terms of ground surface deformation at four geothermal fields in California. The research was performed between 2017 and 2020. The study areas included the Coso geothermal field in the eastern part of central California, and three geothermal fields in Imperial Valley of southern California (Salton Sea, North Brawley, and Heber). The project team observed vertical displacements, with the ground surface sinking (subsidence) or rising (uplift), as well as horizontal movements.

The project made use of a method known as Interferometric Synthetic Aperture Radar (InSAR). For this purpose, Imageair Inc. combined efforts with the Canadian branch of TRE Altamira, an Italian company that has developed advanced InSAR techniques. Satellite data provide cost-effective spatial and temporal coverage of large areas, significantly exceeding the capabilities of the ground-based monitoring traditionally used at geothermal fields.

Surface deformation observations are important because they can indicate the extent of geothermal reservoirs and help in the understanding of the effects of production and injection. In this capacity, they can be very useful to geothermal operators and regulators in reservoir assessment and management. In addition, surface deformation monitoring is imperative in agricultural areas like Imperial Valley that can be adversely affected by even small changes in land elevations. Such changes are widespread in that area, due to both man-made (anthropogenic) and natural reasons. In this project, anthropogenic causes are geothermal production and injection. Natural causes are related to the ongoing extension and subsidence due to the relative movement of the Pacific and North American tectonic plates, networks of faults (many buried or covered by agriculture in Imperial Valley), and naturally occurring (i.e., tectonic) earthquakes.

To demonstrate the surface deformation detecting capabilities of InSAR, the project used radar data from three satellites – Envisat (2003-2010), TerraSAR-X (2012-2013), and Sentinel (2015-2019). Over the years, this approach has been applied through several techniques, the earliest of which failed in Imperial Valley due to its changing landscape from widespread agriculture. However, the project team used a state-of the-art InSAR technique, SqueeSAR, developed at TRE Altamira, which is more successful in agricultural areas due to its capability of detecting surface deformation at thousands of individual points, as well as changes in time. These points are so-called scatterers that persist in satellite images collected at different times, and are of two types – permanent scatterers (PS) and distributed scatterers (DS). PS represent buildings, boulders, points aligned along roads and canals, etc. DS are areas of fallow fields, bare land, and the like, frequently encountered in rural environments. This type of InSAR application made it possible to successfully obtain detailed information on surface deformation in the study areas.

All four study areas showed substantial anthropogenic surface movements, both vertical and horizontal, due to the geothermal operations. The InSAR observations agreed reasonably well with data from ground-based surveys. The InSAR data were also compared with induced seismicity caused by geothermal operations and naturally occurring earthquakes resulting from

tectonic activity. In addition, deformation modeling allowed the project team to suggest the most likely size and depth of the geothermal resources, as well as to connect the surface deformation to fluid depletion resulting from the geothermal operations.

Purpose

The purpose of this project was to demonstrate that using satellite data to monitor surface deformation at geothermal fields represents an advanced, cost-effective technology that can provide detailed spatial and temporal resolution and measurement precision, exceeding the capabilities of traditional ground-based surveys. This work intended to address the current lack of understanding of these advantages by both regulatory agencies and the geothermal industry, which continues to be a barrier to the routine use of such satellite data in geothermal fields. The project also planned to show that surface deformation monitoring of such detail, when integrated with deformation modeling and induced seismicity data, can help geothermal operators and regulators with reservoir assessment and management. The project team intended to build on earlier successful applications in Imperial Valley geothermal fields, aiming at continued monitoring in that area and extending this type of work to the Coso geothermal field. The measurements provided for the four study geothermal fields were expected to be used as a reference point for future monitoring activities.

Objectives

The main goals of the project were to: show that surface deformation in geothermal fields can be monitored cost-effectively with satellite data, with high precision and spatial and temporal resolution; demonstrate that monitoring of surface deformation and induced seismicity can help with operational flexibility, reservoir management, and environmental impact mitigation; help to distinguish between anthropogenic and tectonic causes of surface deformation, especially the sensitive subject of subsidence in agricultural areas; and provide reference measurements for future monitoring.

The main project objectives were to: process satellite data collected in several time periods, applying InSAR to Envisat, TerraSAR-X and Sentinel satellite scenes; analyze and interpret the InSAR data and compare them with ground-based measurements and geothermal operational activities (production and injection); integrate the observations with information on induced seismicity and tectonic earthquakes; perform deformation modeling and interpretation; and disseminate the results at professional meetings and through public outreach.

Conclusions

The project team applied a state-of-the art InSAR technique, SqueeSAR, to process satellite radar scenes collected over four geothermal fields in California – Coso in the eastern part of central California, and three fields in the Imperial Valley of southern California (Salton Sea, North Brawley, and Heber). This type of processing made it possible to detect surface deformation at numerous locations, even in agricultural areas like those in Imperial Valley where earlier InSAR techniques did not work. The processing results consisted of deformation time series and deformation rates at each individual location, in millimeters per year (mm/year). They made it possible to examine average time series within areas and along profiles of interest, as well as progression of deformation in time along profiles. For the most

part, the satellite results agreed well with ground-based measurements at the geothermal fields. However, SqueeSAR has the advantages of:

- Large-area coverage at once, which is more cost-effective than the ground-based surveys.
- Observations multiple times per year, compared with only annual or less frequent surveys.
- Dense spatial coverage, where deformation is measured at thousands of locations compared with only tens of GPS stations or leveling benchmarks on the territories of the geothermal fields.

Details in space and time like these made it possible to identify and characterize dynamic variations in surface deformation associated with changes in production and injection.

In addition, the project made use of ground-based surveys in the form of GPS subsidence surveys at Coso and leveling surveys in the geothermal fields of Imperial Valley. The surveys at Coso started in 1988 and took place every year initially, then more rarely, with a frequency ≥3 years since 2000. These data were provided by the U.S. Navy Geothermal Program Office (GPO). The leveling surveys in Imperial Valley are conducted annually by the geothermal operators. The Imperial County Department of Public Works (ICDPW) provided these data.

Information about the monthly production and injection fluid mass was also used. This information was provided by the GPO for the Coso geothermal field and the California Geologic Energy Management Division, CalGEM (formerly Division of Oil, Gas, and Geothermal Resources, DOGGR) for the fields in Imperial Valley.

Decreasing subsidence was noted as production decreased at Coso and North Brawley, subsidence transforming into uplift with increasing injection and subsequent redistribution of subsidence and uplift areas at Heber, and relatively steady subsidence correlating with stable ongoing production at the CalEnergy units of the Salton Sea.

The project team also examined induced seismicity in these geothermal fields and observed association between the locations of maximum subsidence and microearthquake clusters, some connections with production and injection, and changes in surface deformation caused by moderate earthquakes on the territories of two Imperial Valley geothermal fields and a large earthquake outside the Coso geothermal field.

The study area in Imperial Valley is particularly complicated, with an interplay of numerous factors – including geothermal production and injection wells, significant regional and local tectonic movements, earthquakes, aseismic events, anthropological changes, and substantial agriculture. Therefore, despite some limitations that the project team encountered, the project results are the best that have ever been obtained from satellites in this region, and in such a complex environment. In addition, this project established reference measurements for the four geothermal fields that can be used as a point of comparison in future monitoring activities.

The project findings indicate the need for further monitoring of surface deformation so that geothermal operators and regulators may better understand and prepare for subsidence and uplift likely to occur at new developments over time. The project observations also indicate the presence of induced seismicity from geothermal operations that also needs continued

monitoring. It is worth noting that the rates of subsidence in the fields studied here are significantly lower than those at a neighboring geothermal field, Cerro Prieto, in Mexico, where reinjection is not performed to the extent it occurs in the California facilities. As a consequence, the maximum rates of subsidence at Cerro Prieto are up to six times higher than those at the California's Known Geothermal Resource Areas (KGRAs).

The main findings of the project are as follows:

- Significant subsidence was observed with InSAR in all four geothermal fields. At North Brawley and Heber, uplift was also detected. These findings were confirmed by ground-based surveys.

- Dynamic changes in surface deformation were observed over time that appear related to variations in production and injection amounts and locations.

- The operation of binary geothermal plants is generally assumed to prevent surface deformation because the amounts of produced and re-injected fluids are similar. However, although surface displacements may be mitigated by the binary technology, the project team found that they were apparently not eliminated at the two study fields with binary power plants, North Brawley and Heber. In fact, maximum subsidence at these fields was comparable with, and even exceeded, the deformation observed at the two other study fields, Coso and Salton Sea, where the injection fluid is less than the production fluid due to evaporation in flash geothermal plants.

- The best agreement between InSAR deformation rates and those deduced from ground-based surveys was observed at Coso. The two types of measurements also agreed, but to a lesser extent, at Heber, North Brawley, and Salton Sea (in order of diminishing similarity). This is not surprising, in view of the much better spatial coverage achieved at the dry area of Coso, compared with a relative lack of PS and DS in the agricultural areas of Imperial Valley, including in the vicinities of some of the leveling benchmarks.

- A tendency of the seismicity to cluster in the areas of subsidence was observed, especially at Coso and the Salton Sea. Seismicity rates at North Brawley were clearly higher when the production was larger, and decreased with reduced production. The seismicity rates at Heber were much lower than those at the three other study fields, but still appeared connected to changes in operations. These observations indicate the presence of induced seismicity from the geothermal operations.

- Tectonic seismic events caused additional surface deformation on the territories of some of the study geothermal fields. This included subsidence from a moderate M5.1 earthquake in 2005 at the Salton Sea, and both subsidence and uplift from a M5.4 earthquake in 2012 at North Brawley. InSAR detected substantial surface deformation over the whole Coso geothermal field caused by a large M7.1 event occurring southwest of the field in July 2019 (preceded by a M6.4 earthquake one day earlier).

- Deformation modeling using a poroelastic model was applied to the Envisat and Sentinel InSAR data for the Coso and Salton Sea geothermal fields. It showed that surface deformation is consistent with depleting reservoirs. One important implication was that the observed surface deformation may be largely due to aseismic deformation processes (e.g., thermo-poro-elastic contraction and aseismic slip) and relatively

4

insensitive to changes in background seismicity rates caused by changes in the rates of injection and production.

More specific findings at the individual geothermal fields are listed below. For the vertical movements, negative and positive numbers indicate subsidence and uplift, respectively. For the horizontal displacements, negative and positive numbers denote westward and eastward movements, respectively. Northward and southward horizontal displacements cannot be measured with InSAR.

- A subsidence bowl was observed at the Coso geothermal field from both InSAR and ground-based surveys with GPS stations. The two types of measurements agreed very well. Subsidence decreased with decreasing production. The maximum subsidence of −27 mm/year was observed during the Envisat period. The average subsidence encompassing the center of the subsidence bowl got reduced from −22 mm/year (Envisat), to −16 mm/year (early Sentinel) and −13 mm/year (later Sentinel). Horizontal rate measurements were also provided by InSAR, which is important because ground-based subsidence surveys at Coso do not supply such observations. Average eastward rates in the same area and for the same periods, decreased from 20 mm/year to 11 mm/year, but then increased to 15 mm/year. Westward displacements decreased from −11 mm/year, to −9 mm/year, and then to −5 mm/year. Deformation modeling at Coso using Envisat and Sentinel InSAR surface deformation observations showed a best fit with a model of disk-shaped depleting reservoir at a depth of 3.1 km, radius 2.4 km, and a thickness of 195 m. The modeling results suggested that the decrease in subsidence over time can be readily interpreted as a result of fluid depletion of the hydrothermal system, and not because of changes in the size of the reservoir. That is, the close correspondence with geothermal operational parameters suggested a direct link between net fluid production (production minus injection) and changes in surface deformation.

- Due to relatively steady production, ongoing subsidence of up to −30 mm/year was observed with InSAR in the CalEnergy units of the Salton Sea geothermal field, operating flash power plants since the early 80's. The findings validated results from earlier projects. The satellite and ground-based leveling data agreed to some extent, but not as well as in the other fields. There is no simple association between surface deformation, production/injection, and induced seismicity. Because satellite observations exist since 2003 in this area, they were all post-production. In early 2012, EnergySource LLC started a new geothermal development to the northeast of the CalEnergy units in the Salton Sea geothermal field. In this case, the period covered by satellite data included both pre-production and post-production times, and subsidence of up to −18 mm/year appeared where it was absent before production started. The InSAR rates cited above are in reference to the location of a benchmark used as a reference in the CalEnergy leveling surveys, on Obsidian Butte (southern shore of Salton Sea). Because this point itself subsides at about −22 mm/year, possibly due to the general tectonic extension in the area, the maximum subsidence rate at the CalEnergy units is in fact about −52 mm/year, when the reference is a more stable point outside the valley. In the Sentinel period, the maximum observed subsidence (with that same reference) was a comparable −54 mm/year. There were also significant horizontal movements, of up to 27 mm/year eastward and −28 mm/year westward.

5

Deformation modeling conducted by USGS using observed InSAR surface deformation from a previous CEC-funded project, led to the conclusion that it is consistent with a depleting reservoir. The relatively small changes in average net fluid mass loss over time could explain the sustained subsidence. The best fitting depth of the reservoir depletion model is about 1.3 km, generally coinciding with the depth of the ~300°C geotherm and the shallowest portion of the geothermal resource.

- The North Brawley geothermal field experienced a high subsidence rate when production was relatively high, which substantially decreased with decreasing production. In reference to a local benchmark, observed maximum subsidence was −7 mm/year (Envisat period), −49 mm/year (TerraSAR-X), and −15 mm/year (Sentinel). Maximum observed uplift for the same periods was 6 mm/year, 26 mm/year, and 12 mm/year, respectively. The largest maximum values were seen in the TerraSAR-X period, because this is when the largest production took place. Similarly, significant westward movements were observed, up to −47 mm/year (TerraSAR-X) versus −16 mm/year (Sentinel). It may come as a surprise that deformation of this size was observed while only one binary power plant is operated at that field. In addition, the leveling surveys identified uplift of up to 50 mm from a M5.4 earthquake in 2012, for which there are no InSAR observations.

- InSAR captured variations in surface deformation over time at the Heber geothermal field, connected to changes in operation. During the Envisat period, both subsidence and uplift areas were identified, despite the predominance of binary technology used at the field. This was confirmed by the leveling surveys. The subsidence was up to −45 mm/year, and the uplift up to 22 mm/year. Unlike at the Salton Sea geothermal field, Heber exhibited clear relationship between the surface deformation time series and changes in production and injection fluid masses. The leveling data, going back to 1994, showed that the area Envisat InSAR identified as the location of uplift, used to subside prior to 2005 and this change was directly connected to increase in injection at that time. The Sentinel InSAR observations continued to show subsidence in the same general area, but indicated disappearing uplift initially, which later reappeared south of the Envisat uplift area.

Recommendations

Based on the results of this work, the project team has the following recommendations:

- It is imperative that geothermal operators and regulators become aware of the capabilities of InSAR for the purpose of reservoir management and mitigation of environmental impact. It will be beneficial to ensure the routine collection of such types of measurements, along with attention to induced seismicity. For example, compared with annual (or rarer) ground-based surveys, InSAR is capable of identifying changes in surface deformation much faster, and possibly with more spatial detail. This may signal undesirable effects of particular locations and amounts of production and injection. While this can help with the field operations, mitigation of environmental impact is also facilitated with InSAR, which is particularly important in agricultural areas. Continued lack of knowledge and understanding of such advantages by both geothermal operators and regulatory agencies has so far represented a barrier to the routine use of such

satellite data in geothermal fields. This project sought to remedy this situation, but continued efforts are needed.

- Attention to the project results is also needed in view of future geothermal developments. It would be prudent to view the maximum subsidence (up to -50 mm/year) that the project team observed in the currently operating fields, with an eye to the future. For example, if 1,700 MW additional geothermal capacity gets developed in the extended Salton Sea area, as previously proclaimed, it is important to keep in mind that the current power production in Imperial Valley that is three times lower, is already associated with substantial surface deformation and induced seismicity.

- For all its advantages, the SqueeSAR technique showed some limitations in the agricultural areas of Imperial Valley, so it will be best to plan on enhancements in future monitoring. Although the density of locations at which satellite deformation measurements are possible, is by orders of magnitude larger than the number of leveling benchmarks, there were some areas where deformation could not be measured. This limitation could be improved on, or eliminated, if corner reflectors are installed in known areas of interest where previous satellite observations could not identify deformation. Corner reflectors are relatively small structures that once installed would reflect radar signals back to the satellite, playing the role of artificial PS points in all future satellite data acquisitions. They do not require a power source or any maintenance after installation. Areas suitable for installation of corner reflectors may be around specific wells, locations of benchmarks and GPS stations, bridges, points of interest within agricultural fields, or areas with snow.

Benefits to California

The project demonstrated that the specific InSAR technique (SqueeSAR) applied to satellite radar data is very effective in detecting and monitoring surface deformation in the geothermal fields of California. This can be helpful to geothermal operators in reservoir assessment and management. Such monitoring is also important for mitigation of the possible environmental impact in agricultural areas like Imperial Valley, which are sensitive to surface deformation, especially subsidence. Additionally, this project establishes reference measurements for four geothermal fields that can be used for comparison with measurements from future monitoring activities.

CHAPTER 1: Background

1.1 Objectives

The main subject of the present work is to demonstrate that satellite data can be effectively used for the detection and characterization of surface deformation at geothermal fields. When geothermal operations take place in tectonically active areas, surface displacements are due to both natural and anthropogenic effects. Deformation modeling can help assess the proportion of surface change attributable to anthropogenic factors. Monitoring of surface deformation and induced seismicity presents possibilities for reservoir management and planning, subsurface fluid flow assessment, impact mitigation, and exploration. Understanding these factors can inform geothermal operators about the extent and subsurface characteristics of geothermal resources, the effect of particular combinations of production and injection amounts and locations, and possible planning of modifications as needed.

1.2 Geothermal Study Areas

Geothermal energy is part of the effort to increase the use of renewable energy, reduce the dependence on limited fossil-based resources, and combat the adverse effects of climate change. The natural geothermal resources in the United States are predominantly found in its western part, especially in California where the Renewables Portfolio Standard (RPS) (2015 Senate Bill 350, 2018 Senate Bill 100) seeks to achieve 100 percent of the electricity produced in the state to come from renewable and clean energy resources by 2045. The RPS specifies certain procurement requirements for RPS-obligated entities, creating demand for further geothermal resources development. California is already first in the U.S. for electricity generation from geothermal resources, with 2,712 MW installed capacity. In 2021 California contributed 70.5 percent of the total geothermal electricity in the country https://www.eia.gov/energyexplained/geothermal/use-of-geothermal-energy.php). The largest geothermal producers in California are The Geysers in northern CA, four operating geothermal fields in southern CA, and the Coso geothermal field in the eastern part of central CA. This report provides results from Coso (Chapter 2, Section 2.1) and three of the Imperial Valley geothermal fields in southern California (Chapter 2, Section 2.2), as shown in Figure 1.1.

1.3 Technique

Surface deformation has been commonly monitored in geothermally producing areas (e.g., Kagel et al., 2007). It is traditionally measured by ground-based geodetic data, such as leveling surveys and global positioning system (GPS) stations. Measurements of surface deformation from satellites have significantly improved over the last 30 years and are now vastly exceeding the capabilities of ground-based geodetic methods in terms of spatial coverage. They also significantly exceed the temporal coverage of leveling surveys. A special type of satellite radar data, synthetic aperture radar (SAR), are collected and processed with a method known as interferometric SAR (InSAR). Past and current satellites providing such data include the European ERS, Envisat, and Sentinel, all of which share similar characteristics, such as the wavelength used (5.66 cm, C-band). Other satellites providing SAR data are the

Figure 1.1 Study Areas

Map is from Google Earth. Yellow polygons show the known geothermal resource areas (KGRA) studied in this project.

Source: M. Eneva

Canadian Radarsat (C-band), the Japanese ALOS (L-band, 23.6 cm wavelength), the German TerraSAR-X (TSX) (X-band, 3.1 cm wavelength), and the Italian COSMO-SkyMed (CSM) (X-band).

1.3.1 Terminology

TRE Altamira provided most of the technical description in this section, with some modifications and additions by M. Eneva.

1.3.1.1 InSAR

Interferometric Synthetic Aperture Radar, also referred to as SAR interferometry or InSAR, is the measurement of signal phase change (interference) between radar images. When a point on the ground moves, the distance between the sensor and the point changes, thereby producing a corresponding shift in signal phase. This shift is used to quantify the ground movement. An interferogram is a two-dimensional (2D) representation of the difference in phase values. Variations of phase in an interferogram are identified by fringes, colored bands that indicate areas where and how much movement is occurring. The precision with which the movement can be measured is usually in the centimeter (cm) range as the phase shift is also impacted by topographic distortions, atmospheric effects, and other sources of noise. InSAR is

a method that can be applied through several techniques, such as DInSAR, PSInSAR, and SqueeSAR mentioned further in this text.

1.3.1.2 DInSAR

The classic, earliest technique using InSAR to identify and quantify ground movement, is Differential InSAR (DInSAR). Topographic effects are removed by using a digital elevation model (DEM) of the area of interest to create a differential interferogram. Results can be impacted by atmospheric effects. In DInSAR, two strategically chosen SAR scenes are used; for example, before and after an earthquake. Interferograms from a series of such pairs can be stacked in time. DInSAR is a useful tool for creating deformation maps. Limitations include relatively low precision (cm scale), inability to distinguish between linear and non-linear motion, and failure in vegetated areas. Numerous articles have been published with DInSAR results applied to the surface deformation caused by earthquakes, water pumping for irrigation, production in oil and gas fields, mining, etc. The author of the report used this technique to characterize the subsidence associated with mining and rockbursts in mines (Eneva, 2010b).

1.3.1.3 PSInSAR™

Permanent Caterers SAR Interferometry is an advanced form of DInSAR. The fundamental difference is that it uses multiple interferograms created from a stack of at least 15 radar images (Ferretti et al., 2000, 2001, 2007). PSInSAR was developed to overcome the errors produced by atmospheric artefacts on signal phase. The PSInSAR algorithm automatically searches the interferograms for pixels that display stable radar reflectivity characteristics throughout every image of the data set. In PSInSAR these pixels are referred to as Permanent Scatterers (PS). PS are objects, such as buildings, fences, lampposts, transmission towers, crash barriers, rocky outcrops, points along roads and canals, well pads, etc., which are reflectors of radar microwaves. The result is the identification of a sparse grid of point-like targets on which an atmospheric correction procedure can be performed. Once these errors are removed, a history of motion can be created for each target, allowing the detection of both linear and non-linear motion. The result is a deformation map consisting of PS points that are color-coded according to their deformation rate and direction of movement. The information available for each PS includes its deformation rate, acceleration, total deformation, elevation, coherence, as well as a time series of movement. The PSInSAR algorithm measures ground movement with millimeter accuracy. Earlier work of the project team made use of PSInSAR (Eneva et al., 2009; Eneva and Adams, 2010).

1.3.1.4 SqueeSAR™

In addition to the PS, it was noticed that many other signals are present in the processed data. These do not produce the same high signal-to-noise ratios of PS but are nonetheless distinguishable from the background noise. Upon further investigation it was found that the signals are reflected from extensive homogeneous areas where the back-scattered energy is less strong, but statistically consistent. These areas have been called distributed scatterers (DS). They correspond to rangeland, pastures, bare earth, scree, debris fields, arid environments, etc. (Figure 1.2). The SqueeSAR™ algorithm (Ferretti et al., 2011) was developed to process the signals reflected from these areas. As SqueeSAR™ incorporates PSInSAR, no information is lost and movement measurement accuracy is unchanged. The

Figure 1.2 Permanent and Distributed Scatterers in SqueeSAR
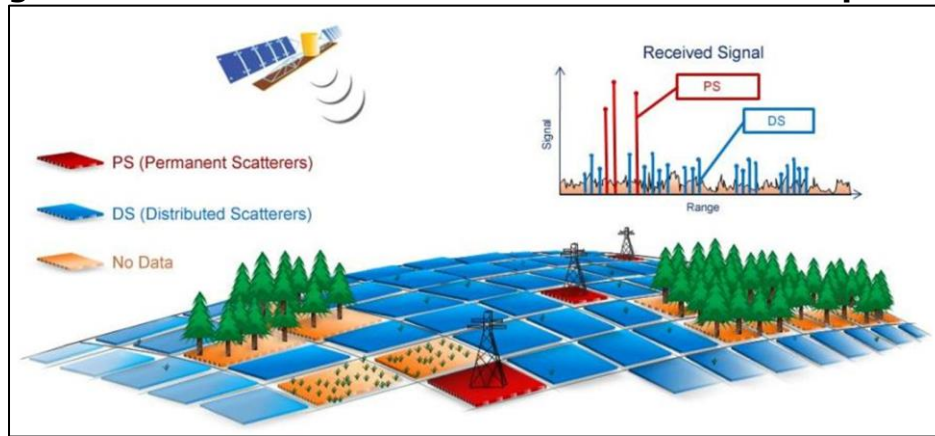
Illustration of how permanent and distributed scatterers (PS and DS) are represented in SqueeSAR. The DS signals (blue) are lower than those from the PS (red), but still significantly above the background noise (orange).

Source: TRE Altamira Inc.

SqueeSAR™ algorithm also produces improvements in the quality of the displacement time series. The homogeneous areas that produce DS normally comprise several pixels. The single time series attributed to each DS is estimated by averaging the time series of all pixels within the DS, effectively reducing noise in the data. Other than in this project, SqueeSAR was previously applied to geothermal fields in southern California (Eneva et al., 2012-2014) and Nevada (Eneva et al., 2011), as well as in the FORGE project at Fallon, NV (Ailing et al., 2018). The Envisat results have been used by Barbour et al. (2016) for the Salton Sea geothermal field, and by Wei et al. (2015) for the North Brawley geothermal field.

For the sake of simplicity, when the generic term "InSAR" appears further in the text, it means the application of the SqueeSAR technique, unless explicitly stated otherwise.

1.3.2 SqueeSAR Methodology

1.3.2.1 Radar Data Acquisition Geometry

InSAR-based approaches measure surface deformation on a one-dimensional plane, along the satellite line-of-sight (LOS). The LOS angle varies depending on the satellite and on the acquisition parameters while another important angle, that between the orbit direction and the geographic North, is nearly constant.

An ascending orbit denotes a satellite travelling from south to north and imaging to the east, while a descending orbit indicates a satellite travelling from north to south and imaging to the west. Figure 1.3 shows the geometries of the image acquisitions for the ascending and descending orbits. The symbol θ (theta) represents the angle the LOS forms with the vertical (also known as "look angle") and δ (delta) is the angle formed with the geographic North. The specific values for these angles for Coso and Imperial Valley are listed in Chapters 2, Sections 2.1 and 2.2, respectively.

The values of these angles are important to determine how sensitive the LOS measurements are to the vertical and horizontal displacement components. The sensitivity is measured between −1 and +1; the closer its absolute value to 1, the more sensitive the measurement:

$$\text{Vertical} = +\cos\theta$$

$$\text{East} = -\sin\theta*\cos\delta \text{ for ascending and } +\sin\theta*\cos\delta \text{ for descending}$$

$$\text{North} = -\sin\theta*\sin\delta$$

When the specific angles for the satellites data used are plugged in the above equations, it turns out that LOS has significant sensitivity to the Vertical (subsidence or uplift) and East horizontal (eastward or westward) components of surface movements, but the sensitivity to the North component (northward or southward) is low and therefore cannot be resolved with InSAR; see details in Chapter 2, Section 2.1 for Coso and Section 2.2 for Imperial Valley.

Figure 1.3 Orbit Geometry of Image Acquisitions
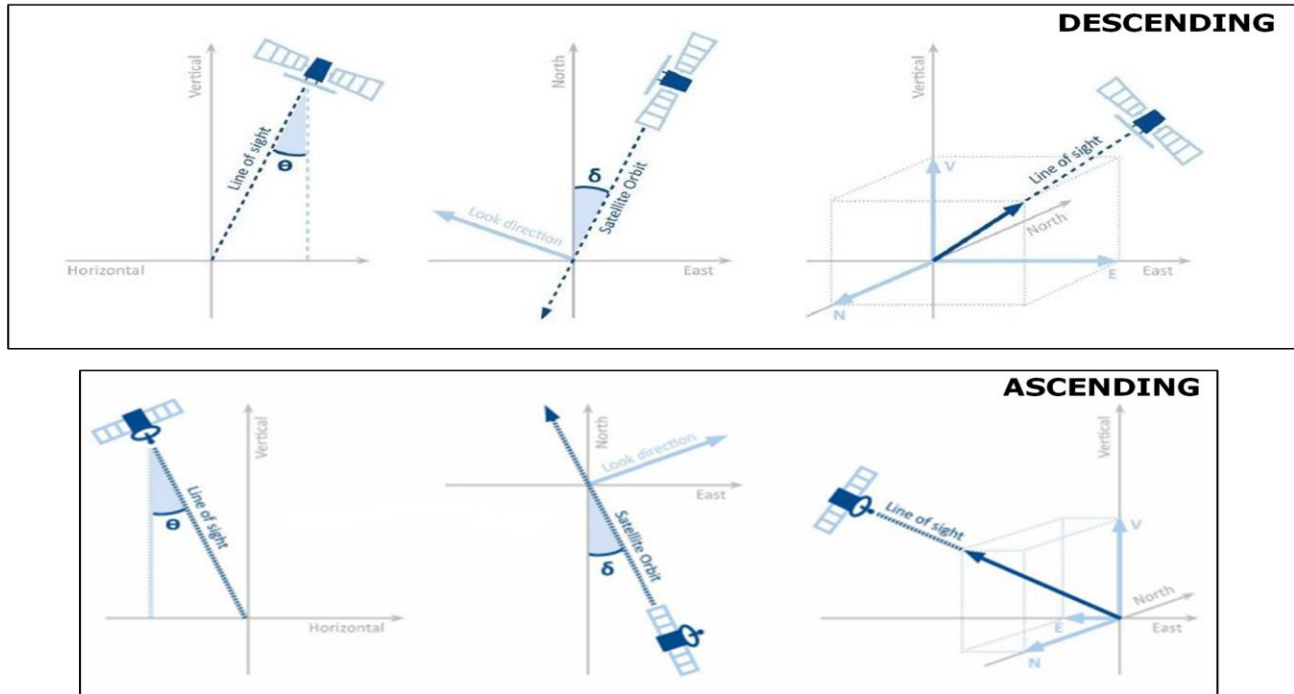
Source: TRE Altamira, modified by M. Eneva

By combining the results from two different LOS datasets, with different acquisition geometries (ascending and descending), acquired over the same area and time frame, it is possible to derive the East and Vertical components of motion (Figure 1.4) using the equations above.

Figure 1.4 Geometry of Motion Decomposition
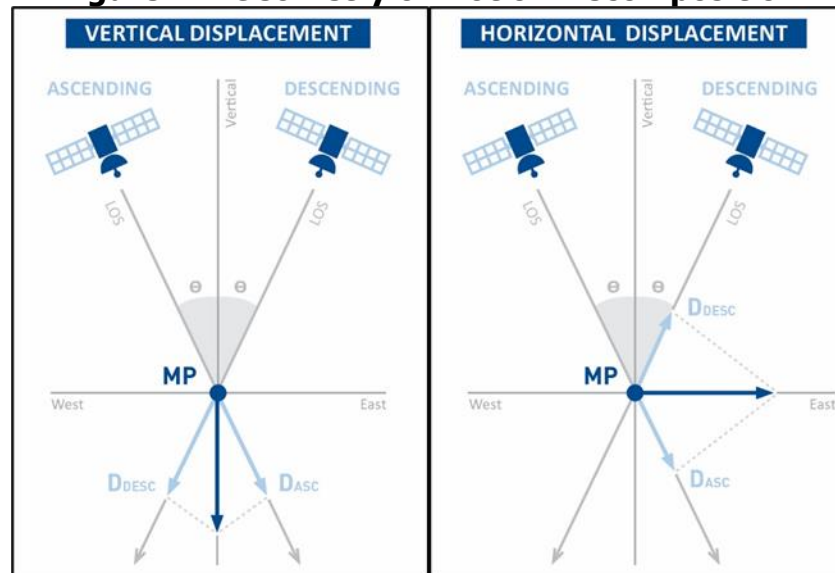
Source: TRE Altamira

The methodology to combine the LOS measurements utilizes trigonometry to calculate the two movement components (Vertical and East) from two independent measurements (ascending and descending), with the assumption that LOS sensitivity to possible motion in the North-South direction is negligible.

1.3.2.2 Data Processing

Measurement points are obtained from existing features across the study geothermal fields, including wellheads, and other man-made structures. Natural features such as rocks and exposed ground corresponding to large areas (up to hundreds of square meters) also form the basis of many measurement points. It is important to consider that all points are represented as individual points in the GIS environment for clarity of presentation and ease of interpretation.

1.3.2.3 Reference points

All deformation measurements are done using a reference point assumed to be motionless. The SqueeSAR analysis incorporates a reference point optimization procedure, where an intensive statistical analysis is performed to examine all of the identified radar targets, in order to select a PS or DS with optimal parameters as the reference point (including high coherence, low standard deviation values and low variability over time). A neighborhood comparison of surrounding points is also performed to ensure the final selection and placement of the reference point is within a stable area.

The use of an optimal reference point ensures the highest quality results are achieved, and allows for the best representation of surface deformation trends. The use of reference points with lower radiometric qualities, while unlikely to affect the reliability of the results, may produce slight increases in noise levels in the time series associated with the measurement points. Still, re-referencing to other points was also performed when necessary. For example, in Imperial Valley, the reference for each geothermal field was the location of the leveling

14

benchmark used as a datum in the leveling surveys. This makes it possible to directly compare deformation measured with the two methods (InSAR and leveling).

1.3.2.4 Standard Deviation and Precision

Standard deviation values of the deformation measurements are a function of the following factors and local ground movement dynamics: spatial density of the PS and DS (higher densities produce higher precisions); quality of the radar targets (signal-to-noise ratio levels); distance from the reference point; umber of images processed; period of time covered by the imagery; climatic conditions at the time of acquisition; and distance between a given measurement point and the reference point.

In addition to each measurement point having an associated standard deviation value to represent the error of the deformation measured, results can also be characterized by the accuracy of the technique. Specifically, three parameters are used to characterize the overall accuracy of the results: precision of the estimated deformation rates; precision of the estimated elevations; and precision of the geocoding.

Table 1.1 summarizes the typical precision values associated with the UTM coordinates of a measurement point at mid-latitudes.

Table 1.1 Typical Precision of the Locations of the Measurement Points

Direction	C-band ERS, Envisat, Radarsat [m]	C-band Sentinel [m]	X-band TSX [m]	X-band CSK [m]	L-band ALOS [m]
North	±2	±8	±1	±1	±2
East	±7	±12	±3	±1	±7
Vertical (elevation)	±1.5	±8	±1.5	±0.5	±2

Typical precision values (one standard deviation, δ) of the UTM coordinates of a measurement point at mid-latitudes. Values are referred to a measurement point at a distance <1 km from the reference point and a dataset consisting of at least 30 SAR scenes. For X-band, StripMap acquisitions are considered.

Source: TRE Altamira, modified by M. Eneva

Furthermore, the typical precision values applicable to PS located within 2 km from the reference point, when at least 45 radar images are processed, are <1 mm/year for the deformation rate and <5 mm for the displacement error (single displacement between contiguous satellite images).

1.3.2.5 Methodology of the InSAR Processing

The identification of PS and DS in a series of radar images comprises a sequence of steps. First, all radar data archives are screened to determine the most suitable source of raw data for the particular area of interest and to select all the high-quality images within the chosen data set. As the signal echo from a single point target contains many returning radar pulses, it appears defocused in a SAR raw image. The first processing step is therefore to focus all the received energy from a target in one pixel. The images are then precisely aligned to each other, or co-registered, and analyzed for their suitability for interferometry. The parameters that are analyzed are the normal baseline and the temporal distribution of the images.

The above is followed by a number of statistical analyses on the phase and amplitude characteristics of the backscattered radar signal that return to the satellite. If a concentrated number of signals reflect off a particular feature within a pixel and backscatter to the satellite, the feature is referred to as a "scatterer." When the same scatterer appears in all, or most, of a data set of SAR images for a particular location, then it is deemed to be "permanent." At this stage, it is possible to identify a subset of pixels, referred to as Permanent Scatterer Candidates (PSC), that are used to estimate the impact on signal phase of ionospheric, tropospheric and atmospheric effects, as well as possible orbit errors. Once the signal phase has been corrected for these effects, any remaining changes in it are considered to directly reflect ground movement.

1.3.2.6 Master Image Selection

SqueeSAR requires that one scene in each data set becomes both a geometric and temporal reference to which all the other images are related. This image is referred to as the "master image." The master image is chosen so that it minimizes the spread of normal baseline values for the other images, the temporal baseline values between the master and each of the remaining images, and the effects of signal noise arising from changes in vegetation cover and/or small changes in the look angle of the satellite from one scene to another.

1.3.2.7 Signal Phase and Amplitude Analysis

General background. Each pixel of a SAR image contains information on the amplitude of signals that are backscattered toward the satellite, as well as on the signal phase. The amplitude is a measure of the amount of the radar pulse energy reflected, while the phase is related to the length of the path of the electromagnetic wave, from the platform to the ground and back again. Analyses of both amplitude and phase of the SAR image provide an indication of the stability of each pixel, over time, whereby it is possible to identify those pixels that are most likely to behave as Permanent Scatterers. Statistical methods are used extensively in this process. Among the different statistical parameters that can be computed, two are of a particular interest: Phase Stability Index (PSI) obtained from the phases of the images within the data set; and Multi Image Reflectivity (MIR) map derived from the amplitude values of the available acquisitions.

Radar phase and coherence. The phase stability is strongly linked to the concept of coherence. Pixels that consistently display high phase stability are said to be coherent. Coherence is measured by an index that ranges from 0 to 1. When a pixel is completely coherent, its coherence value is 1. Correspondingly, if a pixel has a low phase stability, its coherence index will be 0. In general, interferometry is successful when the coherence index is between 0.5 and 1.0.

Radar amplitude and multi-image reflectivity. The amplitude of a pixel within a SAR image is the aggregate of the backscattered energy toward the satellite from within the pixel's equivalent land area. This equivalent land area is referred to as the radar resolution. It is necessary to look into the amplitude values of all the images in the data set, in order to understand exactly what was seen by the satellite at the time of each acquisition. If a target has experienced significant change in its surface characteristics, it will exhibit variation in its reflectivity (electromagnetic response) between two acquisitions. In such circumstances, the possibility of detecting movement by means of SAR interferometry is seriously compromised.

In that case, the signal phase difference between the two images contains not only the contribution due to deformation, but also deviations due to the change in the reflectivity of the target. This prevents, in the worst case, the obtaining of any useful information on ground movement. Accordingly, it is necessary to look into the amplitude values of all the images in the data set, in order to understand exactly what was seen by the satellite at the time of each acquisition.

Another artifact linked to amplitude is known as "speckle." It is a random noise that appears as a grainy salt and pepper texture in an amplitude image. This is caused by random interference from the multiple scattering returns that occur within each resolution cell. Speckle has an adverse impact on the quality and usefulness of SAR images. However, the higher the number of images taken of the same area at different times, or from slightly different look angles, the easier it is to reduce speckle. This increases the quality and level of details of the amplitude image, which makes it useful as a background layer for observing the presence of PS points. The Multi Image Reflectivity (MIR) map is the means by which speckle reduction is accomplished. Averaging a number of images tends to negate the random amplitude variability, leaving the uniform amplitude level unchanged. The information in the MIR map is the reflectivity of each pixel, i.e., the ability to backscatter the incident wave toward the satellite. Flat surfaces (roads, highway, rivers, and lakes) act like a mirror, meaning that if their orientation is not exactly perpendicular to the incident wave, negligible energy is reflected back to the sensor and they appear dark in the image. On the other hand, because of their irregular physical shape, metal structures or buildings reflect a significant portion of the incident signal back to the radar, resulting in very bright pixels in the MIR map.

Interferograms. After the statistical analyses of the SAR images have been completed, a set of differential interferograms is generated. This entails subtracting the phase of each image from the phase of the master image. In doing so, the difference in signal path length between the two images is calculated. This difference is related to possible ground motion. In any SAR image, there are embedded topographic distortions that arise during image acquisition. These are removed using a reference Digital Elevation Model (DEM), leaving ground movement and the signal phase distortions arising from atmospheric effects as the only embedded variables. The differential interferograms represent the starting point for applying the approach based on PS and DS.

Estimation of the Atmospheric Effects. When a radar signal enters and exits a moisture-bearing layer in the atmosphere, its wavelength can be affected, introducing potential errors into the signal path length. The removal of atmospheric impacts is fundamental for increasing the precision of ground movement measurement. A subset of pixels, usually corresponding to buildings, lampposts, antennas, small structures and exposed rocks, is chosen from among those that have high PSI values. These are referred to as PS Candidates (PSC). PSC density is higher in towns and cities compared with forests and vegetated areas. However, it is often possible to obtain good PSC density in rural areas. For each image, the atmospheric impacts are estimated at each PSC location. The process is statistically based and benefits in accuracy by greater number of available images for the analysis. By comparing the atmospheric contribution on neighboring pixels that would be experiencing the same atmospheric conditions, the atmospheric contribution can be reconstructed over the whole image. The

processed data set allows identification of a PSC cluster dense enough to identify and extract the atmospheric contribution over the entire area of interest.

Post-processing. Finally, the processed data undergoes a thorough quality control following ISO 9001:2000 guidelines. The PS and DS data are checked for anomalies, aligned on an optical image.

1.4 Data Used

The project team used satellite data collected over the Coso geothermal field and three fields in the Imperial Valley of southern California – Salton Sea, North Brawley, and Heber. The satellite data were from the European satellite Envisat (February 2003 – October 2010) for Coso, two successor satellites Sentinel (late 2014 – ongoing) for all study fields, and the German satellite TerraSAR-X (Aug 2012 – Oct 2013) for Salton Sea and North Brawley. Envisat results were also used from a previous project with the California Energy Commission (CEC) for Imperial Valley. East Mesa (Ormesa), the fourth operating field in southern California, was not studied in this project, because the track of the processed Sentinel scenes covered only the three other fields; a separate processing of additional satellite images from another track would have been necessary, which would result in increased analysis cost. However, Envisat results for East Mesa are available from the previous CEC project (Eneva et al., 2012).

Further in the text, these satellites, SAR scenes from them, and the periods associated with the individual data sets are denoted as ENV (for Envisat), TSX (for TerraSAR-X), and SNT (for Sentinel). In the case of Sentinel, in order to designate between an earlier and a later Sentinel period for which data were processed separately, the acronyms SNT1 and SNT2 are used.

In addition, the project made use of ground-based surveys in the form of GPS subsidence surveys at Coso and leveling surveys in the geothermal fields of Imperial Valley. The surveys at Coso started in 1988 and took place every year initially, then more rarely, with a frequency ≥3 years since 2000. These data were provided by the U.S. Navy Geothermal Program Office (GPO). The leveling surveys in Imperial Valley are conducted annually by the geothermal operators. The Imperial County Department of Public Works (ICDPW) provided these data.

Information about the monthly production and injection fluid mass was also used. This information is provided by the GPO for the Coso geothermal field and the California Geologic Energy Management Division, CalGEM (formerly Division of Oil, Gas, and Geothermal Resources, DOGGR) for the fields in Imperial Valley.

Finally, information on earthquakes that have occurred on the territories of the four study geothermal fields was incorporated, using various catalogs.

Figure 1.5 Types of Data Presentation
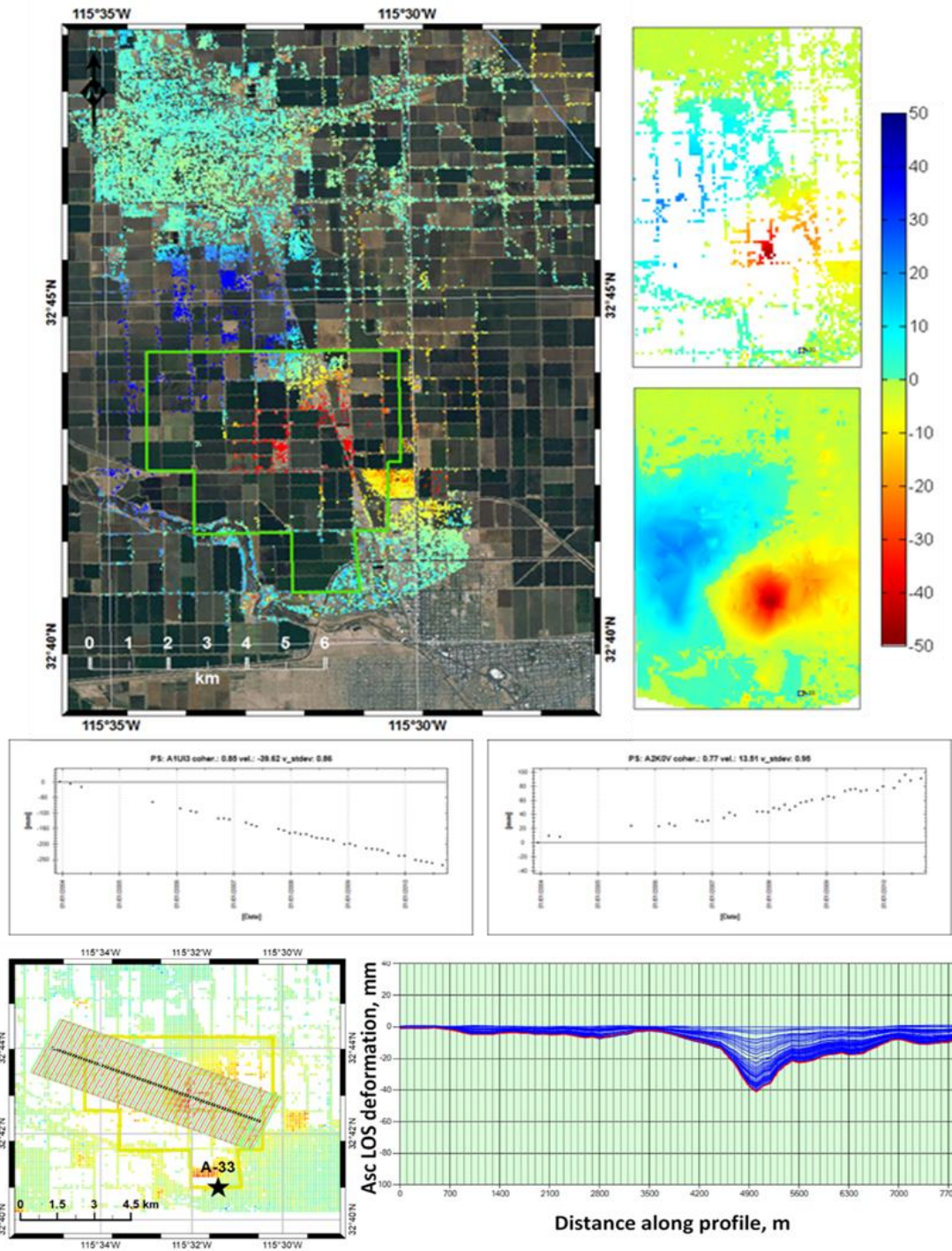
Maps show color-coded annual rates in mm/year. Upper left – ENV ascending LOS rates at individual PS and DS points. Upper right – mean LOS ascending rates within 200-m pixels and interpolated LOS ascending rates from these pixels. Middle – example of LOS time series showing decreasing and increasing trends of deformation. Bottom – example of ascending LOS deformation as it progresses in time along a profile.

Source: M. Eneva

19

1.5 Presentation of Surface Deformation Results

Figure 1.5 shows the type of presentations used in the subsequent text. Imageair Inc. received the InSAR measurements from TRE (using the SqueeSAR technique), in terms of PS and DS locations, ascending and descending LOS deformation time series at these points, mean vertical and east horizontal time series at pixels encompassing PS and DS points from LOS, and estimates of the respective deformation rates from the slopes of straight lines through these time series. The additional analysis Imageair Inc. performed included, but was not limited to, the following: re-referencing when needed; creating deformation maps of LOS rates at individual PS and DS locations, of mean LOS/vertical/east rates in pixels of different sizes (e.g., 100 m), and of interpolated rates; mean time series and rates for polygons of interest; deformation histories along profiles; comparison with seismicity; comparison with leveling surveys; comparisons with production and injection fluid mass; etc.

The annual rates shown in the deformation maps are color-coded (Fig. 1.5). For LOS and vertical movements, "warm" colors (red to yellow) are used to indicate negative movements and "cold" colors (blue) to show positive movements. When LOS deformation is shown, negative and positive displacements mean movements away from and toward the satellite, respectively. For the decomposed vertical movements, negative values indicate subsidence and positive values show uplift. For the decomposed east movements, negative values indicate westward movements and positive values show eastward movements.

Since the satellite look (incidence) angle is steep, the LOS movements are highly sensitive to the vertical displacements, so often the patterns revealed by LOS and vertical movements are visually similar, where LOS movements away from the satellite are indicative of subsidence, and toward the satellite – of uplift. This may not hold however, when the horizontal movements are significantly larger than the vertical ones.

The top portion of Fig. 1.5 shows three types of deformation maps (LOS at individual PS and DS points, pixel-based, and interpolated) used in the analysis. Note the significantly higher density of PS and DS in urban areas, while in agricultural areas the PS and DS align along roads and canals. The latter makes it possible to derive important information on surface deformation, which was impossible with conventional DInSAR. Also note that the map of interpolated deformation shows two adjacent areas, one of subsidence (red), and the other of uplift (blue). The middle portion of Fig. 1.5 shows examples of LOS deformation time series from two individual PS points – the decreasing deformation trend indicates displacement away from the satellite and the increasing time series shows movement toward the satellite. In many cases, mean time series are calculated within pixels or arbitrary polygons. They resemble the time series shown here; for any polygon, four types of such mean series can be calculated, reflecting LOS ascending, LOS descending, vertical, and east horizontal movements. In all cases, the respective annual rates are calculated as the slopes of the straight lines fitted to the time series. Finally, Fig. 1.5 shows an example of the progression of deformation along a profile. This particular profile indicates an ascending LOS movement away from the satellite, actually representing the development of subsidence over time. The examples in Fig. 1.5 are shown here for generic purposes (they happen to be from the Heber geothermal field, which will be discussed in more detail in Chapter 2).

CHAPTER 2:
Geothermal Fields

2.1 Coso Geothermal Field

2.1.1 Description of the Coso Study Area

The Coso geothermal field (henceforth referred to as "Coso") is located on the lands of the military-owned Naval Air Weapons Station (NAWS) at China Lake, in the central part of eastern California (Figure 2.1). It is managed by the U.S. Navy GPO, and is operated by the Coso Operating Company. It has been producing geothermal power since 1987 and currently has four operating plants.

Figure 2.1 Coso Geothermal Field at NAWS

Coso geothermal field within the boundaries of the Naval Air Weapons Station, China Lake, California.

Source: Monastero (2002)

The mean capacity of the Coso KGRA (Known Geothermal Resource Area) is estimated at 518 MW (USGS, 2008). The produced electric power has been often cited as 270 MW (Monastero, 2002), placing Coso third in the U.S (and California), after The Geysers in northern California and the geothermal fields in Imperial Valley of southern California. However, this hot resource has been drying up, and the production has declined by now, despite bringing outside water to inject into the reservoir. The latest information from 2018 for the electric power produced (Table 2.1) indicates gross 156 MW and net 134 MW on average. This still leaves Coso in the third place in California, but it may be occupying a fourth place in the U.S. by now, as the power produced by the [McGinness geothermal complex in Nevada is listed at 140 MW by Ormat](https://www.ormat.com/en/renewables/geothermal/view/?ContentID=89) (https://www.ormat.com/en/renewables/geothermal/view/?ContentID=89), without specifying if this is gross or net power.

Table 2.1 Electric Power Produced at Coso in 2018

Coso Area	Gross, MWh	Net, MWh	Installed Capacity, MW	Gross Power, MW	Net Power, MW	Percentage Net/Gross
BLM	342,874	284,543	100.0	39.14	32.48	83.0%
Navy I	541,402	480,839	102.4	61.80	54.89	88.8%
Navy II	481,709	410,115	100.0	54.99	46.82	85.1%
Total Coso	1,365,985	1,175,497	302.4	155.93	134.19	86.1%

Values in the blue cells of columns 5 and 6 show average electric power from three areas (listed in column 1), calculated from the gross and net energy produced in 2018 (white cells in columns 2 and 3). The blue cells in column 7 show the percentage of net to gross power for the three areas. The yellow cells in columns 2 to 6 show total values, and in column 7 average net/gross ratio percentage, for the whole geothermal field. The gross and net power (yellow cells in columns 5 and 6) are 52 percent and 44 percent of installed capacity, respectively.

Source: Information in white cells is from California Energy Commission, California Geothermal Energy Statistics and Data (https://ww2.energy.ca.gov/almanac/renewables_data/geothermal/index_cms.php). M. Eneva calculated values in blue and yellow cells.

Coso is a volcanic field located in the area of a releasing bend step-over in a dextral strike-slip fault system. The shallow (<2 km) and very hot (200° - 328°C) resource is related to local crustal thinning (Monastero, 2002). There are numerous surface manifestations (Figure 2.2) of geothermal activity, including fumaroles, hot springs, hydrothermally altered rocks, and Late Cenozoic volcanics including 37 rhyolite domes. At least three sets of faults are mapped in the region, controlling most of the volcanic and geothermal activity. The known geothermal resource area (KGRA) is shown in Figure 2.3. There have been numerous geophysical studies at Coso, featuring microseismicity and seismic velocity models (e.g., Seher et al., 2011; Kaven et al., 2011-2015; Trugman et al., 2016), a magnetotelluric experiment resulting in a 3D-resistivity model (Newman et al., 2008), collection and analysis of gravity data (Monastero et al., 2005), temperature studies from 2-m surveys (Combs, 1980; LeSchack and Lewis, 1983; Blake et al., 2020) and thermal infrared satellite imagery (Eneva et al., 2007; Eneva and Coolbaugh, 2009; Eneva, 2012), LiDAR study (Blake et al., 2018), and most relevant to this project, older InSAR studies of surface deformation (Fialko and Simons, 2000; Wicks et al., 2001; Vasco et al., 2002; Eneva, 2010a; Eneva et al., 2009-2013), as well as newer ones, including work by the project team (Eneva et al., 2018-2020; Reinisch et al., 2020).

Figure 2.2 Surface Manifestations of the Geothermal Resource at Coso

Source: Photos by M. Eneva.

Figure 2.3 Coso KGRA
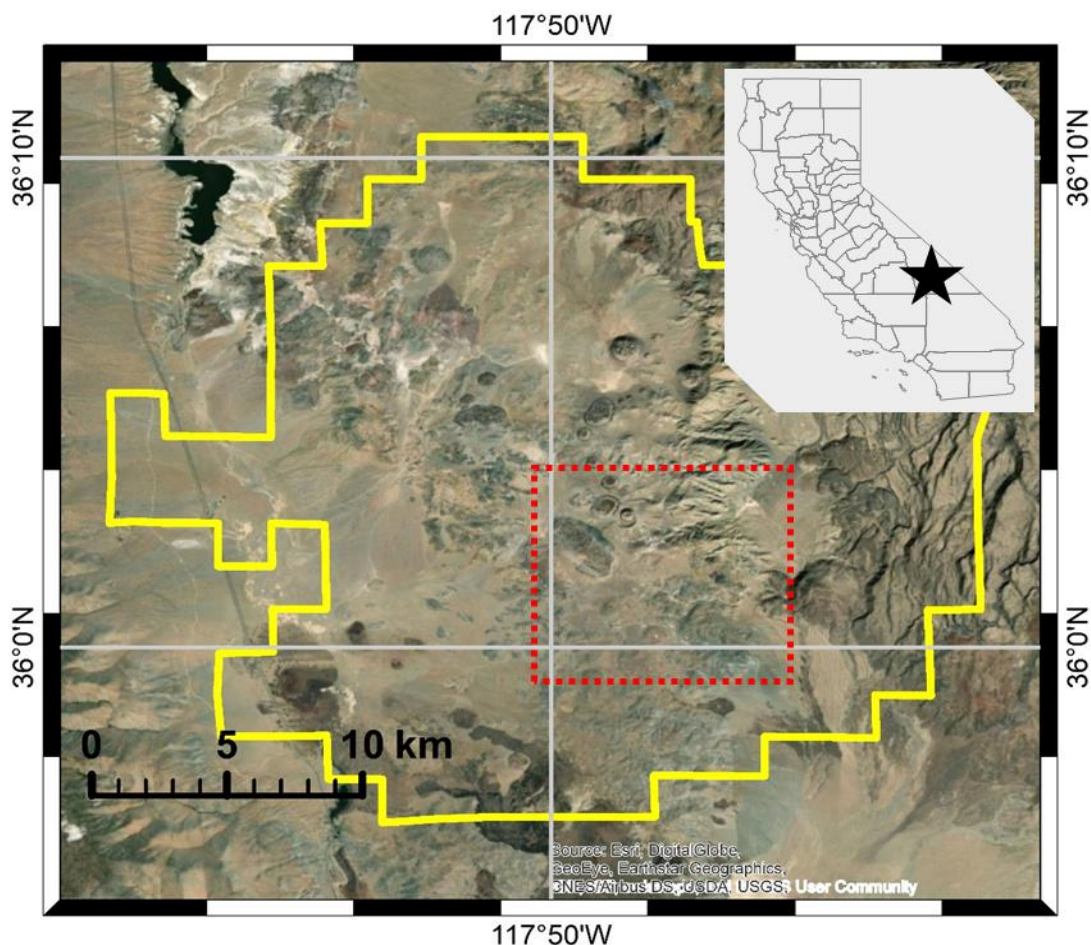
Map of the Coso geothermal field in the eastern part of central California. Yellow polygon marks the known geothermal resource area (KGRA). Dashed red square outlines the location of the geothermal field. Inset shows the state of California, with black star marking the location of the map.

Source: M. Eneva

Since Coso is liquid-limited, injecting supplemental water into the reservoir to stabilize and enhance the field was implemented in December 2009, with the hope to increase electricity production by about 50 MW. Water was pumped through a 14-km pipeline from two wells of the Hay Ranch in Rose Valley to the east of the field. The pumping was suspended for one

year by the Inyo County, starting in June 2016, due to draught and drawdown of the water table, resumed later, but ended by the fall of 2018.

2.1.2 Data Used at Coso

2.1.2.1 Satellite Data

Envisat and Sentinel data were used, processing three data sets, as shown in Table 2.2. The table lists the numbers of ascending and descending images used in the processing, the minimum revisit time that changes from 35 days (ENV) to 6 days (late SNT2, after March 2019), and the periods covered by the ascending/descending data and for which vertical and east horizontal components (Z/E in the table) could be calculated. Two large earthquakes of M6.4 and M7.1 occurred south of Coso on July 4 and 5, 2019, which had a large impact on the overall surface deformation at Coso. For this reason, to isolate the surface deformation associated only with the geothermal operations, a modified SNT2 data set was studied that was cut to July 4, 2019 (i.e., before the first large earthquake occurred). However, the extended SNT2 period was considered to evaluate the effect of the large events. The area size for which ENV images were processed was ~450 km^2, and for SNT1 and SNT2 - ~470 km^2 (extended a little bit to the south from the ENV area).

Table 2.2 Satellite Data Used for Coso

Satellite	Num Asc	Num Desc	Min Rev Time, days	Period Asc	Period Desc	Period Z/E
ENV	45	30	35	June 30, 2004 – Sep 22, 2010	Deb 2, 2006 – Oct 14, 2010	Feb 2, 2006 – Sep 22, 2010
SNT1	65	63	24, 12	Nov 3, 2014 – Apr 22, 2018	Jan 26, 2015 – Apr 16, 2018	Jan 26, 2015 – Apr 16, 2018
SNT 2	34	54	12, 6	May 4, 2018 – Jul 4, 2019	May 10, 2018 – July 4, 2020	May 10, 2018 – Jul 4, 2019
SNT2	41	41	12, 6	May 4, 2018 – Aug 27, 2019	May 10, 2018 – Aug 27, 2019	May 10, 2018 – Aug 27, 2019

Source: Table by M. Eneva, data by TRE Altamira.

2.1.2.2 Production and Injection Data

Figures 2.4 and 2.5 show maps with production and injection wellbores and wellheads. The wells are in three main areas, designated as Navy I, Navy II, and BLM. There are also five BLM-North wells within the Navy I and Navy II areas. The GPO has provided databases of wellbores and time series of fluid masses. A few of the wells are only present in one of the databases. There are some data on a total of 186 wells, including abandoned ones. Time series of fluid masses are available for 99 production and 50 injection wells. There was a production decline over time, due to drying out of the reservoir, which led to the strategy of pumping outside water from two Hay Ranch wells in Rose Valley to the west of Coso (Figure 2.6).

The total monthly production and injection fluid mass at Coso is shown in Figure 2.7, as reported to the California Geologic Energy Management Division, CalGEM (formerly Division of Oil, Gas, and Geothermal Resources, DOGGR). The water pumping from Hay Ranch started in late December 2009 and continued until the fall of 2018, with an interruption between mid-2016 and mid-2017 due to statewide drought. The addition of water pumped from Hay Ranch

24

is seen most clearly as a "bump" in the injection time series in Fig. 2.7. Although this strategy did not boost the production to the desired level, it seems that it did prevent further decline and helped to maintain a steadier net production after late 2011 than it would have been achieved without the injection augmentation. The total monthly time series of the pumped water was first obtained from the Inyo County Water Department. However, because the pumped water was collected in a tank and used later, this time series does not necessarily reflect accurately the time series of augmented injection at Coso, so data provided by the GPO was used for the purpose. The Hay Ranch water was mostly pumped in 12 Navy I wells, with some early limited injection in two Navy II wells and one BLM-North well. Over the eight years of pumping, 23.2×10^9 kg of water was injected in these 15 wells, which represented 20.5 percent of the total injected fluids in the whole field, for the same period (113×10^9 kg). A small portion of the Hay Ranch water was injected in wells designated as production wells in the database from 2018-2019.

Figure 2.4 Map of Wellbores at Coso
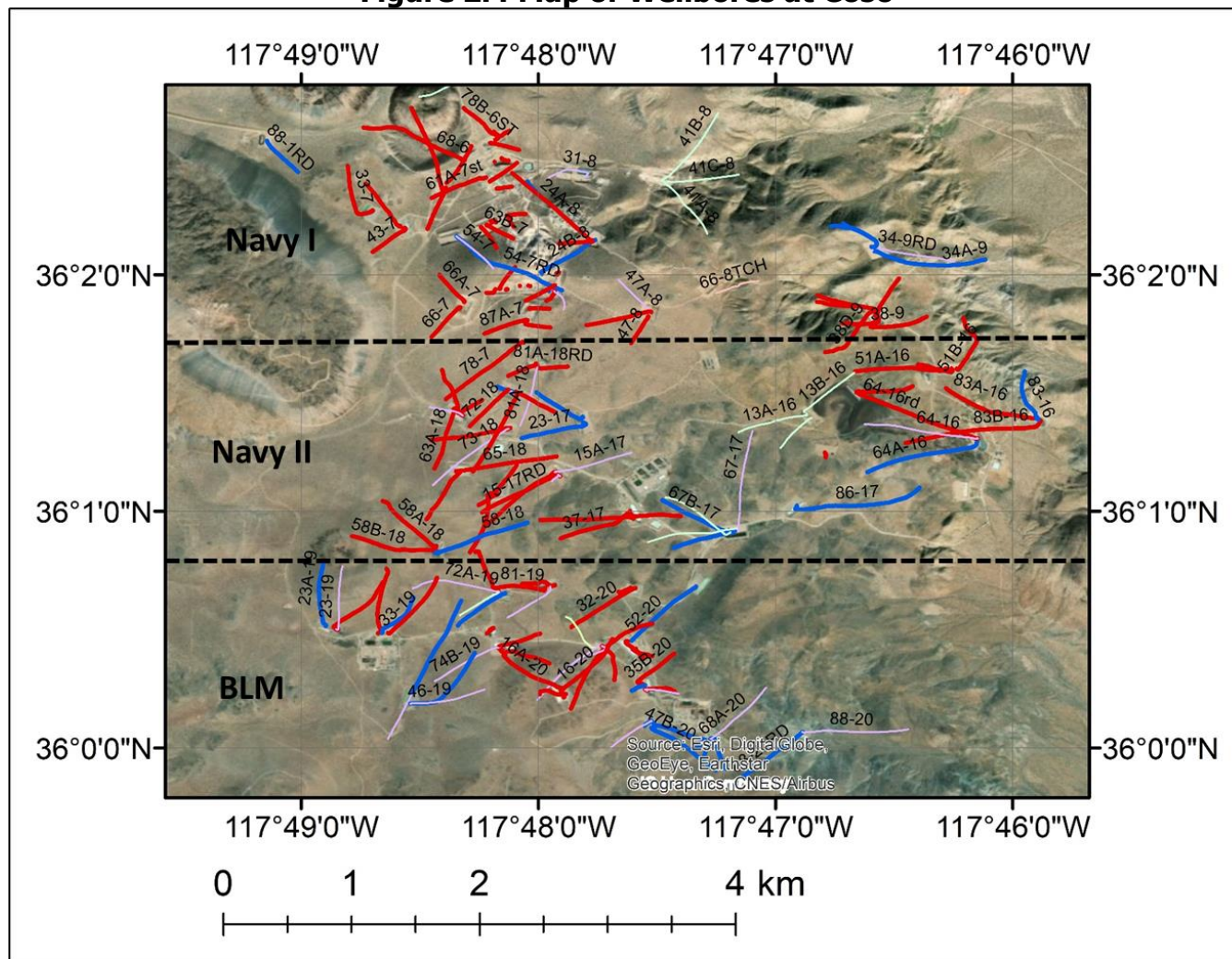
Surface projections of the production (red lines) and injection (blue lines) wellbores at Coso. Thin lines of other colors mark non-active wells, such as abandoned ones. Dashed black lines separate the Navy I, Navy II and BLM areas. Superimposed on a satellite image (from ArcGIS).

Source: Figure by M. Eneva, data by GPO.

Figure 2.5 Map of Wellheads at Coso
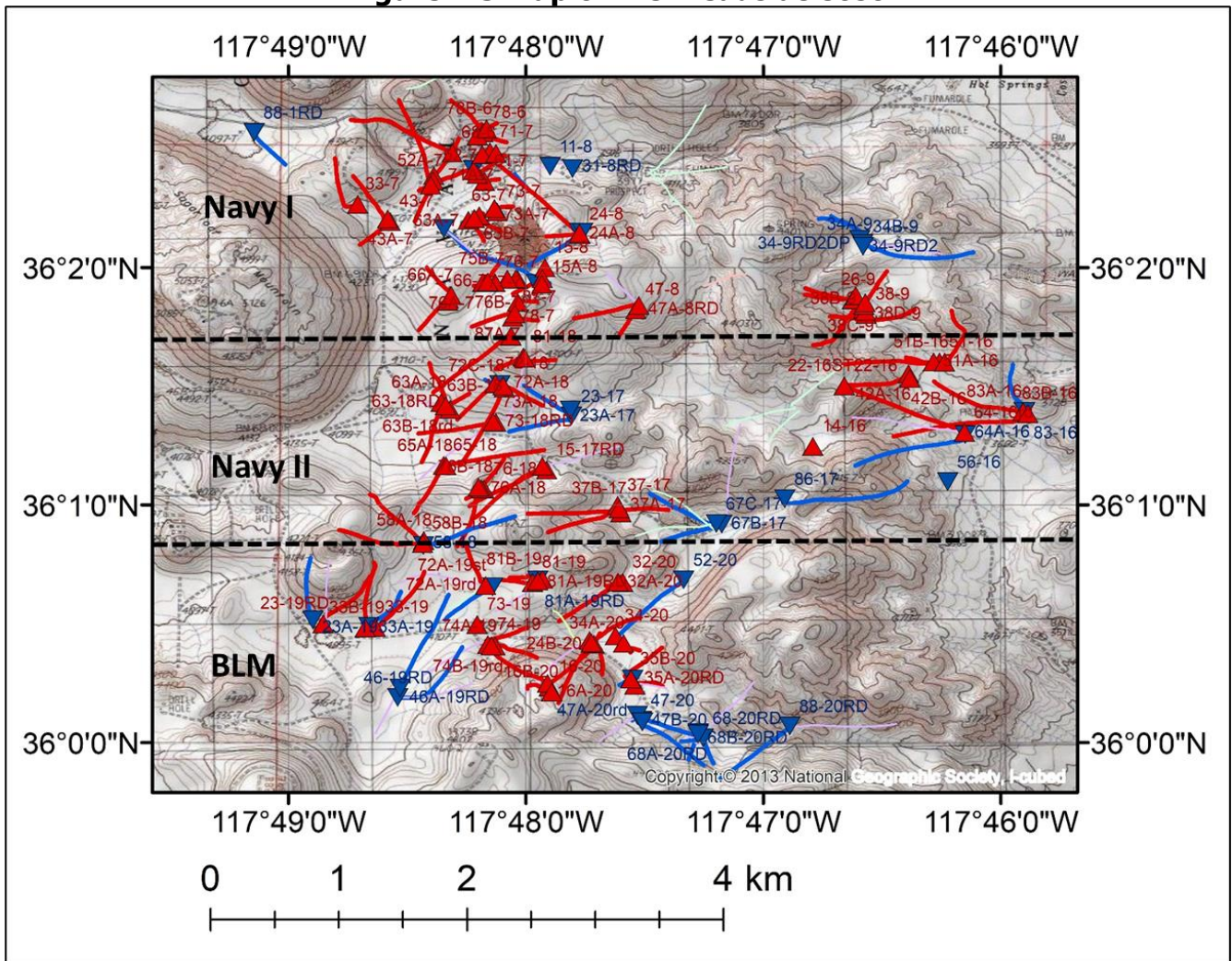
**Map of wellheads and wellbores. Colors like in
Fig. 2.4. Superimposed on a topographic map (from ArcGIS).**

Source: Figure by M. Eneva, data by GPO.

The largest amount of Hay Ranch water was pumped into existing injection wells. In particular, wells 24B-8 and CEGH-1 received 43 percent and 20 percent of the water, respectively, of all the fluid pumped into the wells receiving Hay Ranch water (Fig. 2.6). They were also the only ones that continued after the draught-associated cessation of pumping from Hay Ranch in 2016-2017, for a few months until late 2017 (24B-8) and all the way to the end of pumping, Sep 2018 (CEGH-1). Three other wells received another 22 percent of the fluids. Figure 2.8 shows monthly normalized injection values for all the wells that received water from Hay Ranch, as well as in the individual areas Navy I, Navy II, and BLM-North. The maximum monthly injection from all wells using Hay Ranch water was the denominator in the normalization.

Figure 2.6 Maps showing Coso Wells Receiving Pumped Water from Hay Ranch
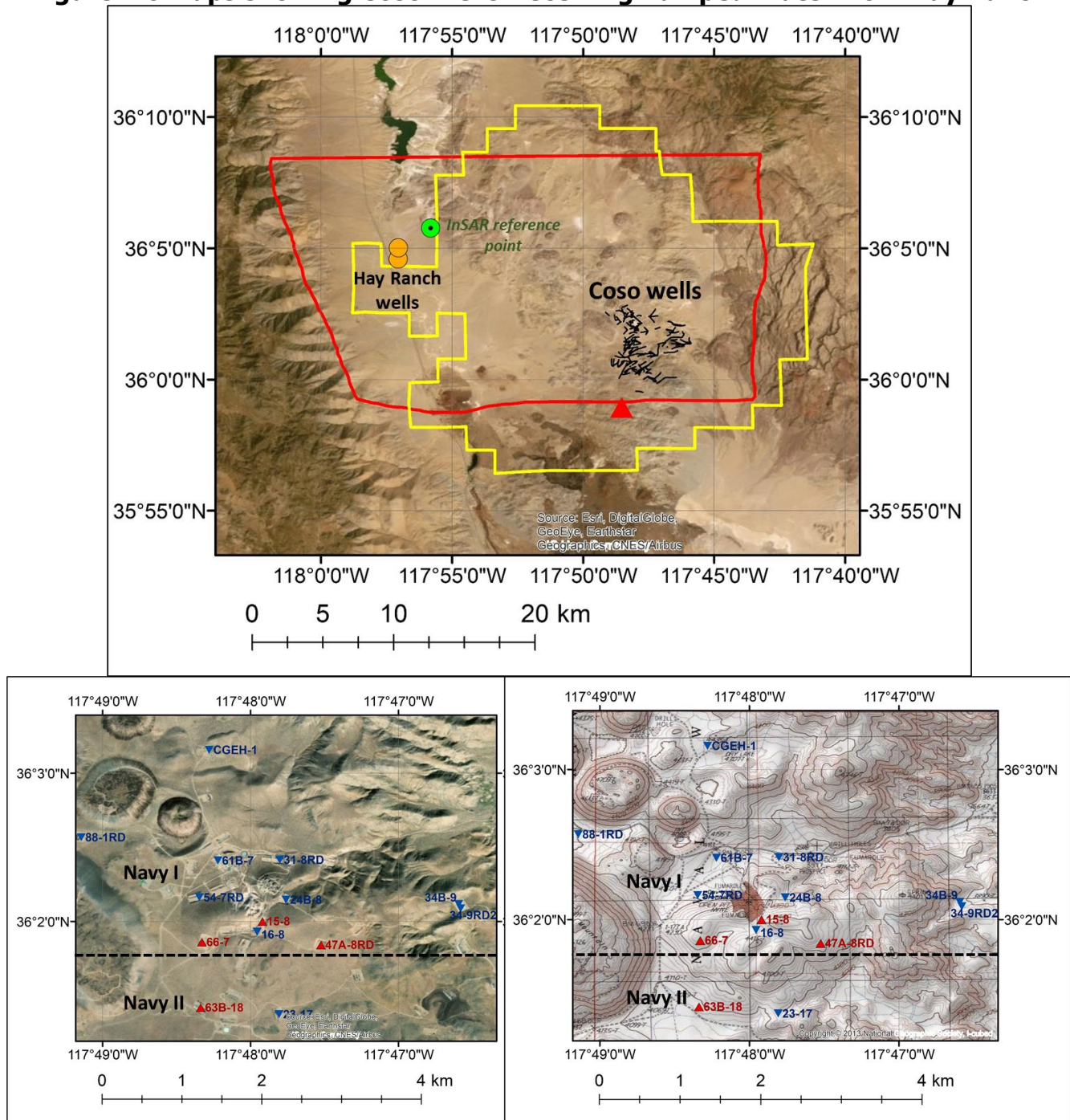
Top – Map of the extended study area (red outline), showing the Coso KGRA (yellow outline), the two Hay Ranch wells (orange circles), the InSAR reference points (green circle), and all Coso wellbore surface projections (black lines). Bottom – maps of the wellheads where Hay Ranch water was pumped; red triangles and inverted blue triangles mark production and injection wells, respectively. Maximum pumping took place in injection wells 24B-8 and CGEH-1 (see text). Superimposed on a satellite image (left) and a topographic map (right) (from ArcGIS).

Source: Figure by M. Eneva, data by GPO.

Figure 2.7 Monthly Fluid Mass Time Series
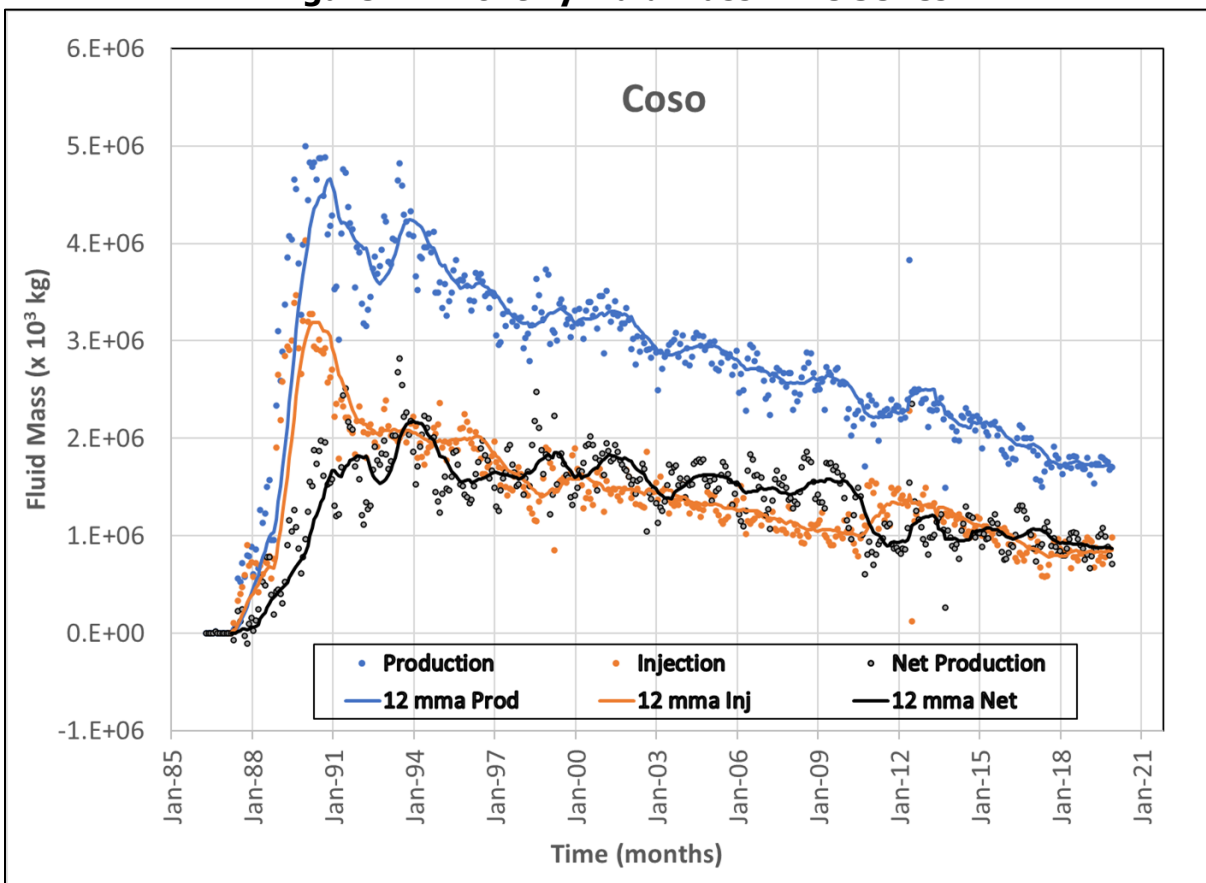
Monthly time series of total produced and injected fluid mass from all Coso wells, as well as of total net production (production minus injection).
Lines show 12-month moving average (mma) values.

Source: Figure by M. Eneva, data from CalGEM (https://www.conservation.ca.gov/calgem).

Figure 2.8 Monthly Time Series of Fluid Mass for Wells Receiving Water from Hay Ranch
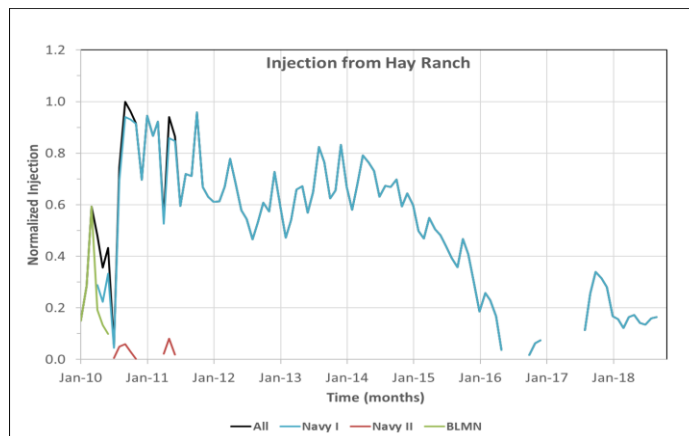
Source: Figure by M. Eneva, data by GPO.

2.1.2.3 Ground-Based Subsidence Surveys

Ground-based subsidence measurements at the Coso geothermal field have been documented in subsidence reports since 1988. These data have been provided by the U.S. Navy GPO. The second survey was in 1992, followed by four more surveys every year (1993-1996), one survey two years later (2000), and after that, five more surveys every 3-3.5 years (2003, 2006, 2009, 2013, and 2017). The subsidence surveys at Coso started with leveling benchmarks, which were replaced by GPS stations in 1996. The subsidence reports state that the certainty of the ellipsoid heights is between 2 mm and 9 mm at the 95-percent confidence level, while the mean vertical positional certainty at the 95-percent confidence level is from ±5.5 mm (earlier reports) to ±3.4 mm (later reports).

Figure 2.9 shows two maps with the locations of 115 GPS stations, but not all benchmark/GPS stations were surveyed each time surveys took place – some were used only in the earlier years, others started later. By the start time of the satellite data processed in this project, measurements were done at 73 GPS stations. Of these surveys, only three took place during the periods covered by the satellite data – two in 2006 and 2009 (ENV period), and one in the fall of 2017 (SNT1 period). The datum benchmark used in the leveling surveys is B14, 2.65 km SW from benchmark CE3 that shows the highest level of subsidence among all benchmarks.

Figure 2.9 Subsidence Surveys at Coso
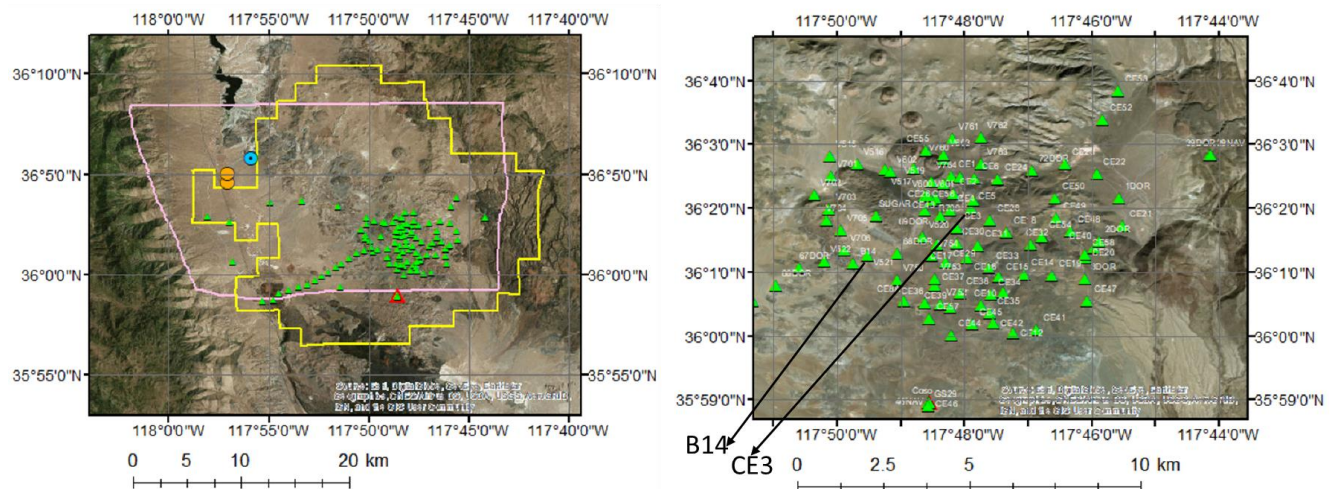
Left: Map of extended study area. Yellow outline – Coso KGRA. Pink outline – InSAR study area in this project. Green triangles – benchmarks/GPS stations used in subsidence surveys. Red triangle – COSO GPS station. Two orange circles – locations of Hay Ranch wells, from which water was pumped into some of the Coso wells. Blue circle – reference point used in the InSAR analysis. Right: Map focused on the geothermal field. Arrows mark stations CE3 and B14 – see main text.

Source: Figure by M. Eneva, well locations by GPO.

Figure 2.10 shows all observed time series from the subsidence surveys. With very few exceptions, subsidence is observed at most stations (compared to the datum, B14). It can be also visually noticed that many stations show reduced subsidence rates (slopes of straight lines) after about 2006, which is likely due to the gradually decreasing production.

Figure 2.10 Subsidence Time Series from Surveys at Coso (Ref. B14)
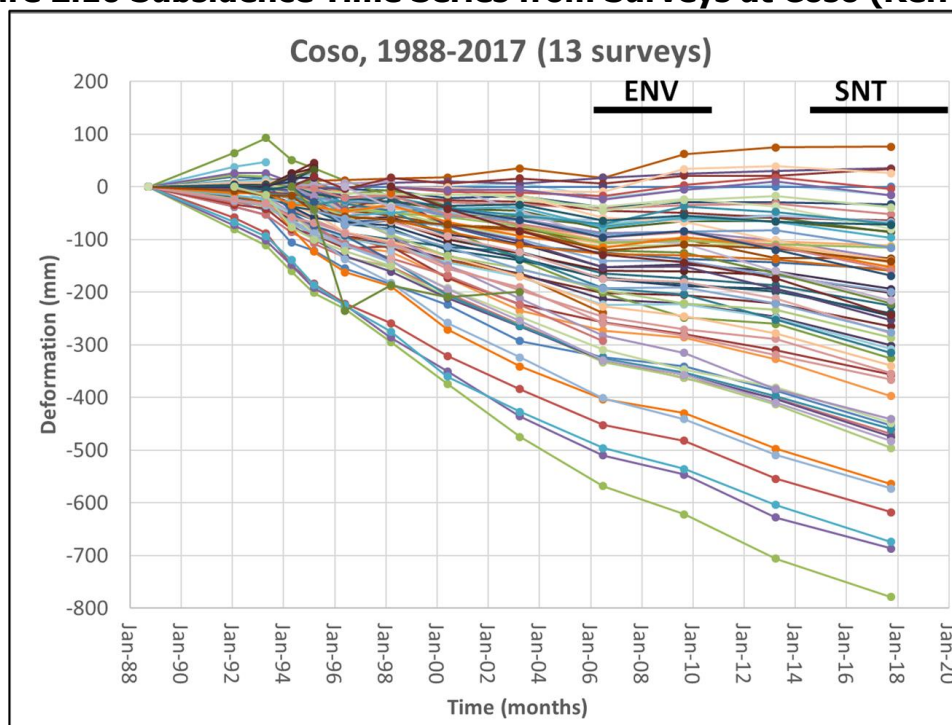
Source: Figure by M. Eneva, data by GPO.

Table 2.3 shows subsidence rates calculated for station CE3 in different periods, in order of decreasing number of surveys used. Obviously, a rate calculated from 13, seven or even five surveys, is more reliable than rates calculated from two surveys. CE3 ranks high in all these periods, and when it does not rank the highest, the rates for the stations ranking higher are calculated only from two surveys and are therefore questionable. The subsidence curve for CE3 is the bottom one (light green) in Fig. 2.10. Both this figure and the table show that an earlier rate calculated from seven surveys (1993-2003) is significantly higher than that for a later period (2003-2017). Such decrease in subsidence with time is representative for many of the other stations, and is confirmed by the InSAR measurements.

Table 2.3 Survey Subsidence Rates at CE3 in Different Periods (Ref. B14)

Period	Number of Surveys	Rate, mm/year	Rank	Notes
1988 – 2017	13	-28.6	2	Another station -33.4 mm/year, but only from two surveys, 1994 and 1995
1993 – 2003	7	-35.7	1	
2003 – 2017	5	-20.7	3	Two other stations up to -22.4 mm/year, but only from two surveys, 2003 and 2006
1988 – 1993	3	-24.2	1	
2006 – 2009	2	-17.0	1	
2013 – 2017	2	-16.2	2	Another station -18.4 mm/year, but only from two surveys, 2013 - 2017

Source: M. Eneva

2.1.2.4 Seismicity Data

The earthquakes in the area around Coso are predominantly dextral strike-slip events, consistent with the minimum of 150-170 km of extension that affected the southwestern Basin and Range region in the late Cenozoic. There have been a number of studies of the seismicity at Coso, both natural and induced. For example, Schoenball et al. (2015), studied the space-time clustering of microearthquakes and their self-similarity, and Kaven et al. (2014, 2015) reported on the seismic moment release. Recent microseismicity within the field is related to production and injection of fluids and is diagnostic of fracture permeability.

Seismic monitoring at Coso began in 1975 with 16 stations operated by the USGS. The U.S. Navy has now a permanent seismometer network operating since the 1980's, which was significantly upgraded in 1992.

In this project, earthquake data from three catalogs were analyzed:

- GPO – the Geothermal Program Office of the U.S. Navy provided the earthquake catalog from their local network for the period 1/1/2010 – 1/1/2018. This catalog contains data gaps as follows: no data for 2011; data gaps in 2015 in the periods Jan 22 – Apr 2, Apr 6 – Jun 3, Oct 2-16, and on Nov 19 and Dec 21; and in 2016, a Jan 1 – Mar 3 data gap.
- Lin et al. – this catalog covers the period 1/1/1995 – 1/1/2019. It is extended from Lin et al. (2007) and Hauksson et al. (2012).
- Kaven et al. – this catalog covers the period 3/1/1996 – 4/6/2015. Waveform data from the GPO network were used to relocate the earthquakes, as described by Kaven et al. (2014).

2.1.2.5 LiDAR Data

LiDAR data were collected in 2017 (Blake et al., 2018). They were used to obtain a digital elevation model (DEM) for the field and to outline lineaments (Figure 2.11) that were compared with the surface deformation obtained from InSAR (see Section 2.1.3).

Figure 2.11 LiDAR Data at Coso
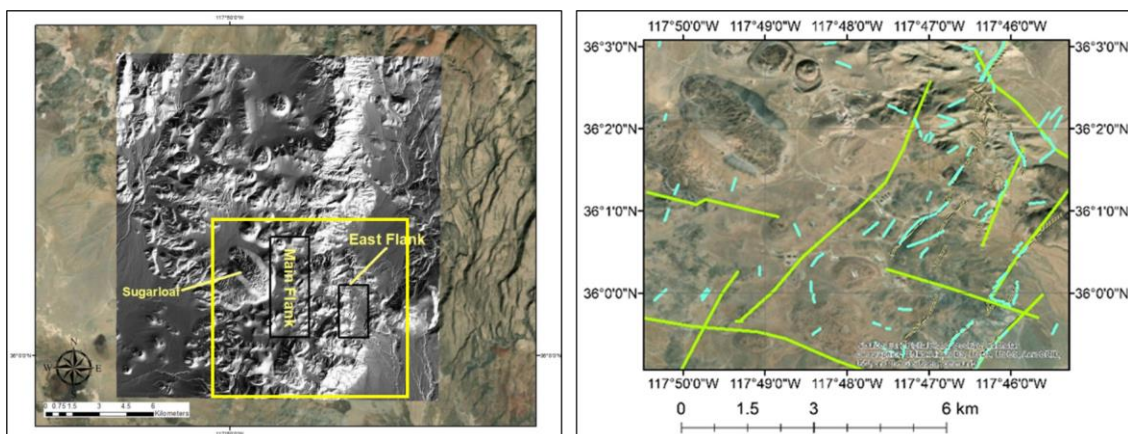
Left – DEM from LiDAR data shown as shaded relief.
Right – lineaments outlined on the basis of the LiDAR DEM.

Source: Left – figure from Blake et al. (2020), right – figure by M. Eneva using GPO data.

2.1.3 Surface Deformation

2.1.3.1 Surface Deformation from Envisat and Sentinel

Table 2.4 shows the angles characterizing the orbital geometries of the two satellites, as they passed over Coso. Table 2.5 shows the sensitivity to the ascending LOS (line of sight), descending LOS, vertical component, and the two horizontal components. See Chapter 1 for details on the angles. Because of the different angles, the sensitivity of the two LOS measurements (ascending and descending) are different for the two satellites. The ENV LOS sensitivities to the vertical component are higher than the SNT LOS sensitivities. Conversely, the SNT LOS sensitivities to the east horizontal component are higher than the ENV LOS sensitivities. As a reminder, for both satellites, the sensitivity to the north horizontal component is too low to be useful.

Table 2.4 Satellite Orbital Geometries for Coso

Angles	Envisat, deg	Sentinel, deg
Ascending θ	24.49	39.18
Ascending δ	11.37	9.61
Descending θ	22.14	41.75
Descending δ	12.64	10.34

Source: Table by M. Eneva, data by TRE Altamira.

Table 2.5 LOS Sensitivity for Coso

Sensitivity to	Envisat	Sentinel
Vertical ascending	+0.91	+0.78
East ascending	-0.41	-0.62
North ascending	-0.08	-0.11
Vertical descending	+0.93	+0.75
East descending	+0.37	+0.66
North descending	-0.08	-0.13

Source: Table by M. Eneva, data by TRE Altamira.

Figure 2.12 shows maps of the ascending and descending SNT1 LOS rates for the whole extended study area. They are visually similar to the maps from the ENV and SNT2 periods (not shown). Note the reference point in the northwestern part of the study area, used in the InSAR processing. The maps look continuously colored, because hundreds of thousands of ascending and descending PS/DS points, each with its individual time series and deformation rate, were identified in this dry area. Furthermore, the majority of 100-m pixels have both types of LOS measurements (ascending and descending), which made it possible to obtain vertical and horizontal components at most pixels – more than 35,000 for ENV and more than 44,000 for SNT. The vertical rates could be calculated with an average precision of ±0.4 mm/

year for ENV, and ±0.8 mm/year for SNT. The average precision of the east rates was ±0.9 from both satellites.

Figure 2.12 LOS Deformation Rates in the Extended Study Area
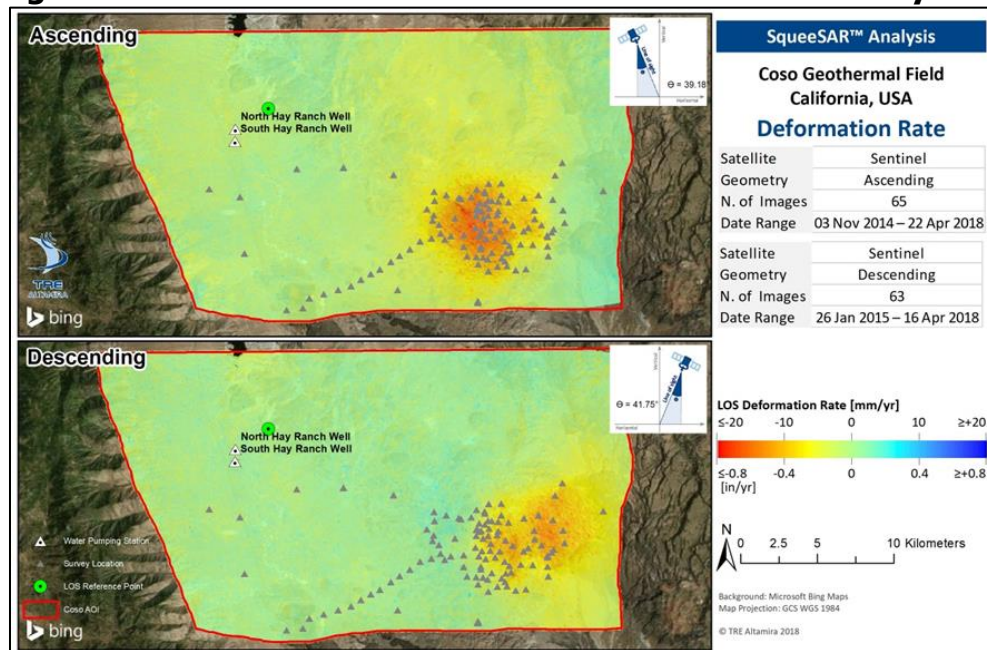
Source: TRE Altamira

It is evident from Fig. 2.12 that the largest deformation is at the Coso geothermal field, so subsequent figures focus on a 93 km^2 area encompassing it. Figure 2.13 shows maps of the ascending and descending LOS surface deformation rates from ENV (Feb 2006 – Oct 2010) and SNT1 (Nov 2014 – Apr 2018). The rates are shown for tens of thousands individual PS/DS points. The number of scatterers commonly identified in dry areas, such as this one, give the appearance of continuous spatial coverage (except for obvious data gaps). The LOS results are further used to calculate the average vertical and east horizontal deformation rates from the individual PS/DS rates within 100-m pixels, shown in Figure 2.14. As a reminder, this is only possible for pixels with both ascending and descending LOS measurements; if at least one of those is missing within a given pixel, it remains empty. The maps indicate decreasing subsidence, confirmed by the maps of the differences on the bottom of the figure. The striped appearance of the maps is due to the 100-m grid used for the pixels. Note that the vertical and horizontal rates from the two satellites can be directly compared, unlike the LOS deformation rates which are influenced by different orbital geometries.

Figs. 2.13 and 2.14 show that the Sentinel spatial coverage is significantly better than the Envisat one. Of the 9,280 100-m pixels for the area shown in Fig. 2.14, 83.9 percent versus 97.5 percent are with vertical (V) and east (E) values from the ENV and SNT1 data, respectively (Table 2.6). As a reminder, negative numbers are used for subsidence and westward movements, and positive numbers for uplift and eastward movements. The maximum ENV subsidence, –27.6 mm/year, is observed 75 m from benchmark CE3, while the maximum SNT1 subsidence is –19.1 mm/year in the same vicinity. For the east component, the maximum eastward rates are +23.9 mm/year (ENV) and +15.9 mm/year (SNT1). The change in the maximum westward rate is significantly smaller, –14.2 mm/year (ENV) to –11.9

mm/year (SNT1). The bottom panels of Fig. 2.14 show difference maps for 82.4 percent of the 100-m pixels that have both ENV and SNT1 values.

Figure 2.13 LOS Deformation Rates at Coso from the ENV and SNT1 Periods
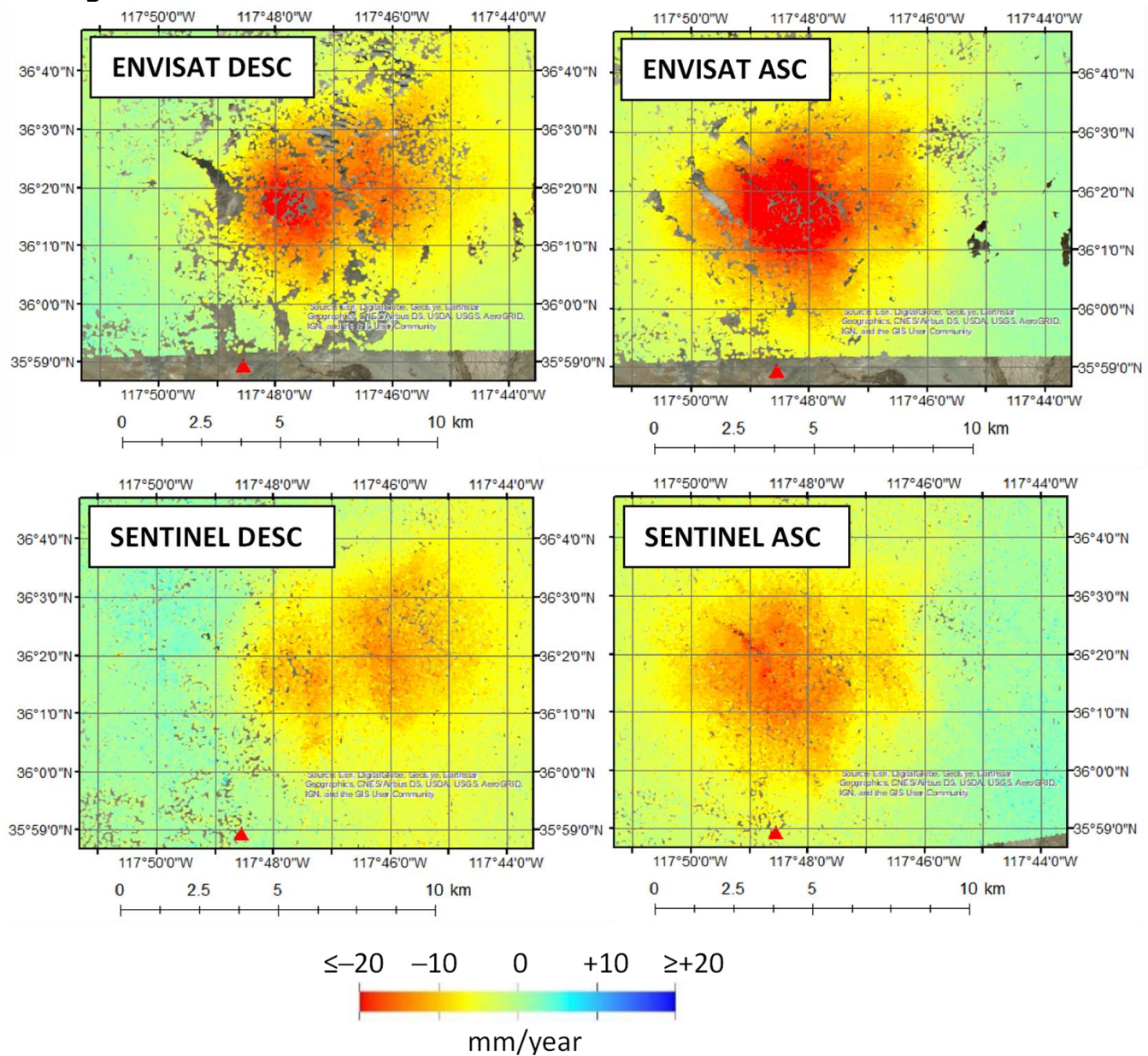
Deformation rates at individual points are color-coded according to color bar on the bottom. Black circle - location of CE3 benchmark. Red triangle – location of COSO GPS station.

Source: M. Eneva

Figure 2.14. Vertical and Horizontal Rates in the ENV and SNT1 Periods
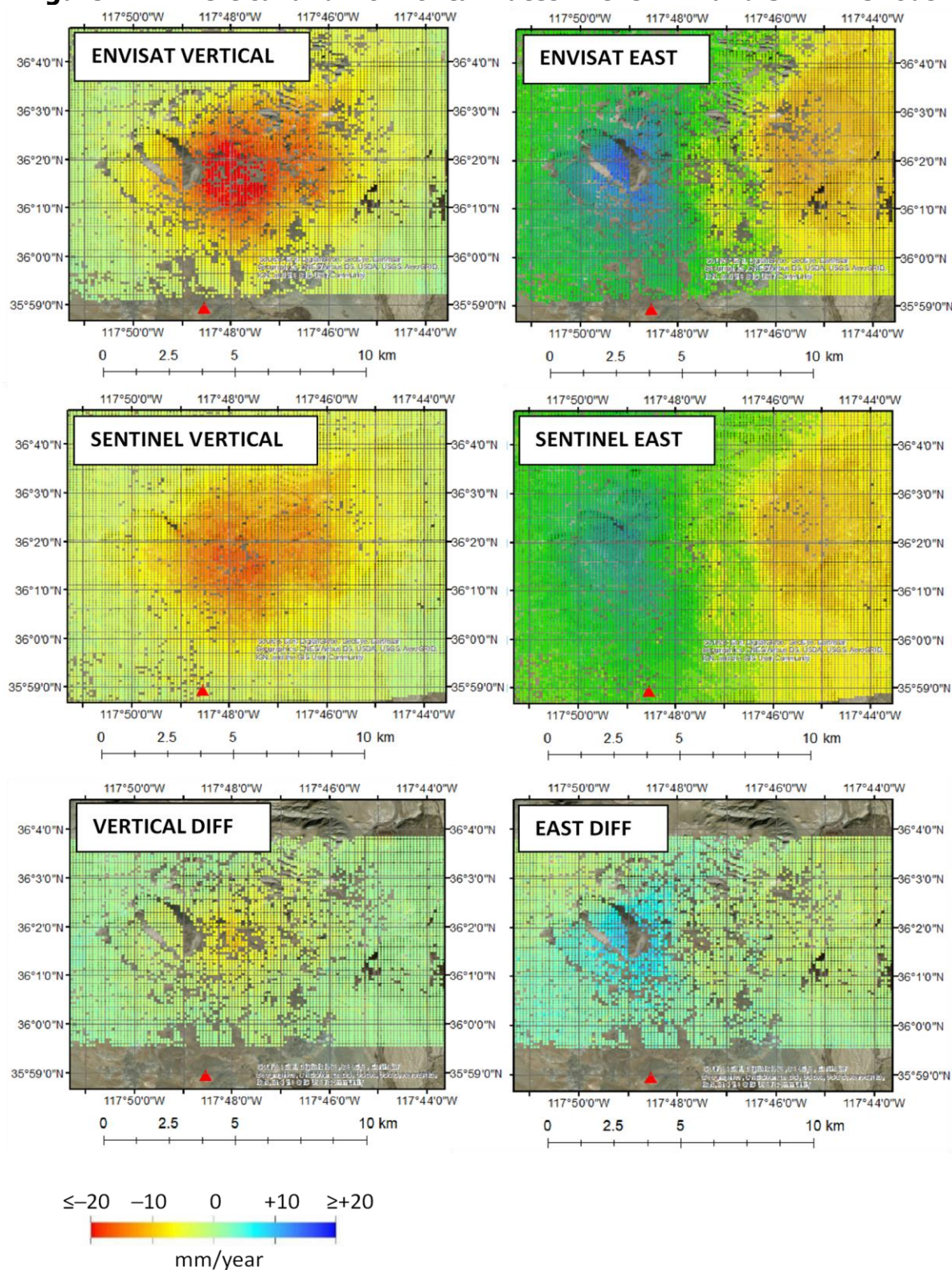
Source: M. Eneva

Table 2.6 Maximum V and E Rates and Differences for the ENV and SNT1 Periods

Parameter	ENV	SNT1	Diff
Number/% of 100-m pixels with vertical & east values (of 9,280)	7,790/ 83.9%	9,049/ 97.5%	7,650/ 82.4%
Max/min vertical rates, mm/year	-27.6 (S)/+ 3.8 (U)	-19.1 (S)/+ 0.7 (U)	-10.6/+5.4
Max/min east horizontal rates, mm/year	-14.2 (W)/+ 23.9 (E)	-11.9 (W)/+ 15.9(E)	-6.1/+5.4

Source: M. Eneva

Surface deformation rates are derived from the slopes of straight lines fitted to the InSAR time series. These can be calculated for individual PS/DS points, individual pixels, or as average values over areas of interest. Figure 2.15 shows an example of an average time series derived from the ENV vertical rates in a 500 m x 500 m area, encompassing several individual 100-m pixels around the survey station showing maximum subsidence, CE3.

Figure 2.15 Average Subsidence Time Series from ENV InSAR in the Vicinity of CE3
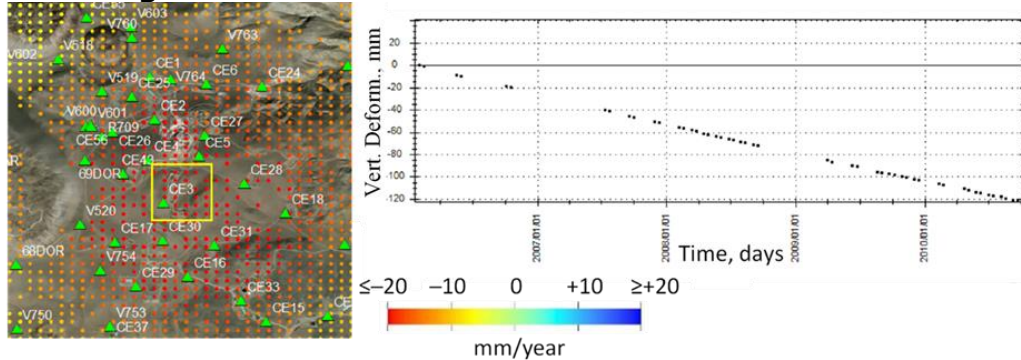
Source: Figure by M. Eneva (using TRE Tool for time series).

Figure 2.16 Scatter Plots Comparing V and E Rates from the ENV and SNT1 Periods

Source: M. Eneva

37
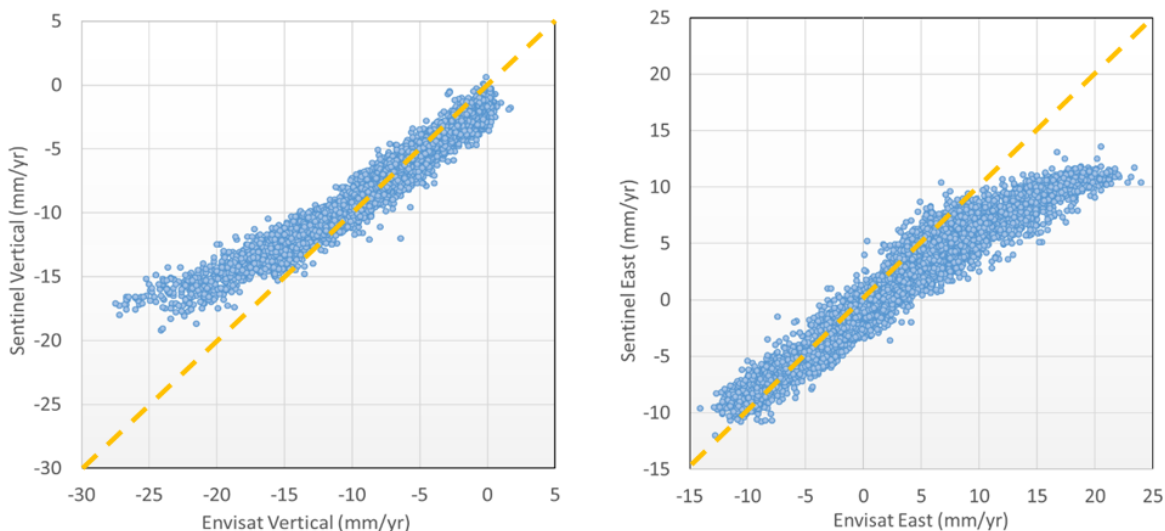
Figure 2.16 provides a complementary representation of the trends discussed above. It shows pixel-to-pixel comparison of the vertical (V) and east (E) rates from the two satellites. If the rates were similar in the ENV and SNT1 periods, they would cluster around the dashed yellow lines in the scatter plots. The smaller subsidence rates are not very different between the two periods, but subsidence exceeding ~−10 mm/year is decreasing during the later, SNT1 period. For the horizontal component, the westward rates (negative values) do not change much, but the rates of eastward movement decrease during the SNT1 period.

Further processing of data from the later Sentinel period (SNT2) confirms the decrease in subsidence with time. Figure 2.17 shows maps of the InSAR-derived vertical deformation rates for the three periods (ENV, SNT1, and SNT2).

Figure 2.17 Subsidence at Coso in the ENV, SNT1, and SNT2 Periods
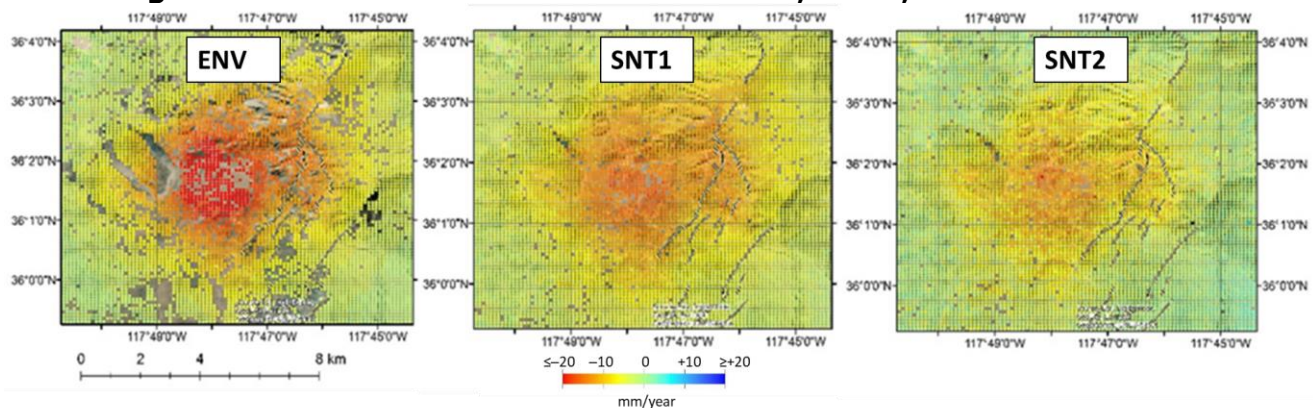
Source: M. Eneva

The subsidence decrease over time can be seen at individual points, or areas of interest. For example, the average vertical ENV InSAR rate around survey station CE3 (slope of time series in Fig. 2.15 above), is −26.0±0.5 mm/year, significantly higher than the SNT1 and SNT2 vertical rates in the same area, −16.7±0.9 mm/year and −14.4±2.6 mm/year, respectively.

It is possible to look for such details in any areas of interest to be determined by geothermal operators. For example, the vicinities of the two wells receiving most water from Hay Ranch, 24B-8 and CEGH-1 (Section 2.1.2.2, Figs. 2.6-2.8 above), could be examined for localized effects on surface deformation. The average InSAR time series from a 500 m x 500 m area encompassing the surface projections of the 24B-8 wellbores are rather linear, with vertical rates of −20±0.5 mm/year, −14.0±0.8 mm/year, and −11.3±2.9 mm/year in the ENV, SNT1, and SNT2 periods, respectively. This does not seem different from the general trend for the subsidence to decrease after the ENV period, so it is not possible to distinguish any particular effect of the large amount of pumping of Hay Ranch water in this well. However, there are no satellite data from the period 2011-2014, and by 2015 the pumping started decreasing (Fig. 2.8). The average vertical rates around CEGH-1 are −8.7±0.5 mm/year, −9.0±0.8 mm/year, and −5.7±3.0 mm/year for the ENV, SNT1, and SNT2 periods, respectively. In this case, the first two periods are indistinguishable, and the last period may or may not be with a lower rate. Overall, no effects of the pumping were identified only around these wells that were different from the subsidence trends elsewhere.

Figure 2.18 Contour Plots of V and E Rates in the ENV, SNT1, and SNT2 Periods
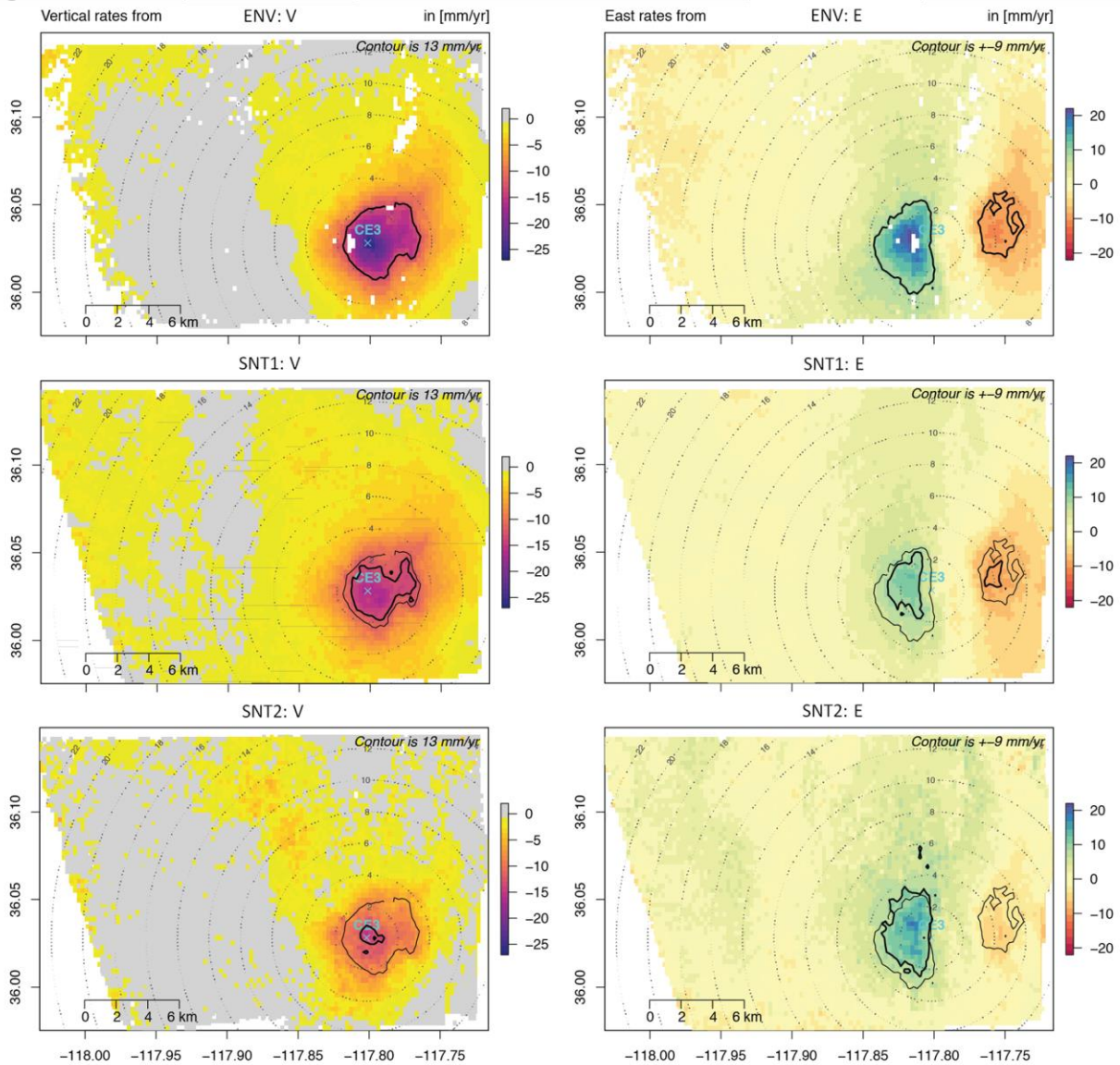
Left columns: vertical (V) rates. Right columns: east horizontal (E) rates. From top to bottom – ENV, SNT1, and SNT2. The thick contours in each frame show the outline of a fixed rate, –13 mm/year subsidence for vertical rates, +9 mm/year for eastward movements, and –9 mm/year for westward movements. To visualize the rate changes in time, the contours from the ENV frames are shown with a thin line in the SNT1 and SNT2 frames. The circular dotted contours are iso-distances in km, away from survey station CE3.

Source: A. Barbour (USGS)

Figure 2.18 shows a different rendition of the same observations, using contour lines. It demonstrates both the steadily decreasing subsidence with time (from color bars), and the shrinking area of a contour with a subsidence of –13 mm/year. The east horizontal movements also show diminishing eastward and westward rates with time, but the areas outlined by contours of constant rates, 9 mm/year eastward and –9 mm/year westward, show a more complicated progression. The area of westward movements diminishes from the ENV to SNT1 period, but disappears in the SNT2 period. The area of eastward movement shrinks

39

from ENV to SNT1, but increases again in the SNT2 period, approaching the ENV area size. More contour maps are shown in Figure 2.19, where contours are outlined with an interval of 5 mm/year. This makes it possible to follow the progression of area sizes within contours of different rates. Similar to Fig. 2.18, Fig. 2.19 (left) indicates a shrinking area of subsidence at the −15 mm/year level (like the −13 mm/year contour used in Fig. 2.18) from the ENV, through the SNT1, and to the SNT2 periods. However, the areas within the contours of −10 mm/year and −5 mm/year subsidence appear similar in the three periods. The progression of the areas within contours of different levels of westward and eastward movements are also clearly depicted in Fig. 2.19.

Figure 2.19 Contour Maps of Deformation Rates in the Three Periods
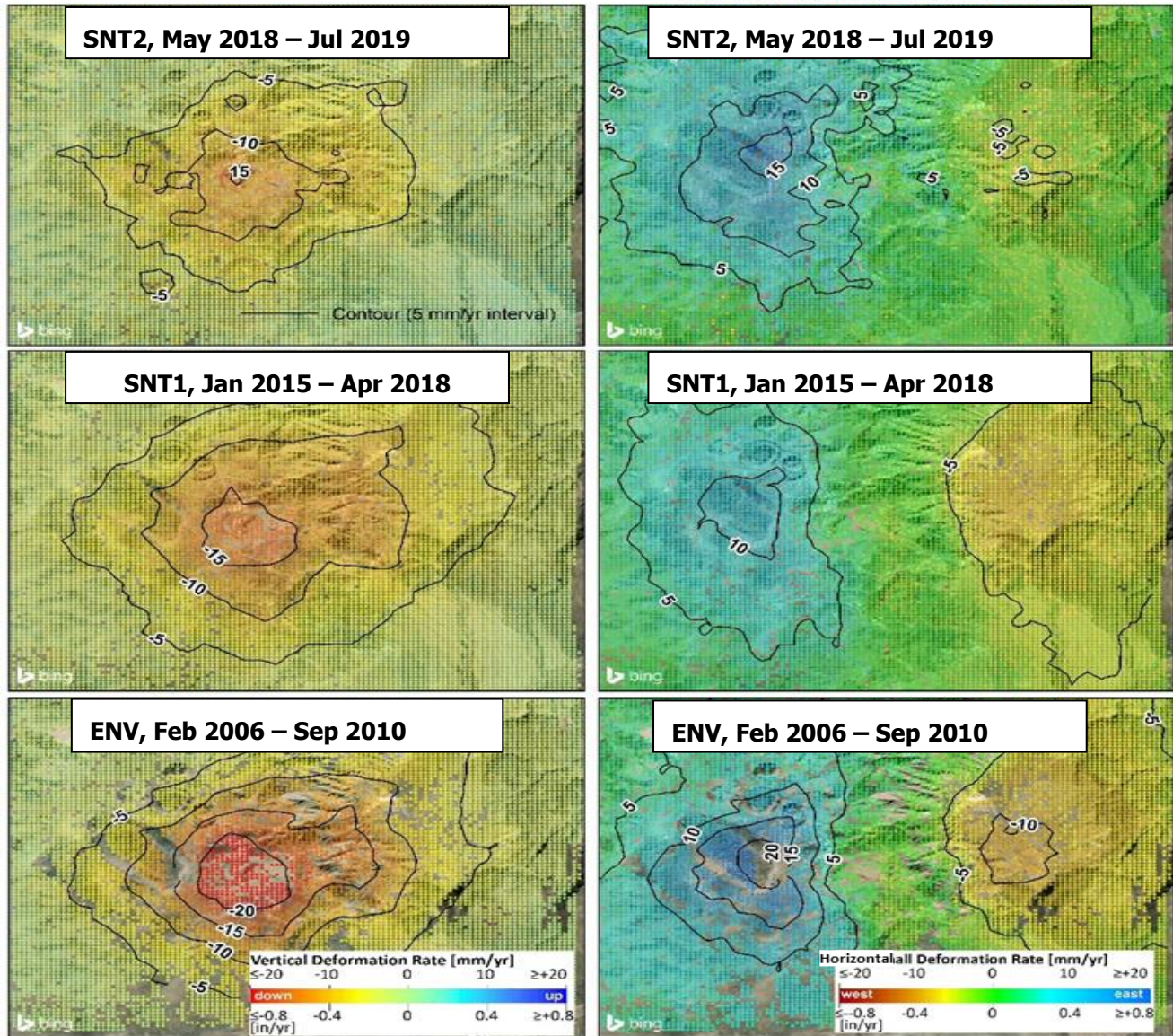
Vertical and Horizontal columns with maps of deformation rates over three periods: May 2018-Jul 2019; Jan 2015-Apr 2018; Feb 2006-Sep 2010.

Source: TRE Altamira, modified by M. Eneva.

40

Figure 2.20 shows the same contour maps as in Fig. 2.19, with superimposed areas (outlined in pink), for which average time series are calculated. These areas are chosen from the ENV contour maps as the areas enclosed by the −20 mm/year contour of vertical, 20 mm/year of eastward, and −10 mm/year of westward movements. The areas for the three periods are labeled, ENV, SNT1 and SNT2, prefaced by a "V" for the vertical movements, and "E" and "W" for the eastward and westward movements. This labeling is also used in Figure 2.21 showing the respective average time series. The average subsidence rate within the chosen area, encompassing the center of the subsidence bowl, decreased from −22.3 mm/year (ENV), through −15.9 mm/year (SNT1), to −12.8 mm/year (SNT2). Also, nonlinear vertical deformation was detected in the SNT2 period.

The average eastward rate in the designated area of maximum ENV eastward rate decreased from 20.9 mm/year (ENV) to 11.3 mm/year (SNT1), and then increased to 15.1 mm/year (SNT2). The average westward rate decreased from −10.7 mm/year, through −9.0 mm/year (SNT1), to −5 mm/year (SNT2). Overall, the eastward rates were larger than the westward ones in all three periods.

Figure 2.20 Areas for Calculation of Average Time Series

Source: TRE Altamira, modified by M. Eneva.

41
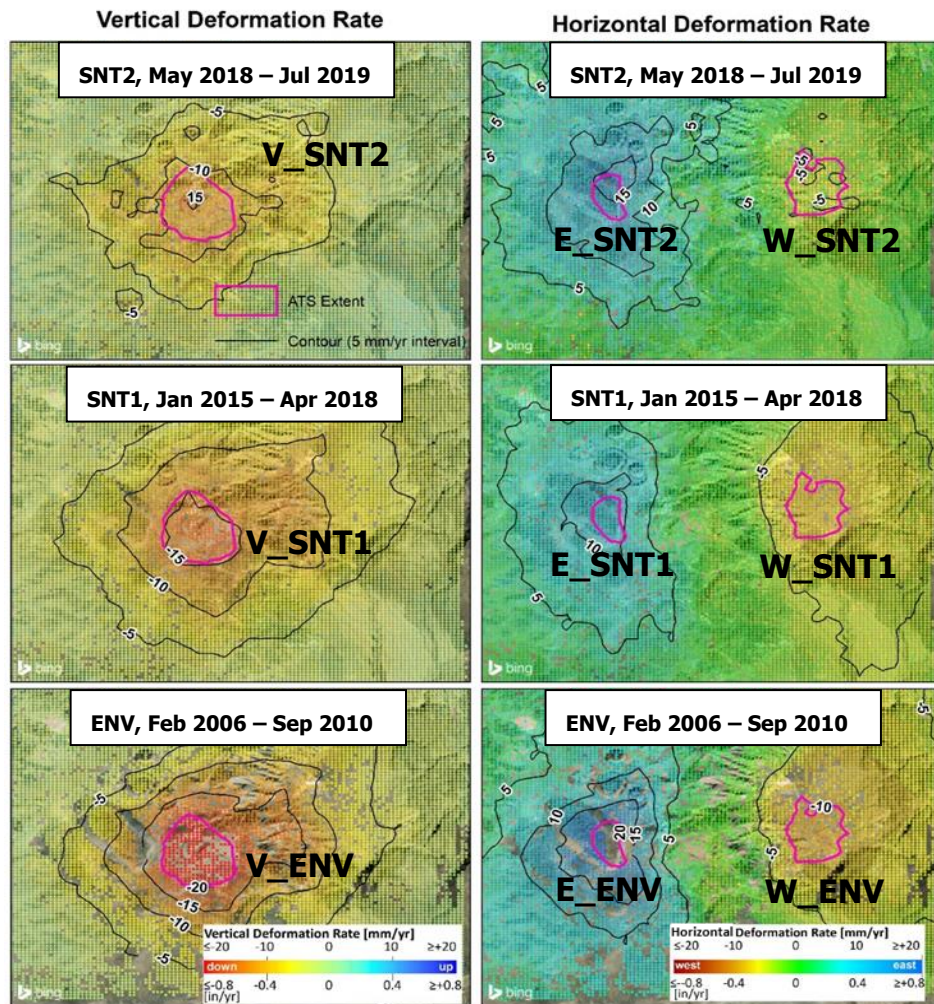
Figure 2.21 Average Time Series in Areas from Fig. 2.20

Legend (top panel)	
V_ENV:	−22.3±0.5 mm/year
V_SNT1:	−15.9±0.9 mm/year
V_SNT2:	−12.8±2.7 mm/year

Legend (middle panel)	
E_ENV:	20.9±1.1 mm/year
E_SNT1:	11.3±1.0 mm/year
E_SNT2:	15.1±3.2 mm/year

Legend (bottom panel)	
W_ENV:	−10.7±1.0 mm/year
W_SNT1:	−9.0±1.0 mm/year
W_SNT2:	−5.0±3.6 mm/year
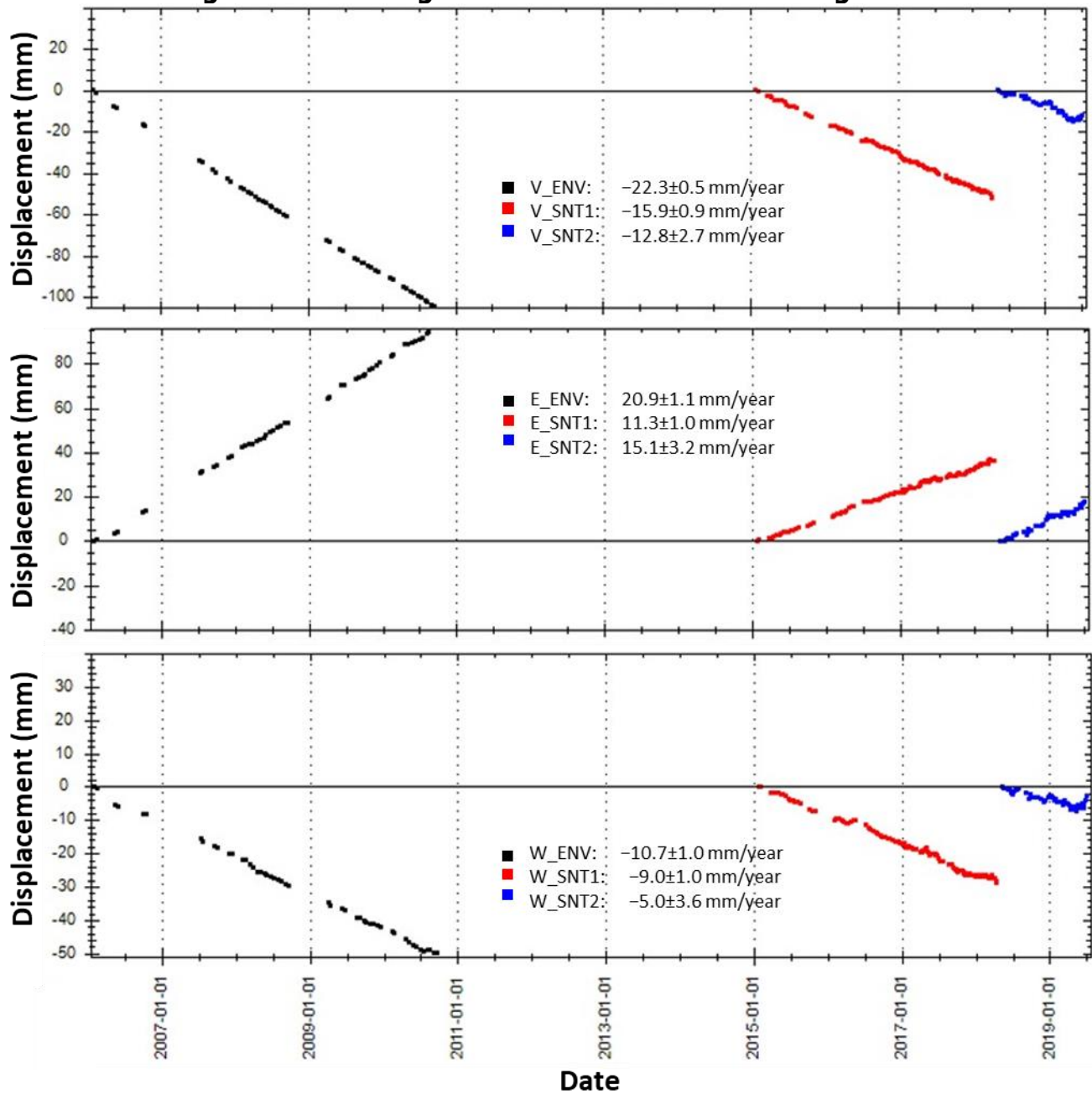
Source: TRE Altamira, modified by M. Eneva.

Furthermore, it is possible to examine the progression of deformation along profiles of interest. Figure 2.22 shows two such profiles. One of them, A1-A2, traces a lineament derived from LiDAR (Blake et al., 2018). It cuts SW-NE through the Main Flank, the area which demonstrates a decrease in shallow temperatures from a 2-m temperature survey (Blake et al., 2020). For convenience, the left panel of Fig. 2.22 shows only the lineaments (same as

right panel of Fig. 2.11 above). Profile B1-B2 is approximately perpendicular to A1-A2 and cuts SE-NW through the middle of the subsidence area.

Figure 2.22 Maps of LiDAR Lineaments and Profiles A1-A2 and B1-B2
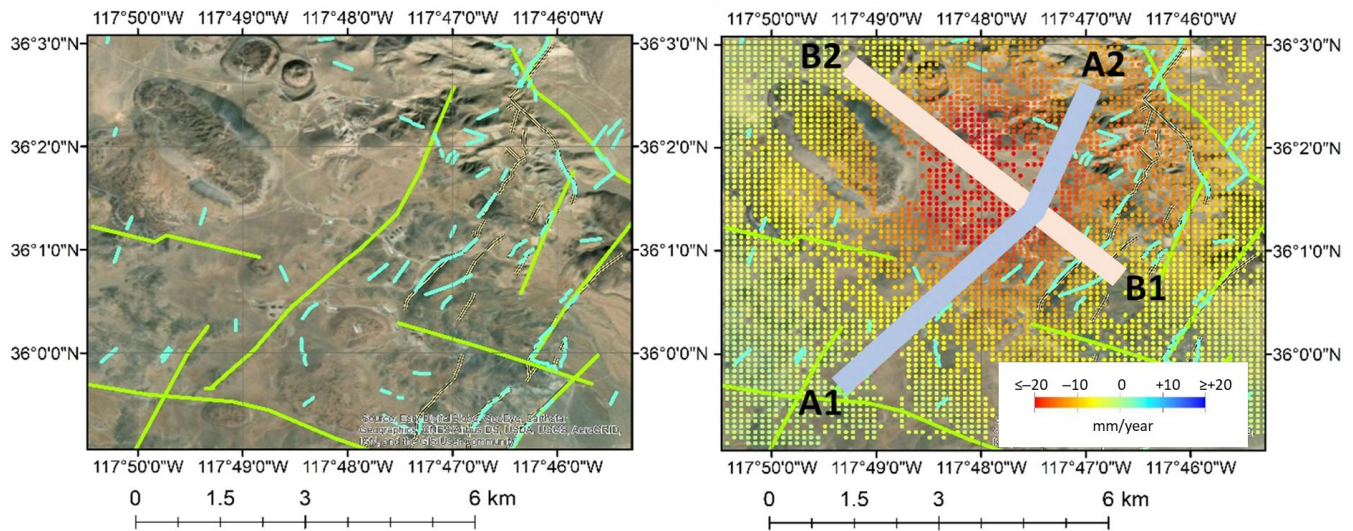
Left: lineaments based on LiDAR data (Blake et al., 2018). Right: two profiles superimposed on map showing ENV vertical deformation rates. Both profiles are 200-m wide.

Source: Left: LiDAR lineaments (Blake et al., 2018), right - M. Eneva.

Gaps in the ENV deformation progression (Figure 2.23) reflect lack of data in some parts of the profile. There are no such gaps in the SNT1 measurements along this profile, and the images were more frequently collected, hence the denser appearance of the SNT1 plot on the bottom of Fig. 2.23. The ENV period is 55 months long, and the duration of the SNT1 period is 40 months, so the smaller maximum of cumulative subsidence in the SNT1 period, −58 mm, compared with −105 mm for the ENV period, is partially explained by the different lengths of the two periods. However, if the rate of accumulation is taken into account and projected over 55 months, the SNT1 maximum would have reached ~−80 mm, still smaller than the ENV maximum. This is yet another demonstration of the decreasing subsidence rate with time. The other profile, B1-B2 in Figure 2.24, intersects the previous profile and passes through the area of maximum subsidence. The maximum cumulative subsidence in the ENV period reaches −125 mm, and in the SNT1 period −55 mm (equivalent to −76 mm if the SNT1 period were 55 months long), once again confirming the decreasing subsidence rate compared with the ENV period. Profile B1-B2 cuts through the subsidence bowl, hence the maximum ENV displacement is larger than that from profile A1-A2 that passes to the south and southeast of the center of the subsidence bowl.

Figure 2.23 Deformation Along the A1-A2 Profile in the ENV and SNT1 Periods
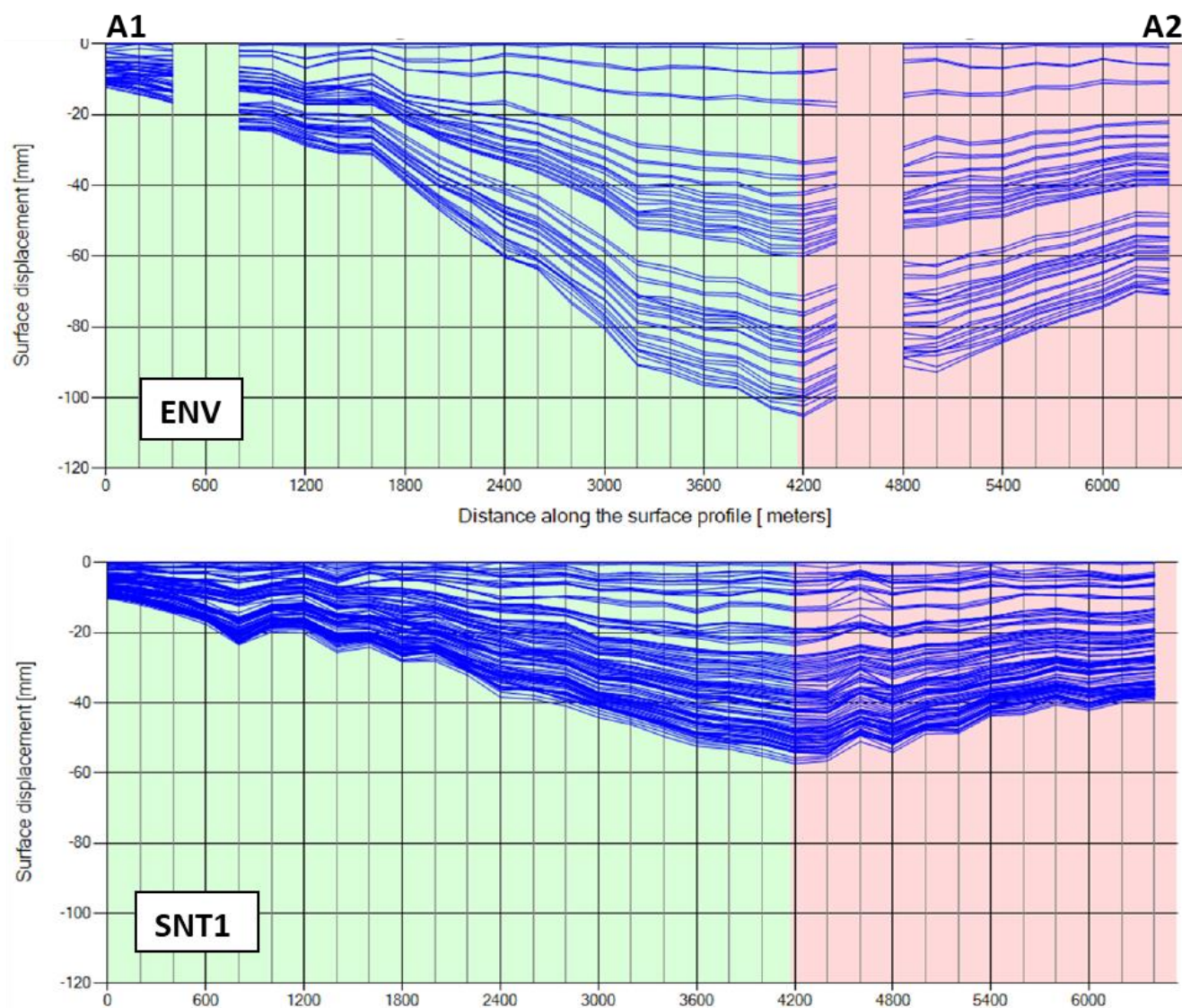
Cumulative deformation along profile A1-A2 in Fig. 2.22, for the ENV and SNT1 periods as marked. Each line corresponds to a single satellite image. The two different colors to the left and right of the 4,200-m mark indicate the location where the profile changes direction.

Source: M. Eneva (using TRE Tool).

The findings in this project were compared with three earlier DInSAR studies using data from ERS-1/2, two satellites preceding Envisat and Sentinel. Vasco et al. (2002) used seven descending and two ascending images from the period 1992 – 1997 to form five descending pairs and one ascending pair. These authors reported LOS deformation rates in the −20 to −30 mm/year range away from the satellite. Because of the steep look angle for ERS-1/2 (similar to ENV), this strongly suggests subsidence, but is not quite the same. Fialko and Simons (2000) used eight pairs from the period 1993-1999 and reported a peak subsidence rate of ~−35 mm/year. The same rate was reported by Wicks et al. (2001), for the period 1992-1997. None of these studies had at their disposal the abundant data available now, and

44

Figure 2.24 Deformation Along the B1-B2 Profile in the ENV and SNT1 Periods
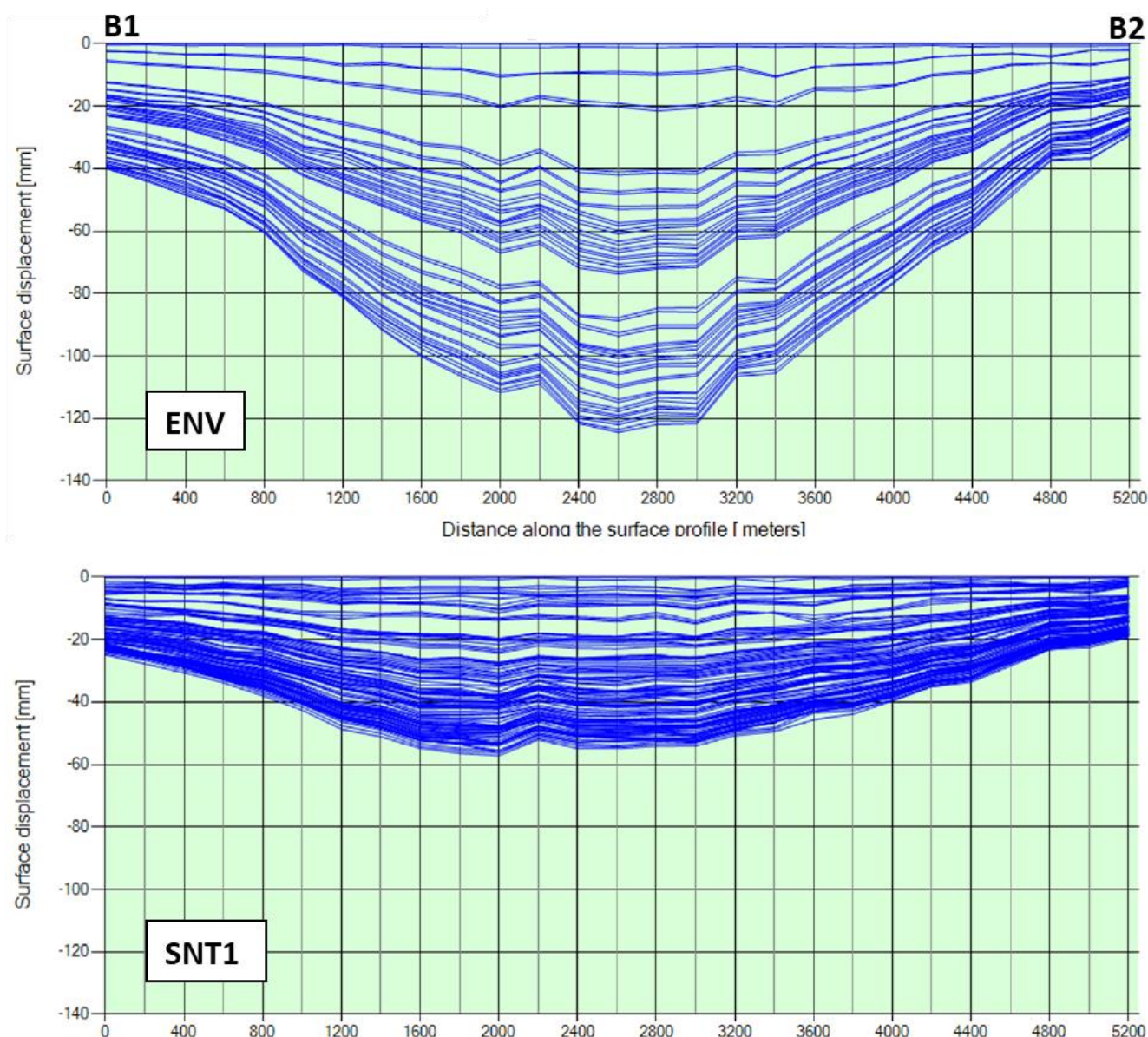
Cumulative deformation along profile B1-B2 in Fig. 2.22. All notations like in Fig. 2.23.

Source: M. Eneva (using TrE Tool).

ascending data were scarce at that time, so it was not possible to perform decompositions into vertical and east components. Also, PS-based techniques were not available at the time, but even if they were, at least 15 images are needed to form a deformation time series. With all these limitations, for direct comparison, the maximum away-from-satellite LOS deformation rates were used (rather than the vertical rates), −30.7 mm/year for the ENV period and −22.8 mm/year for the SNT1 period. Compared with the two latter publications using data from the 1990's, and adding the SNT2 observations from this project, it appears that the subsidence derived from InSAR (regardless of the technique used) might have been decreasing over the whole 1997-2018 period. This is confirmed also by the ground-based survey data - see Fig. 2.10 above.

Similar analysis can be done by examining average time series at specific locations and deformation rates along profiles associated with geothermal plants, individual wells, faults, structural features, etc. Once geothermal operators are aware of the capabilities of this type of analysis, they could determine areas and time periods of interest to investigate in more detail.

2.1.3.2 Comparison with Subsidence Surveys

Station B14. This station was used as a datum (reference) for the ground-based survey data (see Fig. 2.9 above), i.e., it was assumed to be stable. The InSAR measurements are relative to a reference point in the NW part of the extended study area (see Figs. 2.9-left and Fig. 2.12 above), positioned about 15 km NW from B14. In fact, B14, being inside the geothermal field, is expected to move. Therefore, the InSAR vertical measurements in its vicinity were considered, which show −6.4 ± 0.5 mm/year (ENV), −5.8 ± 0.9 mm/year (SNT1), and −4.0 ± 2.3 mm/year (SNT2). It is not surprising that the InSAR rates measured at B14 decrease, as it was already established that the subsidence at Coso generally decreases with time, while the InSAR reference, being quite away from the geothermal field is likely to be much more stable in the vertical direction. Even though these differences are relatively small, they need to be taken into account when survey and InSAR rates are compared.

Station CE3. The surveys generally indicate the largest subsidence at this station (see Table 2.3 above). Its subsidence rate (ref. B14) from two surveys in 2006 and 2009, is −17.0 mm/year. To translate this into the ENV InSAR reference frame (2006-2010), −23.4 mm/year (= −17.0 − 6.4) is obtained using the ENV correction for B14. Comparing this estimate with the maximum subsidence derived from ENV InSAR (−27.6 mm/year from the closest 100-m pixel to CE3, −26.0 mm/year as an average from eight closest pixels, standard deviation ± 0.5 mm/year), a difference of about 2.5 to 4 mm/year is seen. However, the survey rate was derived only from two measurements (in 2006 and 2009), while the InSAR rate was calculated from tens of ENV satellite measurements. Using the same reasoning for the survey measurements in 2013 and 2017, according to which the CE3 rate (ref. B14) is −16.2 mm/year, and applying the SNT1 correction for B14, the corrected rate is −22.0 mm/year (= −16.2 − 5.8). Compared with the SNT1 InSAR subsidence rates from 100-m pixels around CE3, which is around −17 mm/year, the difference is about 5 mm/year. However, other than using only two measurements, in this case the higher survey subsidence rate could be also attributed to the earlier time period captured by the survey period (Apr 2013 – Oct 2017) versus the later SNT1 satellite period (Jan 2015 – Apr 2018), given that the subsidence rates decrease with time. The SNT2 InSAR rate (May 2018 – Jun 2019) from 100-m pixels around CE3 is about −15 mm/year; this period does not contain any surveys for comparison.

COSO GPS/PBO station. It is the closest GPS station to the geothermal field, from the Plate Boundary Observatory (PBO) network. It has three components of the annual rate of motion (data from the Scripps Orbit and Permanent Array Center – SOPAC, 2018). Comparisons with the movements at COSO can provide information for the actual (absolute) movements at GPO stations, as well as at the InSAR reference point, in the North American Reference Frame (NAM08). Table 2.7 shows measurements relevant to the COSO station. The table shows that the InSAR vertical measurements (Up column) around, or close to COSO, during all three

Table 2.7 Movements at the COSO GPS station

Station or from InSAR	Reference	Up	East	North	Notes
COSO (PBO GPS) 1996-1-1 to 2018-08-21 CE46 (GPO)	NAM08 IGS08 B14	-4.3 -4.12 -4.12	-5.14 -17.47 n/a	+14.39 +3.34 n/a	North American Reference Frame International GNSS Service Reference Frame From only two surveys in 1995 and 1996; 28 m NW from COSO
ENV SNT1	InSAR InSAR	-3.45 ±0.40 -2.99 ±0.90	±5.80 ±1.00 +2.63 ±1.33	n/a n/a	From two 100-m picels closest to COSO, but still 500 m noth from four 100-m pixels around COSO
SNT2	InSAR	-0.07 ±3.38	+1.33 ±4.50	n/a	From four 100-m pixels around COSO

Source: M. Eneva

satellite periods are rather small, which is not surprising since this station is outside the geothermal field. They are not very different from the NAM08 subsidence at COSO of –4.3 ± 0.2 mm/year. These small differences show that subsidence measured relative to the InSAR reference point is similar to the absolute NAM08 subsidence. In other words, the InSAR point is really rather stable in vertical direction. However, this is not the case for its horizontal movement. The NAM08 horizontal displacements at COSO (the East and North columns in the table) are to the west and to the north, while in the InSAR framework this station moves eastward. This means that the InSAR reference point actually moves faster to the west (ref. NAM08) than the COSO station. COSO's largest movement is to the north, but this is irrelevant here, because the north horizontal component cannot be recovered from InSAR for comparison. The COSO station location was not included in the ENV study area, but was only about 500 m south of its edge. So, the ENV measurements for comparison were at this edge, just north from the COSO station. All this adds some additional understanding of the tectonic movements in the region, and the stability of the InSAR reference point, but is less important when focusing on localized deformation.

Comparison of all InSAR and survey rates. Table 2.8 shows mean differences and standard deviations of comparisons between the two types of rates for the ENV and SNT1 periods of time (there were no surveys for comparison in the SNT2 period). To avoid differences due to the different reference points for the surveys (B14) and the InSAR measurements (InSAR reference point), the InSAR corrections at B14 were applied to the ENV and SNT1 measurements. The InSAR rates were calculated as averages from the vertical measurements within 200 m from the survey stations. This distance does not have a special meaning – it is a compromise between being close enough to the stations, yet including a representative number of InSAR vertical measurements. The highlighted rows in Table 2.8 are for differences shown in scatter plots and histograms in Figure 2.25. The scatter plots also show lines and their equations from the application of a least-squares linear fit. Some satellite periods are with very few, or even no surveys at the same time, so comparisons either cannot be made, or rates are calculated from only two or three surveys, with the understanding that such rates

Table 2.8 Comparison of Vertical Rates at Coso

Surv/ Sat	Time intervals	Mean difference, mm/year	95% conf. accuracy, mm/year	Number of surveys	Number of survey stations	Number of InSAR points in time series
S ENV	Apr 2003 – Sep 2009 Feb 2006 – Aug 2009	0.7 ±0.3	3.8	3	73 of 73	17 (35 A,20 D)
S ENV	Jun 2000 – Sep 2009 Feb 2006 – Aug 2009	2.0 ±0.2	6.2	4	73 of 73	17 (35 A, 20 D)
S ENV	Apr 2003 – Apr 2013 Feb 2006 – Sep 2009	0.0 ±0.3	3.5	4	73 of 73	25 (45 A, 30 D)
S ENV	Jul 2006 – Apr 2013 Oct 2006 – Sep 2010	-2.2 ± 0.2	5/6	3	71 of 71	23 (30 A, 27 D)
S SNT1	Sep 2009, Oct 2017 Feb 2015 – Sep 2017	3.1 ± 0.3	7.4	3	71 of 71	40 (49 A, 46 D)

Columns from left to right: "S" marks surveys, ENV ad SNT1 mark satellite periods; time intervals compared from the surveys and the satellites; mean differences between subsidence rates derived from InSAR and surveys; 95th percentile of the absolute values of the differences; number of surveys used to calculate rates within the survey periods shown in the second column; number of stations, for which InSAR vertical measurements within 200 m were observed, out of all stations for which rates could be calculated in that period; and number of points in the InSAR time series, from which the vertical rates are calculated, followed by the numbers of ascending (A) and descending (D) scenes in parentheses. Rows highlighted in gray are for periods shown in subsequent figures.

Source: M. Eneva (from Eneva et al., 2020).

are less reliable. Therefore, in order to use data from a few more surveys, the survey periods are sometimes quite longer than the satellite periods. Table 2.8 and the top of Figure 2.25 show that there is a good agreement between the two types of measurements for the survey period Apr 2003 – Sep 2009, with 95 percent of the absolute values of the differences within 3.8 mm/year. The table shows that the result is similar for the Apr 2003 – Apr 2013 period (not shown in Fig. 2.25). Because the subsidence at Coso decreases with time, when the satellite data period overlaps with the survey period only partially, then a systematic bias is observed. Therefore, the plot on the bottom of Fig. 2.25 shows a systematic positive difference (mean 3.1 ± 0.3 mm/year from the table), likely because the SNT1 subsidence rates are generally lower than those derived from the longer period covered by the three surveys in 2009, 2013 and 2017. The reason is that the SNT1 period (Feb 2015-Sep 2017) is in the second half of the survey period (Sep 2009-Oct 2017), when the subsidence is lower. Using a suitably shorter survey period is not possible, because there was only one survey, in Oct 2017, during the SNT1 period. Note that because the area at Coso is so dry, the distribution of PS/DS points is very dense and thus all operating survey stations have InSAR measurements within 200 m (sixth column in Table 2.8). This allowed the project team to make a comprehensive comparison of the two types of rates in the vicinities of all stations. On the other hand, this study is limited by the low frequency of the subsidence surveys in the satellite periods.

Figure 2.25 InSAR vs. Survey Subsidence Rates
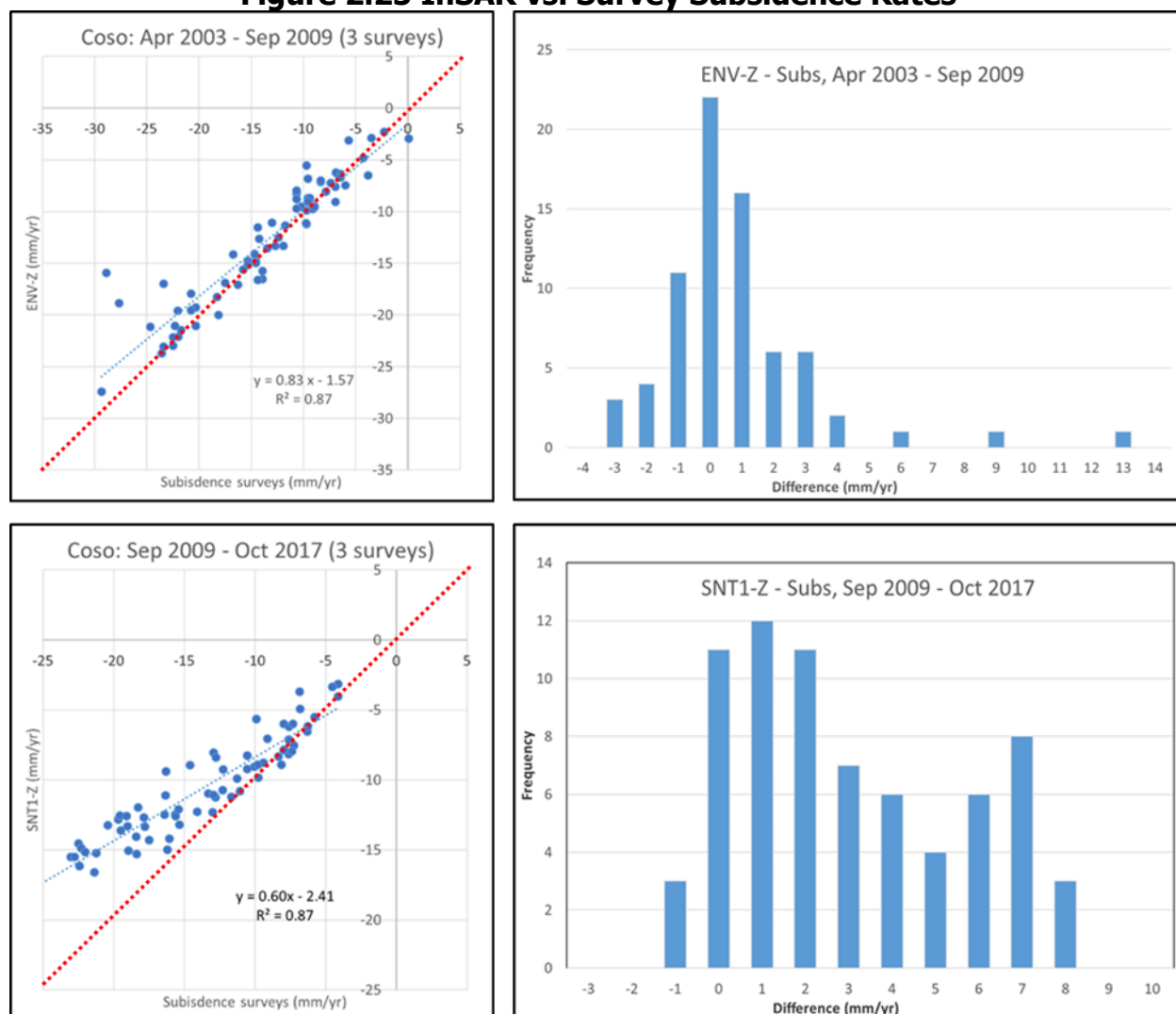
Left – scatter plots of the InSAR rates versus the rates from the subsidence surveys. "Z" denotes vertical rates. Equations are for the straight lines fitted to the data, drawn with blue dashed lines. "R²" show the correlation coefficients. Red dashed lines show where the points would cluster if there were no differences between the two types of subsidence rate estimates.

Source: M. Eneva (from Eneva et al., 2020).

2.1.3.3 Comparison with Production and Injection

As already suggested, the decreasing subsidence with time, as revealed by InSAR, appears to be related to the overall decreasing production at the geothermal field, as illustrated in Fig. 2.7. However, the injection augmentation strategy applied after 2009 could be also considered as a reason for this decline in subsidence. The main argument for the declining production as a driver of this observation, is that the ground-based survey data indicate decreasing subsidence even before the start of the satellite data used in this project (see Section 2.1.2.3 above) and before the pumping of ranch well water. Table 2.9 shows the mean production, injection and net production for the satellite time periods used for calculating the vertical and east horizontal

Table 2.9 Mean Monthly Fluid Masses at Coso in the ENV, SNT1, and SNT2 Periods

Satellite Period	Time Period	Mean Production, 10^9 kg	Mean Injection, 10^9 kg	Mean Net Production, 10^9 kg
ENV	Feb 2, 2006 – Sep 22, 2010	2.56	1.09	1.47
SNT1	Jan 26, 2015 – Apr 16, 2018	1.88	0.89	0.98
SNT2	May 10, 2018 – Jul 4, 2019	1.72	0.82	0.90

Source: A. Barbour (USGS), modified by M. Eneva.

Table 2.10 Fluid Masses in the SNT1 and SNT2 Periods Compared with the ENV Period

SNT Period	Time Period	SNT/ENV Production, %	SNT/ENV Injection, %	SNT/ENV Net Production, %
SNT1	Jan 26, 2015 – Apr 16, 2018	73.2	81.8	66.9
SNT2	May 10, 2018 – Jul 4, 2019	67.2	75.4	61.2

Source: A. Barbour (USGS), modified by M. Eneva.

rates from InSAR. It is evident that they all decrease from the ENV, through the SNT1, to the SNT2 period. Table 2.10 further confirms this, showing the total production, injection, and net production in the SNT1 and SNT2 periods as percentages from the ENV values.

The injection from Hay Ranch might have also contributed to this reduction in subsidence, especially locally around wells receiving the additional water. However, as an overall outcome for the whole field, this would mean to assume a delayed and/or enduring effect of the added water to the drying reservoir. Indeed, by the time of the SNT1 and SNT2 periods, i.e., in 2015 and later, the pumping from Hay Ranch was significantly declining, and even almost entirely stopped between Jun 2016 and Jul 2017 (Fig. 2.8). The water pumping resumed later in 2017, but never reached the pre-2015 amounts, and entirely stopped after Sep 2018.

2.1.3.4 Seismicity

Figure 2.26 shows histograms and cumulative plots of the annual numbers of earthquakes in the Navy I, Navy II, and BLM subareas, as well as in an area encompassing all three subareas. In each case, data from the three catalogs listed in Section 2.1.2.4 are shown. Differences in numbers of events from the three catalogs are due to the different magnitudes of complete recording of earthquakes and different numbers of the underreported events below these magnitude thresholds. For example, in all areas, for the years it is available, the GPO catalog shows significantly more events than the Kaven et al. catalog, which can be only explained with the inclusion of much more smaller earthquakes. Furthermore, the 20-year Kaven et al. catalog shows the largest numbers in 2003-2005 for Navy I and Navy II, and around 1999 in BLM (see histograms in Fig. 2.26). The seismicity rates got significantly reduced after 2011 in all areas. The cumulative plots confirm this significant decrease by flattening out after 2011. Some earlier rate reductions are also observed. It is logical to assume that this is due to the decreasing production, which also caused the decline in subsidence.

Figure 2.26 Histograms and Cumulative Numbers of Earthquakes at Coso
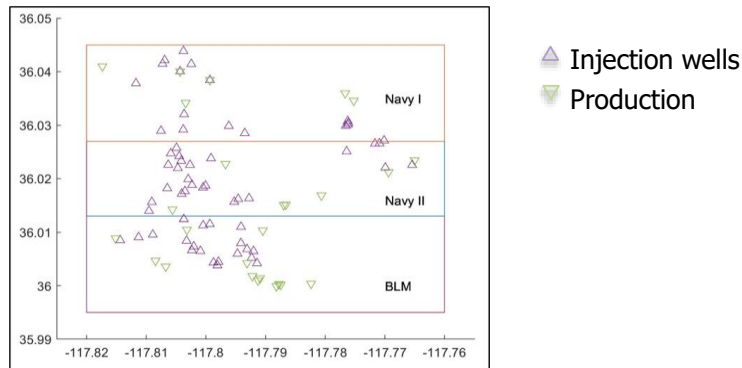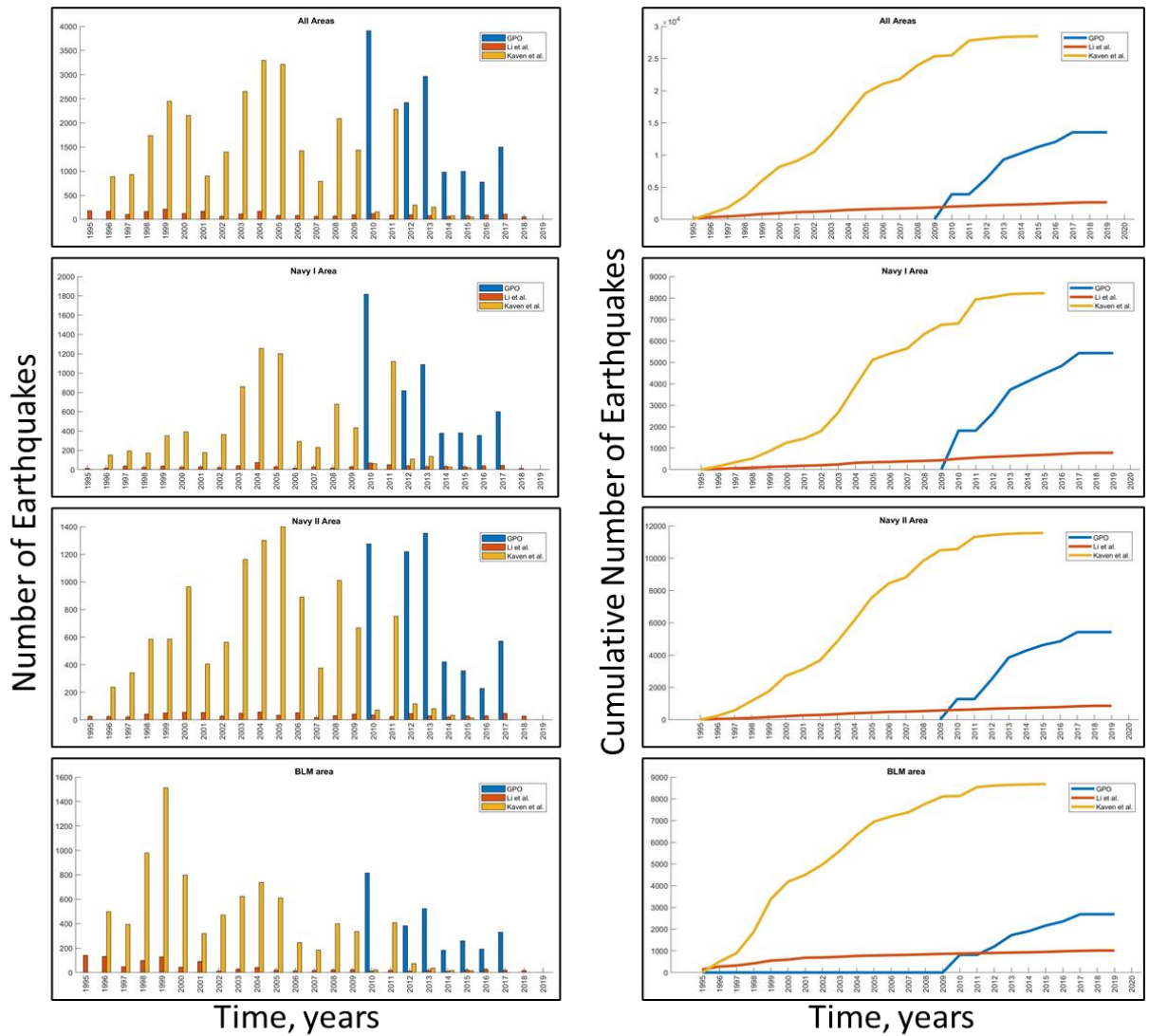
Source: Individual plots by D. Adams, assembled and modified by M. Eneva.

Figure 2.27 also shows histograms and cumulative plots, but this time each plot is for a different catalog, with data from all areas. In addition, this figure shows plots of the magnitude-frequency relationships (MFR) for the three catalogs in the area encompassing Navy I, Navy II, and BLM. The magnitude of completeness is usually considered to be the magnitude below which the MFR curve cannot be approximated by a straight line (although

51

such criteria may be debatable). The MFR plots (the rightmost column in Fig. 2.27) show straight lines for reference (in red). Here it is reasonable to consider magnitudes of completeness M=0 for the GPO and Kaven et al. catalogs, and M=1 for the Lin et al. catalog. The plots show that early on, until 2001, the BLM area experienced a lot more earthquakes than the Navy I and Navy II areas, but became less seismically active than them in later years. This is particularly noticeable in the plots from the Lin et al. catalog featuring the larger events (M≥1). This catalog does not show the same flattening of the cumulative curve after 2011, as the Kaven et al. catalog (M≥0), suggesting that the differences were due to the diminished number of the smallest earthquakes.

Figure 2.27 Histograms, Cumulative Curves, and MFRs from Three Earthquake Catalogs
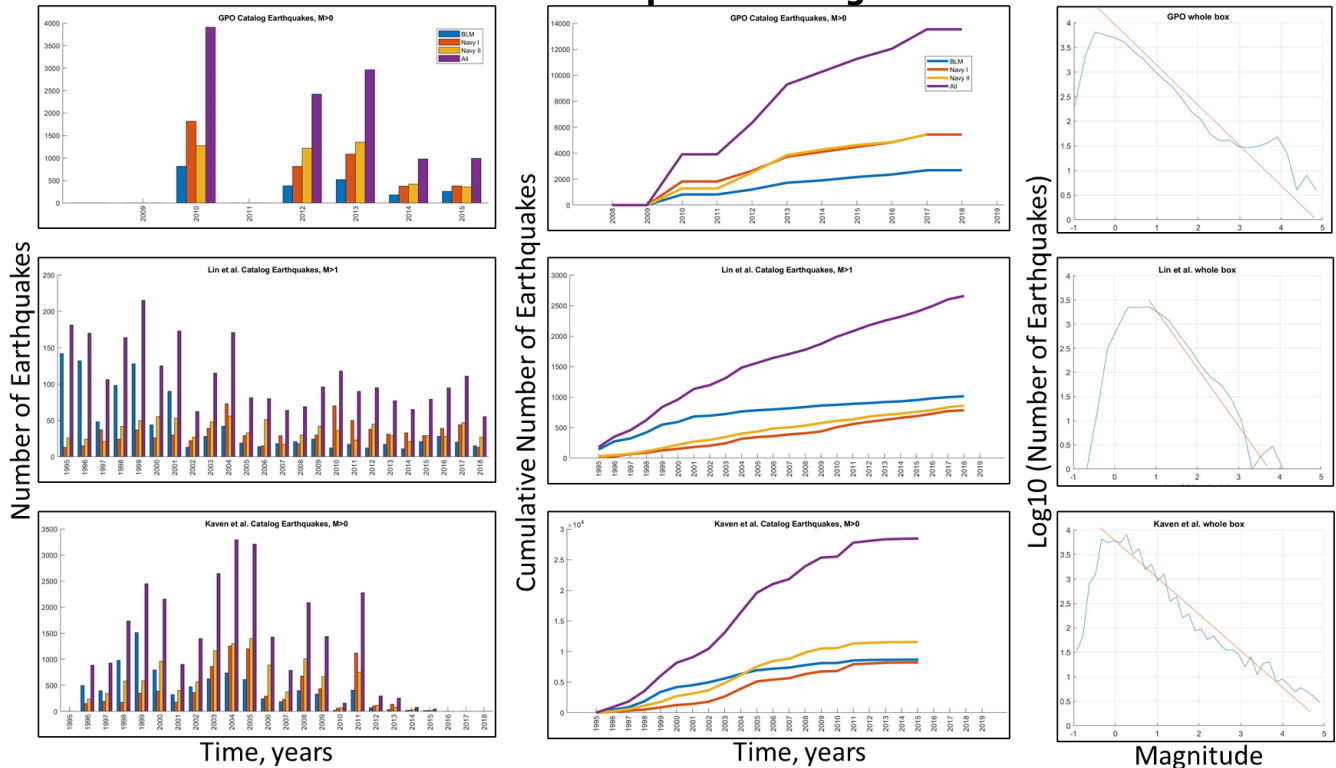
Source: Individual plots by D. Adams, assembled and modified by M. Eneva.

The GPO catalog contains 13,539 events within the whole Coso area covering the BLM, Navy I, and Navy II subareas (map on the bottom of Fig. 2.26). However, it has missing earthquakes for several periods (as listed in Section 2.1.2.4 above), although it is a very rich catalog at other times. It also shows peculiarly large number of the largest events (M≥3) that is not confirmed by the other catalogs; therefore, there might be some problems with the magnitude determination. The Lin et al. catalog, including 2,657 events with M≥1 in the whole Coso area, does not have as many small events as the two other catalogs. The Kaven et al. catalog is considered the preferred catalog for this area, but unfortunately it ends in the early 2015. It includes events also outside the geothermal area - the whole catalog contains 80,523 M≥−1 earthquakes, of which more than 400 M≥3 and more than 100 M≥4 events. In the geothermal area in particular, it includes 28,463 M≥0 events in the BLM, Navy I and Navy II areas together.

Figure 2.28 shows a map and cross-sections with earthquake data from the Kaven et al. catalog for the period Mar 1996 – early Apr 2015. The map illustrates that the earthquakes cluster around the production area at Coso, where the largest subsidence also occurs. The cross-sections of earthquake hypocenters feature four profiles with a 200-m width. Cross-sections of earthquakes only from the ENV period (Feb 2006 – Sep 2010), not shown in Fig. 2.28, display similar spatial distributions, but with fewer earthquakes compared with the whole catalog. This catalog includes only a few earthquakes from the first three months of the SNT1 period.

2.1.4 Effect of the July 2019 Ridgecrest Earthquakes on Surface Deformation at Coso

The third InSAR Sentinel processing (SNT2) in this project was planned for the fall of 2019, to cover the period after SNT1, which ended in April 2018. About two months before the planned SNT2 processing, two large earthquakes, M6.4 and M7.1, occurred on July 4 and 5, 2019 about 60 km and 45 km from Coso, respectively, near the towns of Ridgecrest and Trona, as well as China Lake where the Naval Air Weapons Station (NAWS) and the U.S. Navy GPO are located. These events came to be referred to as the "Ridgecrest" earthquakes. A number of the ruptures associated with these earthquakes occurred within the NAWS boundaries and caused significant damage to facilities there (Ross et al., 2019b). Aftershocks and ruptures propagated bilaterally from the epicenters, with the northwestern trend from the M7.1 mainshock extending towards Coso.

A number of studies have been carried out on the two events and their aftershocks, including DInSAR studies using ALOS (a Japanese satellite using L-band radar waves, ~26 cm) and Sentinel images before and after the large earthquakes. Figure 2.29 shows the first DInSAR map that appeared on the JPL/NASA website on July 9, later also used by Ross et al. (2019b). The fringes indicated a maximum LOS movement of about 60 cm. Soon after, DInSAR results from Sentinel images were shown to the scientific community and later published by Xu et al. (2020); they indicated similar patterns, but with a higher resolution. Both groups used the DInSAR results and field studies to outline the ruptures caused by the Ridgecrest earthquakes.

The M7.1 aftershock zone extended all the way to the northwest of Coso, but the geothermal field itself remained relatively devoid of aftershocks. Figure 2.30 shows a map of the aftershock locations over only one day, soon after the mainshocks, demonstrating that the aftershock sequence was very prolific in those early days. The relative gap in the aftershock distribution persisted for a long time.

Figure 2.31 shows a map with the kinematic summary of the surface ruptures from the Ridgecrest events (Ross et al., 2019b), used in their slip model. The northernmost branch,

Figure 2.28 Cross-Sections of Seismicity at Coso

Source: Individual plots by D. Adams, assembled and modified by M. Eneva.

54
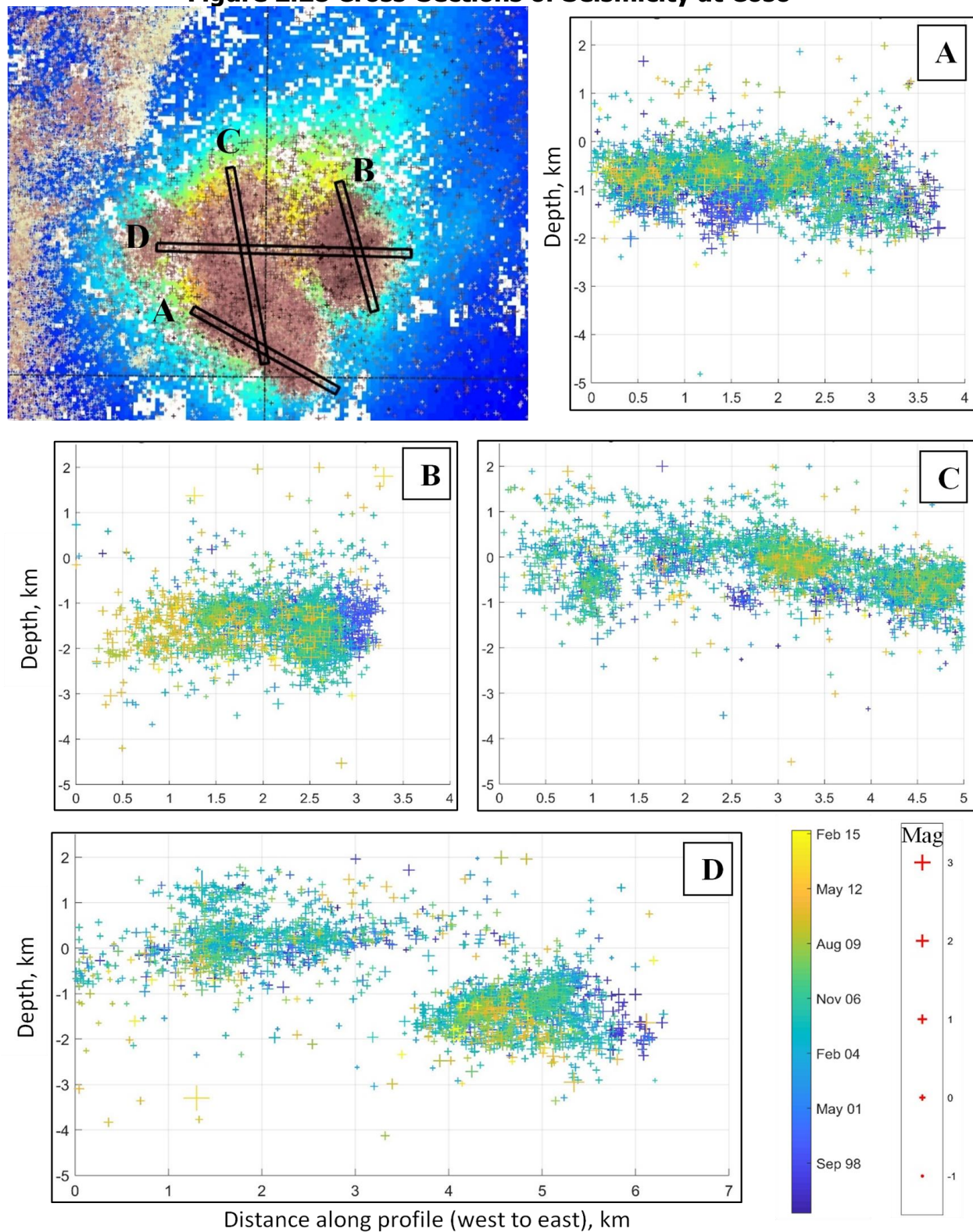
Figure 2.29 Examples of DInSAR from the ALOS satellite
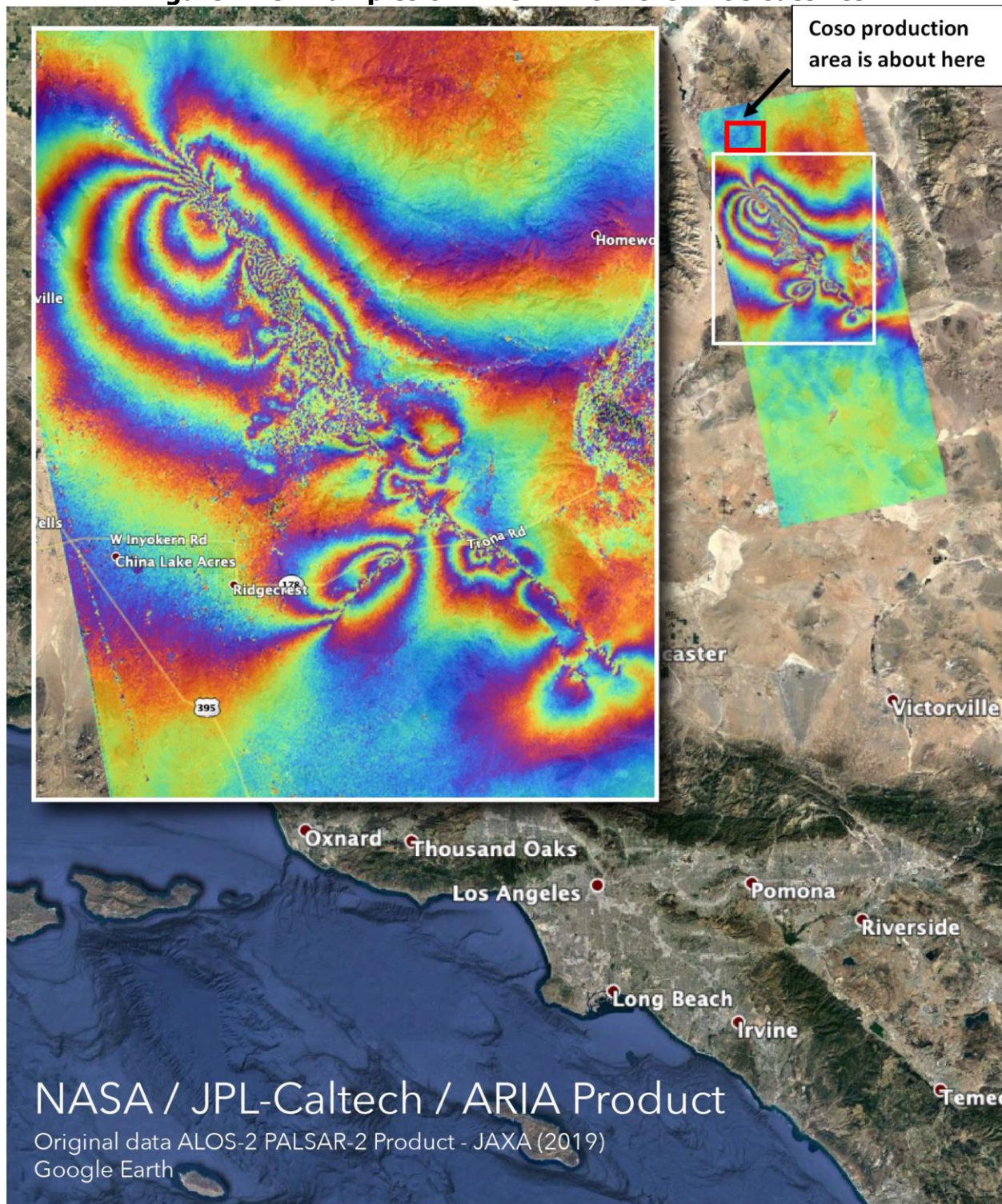
Two ALOS images were used for this interferogram, from April 16, 2018 and July 8, 2019. Each fringe indicates about a 12-cm movement. Linear features interrupting the fringes and noisy areas are associated with surface ruptures and disturbances.

Source: Image from Jet Propulsion Lab / NASA (https://www.jpl.nasa.gov/spaceimages/details.php?id=PIA23150). M. Eneva added red rectangle in the upper right corner to indicate the approximate location of the Coso geothermal field.

Figure 2.30 Example of Aftershock Distribution after the Ridgecrest Earthquakes
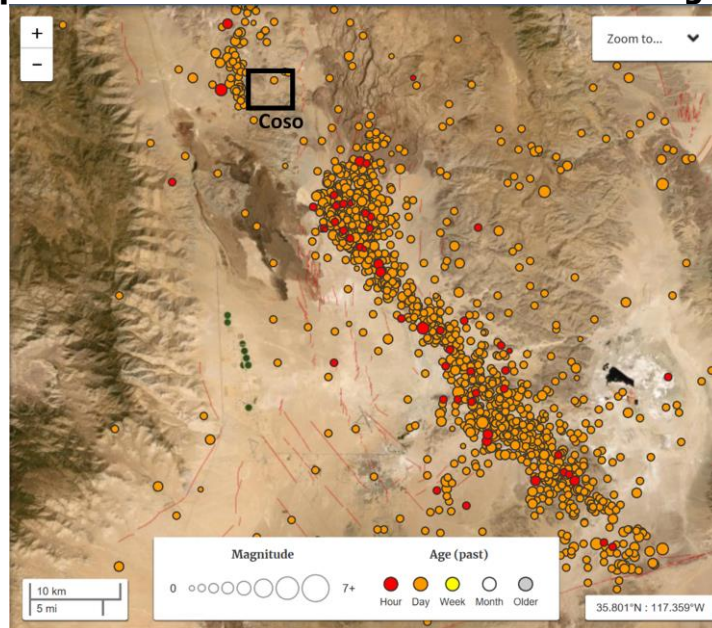
Aftershocks of all magnitudes are shown, occurring over one day ending on July 9, 2019, around 2:00 am Pacific time.

Source: M. Eneva extracted these earthquake data from USGS earthquake database (http://earthquakes.usgs.gov) on Jul 9, 2019 and added the location of Coso on the map.

Figure 2.31 Ruptures Associated with the Ridgecrest Earthquakes
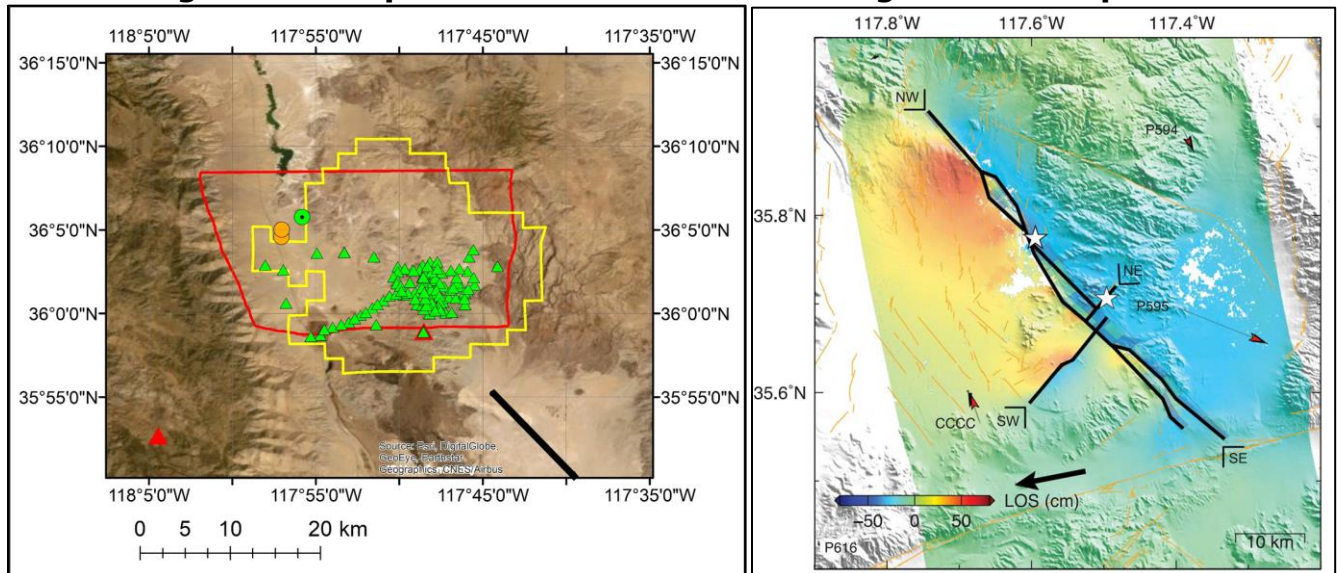
The northernmost straight segment of the M7.1 rupture (left) is shown with a black line in the southeastern corner of the map (right), along with the InSAR study area (red outline), Coso KGRA (yellow outline), ground-based survey stations (green triangles), and InSAR reference point (circle with dot). Other notations like in Fig. 2.6.

Source: Left – figure by M. Eneva, right – figure by Ross et al. (2019b).

Figure 2.32 Vertical Rates in the SNT2 and SNT2 Extended Periods, Whole Study Area
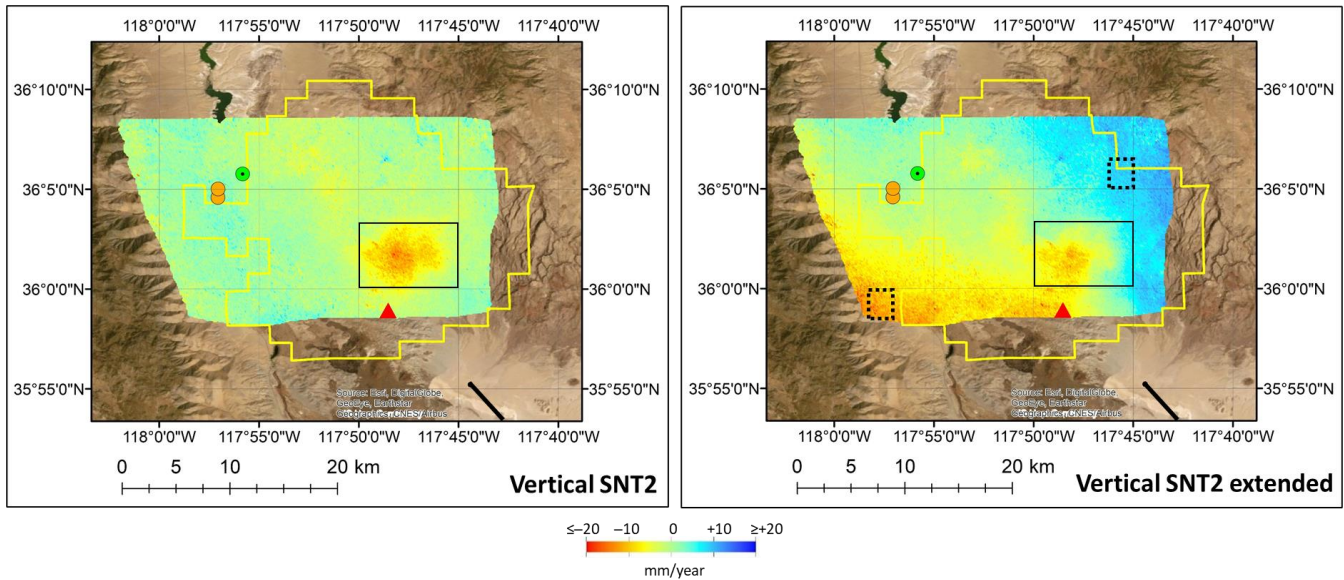
Comparison of color-coded vertical rates between the two periods for the InSAR study area. M7.1 rupture segment from Fig. 2.31 is marked with thick black lines in the southeastern corners of the maps. Black rectangles outline the geothermal field. Rectangles with dashed black outlines on the map for the extended SNT2 period (right) are used for the time series in Fig. 2.33 next. Other notations are like in previous figures.

Source: M. Eneva

about 12 km long, runs the closest to Coso and is also shown in the other map in Fig. 2.31 featuring the InSAR area studied in this project.

Although occurring outside the geothermal field, the Ridgecrest mainshock had a significant effect on the surface deformation detected within the area of geothermal operations, as revealed by InSAR. For this reason, all deformation maps and profiles so far featuring the SNT2 period, included the InSAR processing only until July 4, 2019 (before the M6.4 event occurrence on that date), because otherwise it would not be possible to investigate the deformation associated only with the geothermal operations.

In this section, results are shown from the SNT2 "extended" period until Aug 27, 2019 (see Table 2.2 above), which captures the effect of the M7.1 Ridgecrest earthquake on the territory of Coso and its surroundings. The extended SNT2 period includes eight ascending and six descending satellite scenes in addition to those used for the SNT2 period ending on Jul 4, 2019. At that time, some of the Sentinel scenes, especially the ascending ones, were already available every six days. A dramatic difference is seen in the results. Figure 2.32 shows the color-coded vertical rates from the two periods for the whole InSAR study area. A significant sinking (a drop) of the SW part and uplifting of the NE part of the InSAR study area are observed for the extended SNT2. Figure 2.33 shows average time series from these corners. The time series from the SW corner of the InSAR study area indicates only small displacements before Jul 4, with a drop of −24 mm between Jul 4 and Jul 16. After that, the displacements became small again. The time series from the NE corner in Fig. 2.32 shows an uplift of 20 mm between Jul 4 and Jul 16 (Fig. 2.33, right).

57

Figure 2.33 Vertical Deformation Time Series in the SW and NE Parts of the Study Area
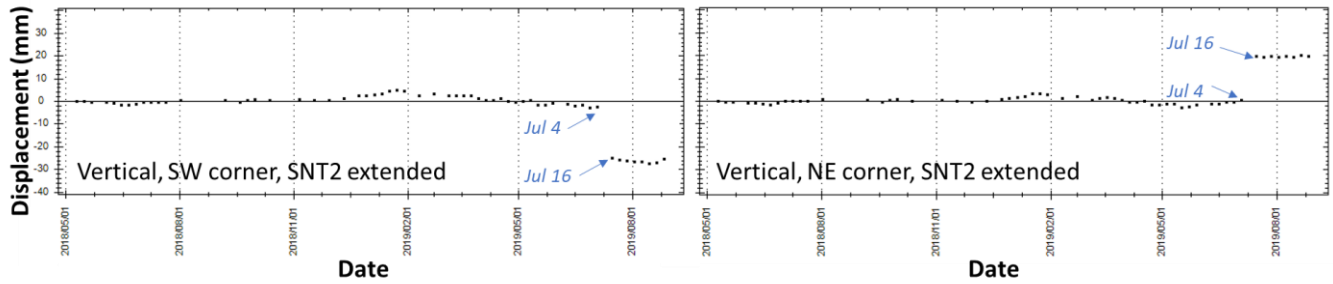
Source: M. Eneva (using the TRE Tool).

Figures 2.34 and 2.35 are like Figs. 2.32 and 2.33, but show maps and time series for the east component of the horizontal movements, as measured with InSAR. The time series from the SW corner indicates westward jump of −36 mm between Jul 4 and Jul 16. The time series from the NE corner show eastward displacement of 28 mm between Jul 4 and Jul 16. Similar to the vertical movements, later horizontal displacements become small again.

The descending satellite scenes are the ones that captured the movements associated with the M7.1 event, while the ascending geometry was apparently unfavorable for the purpose. However, both types of LOS displacements were needed to calculate the vertical and east horizontal components of the surface deformation.

Figure 2.34 East Rates in the SNT2 and SNT2 Extended Periods, Whole Study Area
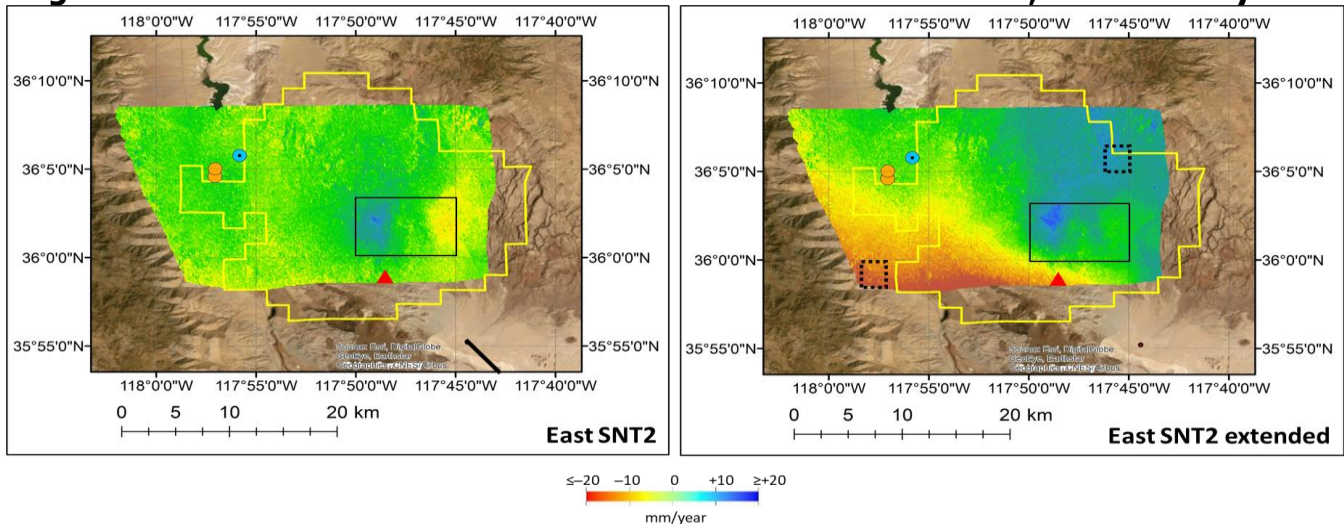
Comparison of the east horizontal components for the two periods. All notations are like in Fig. 2.32.

Source: M. Eneva

Figure 2.35 East Deformation Time Series in the SW and NE Parts of the Study Area
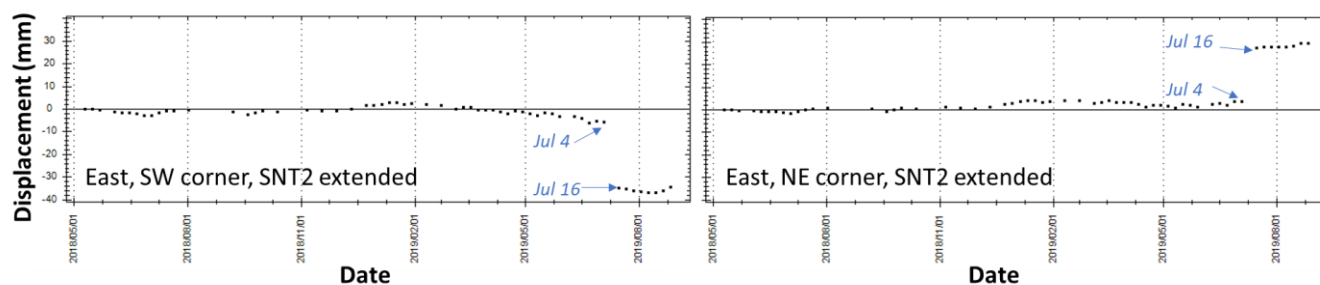
Source: M. Eneva (using the TRE Tool).

Next, the focus is on the geothermal field, where significant differences between the truncated and extended SNT2 periods are also seen (Figure 2.36). Two profiles are marked on the maps for the extended SNT2 period, A1-A2 (trending SW to NE) and B1-B2 (trending NW to SE). Cumulative vertical and horizontal deformations along these profiles, within a 300-m width, are shown in Figures 2.37 and 2.38. In both figures, the cumulative displacements are first shown for all scenes, with a start date in early May 2018. Then, only a few scenes before and after the Ridgecrest earthquakes are shown in order to emphasize the ground movements associated with the M7.1 mainshock. The vertical displacements show the formation of the subsidence bowl around the middle of both profiles, approaching a maximum of −20 mm over the extended SNT2 period (1 year, 4 months). The movements on the flanks of the subsidence bowl are much smaller. Both profiles also show the accumulation of significant eastward displacements to the west of the subsidence area, reaching 22 mm to the SW (along A1-A2) and 30 mm to the NW (along B1-B2).

The M7.1 event is associated with a large tilt occurring along the A1-A2 profile, with its SW edge sinking down to −24 mm and its NE part rising up to 22 mm between July 4 and Jul 16 (Fig. 2.37). In addition, the SW part of the profile shifts up to −38 mm to the west, and the NE part – up to 36 mm to the east. After that, the displacements appear to resume their usual progression.

The displacements along the B1-B2 profile (Fig. 2.38) are also affected by the mainshock occurrence. Uplift and eastward post-mainshock movements in the NW portion of the profile are about 5 mm, increasing along the profile in the SE direction (i.e., towards the M7.1 epicenter), reaching about 15 mm post-earthquake uplift and 18 mm eastward displacement in the SE end of the B1-B2 profile.

59

Figure 2.36 Deformation Rates at Coso in the SNT2 and SNT2 Extended Periods
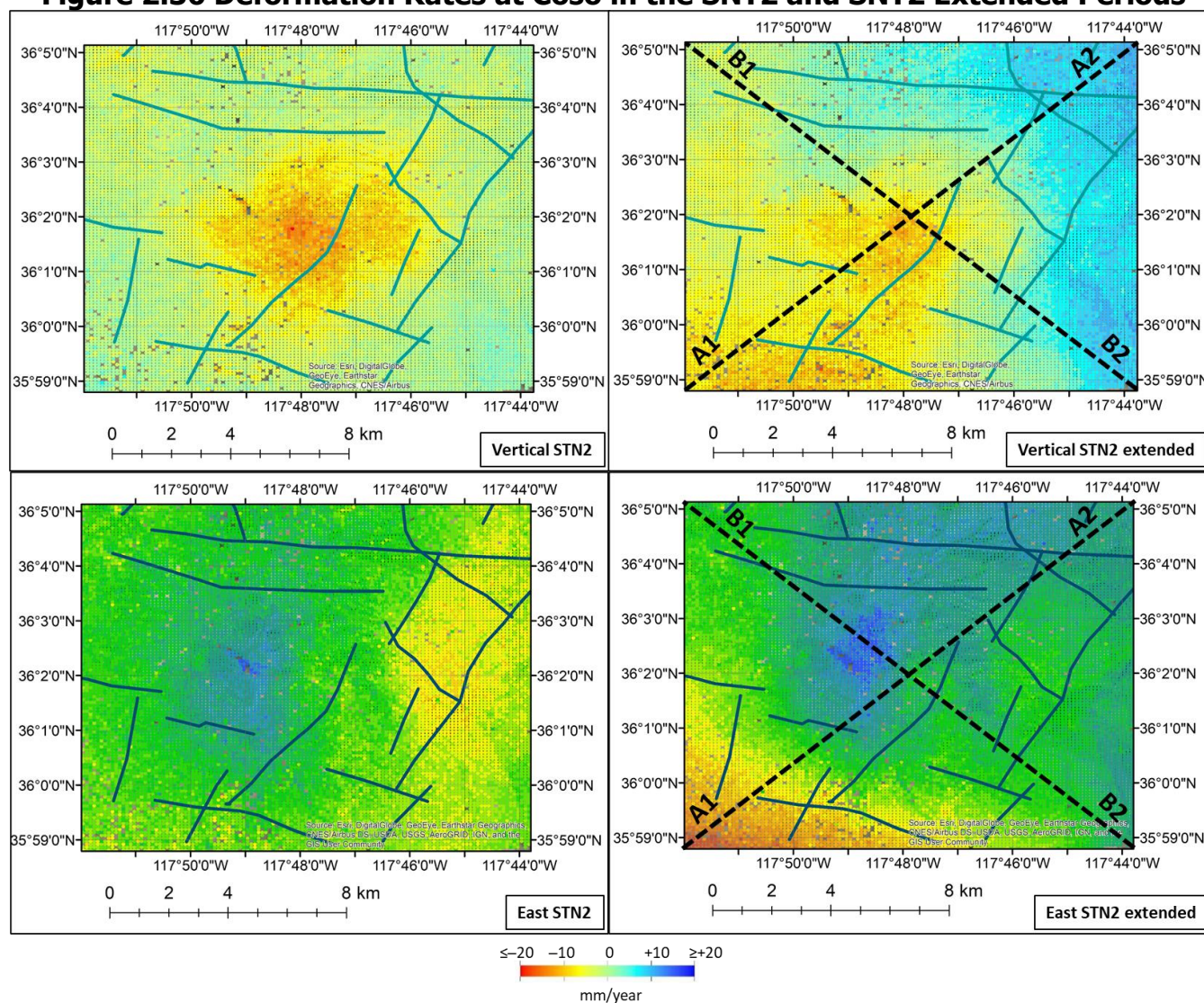
Color coded deformation rates at Coso. Left – STN period. Right – extended SNT2 period. Top – vertical rates. Bottom – east horizontal rates. Green lines show lineaments based on LiDAR. Deformation progressions along profiles A1-A2 and B1-B2 from the maps for the SNT2 extended period are shown in Figs. 2.37 and 2.38.

Source: M. Eneva

60

Figure 2.37 Effect of the M7.1 Earthquake on the Displacements along Profile A1-A2
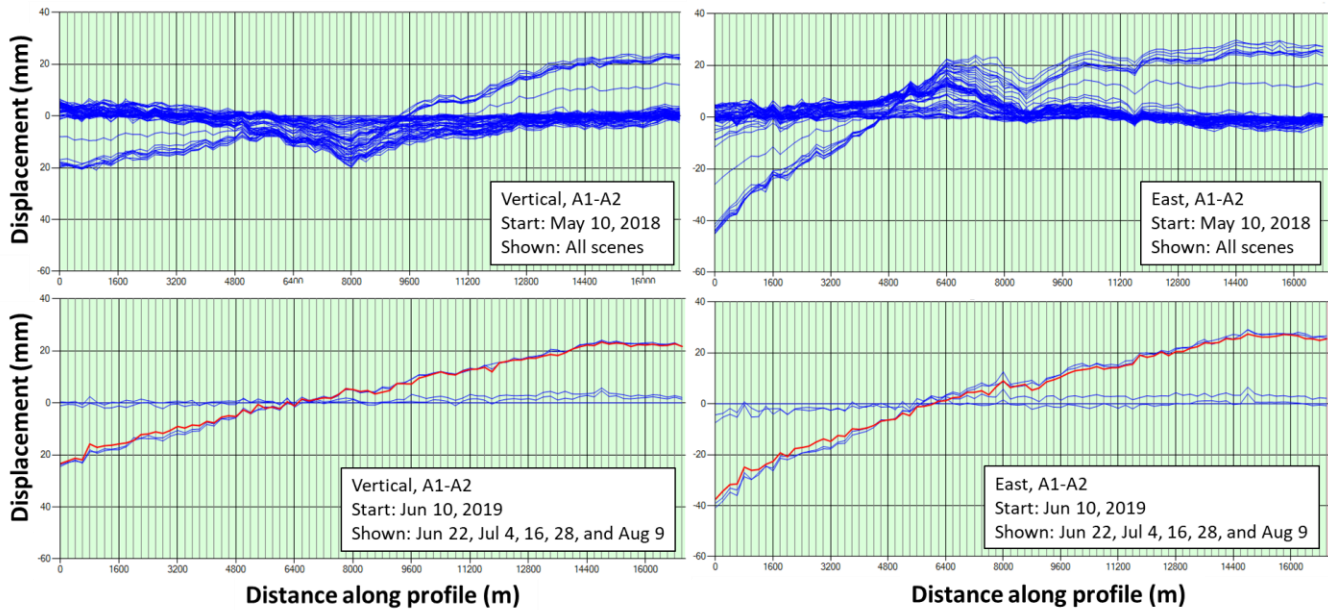
Top – Each curve corresponds to a satellite scene on a certain date; all scenes are shown. Displacements are measured from the date of the first scene in the SNT2 period, May 10, 2018. Bottom – Displacements are measured from Jun 10, 2019. Curves clustered around 0 are for dates before the M7.1 earthquake, Jun 22 and Jul 4. Curve for Jul 16, first date after mainshock, is shown in red. Blue curves around the red curve are from Jul 28 and Aug 9.

Source: M. Eneva (using TRE Tool)

Figure 2.38 Effect of the M7.1 Earthquake on the Displacements along Profile B1-B2
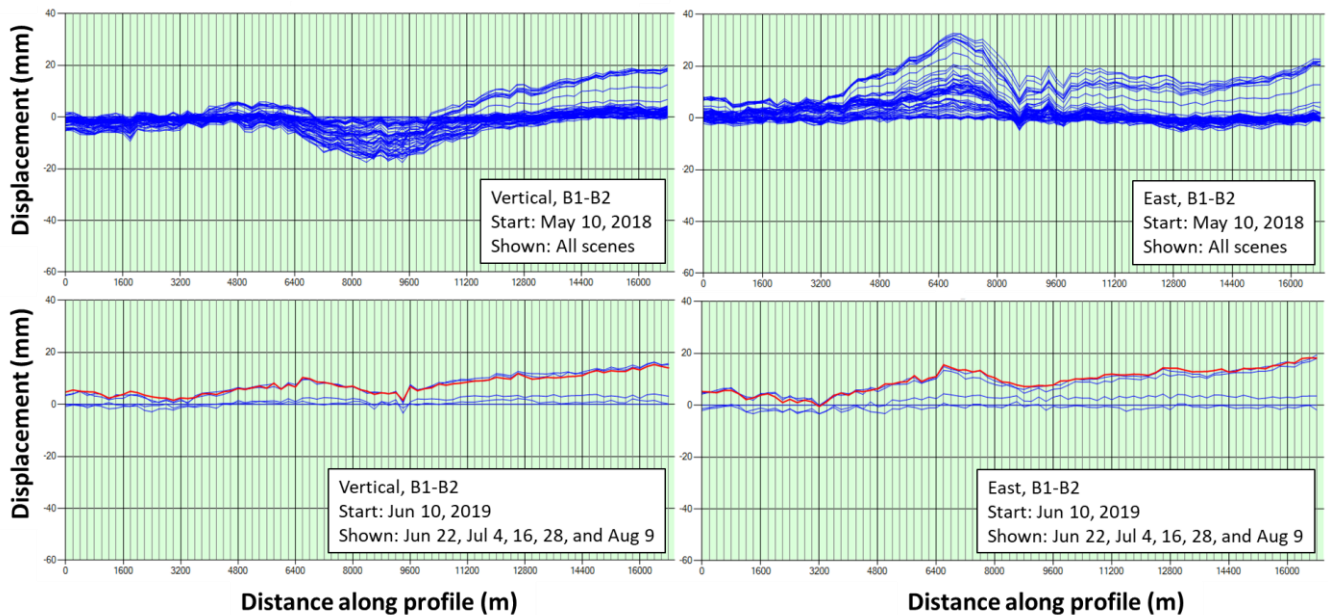
Notations like in Fig. 2.37.

Source: M. Eneva (using TRE Tool)

61

Figure 2.39 Time Series of the Relative Positions of Survey Stations
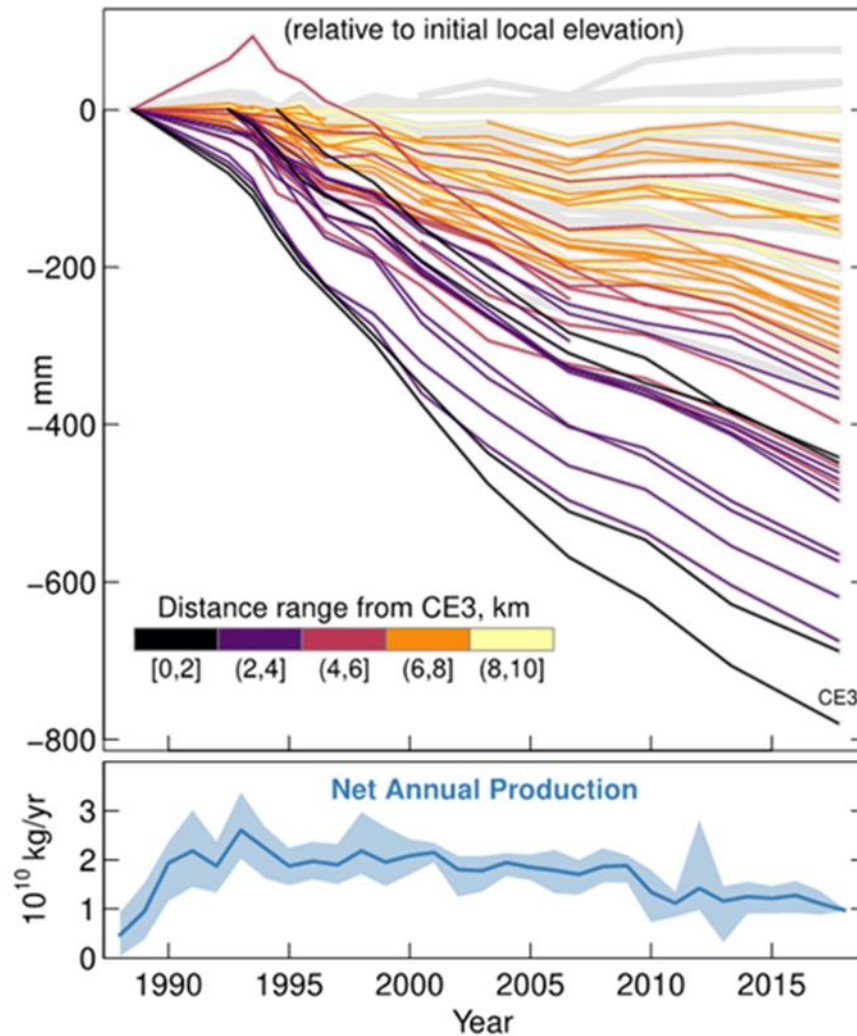
Color indicates radial distance to the fastest-subsiding station, CE3. Survey stations with fewer than three measurements are not included. A time series of the annual net geothermal fluid mass (production minus injection) is shown on the bottom.

Source: A. Barbour (USGS)

2.1.5 Deformation Modeling at Coso

Previous studies (Fialko and Simons, 2000; Vasco et al., 2002) have relied on elasticity to characterize the distribution volumetric strain rates within the Coso reservoir. Because these studies lacked time-varying estimates of surface motion, they could do very little to characterize the time-varying poroelastic response of the reservoir to injection and production of geothermal fluids. The new data here afford an opportunity to test analytical solutions to the problem of reservoir depletion in a poroelastic framework (Segall, 1985, 1989).

To justify using a poroelastic model, synthetic position estimates using the formulation given in Segall (1985) were first compared to the subsidence survey data (Figure 2.39). Simulation parameters are taken from reported volumes and general linear poroelastic properties of rock (Wang, 2000). The synthetic data show clear similarities with the actual data, including axial symmetry and a generally non-linear decrease in subsidence rates over time and radially from

Figure 2.40 Modeling of Subsidence Rates Due to Reservoir Fluid Withdrawal
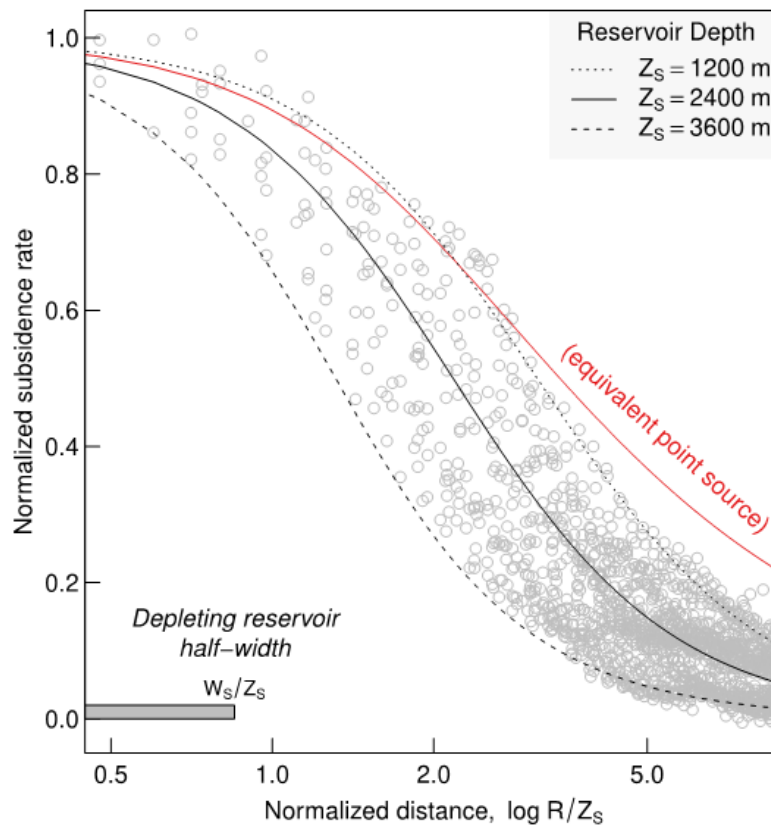
Normalized subsidence rates as a function of normalized distance for a deflating disk-shaped reservoir (Segall, 1989) compared to normalized, spatially averaged subsidence rates from InSAR (circles); the origin is at station CE3.

Source: A. Barbour (USGS)

the source. Poroelasticity is thus a highly plausible physical explanation for the observed subsidence survey data, implying that the observed subsidence distribution represents the effect of relatively steady net fluid loss at Coso since the late 1980's.

First insight into the connection between net production and observed surface rates was gained from incorporating the ENV InSAR vertical rates, which made it possible to independently constrain the likely source depth, and to test whether there is an appreciable effect of reservoir structure on the observed rates. In particular, the approach of Barbour et al. (2016), which treats the surface deformation rates as the manifestation of a point source of volumetric strain at depth, was modified to include finite reservoir dimensions (i.e., Segall, 1989); then, systematic non-linear inversions were used to identify the regions of maximum likelihood. Based on previous studies, this depth was expected to be between 1.5 km and 2.5 km below the surface. A systematic fitting procedure indeed showed a probable depth range between 1.2 km and 3.6 km, with the most probable depth at 2.4 km (Figure 2.40), with a half-width of 0.8 times the source depth, and a thickness of a few hundred meters. Compared with the equivalent point-source solution (i.e., Segall, 1985), this finite-source solution showed a significantly improved fit to the data. As shown, the spatial and temporal characteristics of

Figure 2.41 Profile through Survey Stations
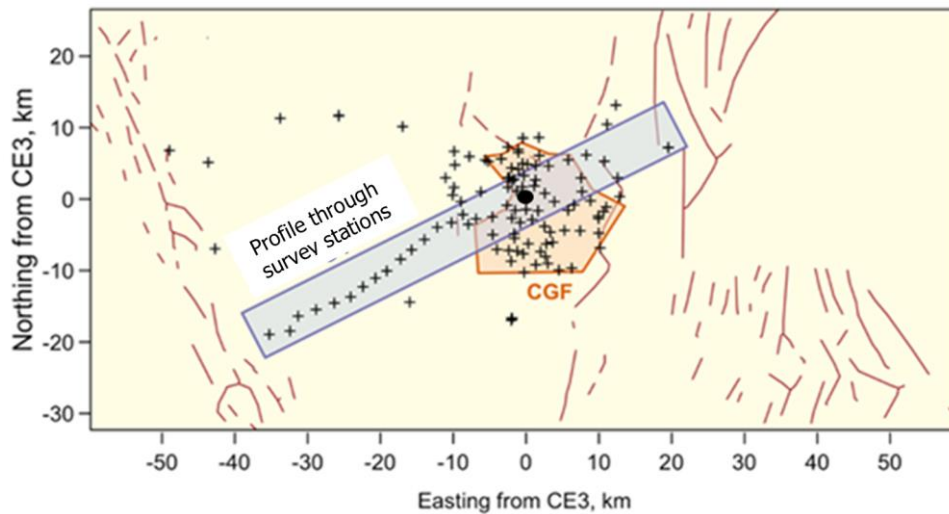
Map showing the survey stations (crosses) and a profile of survey data (diagonal strip) used in subsequent figures. Black circle marks the location of station CE3. CGF denotes the Coso geothermal field.

Source: A. Barbour (USGS)

Figure 2.42 Observed, Modeled, and Residual Displacements
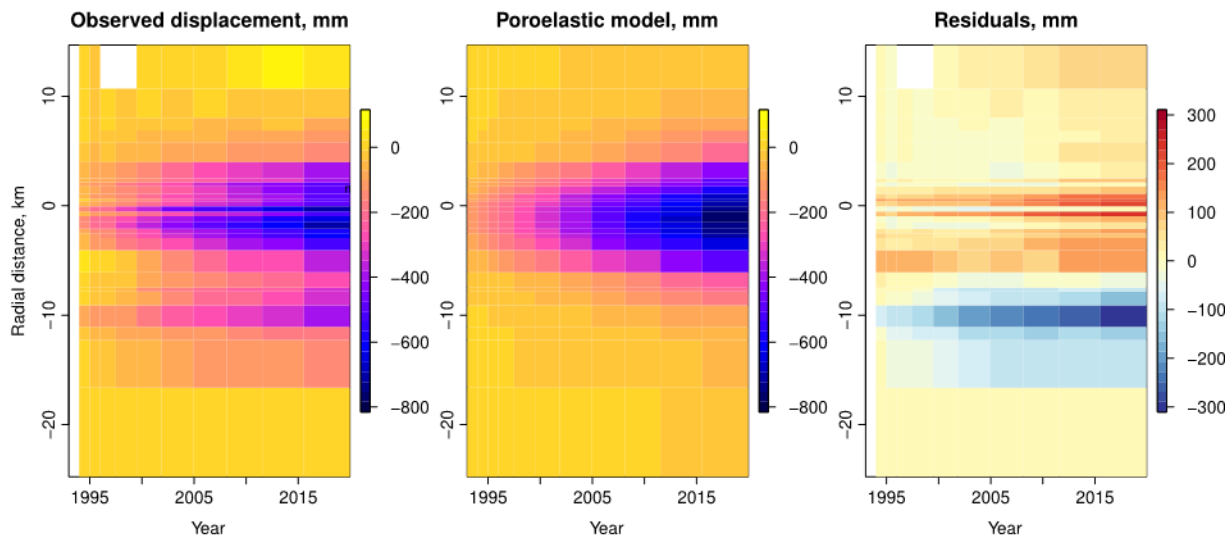
Source: A. Barbour (USGS)

the subsidence survey and InSAR ENV data closely match the expected rates from a simplified model of a contractional volumetric strain source embedded in a uniform, poroelastic half space. Furthermore, using the maximum likelihood depth (2.4 km), Simulated Annealing (Belisle, 1992) was applied to solve for optimal values of hydraulic diffusivity and volumetric loss rates at sources distributed across the reservoir, along a profile that passes through station CE3 (Figure 2.41). In general, the optimal results are in good agreement with data along this profile, however there are locations where additional sources might be present, as suggested by the residual positions (Figure 2.42). This is punctuated by the observation that

64

the ENV InSAR data are best represented by a contracting reservoir with finite dimensions rather than a layer with infinitesimal thickness (Fig. 2.40 above).

The optimal diffusivity estimate based on ground deformation is ~0.01 m^2/s, which is consistent with the lower range of estimates from seismicity migration patterns (Chen et al., 2012). It is important to note, however, that the subsidence surveys were not performed uniformly in space and time, so the first data from some stations were not collected until well after station CE3 was surveyed. Consequently, this non-uniform data coverage was expected to introduce a parameter bias, because the profile of relative positions used in the optimization is inaccurate; this is a problem which is especially acute at short radial distances (assuming the poroelastic model is valid). A limitation of this modeling is that it does not account for spatially variable rates of geothermal fluid injection and production.

The optimal set of properties for the hypothetical depleting reservoir and the hydraulic diffusivity of the medium in this first modeling results were in close agreement with previous work characterizing the geothermal system and local-to-regional scale patterns in seismicity. This modeling did not use time series of production and injection fluids for individual wells, so the preexisting feedback between permeability and moment release – seismic or otherwise – may be largely inseparable from the changes induced by anthropogenic production of the geothermal resource.

Subsequent modeling included the InSAR data from the SNT1 and SNT2 periods. Figure 2.43 is similar to Fig. 2.40 above, but it shows the normalized vertical rates from all three periods as a function of the normalized distance from station CE3. On the vertical axis, the rate at the location of station CE3 during the ENV period, ~ −26.4 mm/year, was used for the normalization of all InSAR vertical rates. On the distance axis, 2.4 km was used for the normalization, as the best-fitting reservoir depth. The maps in Figs. 2.12, 2.14-2.16 above already showed that there is a clear decrease in subsidence rates with time, likely caused by decrease in net production. The spatial profile for all three satellite periods is nonetheless consistent in space over time. That is, even though the amplitude of the subsidence is decreasing, the changes as a function of distance away from CE3 show the same spatial profile over time.

One interpretation of the time-invariant surface profile is that the physical mechanism relating the operation activities at Coso to the surface deformation is not migrating either in depth, or horizontally. The initial modeling applied to the ENV InSAR data, using a poroelastic model of a depleting, disk-shaped reservoir with a thickness of ~800 m, centered at 2.4 km depth, suggests that under this interpretation, the rate of change of reservoir depletion would be the driving factor, rather than changes in the geometry of the reservoir. A simple test of the depth-invariant hypothesis is to recalculate the ENV model with the same geometrical parameters, but change the source strengths with respect to that model. A valid result would recover the relative changes in observed surface motions by simply reducing the source strength proportionally.

As a starting point for the relative strength hypothesis, the mean value in the net-production curve was used for Coso during each of the three satellite periods (Table 2.9 above), and the SNT1 and SNT2 values normalized by the ENV value (Table 2.10 above). Thus, the source strengths for the two models of the SNT1 and SNT2 data were scaled by ~67 percent and 61

percent, relative to the ENV source strength, respectively. This simple approach appears to match all InSAR data remarkably well (Figure 2.44), which suggests a direct link between

Figure 2.43 Subsidence Rate Changes
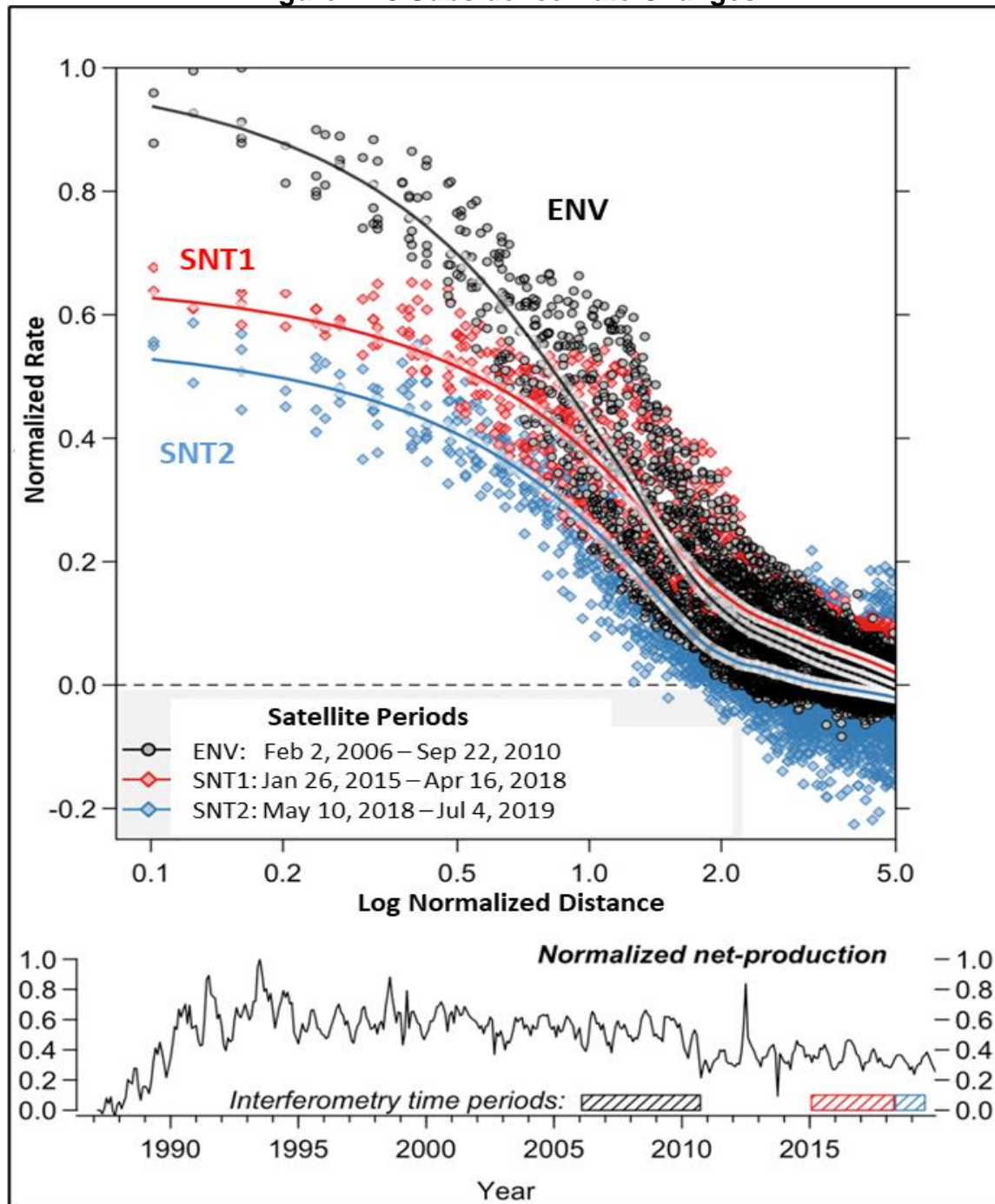
Points mark normalized InSAR vertical rates from the three satellite periods as indicated. Thick lines are drawn from smoothing applied to the points. Curve at the bottom shows the net fluid mass production across the Coso field, with satellite time periods marked.

Source: A. Barbour (USGS), modified by M. Eneva.

66

Figure 2.44 ENV Subsidence Model Applied to SNT1 and SNT2 Vertical Rates
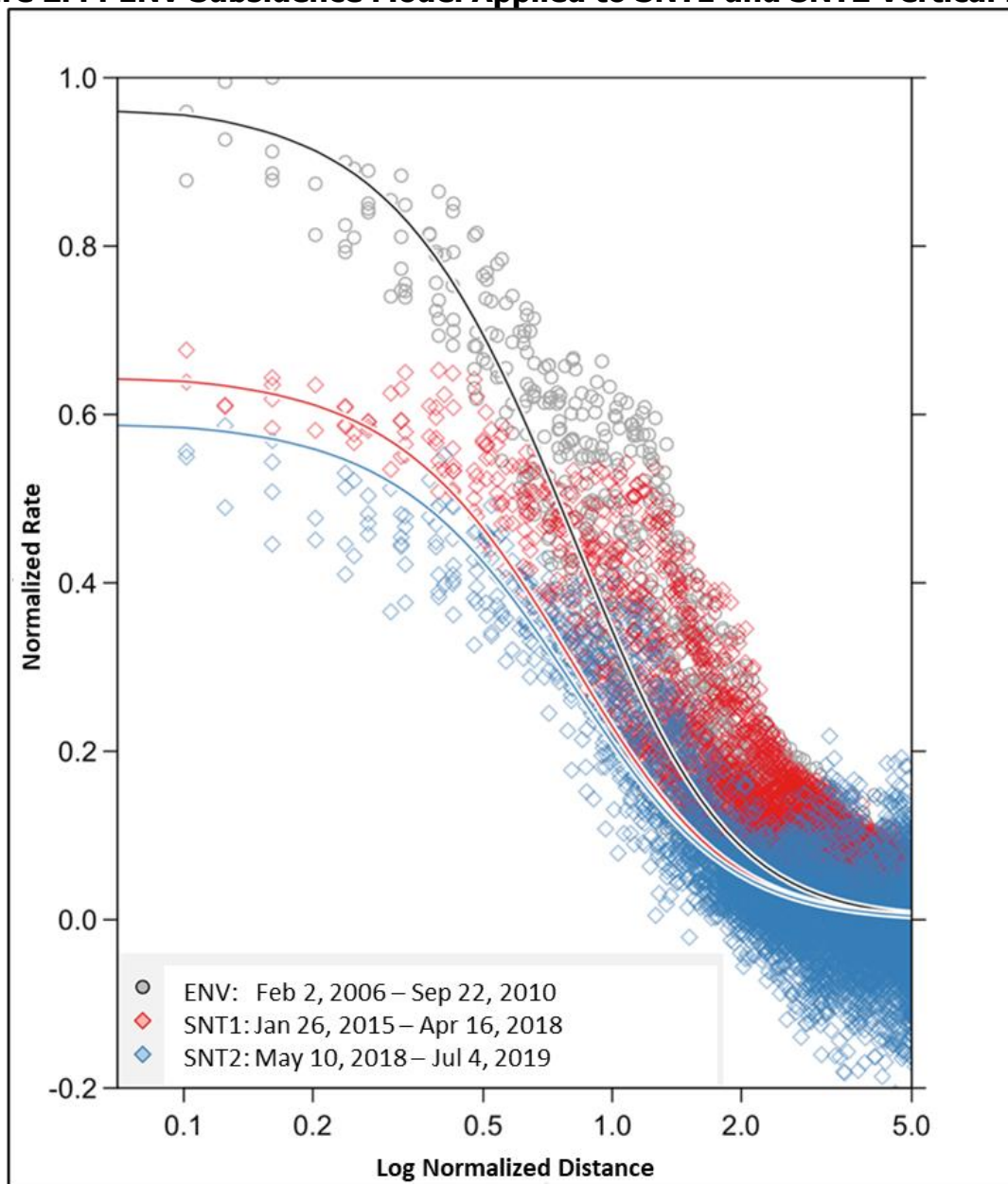
The ENV subsidence model re-fit to the SNT1 and SNT2 observations. The only change is the relative strength of the source, taken directly from geothermal plant operational parameters during the given time periods (Tables 2.9 and 2.10).

The normalization factors are the same as in Fig. 2.43.

Source: A. Barbour (USGS), modified by M. Eneva.

reductions in the difference between production and injection volumes and the strength of the subsidence at the surface. However, there is some indication that the specific reservoir geometry used in the initial ENV model is sub-optimal, in that there are some systematic differences for normalized distance larger than ~1.

Figure 2.45 Updated Model Inversion
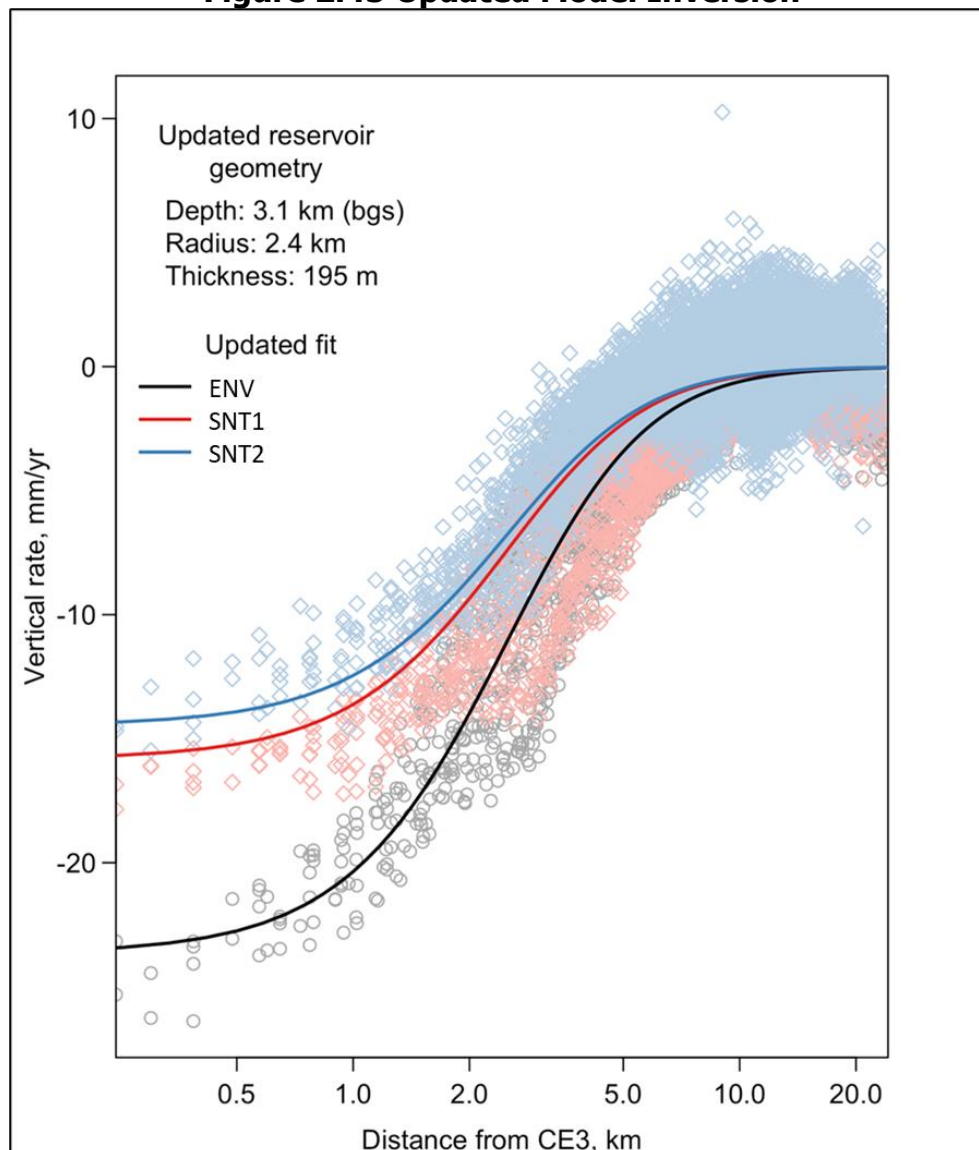
Nonlinear inversion for reservoir geometry using all InSAR data, with prescribed relative pressure changes in the model domain based on geothermal operational parameters for the three satellite time periods (Tables 2.9 and 2.10, Fig. 2.44).

Source: A. Barbour (USGS), modified by M. Eneva

To investigate these systematic misfits further, the entire dataset was re-fitted to allow for new reservoir geometry, while fixing the relative strengths as above. For this purpose, the Levenberg-Marquart non-linear inversion method was employed to estimate optimal parameters for the radius, depth, and thickness of the reservoir that minimize the residual sum of squares between the subsidence model and the observations. Figure 2.45 shows these results, which appear to fit all InSAR data convincingly. A test was applied to see whether the source depths should be shallower or deeper, and in neither case did the fit become more compelling; shallower depths caused the fit to degrade far from the origin, and deeper depths resulted in fit degradation at close and intermediate distances.

In summary, the observed surface deformation at Coso during all three satellite periods is consistent with a depleting reservoir, which has been suggested even when only the ENV data

were considered. However, considering all three periods led to the demonstration of a new finding, that changes in the observed subsidence over time can be easily interpreted as a result of changes in the rate of fluid mass loss from the hydrothermal system, with the size of the reservoir being time-invariant (or unresolvable). In particular, the aggregate injection and production data can be used to constrain the relative changes needed to fit the model. That is, the close correspondence with geothermal operational parameters suggests a direct link between net fluid production rates and changes in surface deformation. One important implication of this might be that observed surface deformation at Coso is largely a result of aseismic deformation processes (e.g., thermo-poro-elastic contraction and aseismic slip) and relatively insensitive to microseismicity induced by the geothermal operations.

2.2 Imperial Valley Geothermal Fields

2.2.1 Description of the Imperial Valley Study Area

The Imperial Valley extends for about 80 km in southern California, from the southern shore of the Salton Sea toward the U.S. – Mexico border (Figure 2.46). Together with the Coachella Valley to the north, it is part of the Salton Trough. It is a spreading center associated with the relative movement of the Pacific and North American Plates. Therefore, it is characterized by active tectonics, with both subsidence and substantial horizontal movements taking place on a regional scale. This is confirmed by current observations at GPS stations in the region. Local sources of deformation are represented by blocks formed by networks of strike-slip and

Figure 2.46 Map of the Salton Trough and Surroundings

Source: Nice (2016), modified by M. Eneva.

normal faults, many of which do not have surface expression, especially in the agricultural areas. The contribution of local tectonics is likely significant, especially in light of studies using seismic reflection data collected from the Salton Sea (Brothers et al., 2009). These authors note that oblique extension across strike-slip faults cause subsidence, leading to the formation of pull-apart basins, such as the Salton Sea and surrounding areas. They project maximum subsidence near the southern shoreline of the sea, approximately coincident with the locations of Quaternary volcanism and a northeast-trending band of very high heat flow. The project results confirm that indeed such a subsidence exists.

The Imperial fault (Fig. 2.46 and Figure 2.47) accommodates close to 80 percent of the relative motion between the Pacific and North American plates, with average slip rates estimated at 15-20 mm/year (Thomas and Rockwell, 1996) to 35-43 mm/year from geodetic surveys (Lyons et al., 2002). Partitioning of the plate boundary deformation further north, between the San Andreas and San Jacinto faults, has been debated. Estimates from GPS

indicate ~21 mm/year and ~15 mm/year, respectively (Fay and Humphreys, 2005) and from GPS/InSAR ~25 mm/year and 19 mm/year (Fialko, 2006). What is happening in between is not that clear; this is the location of the Brawley Fault Zone (BFZ), which is the main transfer zone between the Imperial fault and the southern tip of the San Andres fault (Johnson and Hill, 1982). Close to the Imperial fault, it is clearly expressed as the Brawley fault. The above observations have been made in this, southern part of the BFZ, while it is assumed that not much can be observed further to the north in the BFZ, due to lack of surface exposure and significant cover-up by agricultural fields. Paleoseismic studies measuring the vertical slip from earthquakes and aseismic creep near the southern part of the BFZ indicated acceleration compared with the long-term trend (Meltzner et al., 2006).

In addition to the gradual deformation due to regional and local tectonics, the Salton Trough experiences abrupt surface ruptures due to large earthquakes, as well as aseismic slip (Lohman and McGuire, 2007). Fig. 2.47 shows relocated earthquakes (Hauksson et al., 2012) for the period January 1981 – June 2011. The largest recent earthquake in the extended vicinity, causing extensive triggered slip, was a M7.2 event, which occurred in April 2010 south of the border. Brothers et al. (2009) attribute the larger earthquakes (M ≥6) in the area to the accommodation of the regional extension and subsidence, and the smaller events (M<5) and microseismicity to fracturing and block rotation within narrow (< 5-km-wide), dextral shear zones. A number of M≥5.5 earthquakes have occurred in the 20th century, with most seismic release on the Imperial Fault (e.g., Genrich et al., 1997). The southern tip of the San Andres fault is considered to be ripe for a large earthquake (e.g., Fialko, 2006), while the Brawley fault has ruptured during at least two large earthquakes (M7.1 in 1940 and M6.9 in 1979). The transitional Brawley Seismic Zone (BSZ) has been also marked by numerous small and several moderate earthquakes, most of them in swarms (e.g., in 1981, 2005, 2009, and 2012). Buried (blind, or covered by agriculture) faults in the BSZ and elsewhere in the Imperial Valley may be related to linear features suggested when relocated earthquakes (Hauksson et al., 2012) are displayed on maps and depth cross-sections (see examples in Sections 2.2.3 and 2.2.4). Lohman and McGuire (2007) studied the 2005 M5.1 swarm in particular, which occurred on the territory of the Salton Sea geothermal field. The authors suggested that such swarms are associated with significant aseismic creep, possibly connected to the extensional tectonic setting of the Salton Trough driven by magmatic intrusions (Hill, 1977) and the effects of high

Figure 2.47 Map of Imperial Valley
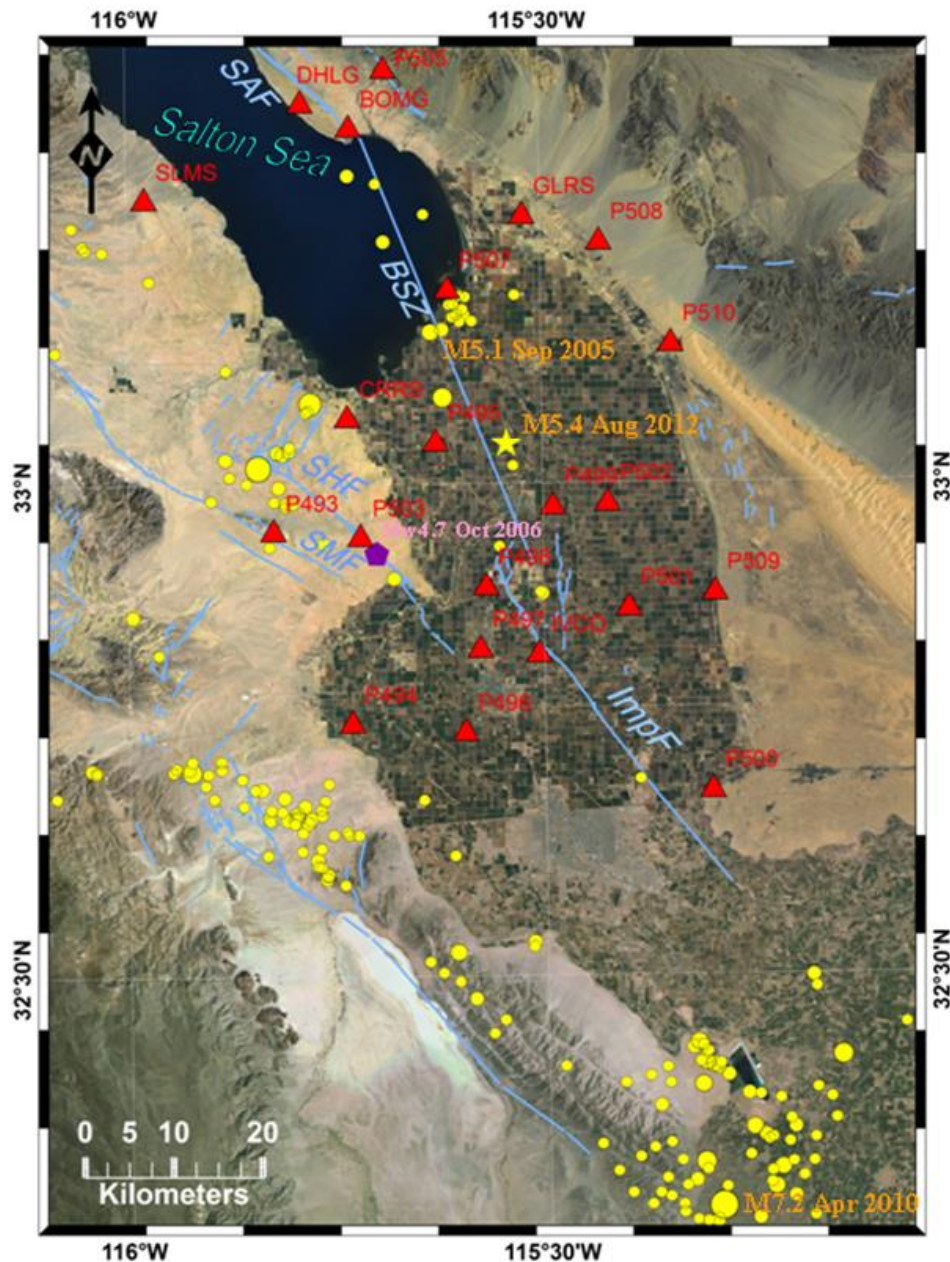
Map of the study area, superimposed on a satellite image. Red triangles mark GPS stations. Yellow circles denote epicenters of M ≥ 4.0 earthquakes occurring between 1981 and mid-2011 (relocated by Hauksson et al. 2012); circle size increases with magnitude. Recent moderate and large earthquakes are labeled with orange letters and numbers. The epicenter of a M5.4 swarm in August 2012 is marked with a yellow star, to indicate that it occurred outside the period of the relocated catalog. An October 2006 aseismic event, labeled with pink letters and numbers, was detected by a creep meter (purple pentagon next to GPS station P503). Blue traces denote faults (source U. S. Geological Survey): SAF (San Andreas fault); ImpF (Imperial fault); SHF (Superstition Hills fault); SMF (Superstition Mountain fault); and BSZ (Brawley Seismic Zone – marked with straight line through its center).

Source: M. Eneva

geothermal gradients (Ben-Zion and Lyakhovsky, 2006). A M5.4 sequence occurred in August 2012 on the territory of the Brawley geothermal field (Hauksson et al., 2013). Although the

main faults in the region are right strike-slip, there is evidence for the existence of intersecting normal faults, some of which have been unknown until earthquakes or triggered slip occurred on them (Rymer et al., 2011; Hauksson et al., 2013).

Aseismic creep has been detected on many occasions in Imperial Valley, usually triggered by larger earthquakes in the region and the wider vicinity (e.g., Rymer et al., 2002). The most notable recent example is the wide-spread triggered slip on faults in the Imperial Valley by the April 2010 M 7.2 event south of the border (Wei et al., 2011). In addition, an October 2006 aseismic event of equivalent moment magnitude Mw4.7 was detected by a creep meter on the Superstition Hills fault, and was confirmed by satellite interferometry (InSAR) and field measurements (Wei et al., 2009). This event occurred without triggering by a larger earthquake.

The high heat flow in this area is associated with significant geothermal resources (Table 2.11 and Figure 2.48). These include four operating geothermal fields: Salton Sea operated by CalEnergy since 1982 (currently 10 geothermal plants), with an additional development started in 2012 by EnergySource LLC (John L. Featherstone power plant, also known as Hudson Ranch-1); and Heber, North Brawley, and East Mesa (also known as Ormesa), all operated by Ormat Technologies. The total installed capacity in the Imperial Valley geothermal fields (last column of Table 2.11) in 2018 was 709.4 MW, while the total mean gross and net power in 2018 were about 475 MW and 400 MW, respectively.

Table 2.11 Geothermal Energy Production in Imperial Valley, 2018

Geothermal field	Gross Energy, MWh	Net Energy, MWh	Mean Gross Power, MWe	Mean Net Power, MWe	Capacity, MWe
Salton Sea – CE	2,608,383	2,359,229	297.8	269.3	370.6
Salton Sea – ES	455,888	415,994	52.0	47.5	55.0
Heber	688,094	456,160	78.6	52.1	161.5
North Brawley	92,865	55,669	10.6	6.4	49.9
Ormesa	314,059	216,494	35.9	27.7	72.4

Values in columns 4 and 5 show average electric power from three areas, calculated from the gross and net energy produced in 2018 (columns 2 and 3). "CE" and "ES" denote the CalEnergy and Energy Source parts of the Salton Sea geothermal field.

Source: Information in blue cells, originally provided for individual power plants, is from California Energy Commission, California Geothermal Energy Statistics and Data (https://ww2.energy.ca.gov/almanac/renewables_data/geothermal/index_cms.php). M. Eneva summed up the values for the individual plants to obtain the total values for the fields and calculated the values in the yellow cells.

Figure 2.48 KGRAs in Imperial Valley
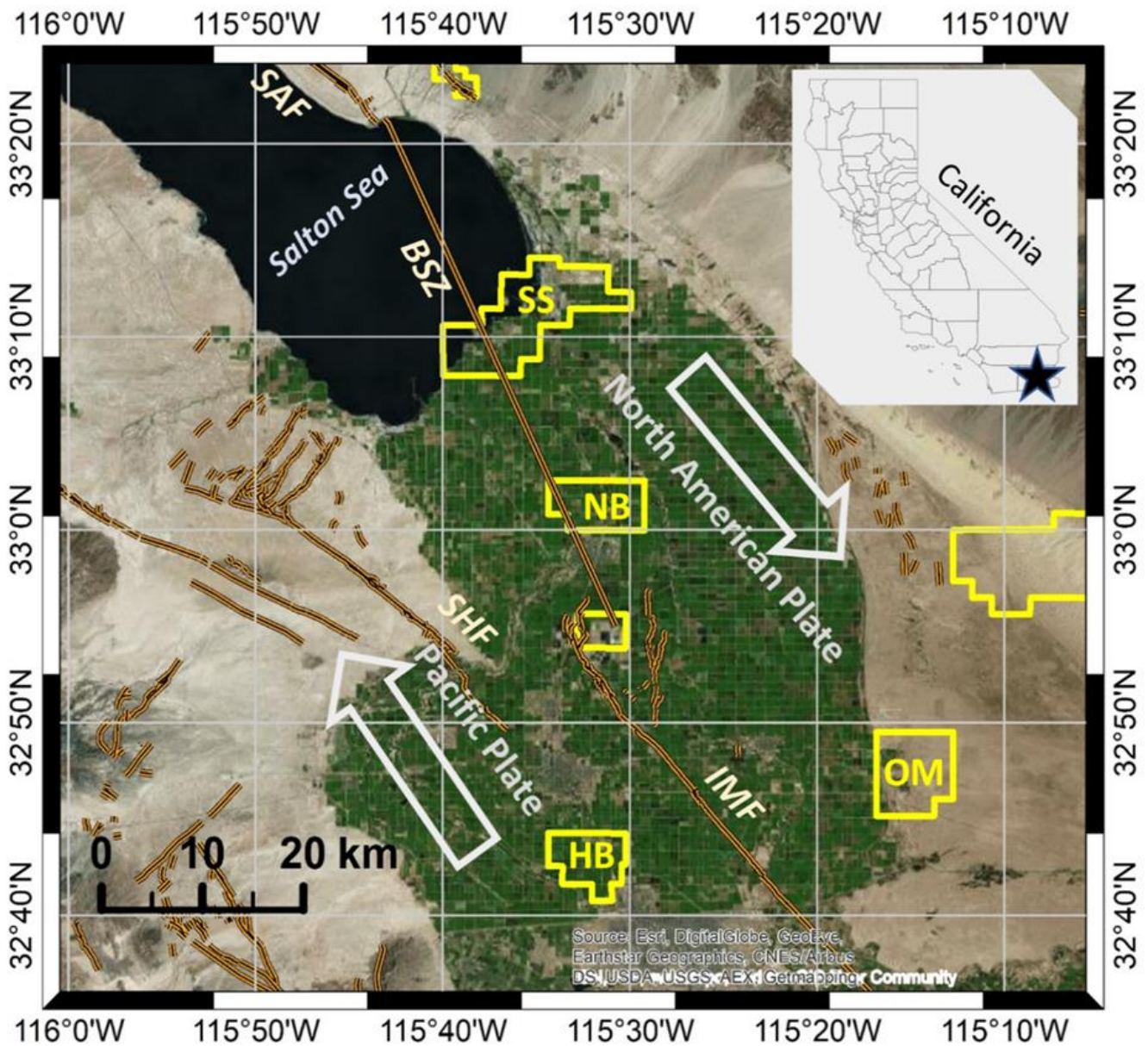
Yellow polygons mark known geothermal resource areas (KGRAs), and yellow letters denote operating geothermal fields: SS – Salton Sea, NB – North Brawley, HB – Heber, and OM – Ormesa (also known as East Mesa). Orange lines mark faults: IMF – Imperial fault, SAF – San Andreas fault, SHF – Superstition Hills Fault, BSZ – the middle line of the Brawley Seismic Zone.

Source: M. Eneva

The operations in the current geothermal fields appear to lead in some cases to induced seismicity and anthropogenic surface displacements superimposed on the tectonic deformation. Surface deformation is of concern because of the agricultural areas in Imperial Valley and the irrigation canals transecting the valley, which can be affected even by small displacements. It is important to thoroughly understand these processes, because significant geothermal development is envisioned in the future for Imperial Valley, and such effects may become more pronounced. In particular, geothermal operators monitor surface deformation by conducting annual leveling surveys; these measurements are reported to the Imperial County

74

Department of Public Works (ICDPW). Anthropogenic effects are believed to be alleviated through reinjection of the brine – more than 80 percent of fluid at the CalEnergy and Energy Source units of the Salton Sea geothermal fields with some evaporation associated with the flash power plants, and about 100 percent for the binary plants at Heber and North Brawley.

In this project, the analysis was done for three geothermal fields in Imperial Valley – Salton Sea, North Brawley, and Heber. These will be denoted hereafter with SSGF, NBGF, and HBGF, respectively. Where necessary, SSGF is split into SSGF-CE and SSGF-ES to mark the CalEnergy units separately from the EnergySource development. Ormesa (East Mesa) was not included in this project to avoid additional cost; being outside of the agricultural areas, surface displacements at this field are generally not of concern.

2.2.2 Data Used in Imperial Valley

2.2.2.1 Satellite Data

Sentinel data were available and processed for all three study geothermal fields. This was done in two stages, SNT1 and SNT2, similar to the Coso analysis. In addition, TerraSAR-X (TSX) data were analyzed for the SSGF and NBGF; such data were not available for the HBGF. The results were compared with those from a previous CEC project, where Envisat (ENV) data were analyzed and results were reported by Eneva et al. (2012-2014). As before, the abbreviations ENV, SNT, and TSX are used to designate both the satellites used and the periods covered by the scenes in the analysis. In addition, SNT1 and SNT2 designate the two adjacent periods of analyzed Sentinel data (not different satellites). In fact, the Sentinel data initially came from one satellite only (Sentinel-1A), but in in 2016, scenes started being collected with a second satellite (Sentinel-1B), which made it possible to reduce the revisit time. Table 2.12 shows the periods covered and the number of satellite scenes used in the analysis.

Table 2.12 Satellite Periods and Numbers of Scenes Used in Imperial Valley

Satellite Period	Period Asc	Period Desc	Number Asc	Number Desc	Min Revisit, Time, days
ENV	Dec 16, 2003 – Aug 31, 2010	Feb 7, 2003 – Sep 3, 2010	39 (33 to the north)	45	35
TSX	Sep 22, 2012 – Oct 23, 2013	Sep 3, 2012 – Sep 12, 2013	17	15	11
SNT1	Apr 3, 2015 – Apr 29, 2018	Mar 10, 2015 – Apr 23, 2018	60	51	24 (12 since 2017)
SNT2	Jan 4, 2018 – Aug 22, 2019	May 18, 2018 – Aug 28, 2019	37	40	12

Source: M. Eneva

Table 2.13 shows the orbital angles and sensitivities of the LOS measurements to the vertical and east horizontal displacement components. For all satellite data, LOS is most sensitive to the vertical component, with decreasing sensitivity from ENV to TSX and then SNT. For this reason, the spatial deformation patterns are very similar between maps of LOS and vertical

rates, just with different numerical values. In contrast, because LOS is less sensitive to the east horizontal component, its spatial deformation patterns cannot be deduced from the appearance of LOS deformation maps, and decomposition of the ascending and descending LOS measurements is the only way to provide such information. The sensitivity to the east horizontal component is the highest for SNT, followed by TSX and ENV. For all satellites, as already discussed in the case of Coso, the sensitivity to the north horizontal component is low enough that it cannot be recovered.

Table 2.13 Orbital Geometry and Sensitivities in Imperial Valley

Angles	Envisat, deg	TerraSAR-x deg	Sentinel, deg
Ascending θ	20.27 SS, 20.92 HB	26.62	36.65
Ascending δ	12.94 SS, 12.97 HB	11.53	11.22
Descending θ	22.13 SS. 21.14 HB	29.03	36.96
Descending δ	11.32 SS, 11.39 HB	9.83	9.66

Sensitivity to	Envisat	TerraSAR-X	Sentinel
Vertical ascending	+0.94 SS, +0.93 HB	+0.89	+0.80
East ascending	-0.34 SS, -0.35 HB	-0.44	-0.59
North ascending	-0.08 SS, -0.08 HB	-0.09	-0.12
Vertical descending	+0.93 SS, +0.93 HB	+0.87	+0.80
East descending	+0.37 SS, +0.35 HB	+0.48	+0.59
North descending	-0.08 SS, -0.07 HB	-0.09	-0.11

The InSAR ENV analysis for Imperial Valley was done in a previous CEC project. The data were processed in two tiles – northern and southern parts of the study area. For this reason, θ and δ are slightly different for the Salton Sea geothermal field (marked with SS in the table) and for the Heber geothermal field (marked with HB). Single tiles were used for InSAR processing in the current project of the TSX data (for SSGF and HBGF) and the Sentinel data (for all three study fields).

Source: M. Eneva

2.2.2.2 Leveling and Well Data

The geothermal companies in Imperial Valley submit annual leveling reports to the Imperial County Department of Public Works (ICDPW). These reports state that a classical differential leveling technique is used to measure vertical elevations with high order of accuracy. The National Geodetic Survey (NGS) specifications are followed, according to which the minimum accuracy standard of $\pm 6mm * \sqrt{d}$, for 2nd order class I leveling, with d being the length of section or loop in kilometers, was used in determining allowable tolerances in field error of closure on all sections and loops. All surveys are referenced to local benchmarks (S-1246 at SSGF-CE, B-1226 at SSGF-ES, A33 at HBGF, and Y-1225 at NBGF). These datum points were also used to re-reference the InSAR results, so that direct comparisons are possible.

Figure 2.49 Leveling Benchmarks and Datum Points in Imperial Valley
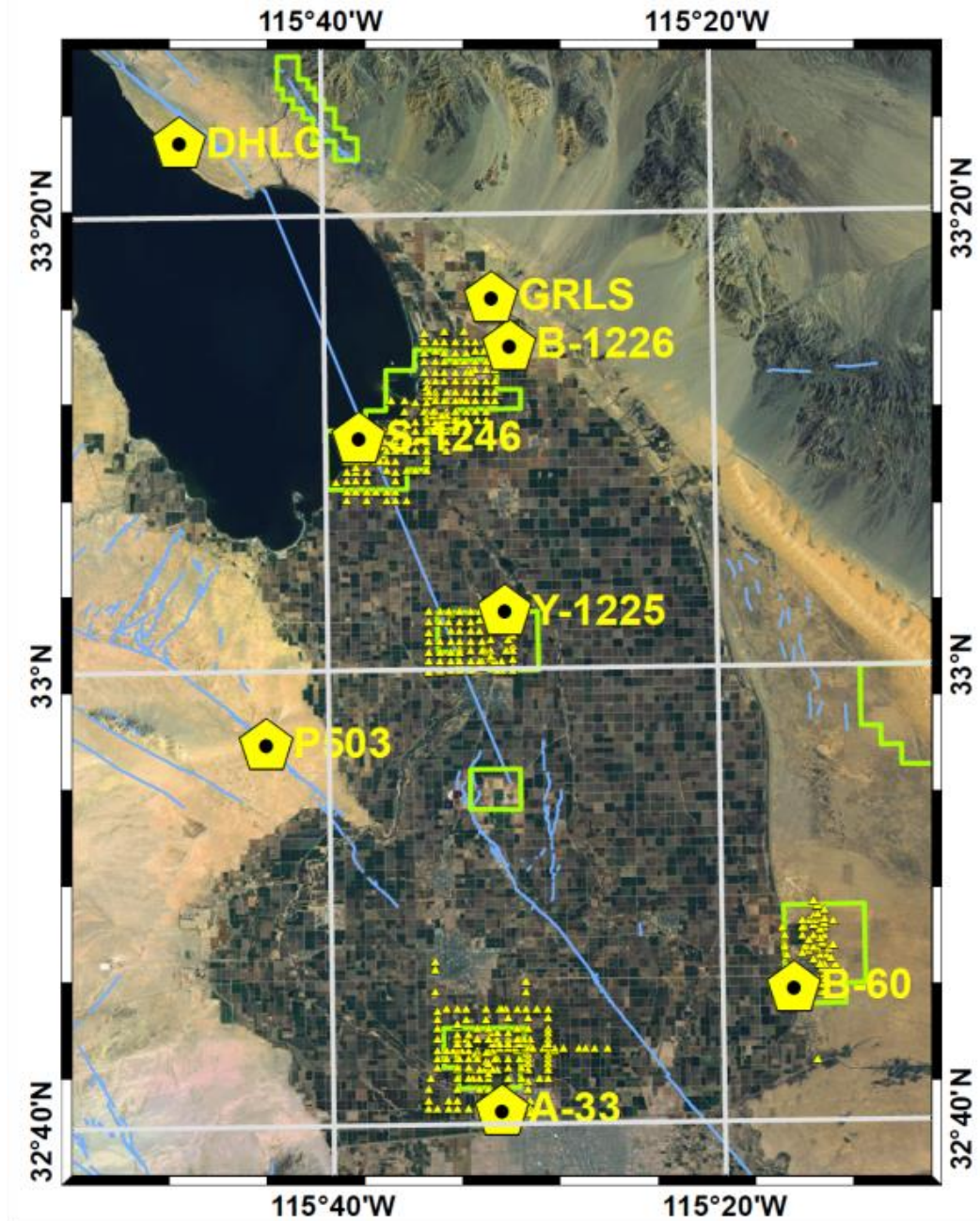
Yellow triangles show the locations of all benchmarks. Yellow pentagons mark locations of datum benchmarks (S-1246, B-1226, Y-1225, A-33, and B-60) and some GPS stations. Green polygons outline geothermal areas. Blue traces mark faults.

Source: M. Eneva2.49 shows the locations of the benchmarks at all operating fields in Imperial Valley and the datum points. Table 2.14 shows information about the surveys in the four fields.

Table 2.14 Information About the Leveling Surveys in Imperial Valley

	SSGF-CE	SSGF-ES	HBGF	NBGF
Period of surveys	Annual May 1998 – Nov 2018	1992, Annual Dec 2011 – Nov 2018	Annual Jan 1994 – Dec 2018	Annual Nov 2009 – Nov 2018
Number of surveys	20	9	25	10
ENV period	7	8	6	1
TSX period	1	2	n/a	2
SNT1 period	3	3	3	3
SNT2 period	1	1	1	1
Number of benchmarks	120/119/109	24 in 1992, 95/95/92	138/121/106	80/80/71

"CE" and "ES" mark the CalEnergy units and the EnergySource development at the SSGF. Last row shows three numbers of benchmarks - those used at any time, after satellite coverage started, and at the time of the last surveys for which data were available from the ICDPW.

Source: M. Eneva

Figure 2.50 shows maps with the locations of the leveling benchmarks and the injection and production wells at each of the three study fields. These locations were obtained from ICDPW for the benchmarks and from CalGEM for the wells.

2.2.2.3 Seismicity Data

Some of the earthquake data used to investigate induced seismicity at the three geothermal fields were from a relocated catalog using a method described first by Lin et al. (2007) and then also used by Hauksson et al. (2012); the same one was also used at the Coso geothermal filed. The earthquakes in this 1981-2018 catalog are relocated compared with the events from the Southern California Seismic Network (SCSN). Other earthquake data are from Ross et al. (2019a), using a template matching method to identify ten times more earthquakes in southern California than the SCSN data, starting in 2007.

The SSGF has the largest number of induced microearthquakes. It experienced a M5.1 event (see Fig. 2.47 above) and about a three-month associated swarm in the fall of 2005, which was in the ENV period, analyzed in a previous CEC project (Eneva et al., 2012-2014), included also here for the sake of comparison with the TSX and SNT periods.

The NBGF had more significant induced seismicity when production was higher early on, but it decreased with the decreasing production. However, a M5.4 event occurred in Aug 2012 on its territory, followed by aftershocks (Hauksson et al., 2013). While the mainshock was considered to be too large to be directly induced by geothermal operations, Wei e al. (2015) hypothesized that induced aseismic slip might have triggered the earthquake on a previously unknown fault.

Compared with SSGF and NBGF, the level of induced seismicity at the HBGF is much lower. In that case, the microearthquake catalog recorded by the local seismic network was also available; it provided several times more microearthquakes than the Lin et al. catalog. Most of it was supplied by the ICDPW, except for 2019 – these data were provided by Dr. G. Foulger, with Ormat's permission. Foulger & Associates has been contracted by Ormat to locate the microearthquakes from the local network since 2011.

Figure 2.50 Leveling Benchmarks and Geothermal Wells in Imperial Valley
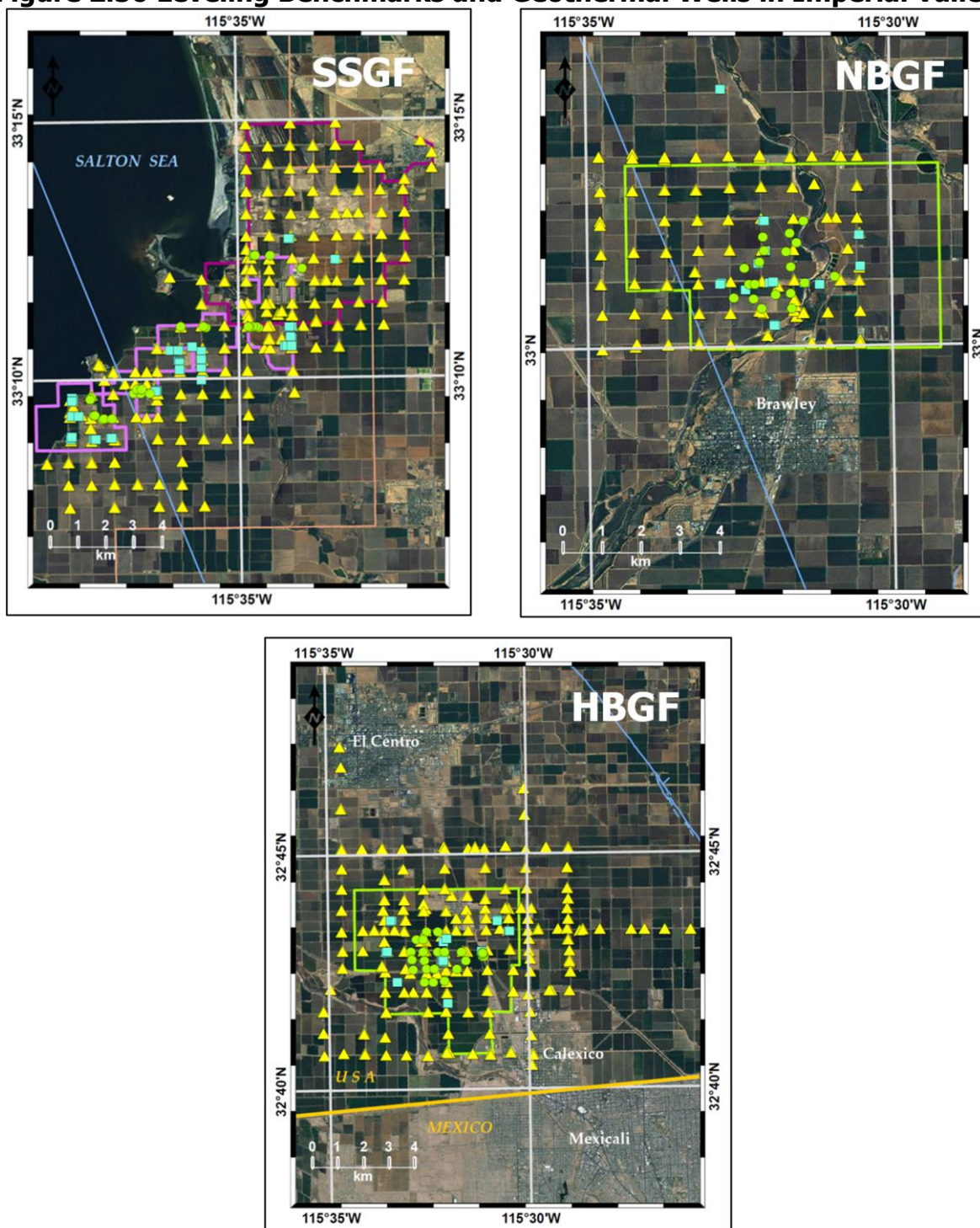
Yellow triangles – benchmarks. Green circles – production wells. Blue squares – injection wells. Pink polygons – CalEnergy units. Dark red – area monitored with benchmarks by EnergySource. Light orange – Salton Sea KGRA (only a portion is seen). Blue lines – fault traces and a central line through the Brawley Seismic Zone (BSZ).

Source: M. Eneva

Figure 2.51 SNT1 LOS Deformation Rates in Imperial Valley
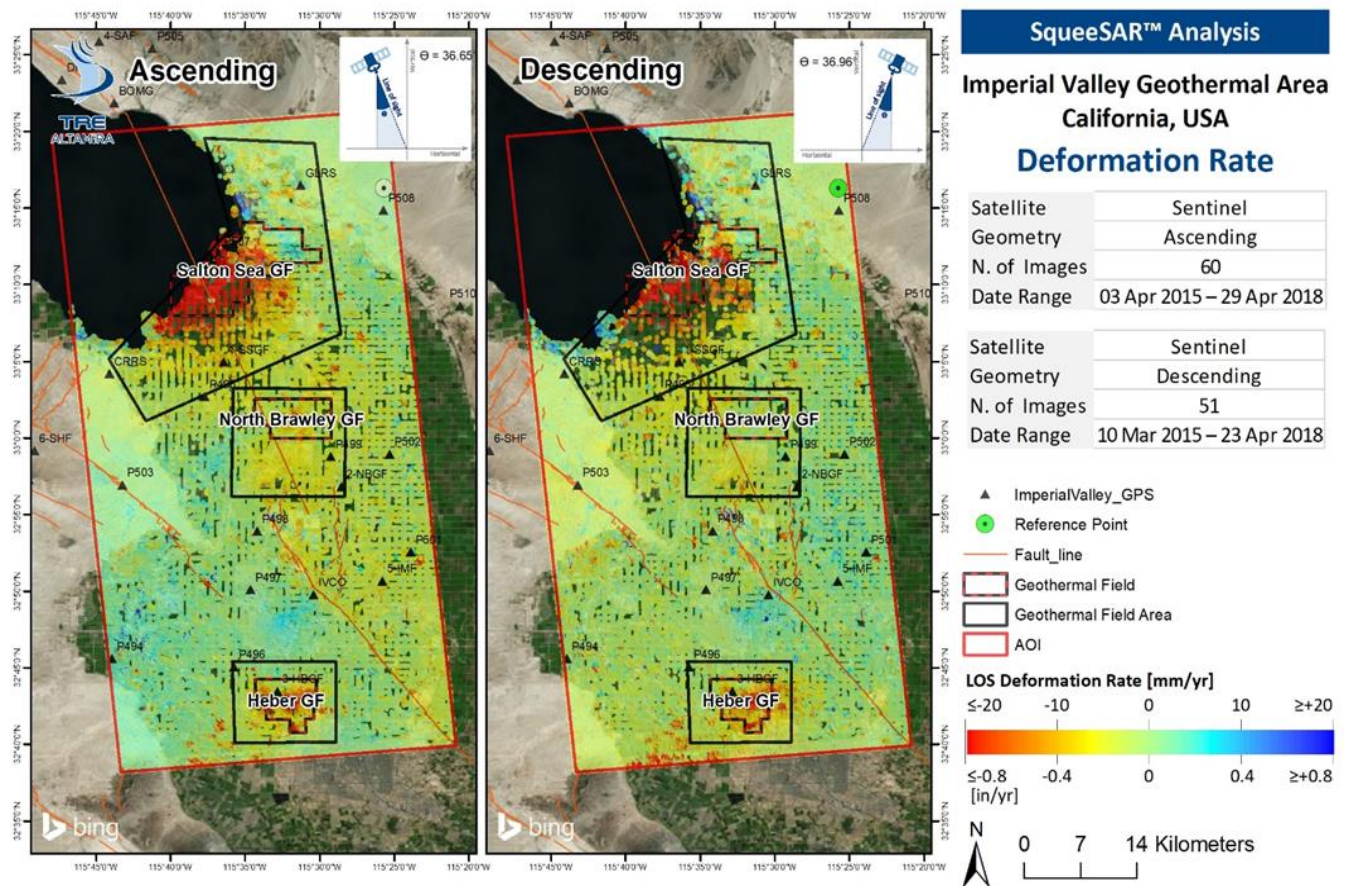
Source: TRE Altamira

2.2.2.4 Surface Deformation from InSAR in Imperial Valley

Subsequent sections will provide information on surface deformation measured by InSAR for the individual geothermal fields, but results for the whole Imperial Valley covered by these data are first shown here. Figures 2.51 and 2.52 show SNT1 results covering all three geothermal fields and the areas between them. The reference points are located outside the valley, in the NE corner of the study area, near a GPS station, P508. Later on, when individual geothermal fields were considered, these results were re-referenced to the locations of the datum benchmarks used in them; this made it possible to make direct comparisons with the leveling data. Figure 2.51 shows distinct LOS movements away from the satellite (i.e., indicative of subsidence) on the territories of the geothermal fields. This generally confirms the patterns already observed in the ENV results for SSGF and HBGF from a CEC project preceding this one (Eneva et al., 2012-2014), and for the SSGF, from a Canadian satellite, Radarsat, in the earliest CEC project (Eneva et al., 2009; Eneva, 2010a; Eneva and Adams, 2010). The decomposition was done in pixels of linear size 100 m; as a reminder, only pixels that contain PS and DS from both types of LOS, ascending and descending, can have estimates of the vertical and east horizontal movements (Fig. 2.52). So, while maps of vertical and east horizontal movements are more intuitive than LOS ascending and descending maps, decomposition does lead to loss of information in this agricultural region, because some of the 100-m pixels without vertical/horizontal estimates, do contain PS/DS points with one type of

Figure 2.52 SNT1 Maps of Vertical and East Horizontal Deformation
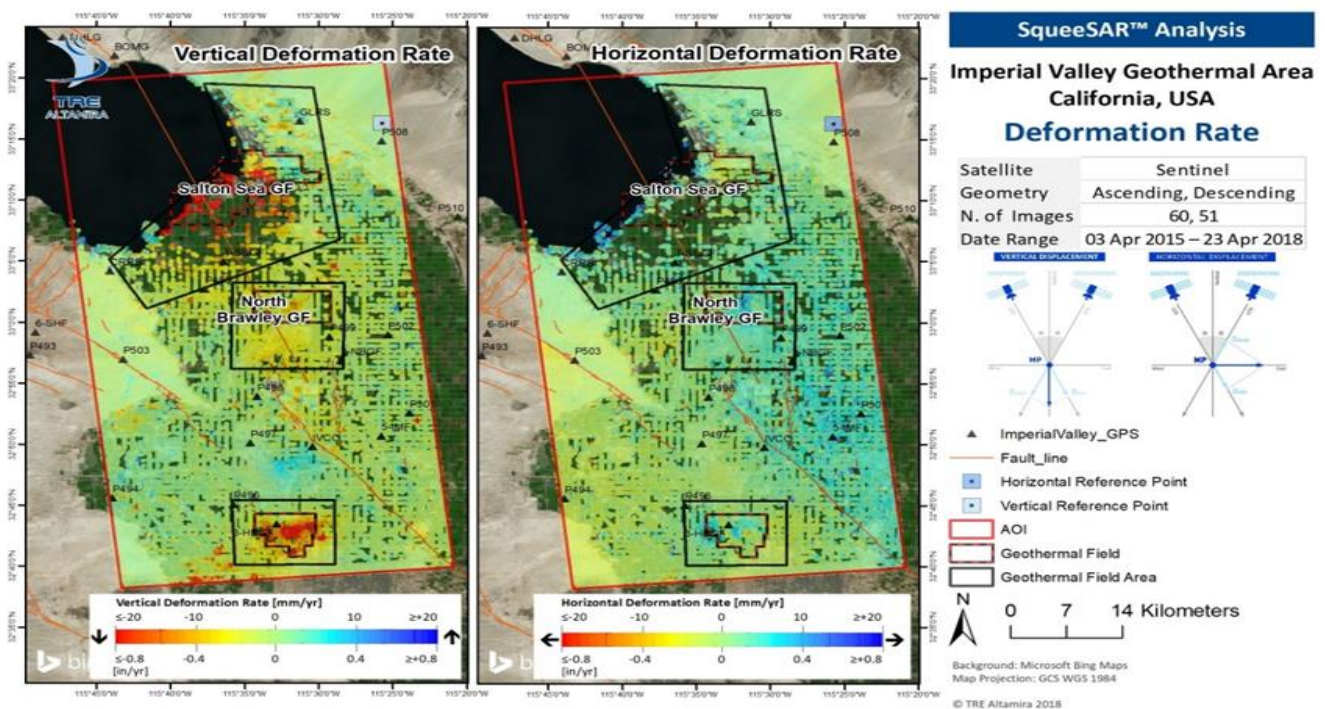
Source: TRE Altamira

LOS measurements. In this connection, although the general appearance of the spatial pattern in the vertical deformation map (Fig. 2.52, left) is similar to that in the two LOS deformation maps in Fig. 2.51 (as it should be, due to the steep look angle), the pixels indicating subsidence at the SSGF are relatively sparse compared with the numerous ascending and descending PS and DS points. As explained before, while the LOS maps are indicative of the vertical maps, information on the east horizontal displacements is only obtained after decomposition (Fig. 2.52, right).

Figure 2.53 shows the vertical and east horizontal maps from the SNT2 period. Even at this coarser scale, some differences are very noticeable. For example, while only subsidence (red areas) is observed at the HBGF in the SNT1 period (Fig. 2.52), both subsidence and uplift (blue areas) are seen in the SNT2 period (Fig. 2.53, left). In fact, uplift at the HBGF was also observed in the ENV results (Eneva et al., 2013b), to the north of the SNT2 uplift. The combination of SNT2 uplift and subsidence is associated with corresponding westward and eastward horizontal movements (Fig. 2.53, right). More details on this change in time are provided below, in Section 2.2.5, dedicated to the HBGF.

Another difference between Figs. 2.52 and 2.53 is that the SNT2 map of vertical deformation shows more pixels with subsidence at the SSGF. This means that more 100-m pixels had both ascending and descending PS/DS in order to do the decomposition in the shorter SNT2 period.

Figure 2.53 SNT2 Maps of Vertical and East Horizontal Deformation
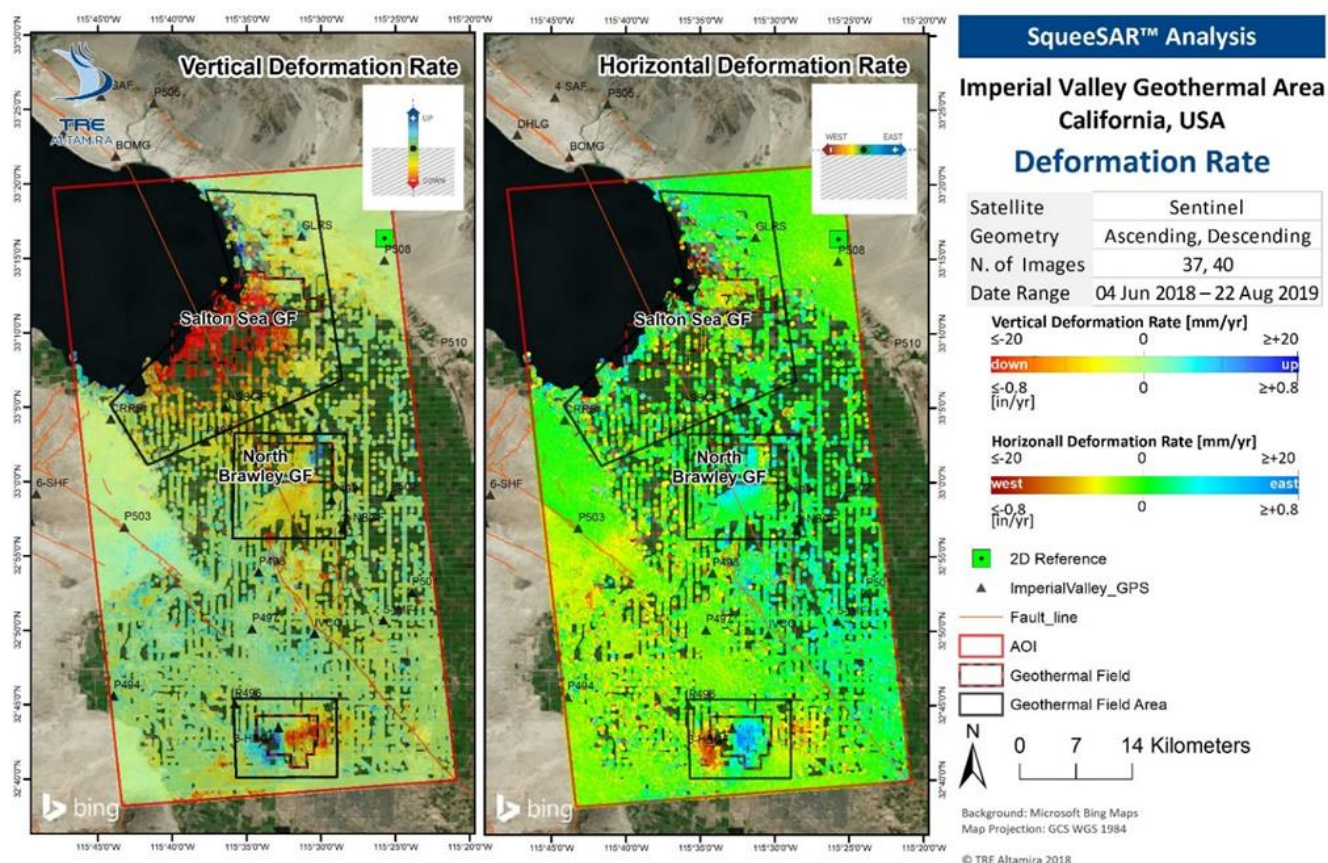
Source: TRE Altamira

Table 2.15 shows maximum observed subsidence (S), uplift (U), eastward (E), and westward (W) deformation rates for the SNT1 and SNT2 periods. The reference point for these values is the one near P508 outside the valley, so when re-referencing is done in subsequent sections of this report for individual geothermal fields, using the locations of their datum leveling benchmarks, the numerical values are different from those in Table 2.15.

Table 2.15 Maximum Rates at the Geothermal Fields in the SNT1 and SNT2 Periods

Geothermal Field	Max U / Max S SNT1 Vert Rate (mm/year)	Max U / Max S SNT2 Vert Rate (mm/year)	Max E / Max W SNT1 Horiz Rate (mm/year)	Max E / Max W SNT2 Horiz Rate (mm/year)
SSGF	16.0 (U) -43.2 (S)	14.0 (U) -54.1 (S)	20.1 (E) -16.0 (W)	26.7 (E) -28.2 (W)
NBGF	3.9 (U) -19.3 (S)	26.0 (U) -24.9 (S)	17.5 (E) -5.7 (W)	21.9 (E) -21.0 (W)
HBGF	4.1 (U) -47.2 (S)	20.5 (U) -31.5 (S)	17.8 (E) -19.4 (W)	23.5 (E) -16.8 (W)

Source: M. Eneva, modified from two TRE Altamira reports.

Figure 2.54 TSX Maps of Vertical and East Horizontal Deformation
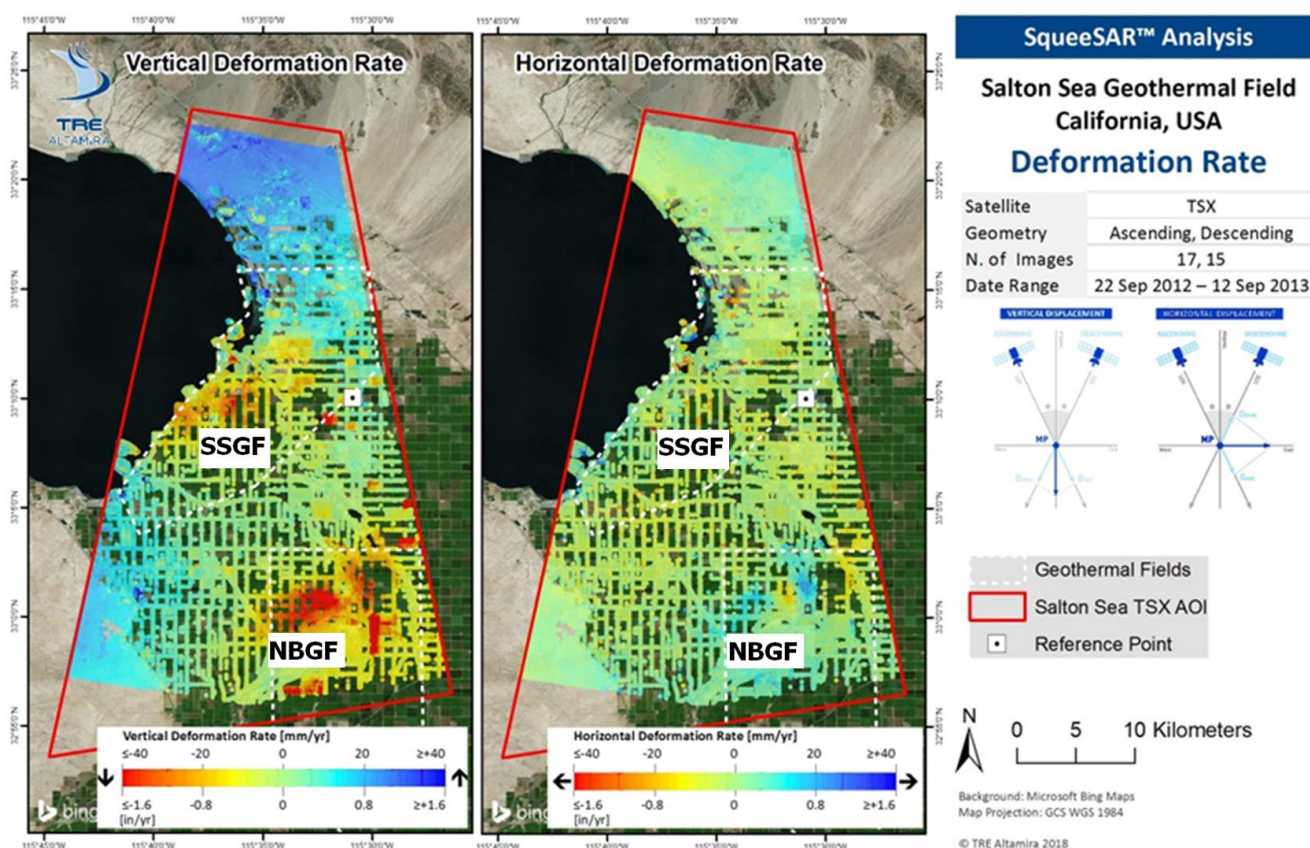
Source: TRE Altamira; modified by M. Eneva

Figure 2.54 shows deformation maps from the TSX satellite, covering a one-year period ending about 1.5 year before the start of the SNT1 period (see Table 2.12). Unlike the SNT data that are C-band (radar wavelength 5.6 cm), the TSX data are X-band (wavelength 3.1 cm). For this reason, the spatial resolution of the TSX data is 3 m x 3 m, compared to 5 m x 20 m for SNT. The better spatial resolution made it possible to calculate the vertical and east horizontal rates in 20 m x 20 m pixels, compared with the 100 m x 100 m pixels used for SNT. The vertical deformation map (Fig. 2.54, left) shows significantly more subsidence at the NBGF than the SNT maps (Figs. 2.52 and 2.53). This is due to larger production at that time, as discussed further in Section 2.2.4 dedicated to that field.

Although the TSX data are of better spatial resolution and precision than the SNT data, the TSX scenes covered only one year and there were large gaps between the collected images, so only 17 ascending and 15 descending scenes were used (Table 2.12). If the 11-day revisit capability of TSX were fully utilized, about 33 scenes of each orbital geometry would have been available.

The number of PS/DS points for which individual ascending and descending time series are obtained from InSAR for the satellite periods, is by orders of magnitude larger than the number of leveling benchmarks at the geothermal fields. Table 2.16 shows these numbers for the areas of the three fields ("A" and "D" mark ascending and descending PS/DS).

Table 2.16 Numbers of PS/DS at the Three Geothermal Fields in Imperial Valley

Satellite	SSGF ~ 460 km²	NBGF ~ 45 km²	HBGF ~ 440 km²
ENV	A 16.2k, D 20.8k	A 2.6k, D 1.7k	A 39.2 k, D 25.7k
SNT1	A 50.1k, D 39.4k	A 4.5k, D 3.9k	A 94.2k, D 104.5k
SNT2	A 40.9k, D 46.5k	A 3.5k, D 1.8k	A 111.8k, D 111.6k
TSX	A 429.5k, D 437.5k	A 23.1k, D 23.0k	-

Source: M. Eneva

In the next sections of this chapter, the focus is on more specific information and results from the three Imperial Valley geothermal fields. This includes well, leveling, and earthquake data, as well as deformation results from InSAR.

2.2.3 Salton Sea Geothermal field

2.2.3.1 General Description of the SSGF

The Salton Sea geothermal field (SSGF) is located along the southern shore of the Salton Sea (see Fig. 2.48 above). The southwestern and central areas of the field have been operated by CalEnergy Generation since the early 1980's. There are 10 flash power plants near Calipatria, CA; the first unit of a 10 MW capacity came online in 1982, built by a joint venture of Union Oil Company and Southern California Edison, and the tenth plant came online in 2000. The power produced is supplied to Southern California Edison Company. The total installed capacity of the ten units is shown as ~340 MW (https://www.power-technology.com/), but CEC lists ~370 MW (Table 2.11). According to CEC, the 2018 mean produced gross power was ~298 MW.

In March 2012, EnergySource LLC started operating the Hudson Ranch – 1 (HR-1) flash power plant to the northeast of the CalEnergy units. It was later renamed to John L. Featherstone, one of the founders of EnergySource, who was also a technology pioneer in this area. The plant was declared to have an installed capacity of 49.9 MW. CEC lists 55 MW capacity, with 2018 mean gross power of 52 MW (Table 2.11). This was the first new stand-alone geothermal plant in over 20 years in the Salton Sea area. It provides electricity for about 50,000 houses, created more than 200 jobs during construction, and 55 operational jobs. The power is purchased by Arizona's Salt River Power Company, with a 30-year Power Purchase Agreement.

A new plant is planned to start commercial operations in this area in 2023 (Roth, 2020). This 140 MW project, known as Hell's Kitchen, is envisioned by an Australian developer, Controlled Thermal Resources. The intention is to not only produce power, but also to create a major new domestic source of lithium, which is a key ingredient used in batteries for electric cars and energy storage. IID agreed to buy 40 MW with a 25-year contract, and additional contracts for both power and lithium sales are being negotiated. The Covid-19 pandemic may have delayed some plans.

Figure 2.55 Images from the Salton Sea Geothermal Field
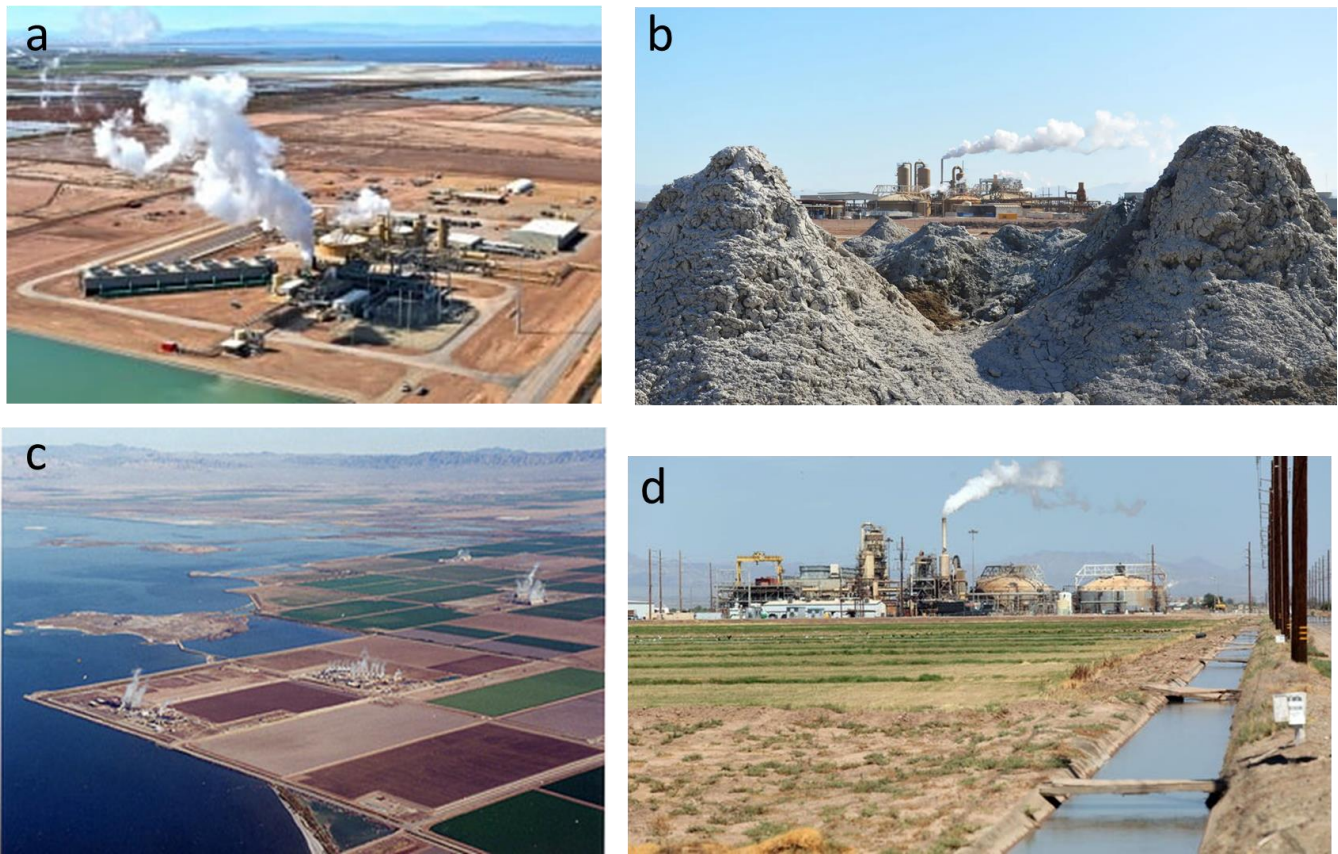
Top - EnergySource's John L. Featherstone power plant: (a) one view of the plant; (b) plant in the background, with bubbling mud pots in the foreground. Bottom - CalEnergy units: (c) four of the 10 plants are visible; (d) Hoch geothermal plant.

Sources: (a) Courtesy of EnergySource; (b) Robert Hopwood/*The Desert Sun*; (c) Center for Land Use Interpretation (http://clui.org/ludb/site/salton-sea-geothermal-plants); (d) Richard Liu/*The Desert Sun*.

Figure 2.55 shows images from the SSGF. Although this field is the largest power producer in southern California, second in the U.S. only to The Geysers, it occupies only a small portion of the Salton Sea KGRA, which extends under a large part of the Salton Sea and surrounding areas. USGS estimated the mean capacity of the whole KGRA at 2210 MW (USGS, 2008); others expect a ~1,400 MW development potential in this area (https://www.power-technology.com/). The IID pledged to build up to 1,700 MW of geothermal power by the early 2030's at the Salton Sea (Matek, 2014).

Local sources of deformation are represented by networks of strike-slip and normal faults (e.g., Brothers et al., 2009; Crowell et al., 2013), many of which are either buried or covered by agriculture. The BSZ transecting the SSGF is known to be characterized by significant seismic activity, often in swarms, as the background of numerous induced events due to the geothermal operations. The largest earthquake that has occurred on the territory of the SSGF during the periods covered by SAR satellite data, was a M5.1 event in the fall of 2005, followed by aftershock activity for about three months. Brodsky and Lajoie (2013), Llenos and Michael (2016), and Trugman et al. (2016), among others, have studied the seismicity at the SSGF associated with geothermal operations.

2.2.3.2 Satellite Data at the SSGF

Similar to the NBGF (Section 2.2.4 below), both TSX and SNT data were processed in this project for the SSGF (Table 2.12). In a previous CEC project, ENV data were also processed for the SSGF (Eneva et al., 2014), as well as TSX data over a portion of the field. The number of PS/DS from TSX is about an order of magnitude larger than that from SNT, and more than 20 times larger than the number of ENV PS/DS (Table 2.16). The SSGF is the very first studied using InSAR, in the earliest CEC project on the subject (Eneva, 2010a). At that time, data from the Canadian satellite Radarsat-1 were used, for the period May 2006 – March 2008, which consisted of 21 ascending and 18 descending scenes (Eneva et al., 2009; Eneva and Adams, 2010).

2.2.3.3 Well Data at the SSGF

The locations of the injection and production wells at the SSGF were shown in Fig. 2.50. Figure 2.56 illustrates the time series of monthly production, injection, and net production at the SSGF. On average, about 82 percent of the produced brine is reinjected with the rest being lost to evaporation.

**Figure 2.56 Monthly Production and Injection Fluid Mass at the SSGF**
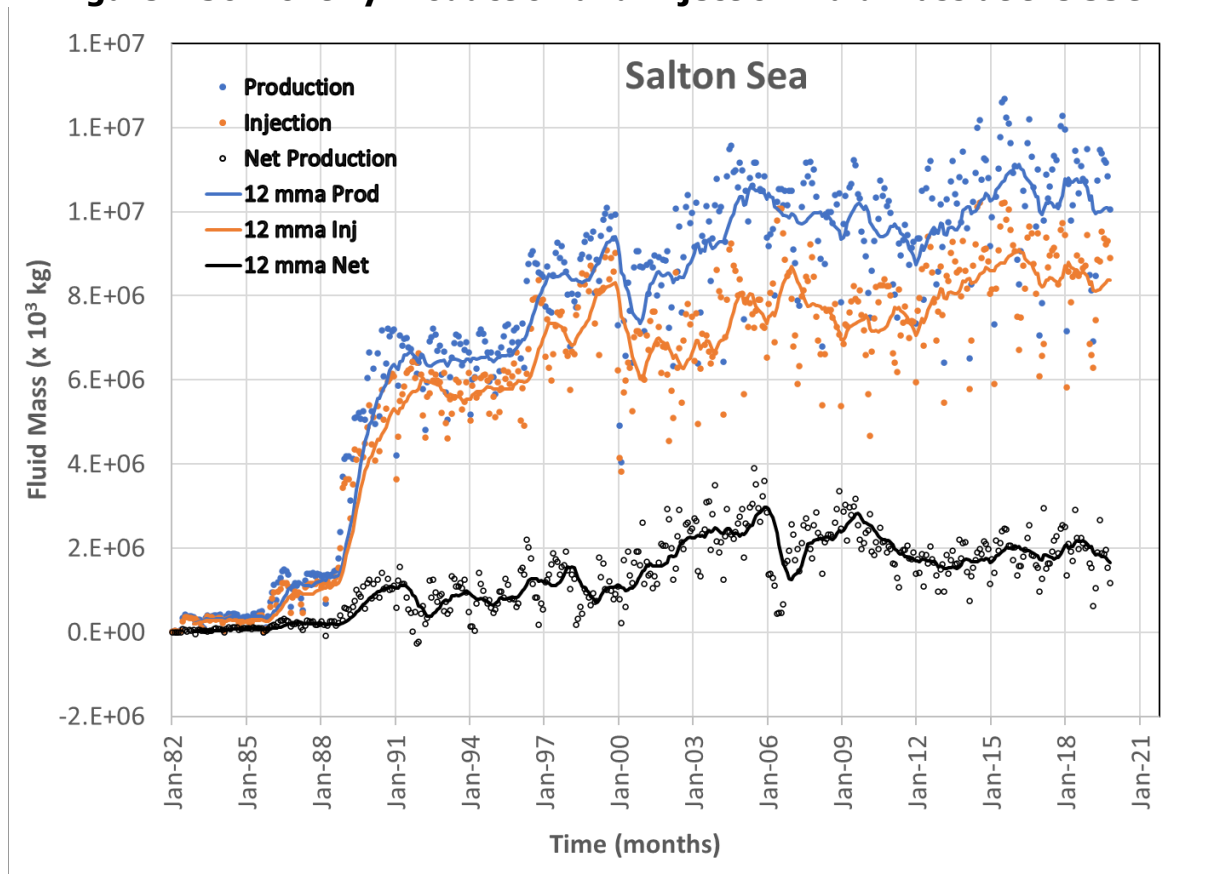
**The lines are drawn through the monthly fluid mass values using 12-months moving average (mma).**

Source: M. Eneva

2.2.3.4 Leveling Data at the SSGF

There have been up to 120 leveling benchmarks surveyed approximately annually by CalEnergy and up to 95 benchmarks surveyed by EnergySource (Table 2.14 above). These data are routinely provided to the ICDPW. This project used data from 20 CalEnergy surveys (1998 - 2018) and from 8 EnergySurce surveys (2011 - 2018). Figure 2.57 shows the time series from the leveling data ("CE" stands for CalEnergy and "ES" for EnergySource).

Figure 2.57 Leveling Time Series at the SSGF
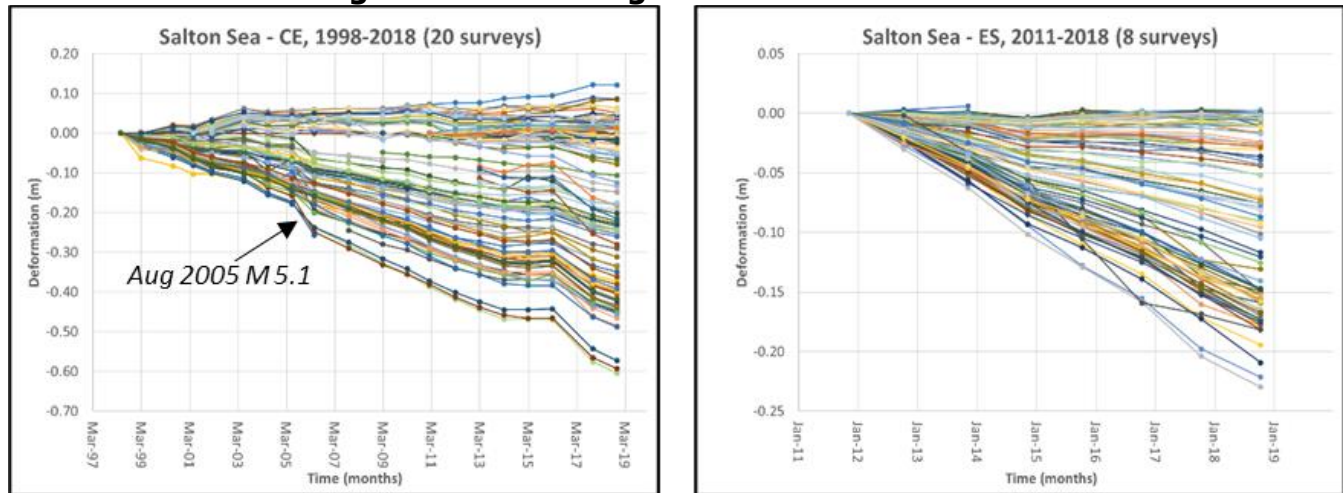
Source: M. Eneva

The CalEnergy leveling time series (Fig. 2.57, left) use as a datum the S-1246 benchmark on Obsidian Butte (see map in Fig. 2.49 above). Because in reality (i.e., in absolute terms) S-1246 subsides by about −22 mm/year, any benchmarks that subside more slowly would appear to uplift, so their time series are increasing. Most of the benchmarks subside faster than the datum, so their time series are decreasing. It is evident that the M5.1 event that occurred in 2005 on the territory of the SSGF has caused many benchmarks to "jump," after which the time series proceed more or less at the same rates as before the event, until about 2014. After a temporary arrested surface deformation, as indicated by the measurements between 2014 and 2016, deformation proceeded at an accelerated rate between 2016 and 2018.

The EnergySource leveling time series (Fig. 2.57, right) use as a datum the B-1226 benchmark (see map in Fig. 2.49 above). Most benchmarks show a steady subsidence during the 8 years for which leveling data were available for this part of the SSGF.

2.2.3.5 Earthquake Data at the SSGF

Llenos and Michael (2016) used a stochastic epidemic-type aftershock sequence models to detect possible changes in the underlying seismogenic processes as a result of the geothermal operations. They found that the background seismicity rate increases significantly, roughly corresponding with net fluid production rate increases. They suggested that the geothermal operations in this tectonically active region may not significantly change the physics of earthquake interactions, but the earthquake rates may still be driven by fluid injection or extraction rates. Earlier, Brodsky and Lajoie (2013) modeled the earthquake rate with a linear combination of the injection rate and the net production rate (production minus injection).

These authors also observed that the number of earthquakes per injected fluid volume decreases over time.

Figure 2.58 Magnitude-Frequency Relationships for the Catalogs Used at the SSGF
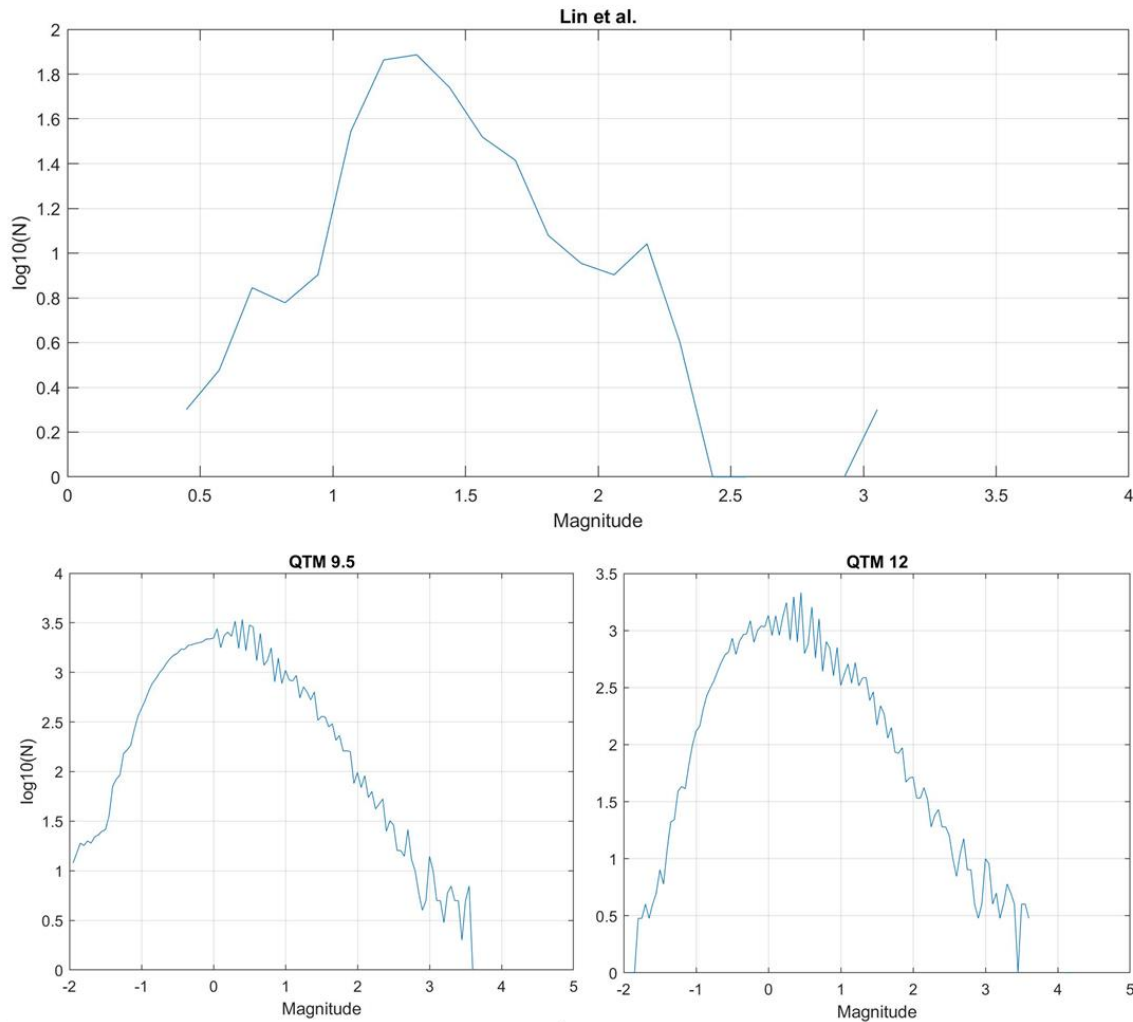
Source: Individual plots by D. Adams, assembled by M. Eneva.

Three earthquake catalogs were examined for the SSGF. One of them is referred to as "Lin et al." (Lin et al., 2007; Hauksson et al., 2012); it covers the period 1981 – 2018. The two other catalogs are from Ross et al. (2019a), and are for the period 2008 – 2017. These are marked with "QTM9.5" and "QTM12," because they were obtained using two different quality parameters; Ross et al. (2019a) call them "full" and "relocated," respectively. These authors used a method of template matching (hence QTM) applied to the SCSN seismic waveforms, which resulted in a 10-fold increase of identified earthquakes in southern California. The QTM catalog is nearly complete for M_c>0.3 events, while M_c~1.7 for the original SCSN catalog. Figure 2.58 illustrates QTM's magnitude of completeness, M_c - i.e., the magnitude above which the magnitude-frequency relationship (number of events vs. magnitude) can be approximated with a straight line. The curves in Fig. 2.58 indicate that although M_c~0.3 is similar for QTM9.5 and QTM12, the former catalog includes significantly more smaller events with $M < M_c$. Fig. 2.58 also shows M_c ~1.3 for the Lin et al. catalog.

Figure 2.59 shows plots of the time series of monthly production and injection masses at the CalEnergy units of the SSGF, together with the time series of the monthly numbers of events. This is for an area encompassing the **wells** at the field (outermost red rectangle in Fig. 2.59-a). Spikes in the seismicity rates are often associated with the occurrence of some larger events, with the most prominent spike reflecting the increased number of events (aftershocks) following a M5.1 earthquake in the fall of 2005, the largest event on the territory of the SSGF, from the Lin et al. catalog (Fig. 2.59-b).

Figure 2.59 Production, Injection and Seismicity at the SSGF-CE
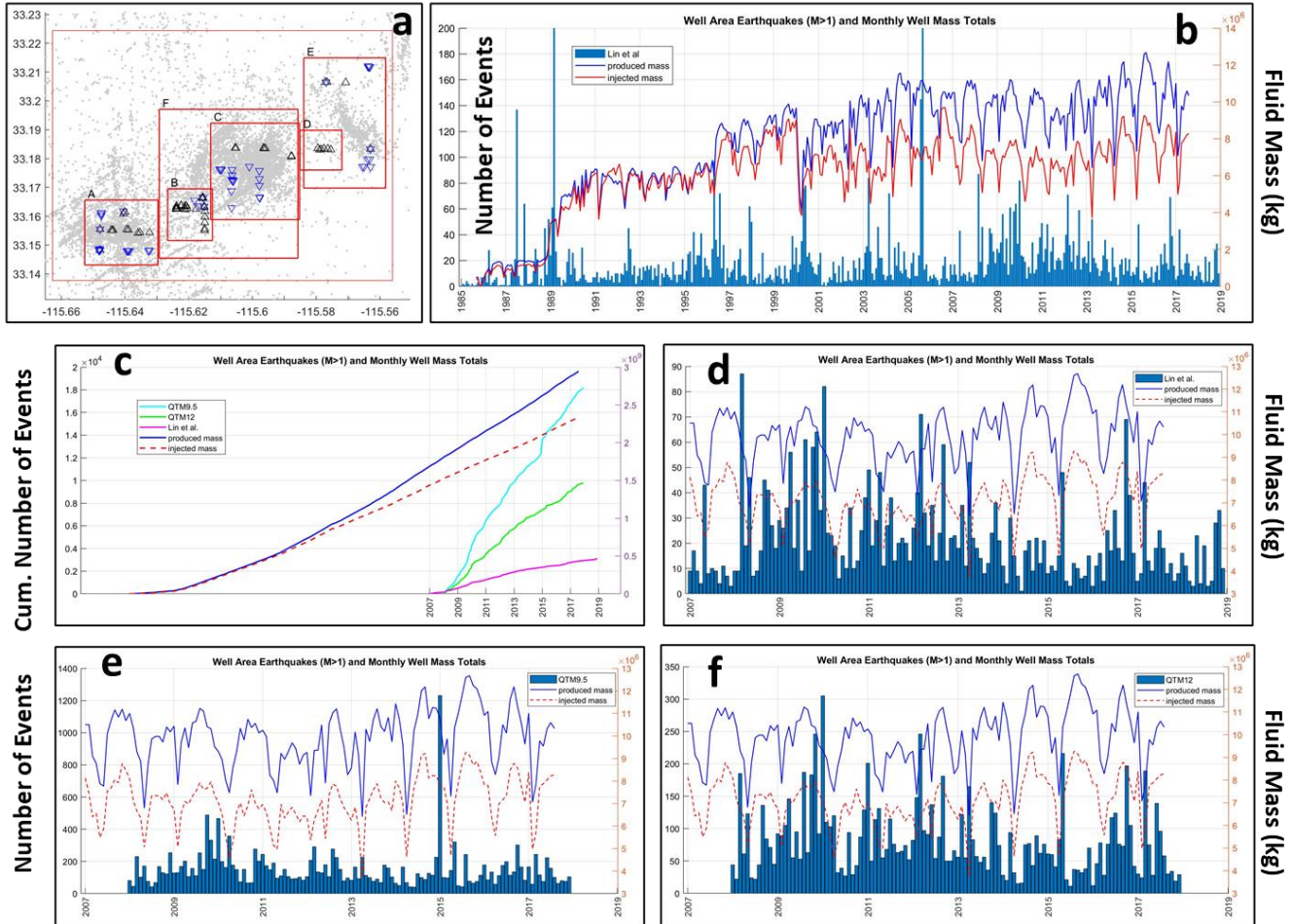
(a) Map shows earthquake epicenters from the Lin et al. catalog with gray circles. The outermost red rectangle shows the area encompassing the wells at the CalEnergy units. All other plots in this figure are for this area. Also shown are subareas (A to F) used in Fig. 2.60 next. Black triangles mark the locations of production wells. Inverted blue triangles show the locations of injection wells. (b) Monthly time series of production, injection and number of M>1 events from the Lin et al. catalog (1981 − 2018). (c) Cumulative fluid masses and cumulative numbers of events from the three catalogs for the period 2008 − 2017. (d) to (f) Like (a), but for the period 2008 − 2017, and all three catalogs - Lin et al., QTM9.5, and QTM12, respectively.

Source: Individual plots by D. Adams, assembled and modified by M. Eneva.

89

Figure 2.60 Cumulative Seismicity and Fluid Mass at the SSGF-CE
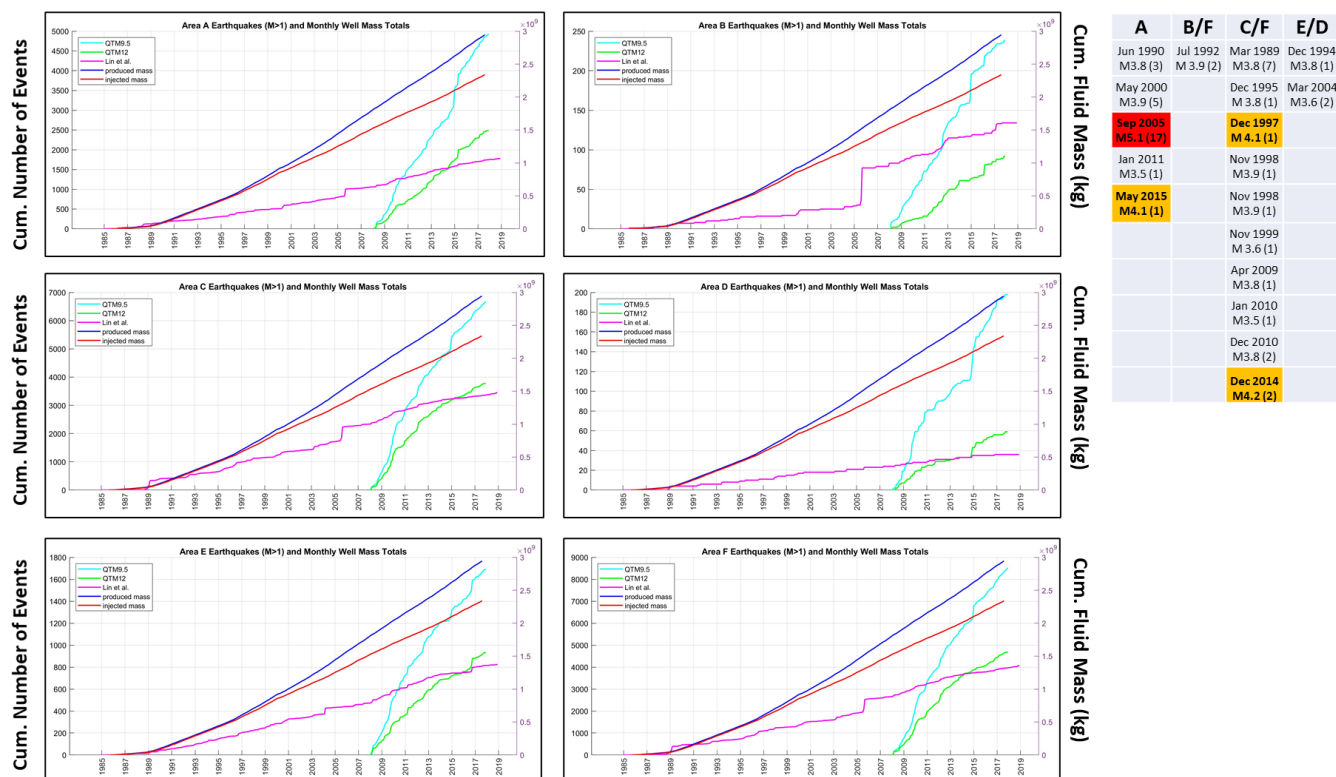
The cumulative curves are for individual subareas A to F, as indicated in the plot titles. The subareas are shown as rectangles on the map in the previous figure (Fig. 2.59a). The table shows a list of M≥3.5 main events occurring in the various subareas. Each cell shows the month and year of occurrence and event magnitude, followed in parentheses by the number of all M≥3.5 events occurring in sequences (1 means that the event was not followed by M≥3.5 aftershocks).

Source: Individual plots by D. Adams, assembled and modified by M. Eneva.

Figure 2.60 shows cumulative curves of the fluid masses and the numbers of M≥1 earthquakes from the three catalogs in subareas A to F (from map in Fig. 2.59a). When such cumulative curves increase linearly, they show sustained seismicity rates (say, numbers of events per month). The slopes of such lines indicate the seismicity rates. Changes in the slopes, and especially "jumps," occur whenever the seismicity rates change. Because of the different numbers of events in the three catalogs, the three seismicity curves diverge from each other, but they all show jumps at times when larger earthquakes occur. The most prominent event, M5.1, in the fall of 2005, was followed by 16 M≥3.5 aftershocks (half of which were of M≥4.0). It shows as a jump in the Lin et al. cumulative curve in all subareas, because although its epicenter was in subarea A, the aftershocks occurred across the whole SSGF area. Other events listed in the table in Fig. 2.60 also cause changes in the cumulative seismicity curves. For example, the Dec 2014 M4.2 occurring in area C is associated with a jump in the QTM9.5 catalog, but nothing obvious in the others, which means that most aftershocks in area C were rather small (the QTM 9.5 catalog has more small events). However, there were likely larger aftershocks in area D, because both the QTM9.5 and QTM12 curves show seismicity rate changes at that time. Overall, cumulative seismicity representations are very informative about changes in the seismicity rates, which may not be as obvious in non-cumulative plots (e.g., Fig. 2.59 b, d-f).

90

2.2.3.6 Deformation from InSAR at the SSGF

The SSGF was studied the longest among the other geothermal fields featured in this report. In the first InSAR project with CEC, May 2006-Mar 2008 data from were used from the Canadian satellite Radarsat-1 (RAD). The project team was the first to successfully apply PS-based InSAR to outline two subsidence bowls at the SSGF (Eneva et al., 2009; Eneva and Adams, 2010), which was not possible with earlier techniques. This observation was further confirmed in the subsequent InSAR project with CEC, in which ENV data were analyzed for all four operating fields in Imperial Valley (Eneva et al., 2012-2014). In that project, TSX data over the SSGF were also included. Figure 2.61 summarizes findings from these earlier projects.

Figure 2.61 Summary of Earlier InSAR Results from the SSGF
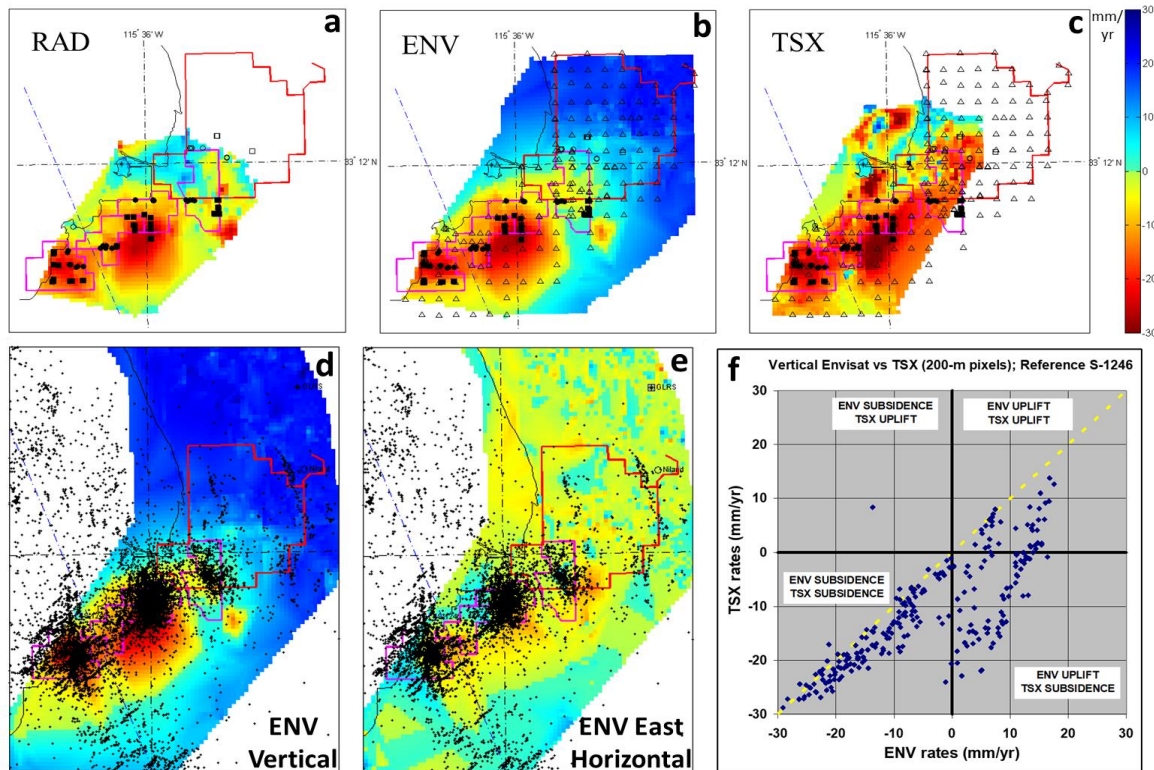
(a)-(c) Maps of interpolated vertical deformation rates from InSAR applied to Radarsat-1 (RAD), ENV and TSX data, as indicated on the plots. Reference point was benchmark S-1246. The color scale is to the far right (red shows subsidence). Pink polygons outline the CalEnergy units of the SSGF. The red polygon outlines the area monitored with leveling surveys by EnergySource. Empty triangles mark the locations of leveling benchmarks. Solid squares and triangles show the locations of production and injection wells. (d)-(e) Earthquake epicenters from the Lin et al. catalog superimposed on the maps of interpolated vertical and east horizontal rates from the ENV period. (f) Comparison of ENV and TSX vertical rates in 200-m pixels. If rates were the same, they would cluster around the yellow dashed line.

Source: M. Eneva

One of the main observations depicted in Fig. 2.61 is that all satellite data showed two subsidence areas at the SSGF. The maximum subsidence measured was ~−30 mm/year, using benchmark S-1246 as a reference point. (As a reminder, S-1246 was found to subside itself at a rate of −22 mm/year). Another observation was that seismicity clustered over the subsidence areas. These results, along with average time series in subareas of interest and

91

deformation progressions along various profiles, were shown in Eneva et al. (2009-2012). A third finding was that while ongoing subsidence was observed at the CalEnergy units of the SSGF for both the ENV (2003-2010) and TSX (2012-2013) periods, the EnergySource area showed subsidence in the TSX period (after the HR-1 production started in March 2012) that was not observed in the ENV period (before HR-1). These results and various deformation time series and profiles supporting them were reported by Eneva et al. (2014).

Fig. 2.61-f summarizes the differences between the ENV and TSX results; it has not been published before. If vertical rates in the ENV and TSX period were similar, all points would align around the dashed yellow line, which is obviously not the case here. The four quadrants of the figure show different relationships between the ENV and TSX rates. The lower left quadrant contains primarily rates from the CalEnergy units. The points do align along the dashed yellow line, but mostly fall below it. Although the maximum subsidence in both periods is around −30 mm/year (ref. S-1246), the points mostly fall below the line, which means that in many areas, subsidence during the TSX period was larger than that in the ENV period. The two quadrants on the right contain mostly measurements from the EnergySource area of the SSGF. The top right quadrant shows areas that experienced uplift during both the ENV and TSX period (ref. 1246, so in many cases this uplift just indicates slower subsidence than S-1246). Because most points fall below the line, uplift has largely decreased from the ENV to the TSX period. Finally, the lower right quadrant shows points from areas that uplifted during the ENV period but subsided in the TSX period, as a result of the new geothermal operation that started in this part of the SSGF in March 2012.

The above results demonstrate how powerful the InSAR observations can be in identifying surface deformation and changes in response to geothermal operations. In this project, a repeat analysis of the TSX data was performed in order to cover larger area (including the NBGF). Also, SNT data in two periods were analyzed, as was done for the other three geothermal fields in this project.

Table 2.15 above already showed the maximum rates observed at the SSGF in the SNT1 and SNT2 period (ref. point outside the valley). The maximum observed subsidence rates, −43.2 mm/year for SNT1 vs. −54.1 mm/year for SNT2, are different, but they are not at the same points. Because the reference point for these measurements is outside the valley and does not move much, it could be estimated that the SNT2 maximum subsidence rate in reference to S-1246 would be decreased by ~−22 mm/year (the subsidence rate for that benchmark), thus obtaining ~−32 mm/year (ref. S-1246). This is similar to the maximum subsidence rates observed in the ENV and TSX period (e.g., Fig. 2.61-f). However, similarly estimated, the SNT1 maximum observed subsidence rate would be lower, ~−21 mm/year. The reason is that the SNT1 data actually do not probe the area of true maximum subsidence (i.e., do not have both descending and ascending LOS measurements there), but is from the periphery of the larger subsidence bowl. Larger differences are seen also in the maximum observed westward rates (Table 2.15): −16.0 mm/year SNT1 vs. −28.2 mm/year SNT2 (ref. point outside the valley). The maximum observed uplift rates (16 mm/year SNT1 vs. 14 mm/year SNT2) and eastward rates (20.1 mm/year SNT1 and 26.7 mm/year SNT2) are more similar in the two periods.

Figure 2.62 shows maps of SNT1 and SNT2 vertical and horizontal deformation rates at the whole SSGF, as well as average deformation time series from two subareas (ATS1 and ATS2) from the SNT1 and SNT2 periods (Apr 2015-Apr 2018 and Jun 2018-Aug 2019).

Figure 2.62 Rates and Time Series at the SSGF from the SNT1 and SNT2 Periods
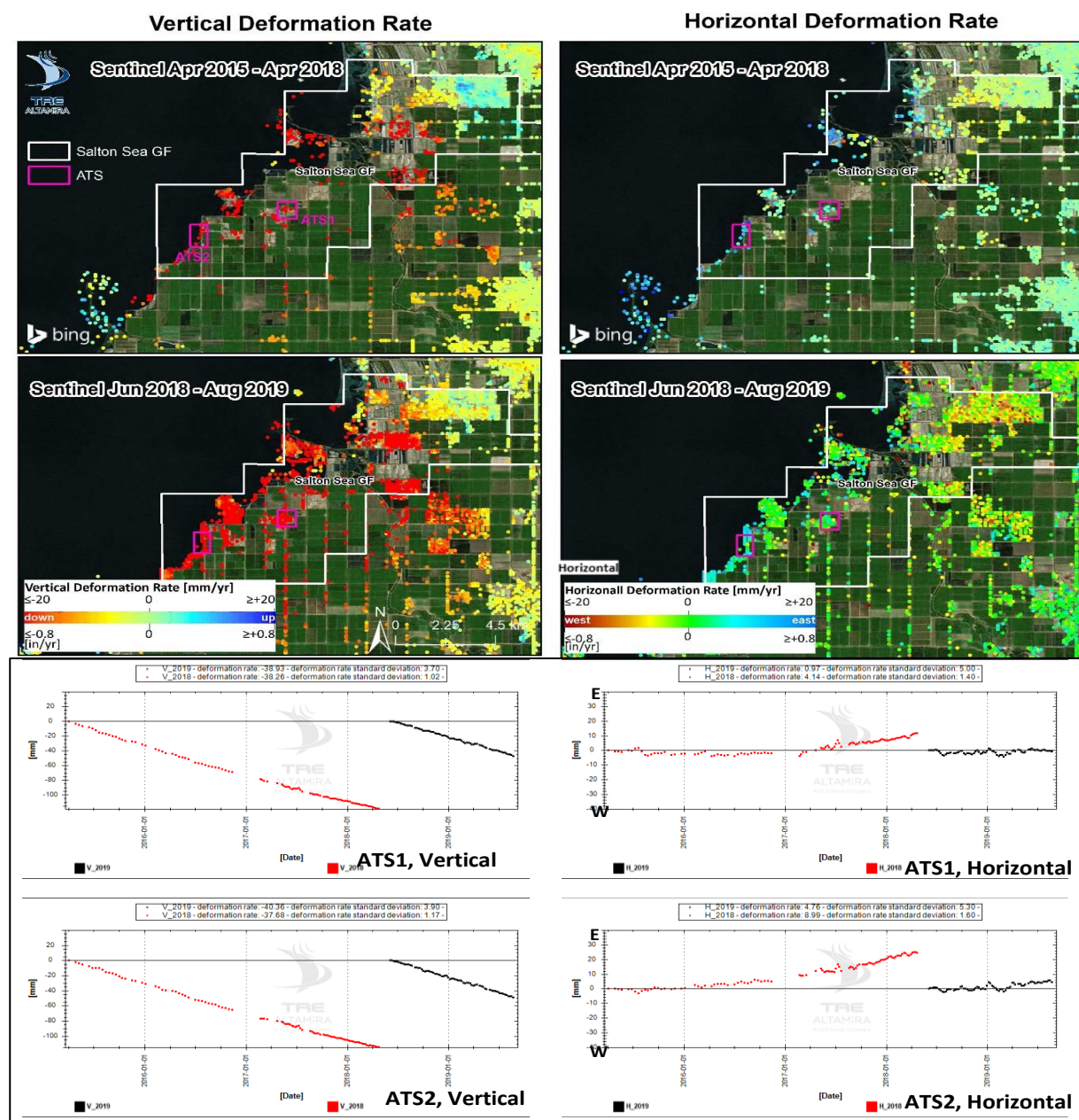
Source: TRE Altamira

The maps in Fig. 2.62 show that the InSAR analysis identified significantly more PS/DS points in the SNT2 period compared with the SNT1 period. The likely reason is that the SNT1 period (duration 3 years 1 month) is significantly longer than the SNT2 period (duration 1 year 3 months). Any given point is identified as a PS only if it appears in all satellite scenes in a time series. It is more challenging for a point in agricultural area like the SSGF to persist over a longer period. This likely explains the missing SNT1 observations at the area of true maximum subsidence.

The average time series in Fig. 2.62 show steady subsidence for both subareas, with similar subsidence rates in the SNT1 and SNT2 periods. For subarea ATS1, the subsidence rates in the two periods are −38.3±1.0 mm/year and −38.9±3.7 mm/year, respectively (ref. point outside

93

the valley). For subarea ATS2, these rates are −37.7±1.2 mm/year and ±40.4+3.9 mm/year. Therefore, both subareas show similar average subsidence rates for the whole SNT period (Apr 2015-Aug 2019).

However, the horizontal average time series in the two subareas differ between the SNT1 and SNT2 periods (Fig. 2.62, time series on the right), as well as there is evidence for non-linear time series in the SNT1 period. In the ATS1 subarea, there is not much eastward movement until about mid-2017 in the SNT1 period, after which it decreases again in the SNT2 period. In the ATS2 subarea, the eastward movement is also non-linear, being negligible until about mid-2016 in the SNT1 period, after which it takes off at a higher rate than in the ATS1 area, but decreases again in the SNT2 period.

Figure 2.63 shows a similar comparison between the results in the TSX and SNT1 period, for the same subareas, ATS1 and ATS2. The significant difference is that because TSX uses X-band (~ 3-cm wavelength), much more PS/DS are identified (numbers in Table 2.16 above). However, the one-year TSX period does not have as many scenes (Table 2.12) as SNT1, and there is a large data gap in the middle of the period. The time series for the SNT1 period are the same as in Fig. 2.62. The TSX subsidence rates are −24.0±1.8 mm/year and −25.3±1.8 mm/year in the ATS1 and ATS2 areas, respectively. These appear lower than the SNT1 rates only because a different TSX reference point is used that is on the edge of the SSGF i.e., not outside the valley). When the two reference points are reconciled, the differences are much smaller. Similar to the SNT2 period, the TSX horizontal rates appear to be eastward, but are negligible.

Even though the InSAR technique used in this project (SqueeSAR) is the only one that provides satellite deformation measurements in this agricultural area, and the number of SNT PS/DS points is hundreds of times larger than the number of leveling benchmarks, the maps in Fig. 2.62 show that many of the PS/DS points are clustered and there are many areas devoid of scatterers. One may think that a solution to the lack of SNT PS/DS points it to simply use TSX data instead, over longer periods of time. However, this is not practical at present, because they are not routinely collected and are available at a cost, while the SNT data are free and routinely collected. In the future, it would be best to install so-called corner reflectors (e.g., Garthwaite et al., 2015) in areas of interest currently devoid of SNT PS/DS. These reflectors would show in all subsequent satellite scenes and would ensure both descending and ascending LOS measurements, which in turn could be used to calculate vertical and east horizontal deformation rates. TRE Altamira has vast experience in this respect (Figure 2.64).

Figure 2.63 Rates and Time Series at the SSGF from the TSX and SNT1 Periods
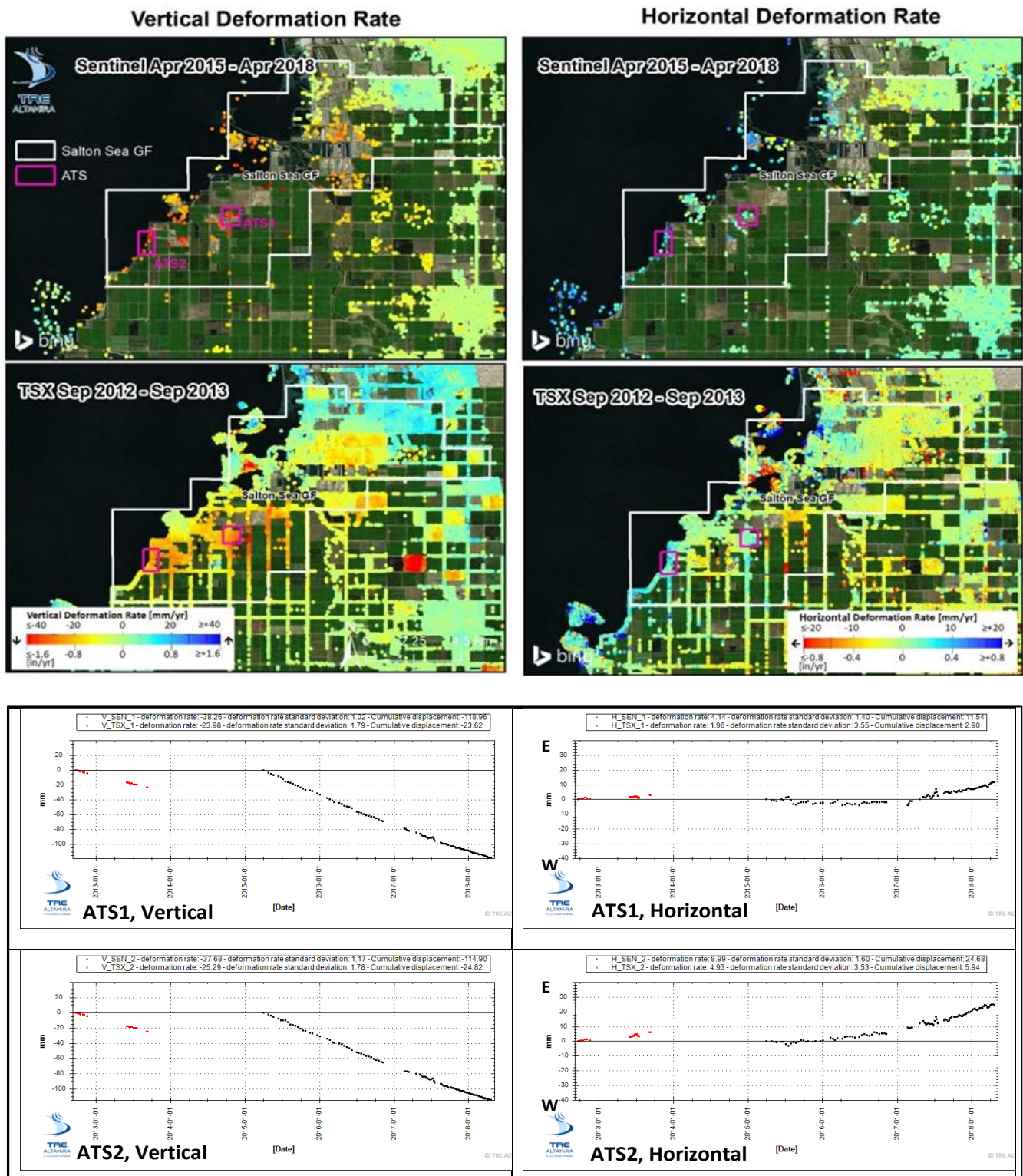
Four maps and four graphs demonstrating vertical and horizontal areas and timeframes of deformation rates.

Source: TRE Altamira

Figure 2.64 Examples of Corner Reflectors

Source: Individual photos from TRE Altamira, assembled by M. Eneva

2.2.3.7 Deformation Modeling at the SSGF

The deformation modeling for the SSGF was done by A. Barbour (USGS), as a continuation of his earlier published work, in which only ENV data were used (Barbour et al., 2016). The InSAR vertical data for all four periods were coarsened from the original 100 m to 500 m, by taking mean values of all cells contained within the coarser grid. The reference point used in this analysis was benchmark B-1226 (EnergySource's datum in their leveling surveys). The original InSAR data obtained from TRE Altamira sometimes use different reference points for the various data sets; for the sake of direct comparison, here everything was re-referenced to B-1226. It is at a more stable location than the S-1246 benchmark used by CalEnergy. The maps of coarsened re-referenced vertical rates for the four periods are shown in Figure 2.65.

There are relatively small differences in average fluid injection and production masses among the four time periods (Table 2.17). They lowest mean injection mass was during the ENV period. The relative differences in net production (produced fluid mass minus reinjected fluid mass) range from 72 percent to 90 percent (Table 2.18).

Barbour et al. (2016) used cross-validated Bayesian kriging (a sophisticated kind of interpolation) to fill in areas devoid of ENV measurements of vertical rates. Such interpolation is not needed for the TSX data, because of their much denser coverage. Figure 2.66 suggests a link between deformation rates (velocities) and geothermal activities (i.e., locations of production and injection wells), with the largest subsidence occurring closer to the wells. The congruence between the spatial profiles for all four datasets reinforces previous findings that depletion of the SSGF reservoir is the predominant source of surface deformation (Barbour et al., 2016). To test the robustness of this observation further, this profile is compared with a profile based on randomized distances, as shown in Figure 2.67. For this purpose, random locations in space were selected, with the number of points being equal to the number of SSGF wells, and then the distance profile was recalculated. If the spatial profile from the randomized locations is featureless (i.e., like noise), then the hypothesis that any connection between the well locations and the deformation rates is coincidental (i.e., does not really exist), can be rejected. Indeed, unlike the real well locations, no pattern in distance was observed for the randomized locations, which supports the notion that there is an overall link between geothermal operations and surface deformation.

Figure 2.65 Vertical Rates at the SSGF in the ENV, TSX, SNT1, and SNT2 Periods
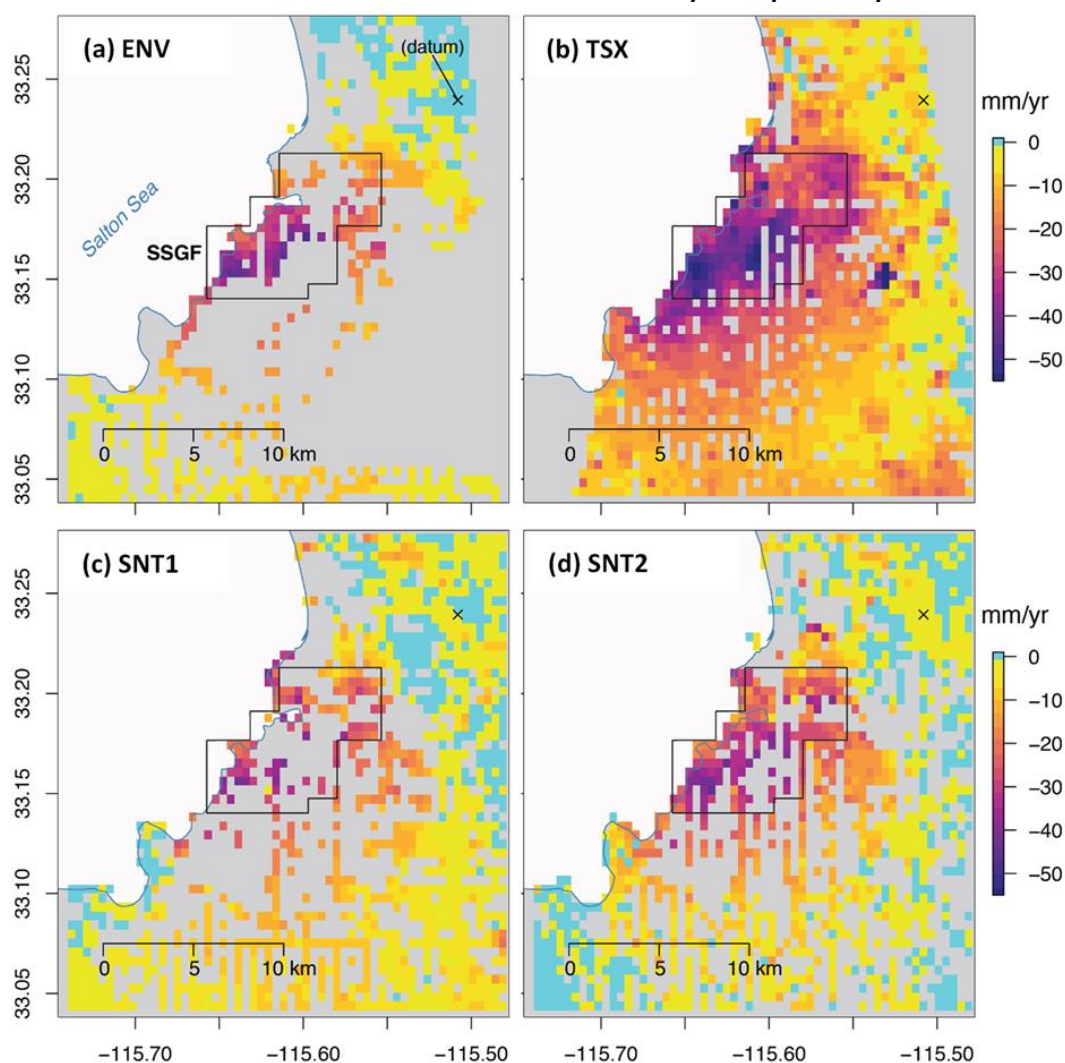
Source: A. Barbour (USGS), slightly modified by M. Eneva

Table 2.17 Mean Production, Injection, and Net Production Masses at the SSGF

| Satellite	Time Range	Mean Production [10^9 kg]	Mean Injection [10^9 kg]	Mean Net-production [10^9 kg]
ENV	2006-02-02 – 2010-09-22	9.78	7.65	2.14
TSX	2012-09-01 – 2013-10-01	10.50	8.60	1.93
SNT1	2015-01-26 – 2018-04-16	10.20	8.28	1.92
SNT2	2018-05-10 – 2019-07-04	9.62	8.09	1.53

Source: A. Barbour (USGS)

97

Table 2.18 Mean Operational Parameters Normalized by ENV Value

Satellite	Normalized Production	Normalized Injection	Normalized Net-production
TSX	1.08	1.12	0.904
SNT1	1.04	1.08	0.895
SNT2	0.98	1.06	0.716

Source: A. Barbour (USGS)

### Figure 2.66 Profiles of InSAR Vertical Rates at the SSGF
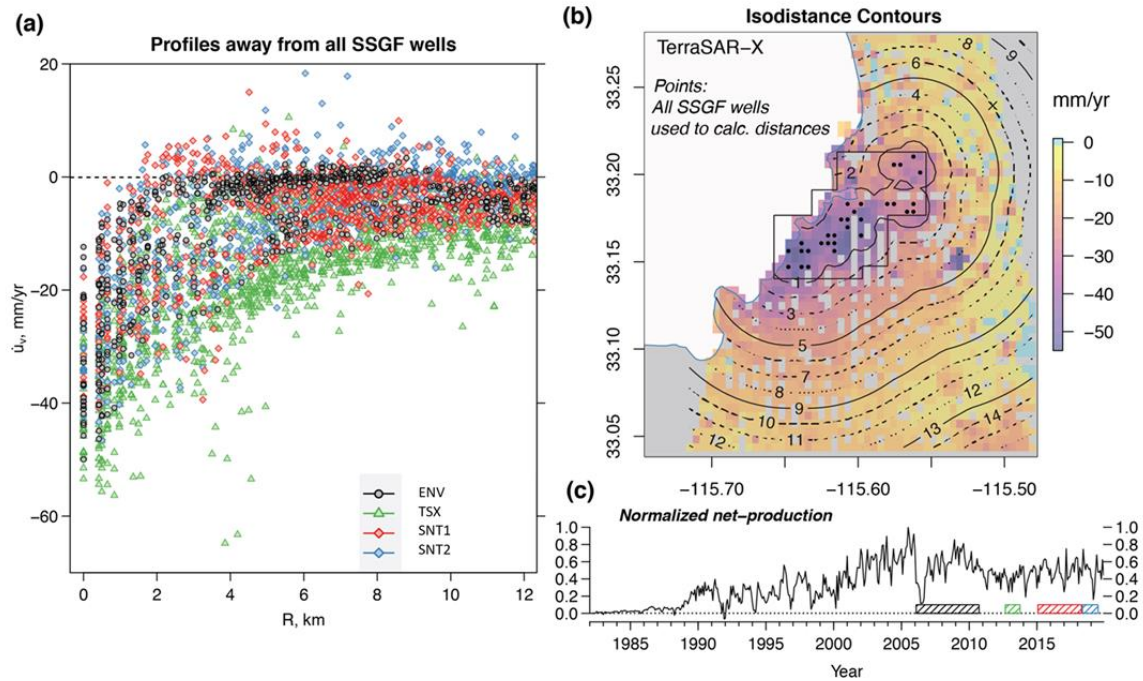
(a) Vertical rates as a function of distance from the SSGF wells. (b) Map of geothermal wells and isodistance contours overlain on the TSX vertical rates. (c) Time series of net fluid production at the SSGF with each satellite time period shown in hatched boxes. There appears to be little difference in the spatial profiles of the four different InSAR datasets, aside from significantly better spatial coverage of the TSX data (see also Fig. 2.65).

Source: A. Barbour (USGS), slightly modified by M. Eneva.

Although there is a wide range of surface deformation rates, which makes it somewhat difficult to compare spatial patterns (Fig. 2.66), calculating the mean rates in 1-km distance increments reveals similar spatial profiles for the four datasets (Figure 2.68).

In the deformation modeling at Coso, fixing the relative source strengths in the inversion satisfactorily reproduced the InSAR vertical rate profiles. A similar approach was applied also

Figure 2.67 Comparison of Actual and Randomized Profiles at the SSGF
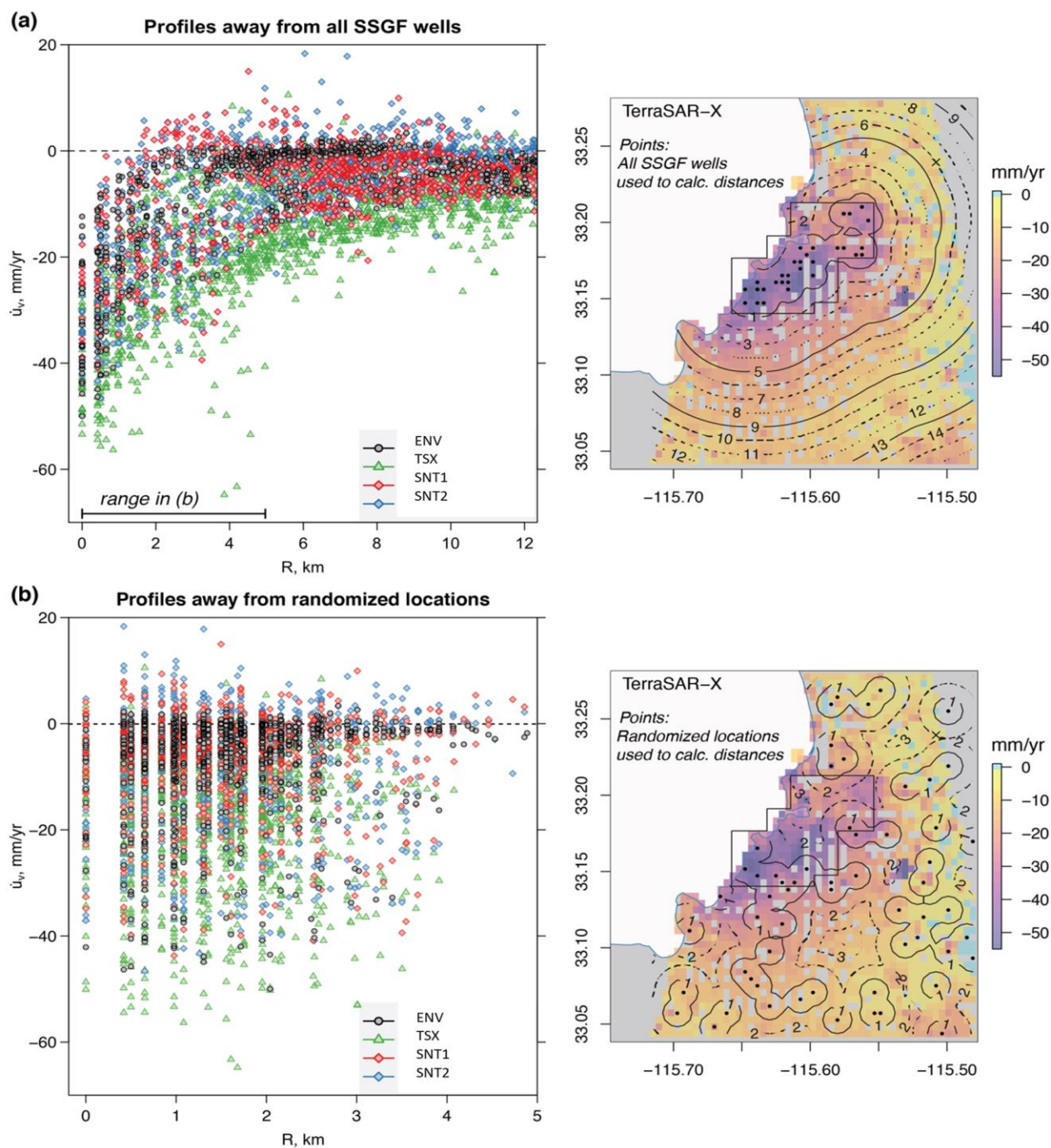
Source: A. Barbour (USGS), slightly modified by M. Eneva.

Figure 2.68 Average Deformation Rates as a Function of Distance from SSGF Wells

Average Vertical Velocities
polygons show ± 1σ variability
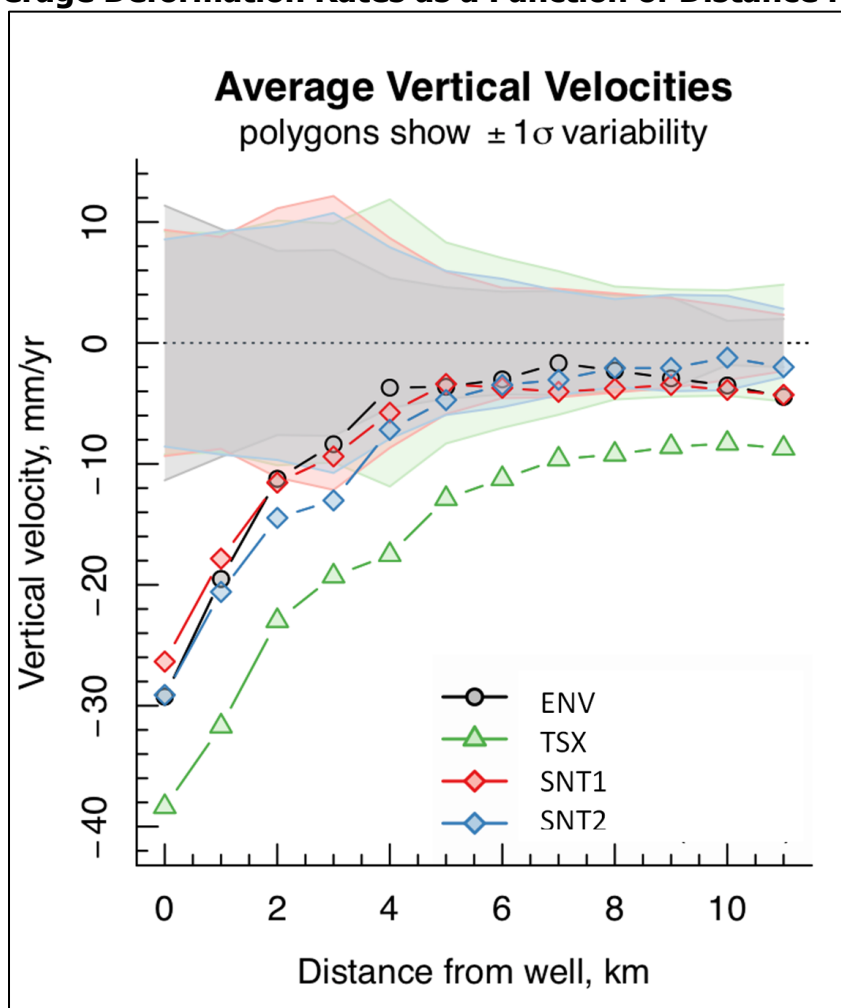
Filled polygons show the standard deviation of all observations in that distance bin (see Fig. 2.66)

Source: A. Barbour (USGS), slightly modified by M. Eneva.

for the SSGF, using the values from Table 2.18. Fitting the ENV data alone, Barbour et al. (2016) found the source depth to be between 1.0 and 2.4 km. This range is wide but not implausible, as these depths bracket the range of open-hole sections of the geothermal wells. In fitting the full collection of InSAR data sets, an optimal depth of 1.3 km was found, but also some systematic differences between the best-fitting model and the InSAR profiles (Figure 2.69). The source of these biases is presently unknown, but it might be related to uncertainties associated with the reference point (datum B-1226) used. The size of these biases is tabulated in Table 2.19. Note that the bias for the SNT2 data set does not appear to be statistically significant.

In view of the above, the conclusion is that the observed surface deformation at the SSGF is consistent with a depleting reservoir, as previously found based only on the ENV data. The vertical rates are apparently spatially linked to the geothermal operations, but no major changes were observed in the subsidence over time. This is consistent with a relatively constant rate of reservoir depletion, supported by the relatively small changes in average net fluid mass loss over time. The best fitting depth of the reservoir depletion model is at roughly 1.3 km below the surface, a depth that generally coincides with the depth of the ~300°C

geotherm and the shallowest portion of the geothermal resource. Similar to Coso, one important implication of this is that the observed surface deformation at SSGF may be largely a result of aseismic deformation processes (e.g., thermo-poro-elastic contraction and aseismic slip) and relatively insensitive to changes in background seismicity rates caused by changes in the rates of injection and production.

Figure 2.69 Deformation Model Fitting to All Four InSAR Data Sets at the SSGF
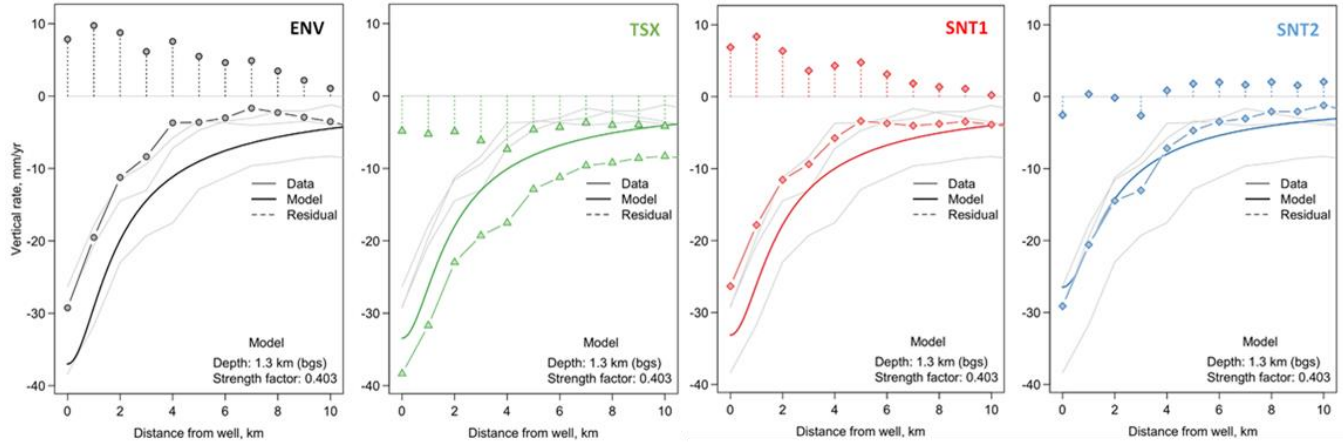
Reservoir depletion model from Barbour et al. (2016) is fit to all InSAR datasets, assuming a single-source depth and relative source strengths based on changes in the mean net production during the four time periods (Table 2.18). The points connected to zero by vertical lines show model residuals. The model biases (means of model residuals) are shown in Table 2.19.

Source: A. Barbour (USGS), modified by M. Eneva

Table 2.19 Subsidence Model Biases from Fig. 2.69

Satellite	Model bias (mm)	Std. error (mm)	Significance (p-value)
ENV	5.8	0.4	< 2e-16
TSX	-5.2	0.3	< 2e-16
SNT1	2.9	0.3	< 2e-16
SNT2	0.6	0.3	0.0178

Model bias is obtained by least squares regression. "Std. error" is the uncertainty associated with each bias estimate. The significance probability is related to the size of the t-statistic (not shown) relative to Student's t-distribution function (a very small number indicates high statistical significance).

Source: A. Barbour (USGS), slightly modified by M. Eneva.

2.2.4 North Brawley Geothermal Field

2.2.4.1 General Description of the NBGF

Figure 2.70 shows a photo of the binary power plant at the NBGF and the current configuration of wells and leveling benchmarks. This geothermal resource was the first to be utilized in Imperial Valley, with a 10 MW experimental power plant that went online in 1980 (http://openei.org). It was the first flash-steam project in the U.S., which demonstrated that steam from high-salinity brine could be used for power production. However, heavy scaling caused shutdowns for maintenance, clogged reinjection pumps, and buildup in the wells that led to reduced steam supply to the power plant. After five years of operation, the plant was decommissioned, mostly due to scaling problems in the production wells. The project was still considered successful, because of lessons about how to utilize geothermal fluids with high levels of dissolved solids and corrosive gases.

Figure 2.70 North Brawley Geothermal Plant and Map with Benchmarks and Wells
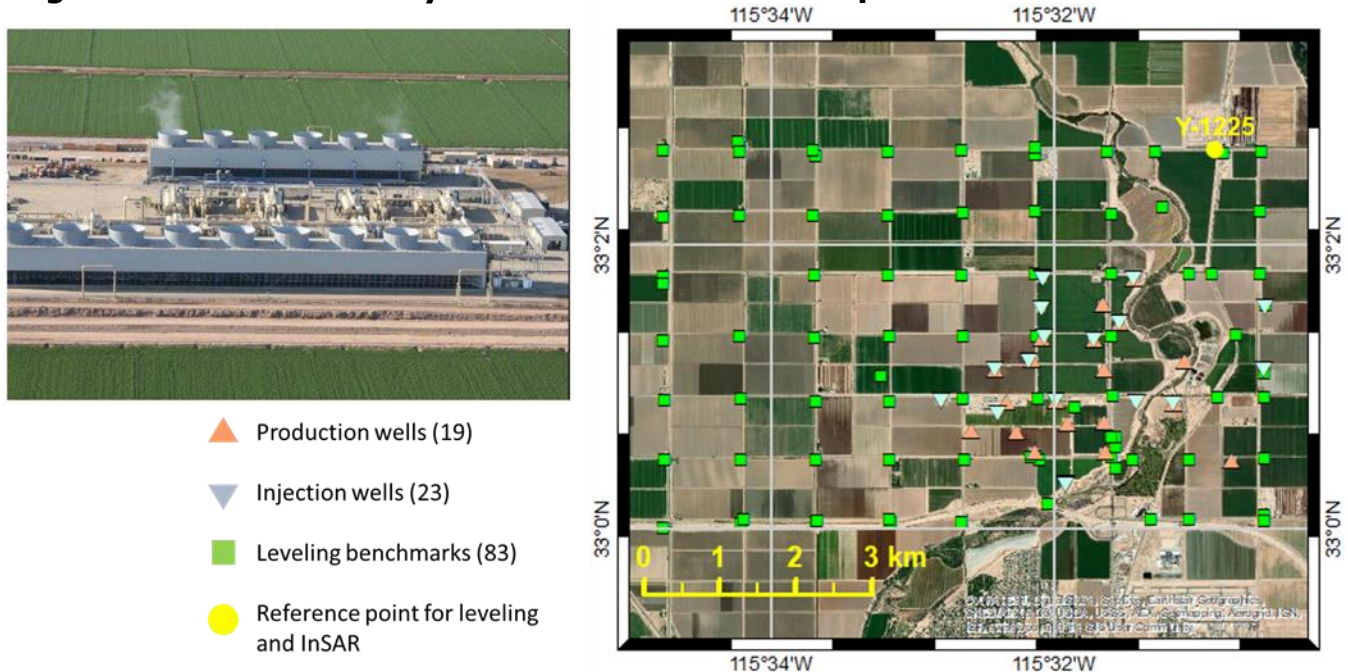
Source: Photo from http://ormat.org. Map by M. Eneva.

Another attempt at development led to the installation of a 50 MW binary plant in 2008. The earlier experimental power plant had utilized deep high-temperature (>200°C) fluids from the geothermal reservoir, but the scaling and corrosion problems made this approach uneconomical. Therefore, Ormat decided to tap into shallower and lower-temperature fluids (149-204°C) from a part of the reservoir with matrix dominated permeability (Matlick and Jayne, 2008), in the hope that there would be fewer dissolved solids, and consequently, scaling and corrosion problems would be more manageable. However, although five exploration wells drilled in 2007 yielded promising data for commercial power generation, the actual production did not reach the expected level (well field capacity of 35 MW), mostly due to equipment failures due to similar problems as in the 1980's. Challenges included undissolved sand in the geothermal fluids, inhibited injection circulation pathways, problems with filtration and cleanout of injection wells, and failures of production pumps. By early 2013,

102

a decision was made to settle on an output of ~27 MW, instead of continuing to invest in raising the power output. However, decline in production continued and the plant power reported by Ormat is 13 MW (http://ormat.com); the time of this estimate was not reported. According to calculations made using CEC data (Table 2.11 above), the mean gross power was 10.6 MW in 2018, and the mean net power – 6.4 MW.

The NBGF is in the Brawley Seismic Zone, located within the transitional zone between the southern tip of the San Andreas fault and the northern tip of the Imperial fault, both major strike-slip faults (Fig. 2.48 above). The faulting patterns are complicated and there are likely numerous secondary faults without obvious surface expression. The geologic structure of the area seems to represent a flat agricultural land on top of wide alluvium and marine deposits. A low-magnitude seismic swarm occurred in 1975 (before geothermal production), at depths between 4 and 8 km. Other minor clusters occurring in 2010 and 2011 might have been induced earthquakes. In August 2012, the Brawley area experienced a more significant earthquake swarm, with the three largest events being of magnitudes 4.9, 5.3, and 5.4 (Hauksson et al., 2013). These events are generally considered to be too large to be induced by the geothermal operations, especially in view of the ongoing natural seismicity in the region. However, Wei et al. (2015) considered an indirect triggering mechanism facilitated by aseismic slip potentially caused by geothermal injection.

The elevation at the NBGF is ~40 m below sea level, so even a small amount of subsidence could disrupt the water flow patterns and irrigation systems in the surrounding agricultural areas. It is generally assumed that the operation of binary plants does not cause substantial surface deformation, because most of the produced geothermal fluids are re-injected back in the ground. However, as previously demonstrated, the surface deformation at the HBGF, also with binary plants (Eneva et al., 2013b), is comparable to that observed at the SSGF (Eneva et al., 2014), which operates only flash plants. Similarly, the presence of surface deformation at NBGF is evident during the times of the highest levels of production and injection.

2.2.4.2 Satellite Data at the NBGF

Like in the other fields, SNT performed better than ENV, and identified significantly more PS/DS at the NBGF. On the territory of the NBGF (map in Fig. 2.70), the numbers of the ENV and SNT ascending PS/DS points are around 2,500 and 4,500, respectively, and for the descending PS/DS – around 1,700 versus 4,000. The examples in Figure 2.71 show that the ENV PS/DS are not only fewer in numbers, but they are also mostly located away from the wells. This is probably due more to the construction work during the ENV period than to the generally better performance of SNT. Therefore, the ENV data are not particularly informative about the field, but they provide information about the pre-production time when the average subsidence rate was found to be only about −5 mm/year across the field (Eneva et al, 2013a). In contrast to both ENV and SNT, much more PS/DS are identified by TSX at the NBGF, as expected due to its use of X-band – about 23,000 each ascending and descending PS/DS. The TSX PS/DS are located mostly where the SNT points are, but are five to six times more numerous.

Figure 2.71 Comparison of the Distributions of PS/DS in the ENV and SNT Data

Left – well pads are seen in this satellite image as light brown squares. Middle – red circles mark the locations of the ENV descending PS/DS; note the lack of points around the wells. Right – green circles denote the locations of the SNT descending PS/DS. The comparison is similar for the ascending PS/DS (not shown).

Furthermore, the vertical and east horizontal components of the surface displacements at NBGF are calculated in 100-m pixels, where both descending and ascending LOS measurements are available. The territory of the NBGF is covered by more than 4,000 such pixels. Only about 400 pixels (10 percent) could be assigned decomposed ENV values, because many of them either did not have any LOS observations, or only had PS/DS points of one type (i.e., only ascending or only descending). SNT performed twice better in this respect – about 1000 (25 percent) of the pixels have vertical and east horizontal estimates. For TSX, this number is about 1,500 (32 percent).

An earthquake swarm occurred in the beginning of the period covered by the TSX scenes, but the first TSX scenes were not used, because they are not suitable for the InSAR time series analysis in this study. However, Hauksson et al. (2013) applied the classic method, DInSAR, to four TSX scenes collected immediately before and after the largest events in the swarm. The authors reported that small surface ruptures were identified by both discontinuities in the interferograms and field studies. They also observed a LOS change of −3 cm at a certain location in the field.

2.2.4.3 Well Data at the NBGF

During the total study period, 23 injection and 19 production wells were active at NBGF (locations are shown in Fig. 2.70). Figure 2.72 shows the total monthly production and injection amounts, as reported by CalGEM. Binary power plants are generally characterized by total production and injection time series following each other rather closely, resulting in a net production (i.e., production minus injection) that is close to zero. However, this is true when the whole territory of the NBGF is considered. In subareas of the field, there are times of distinct net production; one of the more prolonged such periods coincides with the time of TSX coverage. This helps explain why despite the use of binary technology, significant surface deformation was still observed.

Figure 2.72 Monthly Production and Injection Fluid Mass at the NBGF
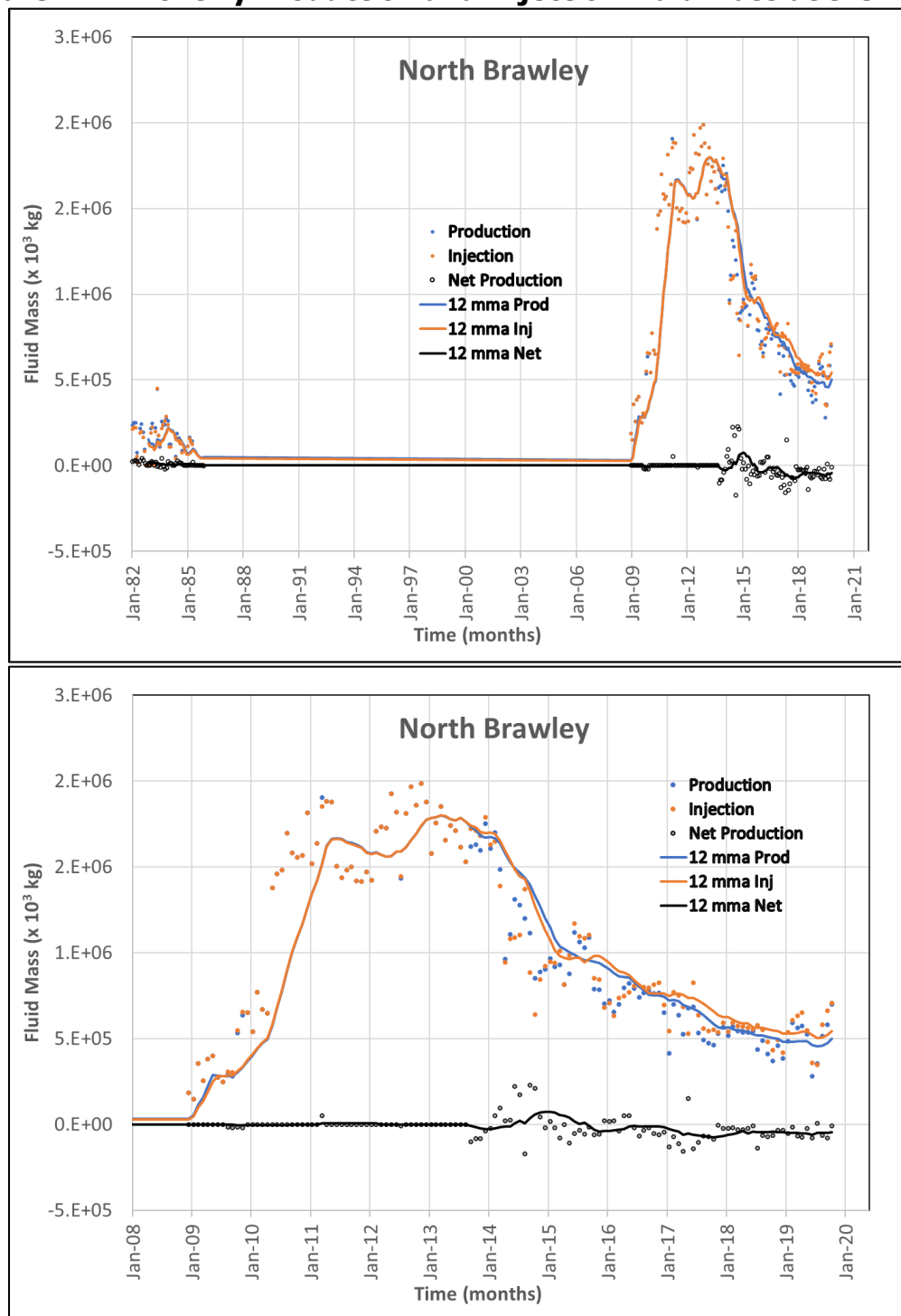
Top – a longer time period showing production at the NBGF in the early 80's and since 2009.
Bottom – Focus on the later geothermal development since 2009. Note that the maximum
production is during the TSX period (Sep 2012 – Sep 2013). The lines are drawn using 12-months
moving average (mma).

Source: M. Eneva

Figure 2.73 Leveling Time Series at the NBGF
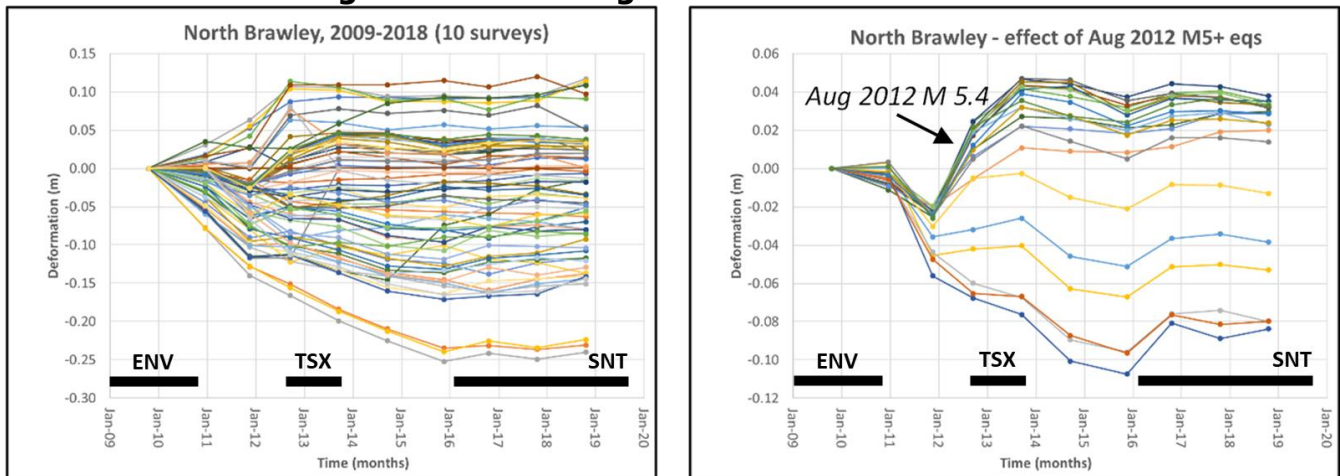
Left – all leveling time series at the NBGF. Right – the time series for some leveling benchmarks show uplift between two annual leveling measurements encompassing the M5.4 swarm on the territory of the NBGF.

Source: M. Eneva

2.2.4.4 Leveling Data at the NBGF

There are 83 leveling benchmarks in the area of NBGF, which are surveyed approximately annually. Ormat provides these data to the ICDPW. Data from 10 leveling surveys between 2008 and 2017 were used in this project. They cover only the end of the ENV time period, but include the whole TSX and SNT periods, as well as the whole period, for which production and injection data are available. Figure 2.73 shows the time series from the leveling data. Note that many benchmarks show increasing subsidence early on, at the times of highest production, but then the surface deformation levels out when the production decreases significantly. However, a number of the benchmarks show large uplift between the leveling surveys in late 2011 and late 2012, capturing surface deformation from the M5.4 swarm in Aug 2012. Some of these jumps appear to be 40-50 cm. Interestingly, continued uplift of up to 25 cm is observed for these benchmarks in the measurements between late 2012 and late 2013, raising the question whether a prolonged post-seismic deformation has occurred. Later surveys at these benchmarks, following the 2013 measurements, show resumed subsidence for about two years, or leveling out, likely associated with the decreasing production.

2.2.4.5 Earthquake Data at the NBGF

An earthquake catalog of relocated events was used; the applied relocation method is described by Hauksson et al. (2012) and Lin et al. (2007). Such hypocenter data are available for the period Jan 1981 – Dec 2017. After that, data from the Southern California Seismic Network (SCSN) were used that are not relocated, but few such events occurred at the NBGF. Fault-plane solutions (Yang et al., 2012) of many of these earthquakes are also available, showing that most events are with strike-slip mechanisms, and with nodal planes striking north-east or north-west. As already indicated, the seismicity in the NBGF is dominated by the aftershocks of the Aug 2012 earthquakes (Hauksson et al., 2013).

Figure 2.74 Vertical Deformation Rates from InSAR in the TSX Period
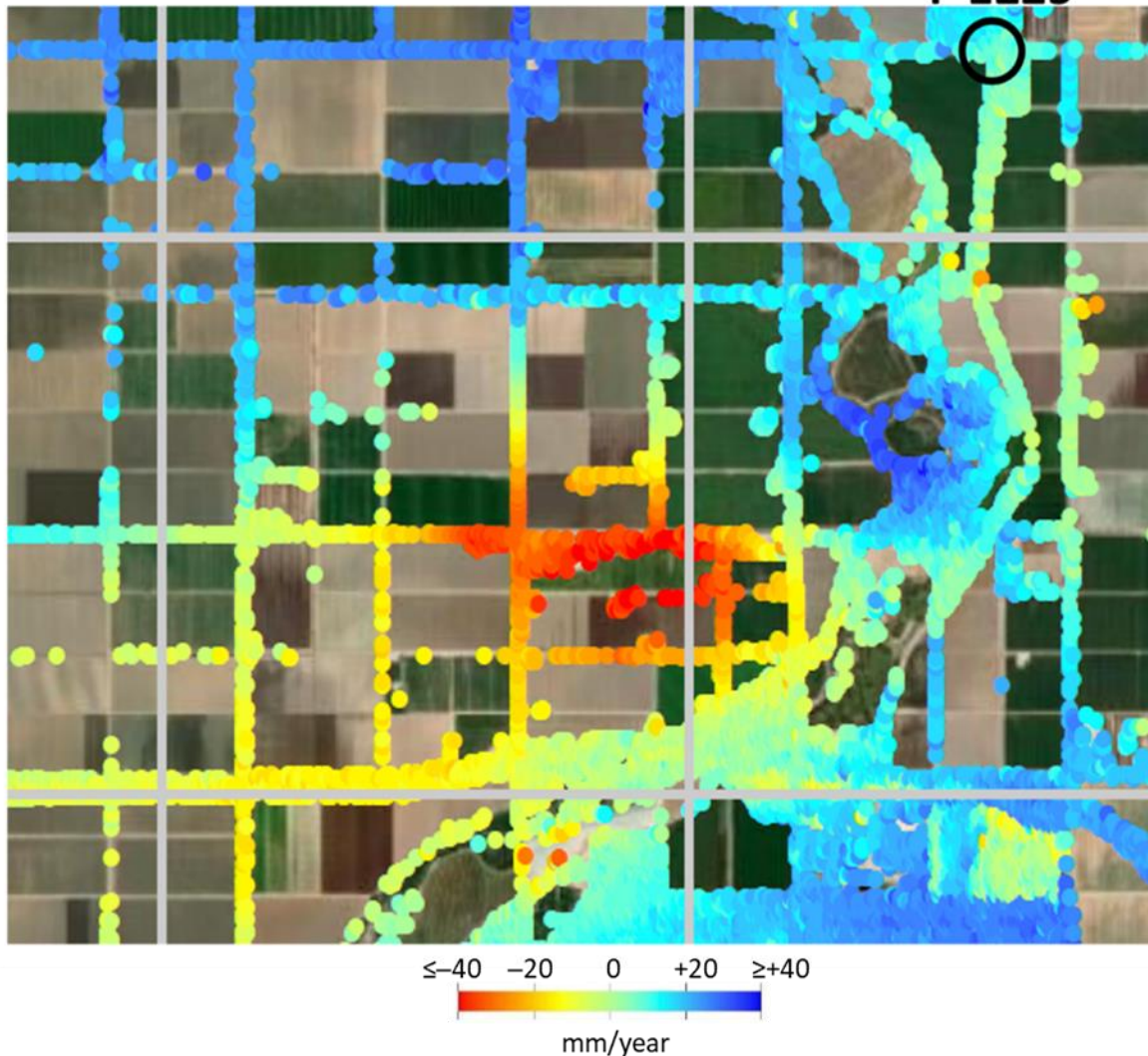
Source: M. Eneva

2.2.4.6 Deformation from InSAR and Comparison with Other Data at the NBGF

Similar to the leveling data, InSAR shows the largest deformation during the TSX period. Figure 2.74 shows the vertical rates in 100-m pixels, calculated using the local datum benchmark Y-1225 as a reference point for InSAR. The other satellite periods show much smaller displacements (Figure 2.75). It is clear that the rates during the ENV period are not only low, but also observations are largely missing around the wells, due to the construction period, as mentioned before. However, the TSX and SNT periods have plenty of pixels with rates around the wells. There was a significant subsidence during the TSX period, which coincides with the time when the levels of production and injection at NBGF were high (see Fig. 2.72). By the time of the SNT1 time period, the levels of production and injection were already about three to four times lower; consequently, the SNT1 deformation map shows low vertical rates. Also, it is notable that uplift in the TSX data (blue area northwest from the subsidence) has turned into a slight subsidence (light yellow) in the SNT1 period. The maximum InSAR subsidence rates at the NBGF, using Y-1225 as a reference, were −6.7,

Figure 2.75 Vertical Rates at the NBGF for Different Satellite Periods
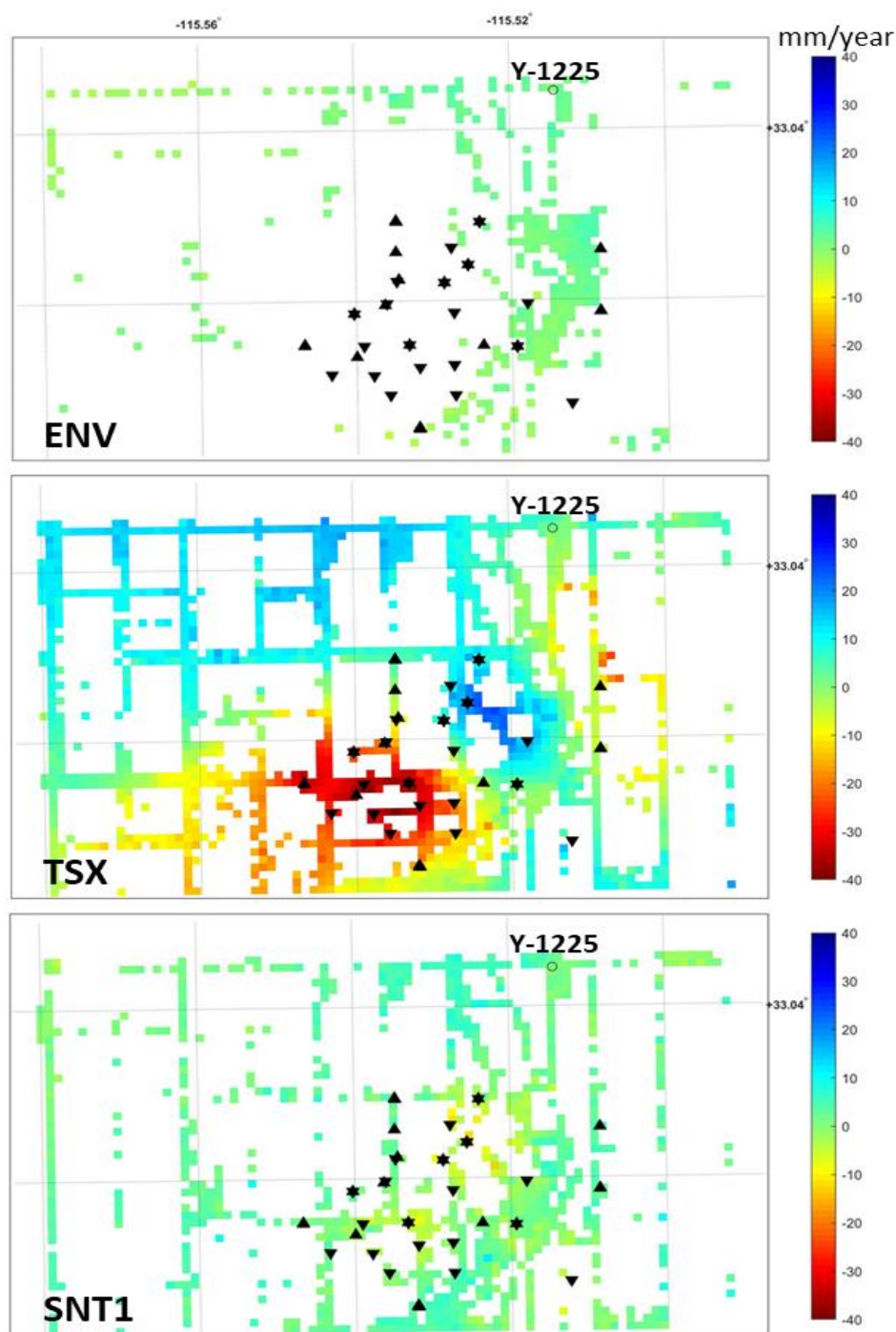
Production and injection wells are marked with triangles and downward triangles, respectively. Apparent stars show production and injection wells in very close proximity, or wells that were switched at some point from one type to the other.

Source: Individual plots by D. Adams. Assembled and modified by M. Eneva.

−38.9, and −14.6 mm/year in the ENV, TSX and SNT1 periods, respectively. The maximum uplift rates for these three periods were 5.8, 26.0, and 12.1 mm/year. Thus, the TSX vertical rates are several times larger than those in the other satellite periods, but they capture the times of the largest production, and perhaps some post-seismic movements from the M5+

events. As a reminder, none of the ENV maxima are close to any wells, so the maximum ENV vertical rates are in completely different locations from those in the two other periods.

Figure 2.76 shows the rates of horizontal movements. During the TSX period, a distinct westward movement (negative values) is seen in the eastern part of the subsidence area and to the northeast of it. The maximum observed westward rates (in reference to Y-1225) were −4.1, −46.8, and −15.7 mm/year in the ENV, TSX, and SNT1 periods, respectively. The maximum eastward rates for these periods, in the same order, were 9.8, 15.7, and 10.6 mm/year. Like the vertical rates, the TSX maximum westward rates were several times larger than those in the other periods, but the maximum eastward rates did not change that much.

Figure 2.77 shows the TSX vertical deformation map (same as Fig. 2.74 and the middle panel of Fig. 2.75), along with the epicenters of M$\geq$1 earthquakes. A lot of the seismicity aligns along linear features that may indicate the presence of small local faults in the area. Most of these earthquakes are part of the 2012 M5.4 swarm that transected the area of largest subsidence. The black rectangle in the figure encompasses both the locations of the earthquakes in the swarm and areas of substantial subsidence. It is used for the hypocentral depth cross-section also displayed in Fig. 2.77, which indicates the existence of two clusters of hypocentral depths, around 4 km and 9 km. The shallower cluster is under the area of largest subsidence during the TSX period.

Figure 2.78 summarizes different types of data, all extracted from the area of maximum subsidence (i.e., not from the whole NBGF) during the TSX period, as shown in the inset. Except for the leveling time series that are shown for individual benchmarks within the rectangle outlining the subsidence, all other data are averaged over that area. These include the InSAR time series of vertical deformation, and the monthly amounts of production and injection. Note that because not all wells are included here, the production and injection amounts are not as close as when all wells were considered (Fig. 2.72), so there is a more substantial net production for this particular part of the NBGF. That is, the binary plant operation entails an overall lack of net production, but this assumption does not hold in individual areas of the field.

As a reminder, individual types of deformation time series start at 0, so the annual leveling data are shown with continuous curves between 2008 and 2017, but the InSAR deformation time series from the three individual, non-adjacent satellite periods, each start at 0, and are thus not superimposed on the leveling data. However, similar slopes of parts of the curves indicate similar rates. It is evident then that the rate suggested by the short TSX InSAR time series is very similar to the leveling rates from several benchmarks (based only on two annual surveys in late 2012 and 2013). Just before that, the leveling curves from two annual surveys, in late 2011 and late 2012, mark arrested subsidence, and even slight uplift, likely related to the Aug 2012 earthquakes. Furthermore, it is evident that many of the leveling curves in the subsidence area significantly flatten out during the SNT1 period when production and injection decrease. One of the leveling benchmarks shows a significant uplift, for which the origin is not

Figure 2.76 East Horizontal Rates at the NBGF for Different Satellite Periods
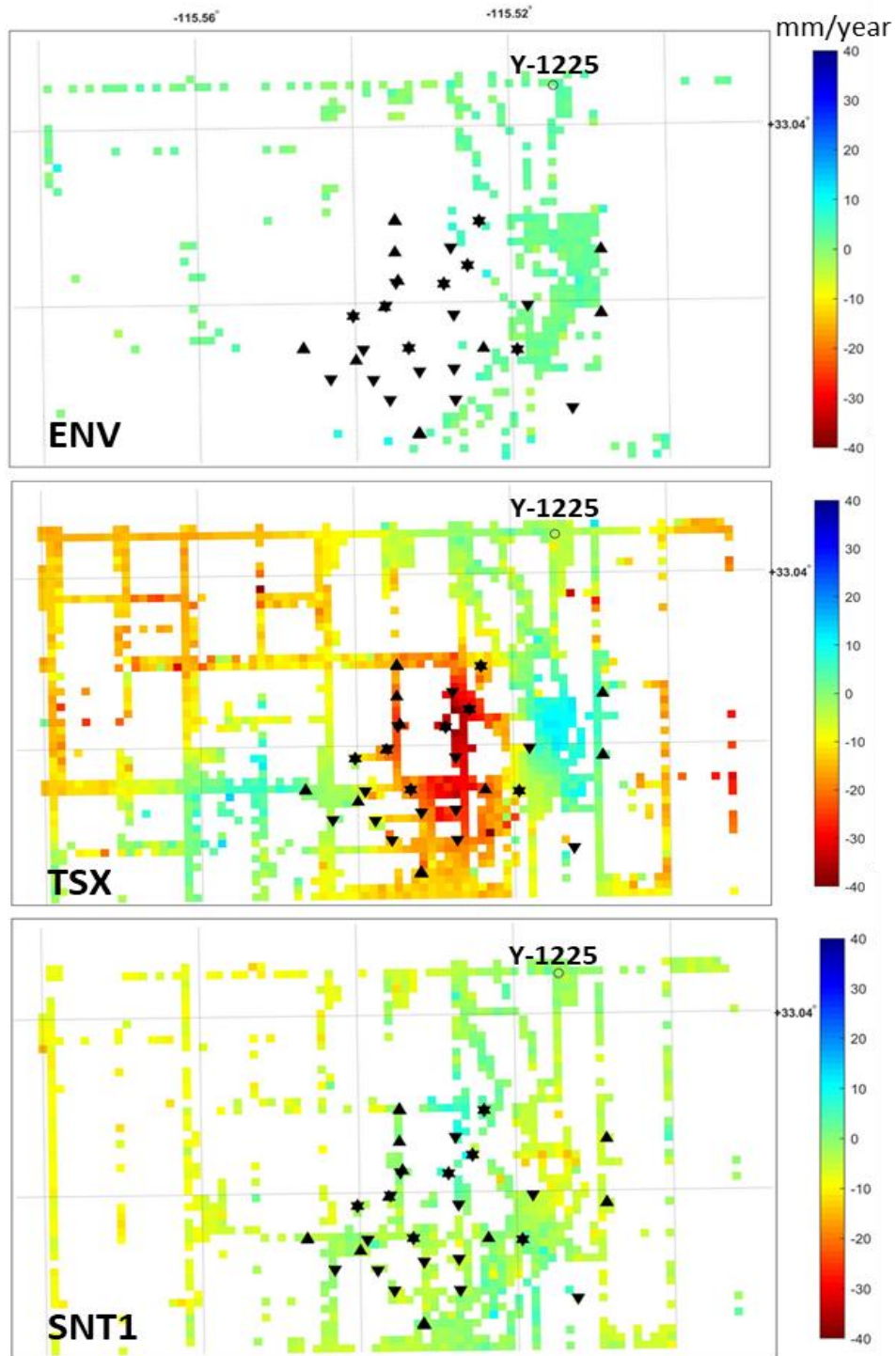

Notations are like in Fig. 2.75, only negative values here show westward movements and positive values indicate westward movements.

Source: Individual plots by D. Adams, assembled and modified by M. Eneva.

# Figure 2.77 Vertical Rates of Surface Deformation from InSAR and Seismicity
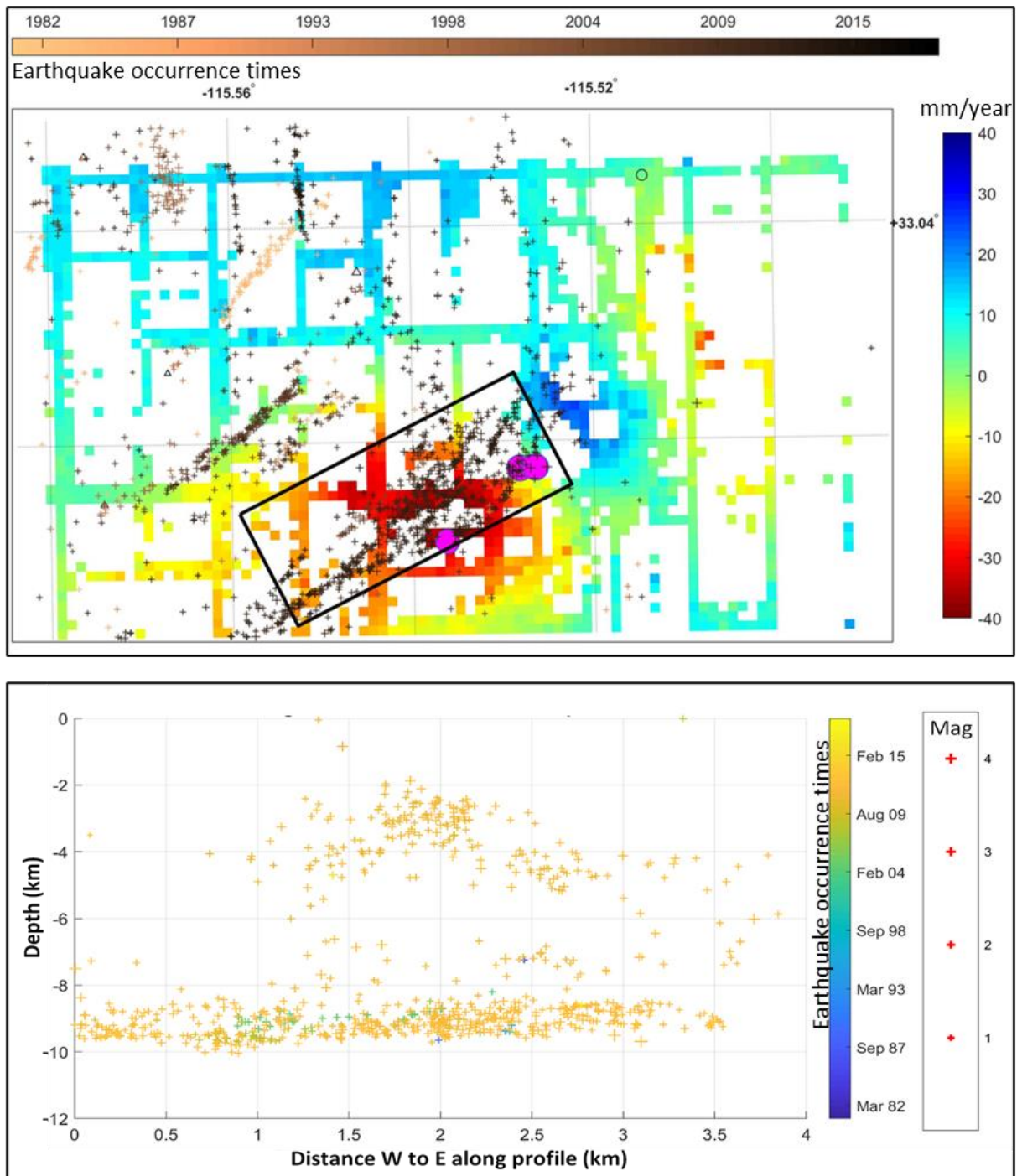
Top – M>1 earthquake epicenters (crosses) are superimposed on the TSX vertical deformation map. Crosses are color-coded according to color bar on the tope. Deformation rates are color-coded according to the color bar to the right. Pink circles mark the epicenters of the largest events in the Aug 2012 swarm. Black rectangle outlines approximately the aftershock area. Bottom – depth cross-section oriented along the black rectangle on the top, showing the hypocenters of the earthquakes within the rectangle. Occurrence times and magnitudes are coded according to bars to the right.

Source: Individual plots by D. Adams, assembled and modified by M. Eneva.

111

Figure 2.78 Various Time Series in the NBGF Subsidence Area During the TSX Period
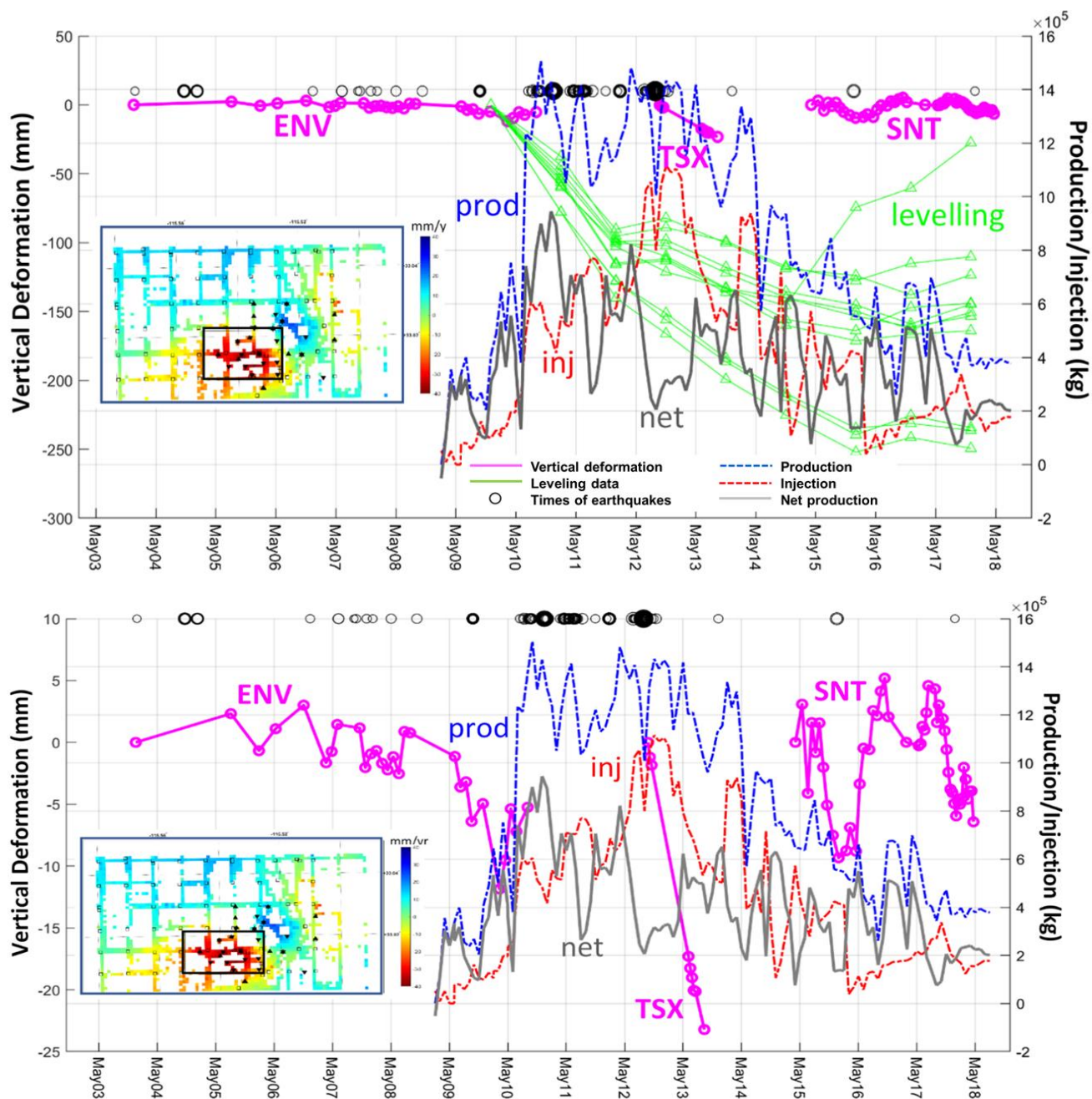
Top - Time series of vertical deformation from InSAR (pink), leveling (green), production (dashed blue), injection (dashed red), and net production (dark gray) for the area of maximum subsidence during the TSX period (black rectangle in inset). Inset shows the same map of TSX vertical deformation rates as in Fig. 2.74 and the middle frame of Fig. 2.75, with the same symbols for the wells. In addition, leveling benchmarks are displayed with empty squares in the inset. Black circles on top indicate earthquake occurrence times, with circle size proportionate to magnitude. Bottom – same plot, but with a smaller range on the vertical axis in order to emphasize the InSAR time series, and without the leveling time series.

Source: Individual plots by D. Adams, assembled and modified by M. Eneva.

known at this time. The SNT1 InSAR time series does not show significant subsidence overall, but appears to indicate seasonal changes. As to the early ENV InSAR time series, it mostly covers the pre-production period when it does not show subsidence, but starts trending downward after geothermal production and injection are initiated in 2009. Note that most earthquakes appear after the start of operations and occur steadily after mid-2010 while the production is relatively high, so it is likely that these are induced events. Their number greatly diminishes after the August 2012 swarm, and when production notably decreases after 2014.

The bottom part of Fig. 2.78 zooms in on the top panel, in order to show details of the InSAR time series. It demonstrates more clearly that the ENV observations are characterized by subsidence (~ -11 mm) at the start of production and injection, followed by ~ 7 mm of uplift, before the ENV observations end in 2010. There are no InSAR data for the next two years, until the TSX coverage begins. Starting in Sep 2012, a subsidence of ~ -24 mm is observed over the year-long TSX period. This value is smaller than the maximum TSX subsidence rate listed above in connection to Figs. 2.74 and 2.75, because it is averaged over the whole subsidence area. After another InSAR data gap of about a year and a half, the SNT1 observations display seasonality, with subsidence of up to -12 mm in the first half of the year and uplift of up to 13 mm in the second half of the year. The smaller range on the vertical axis in the bottom panel makes it possible to suspect seasonality in the ENV data as well. In this connection, the seasonal fluctuations need to be investigated against the irrigation records for the agricultural fields in the vicinity of NBGF, as well as the net production (production minus injection) variations in the subsidence area. The project team contacted the IID and learned that irrigation records for individual agricultural fields are proprietary (Tina Shield, pers. communication). Still, IID suggested that some records might be possible to obtain if farmers agree to release them. M. Eneva provided locations of areas of interest, but IID did not follow up the earlier communication within the timeframe of the project.

While the SNT1 period covers ever declining production, the SNT2 period coincides with the time when the relatively low production reached at the end of SNT1, is already stabilized (see Fig. 2.72). Figure 2.79 shows maps of vertical and east horizontal rates for the SNT1 and SNT2 periods. Four small areas are outlined, for which average time series are calculated and shown in Figure 2.80 back-to-back for the two periods. Some of these small areas show distinct seasonal changes in the SNT1 period. The STN2 period is too short to readily show such variations on its own. As a reminder, time series from individual periods start at 0, so it is necessary to compare trends and slopes. It is evident that for some of the areas, deformation trends are continued from SNT1 to SNT2, but in other cases they look rather different. This is likely due to both changes in irrigation patterns and geothermal operations. Note that while Figs. 2.74 to 2.78 used Y-1225 as a reference, Figs. 2.79 and 2.80 use the original reference point for the whole Imperial Valley, because of the different source of these figures. This affects the numerical values of the observations, but not the overall spatial and temporal patterns of deformation.

Figure 2.81 shows an additional view of the seismicity at the NBGF and its possible connection to the production and injection variations in the field, as well as deformation measured by GPS instruments in the surroundings of the field.

Figure 2.79 Maps of Vertical and Horizontal Deformation SNT1 and SNT2 Rates
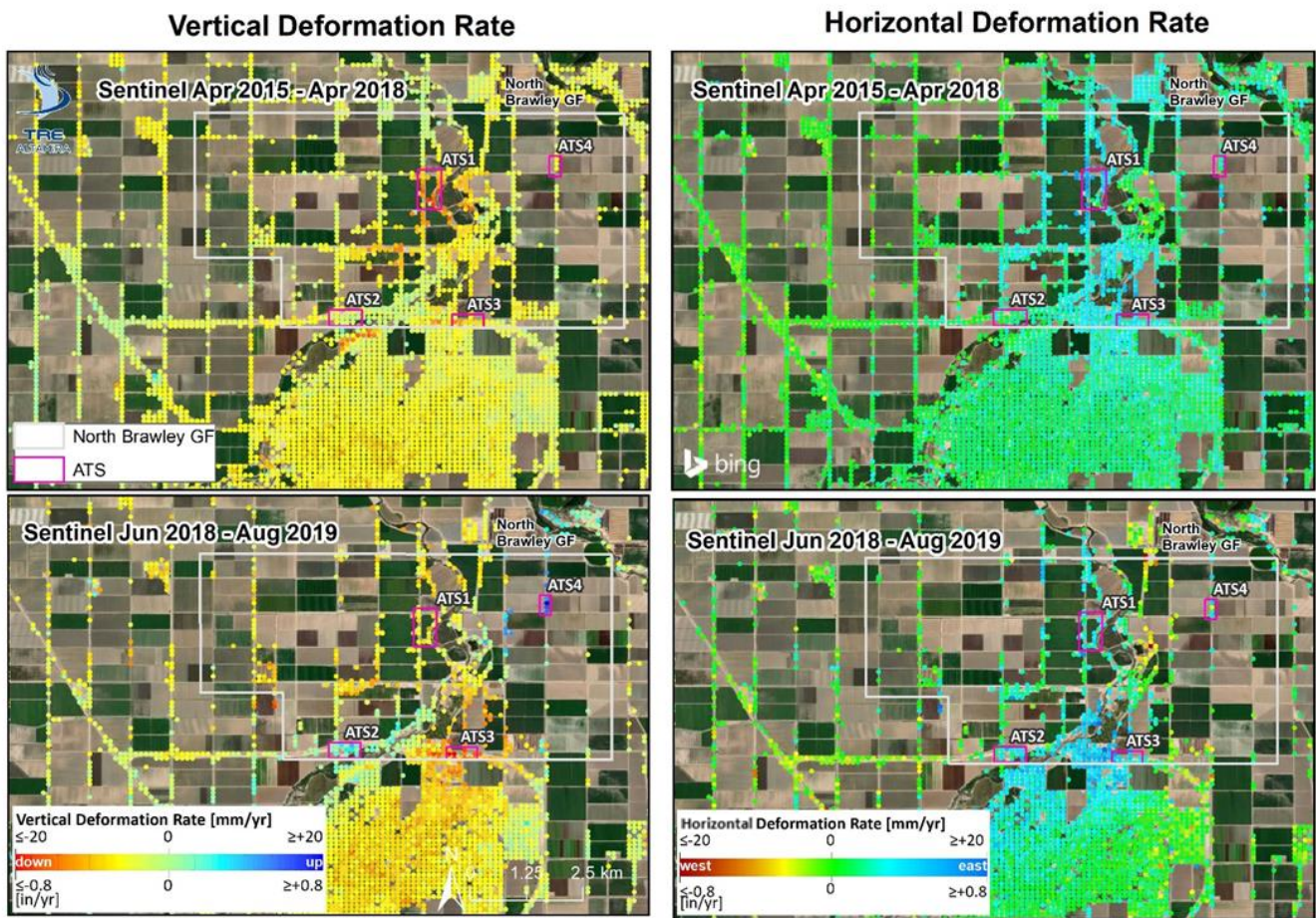
Four maps of vertical and horizontal deformation rates of the North Brawley Geothermal Field.

Source: TRE Altamira

Overall, the maximum surface deformation at NBGF may be viewed as surprisingly large, as it is comparable in size with the maximum displacement rates at significantly larger geothermal fields in the area (e.g., Eneva et al., 2019, 2014). However, it is significantly smaller than the deformation observed in Mexico just south of the border, at the Cerro Prieto geothermal field (Sarychikhina et al., 2011, 2018), where the amounts of reinjection are much smaller, and a subsidence of up to −170 mm/year was observed. Thus, geothermal facilities that reinject more of the production fluids appear to significantly reduce the amount of subsidence that would occur otherwise.

Figure 2.80 Deformation Time Series in Four NBGF Areas, SNT1 and SNT2 Periods
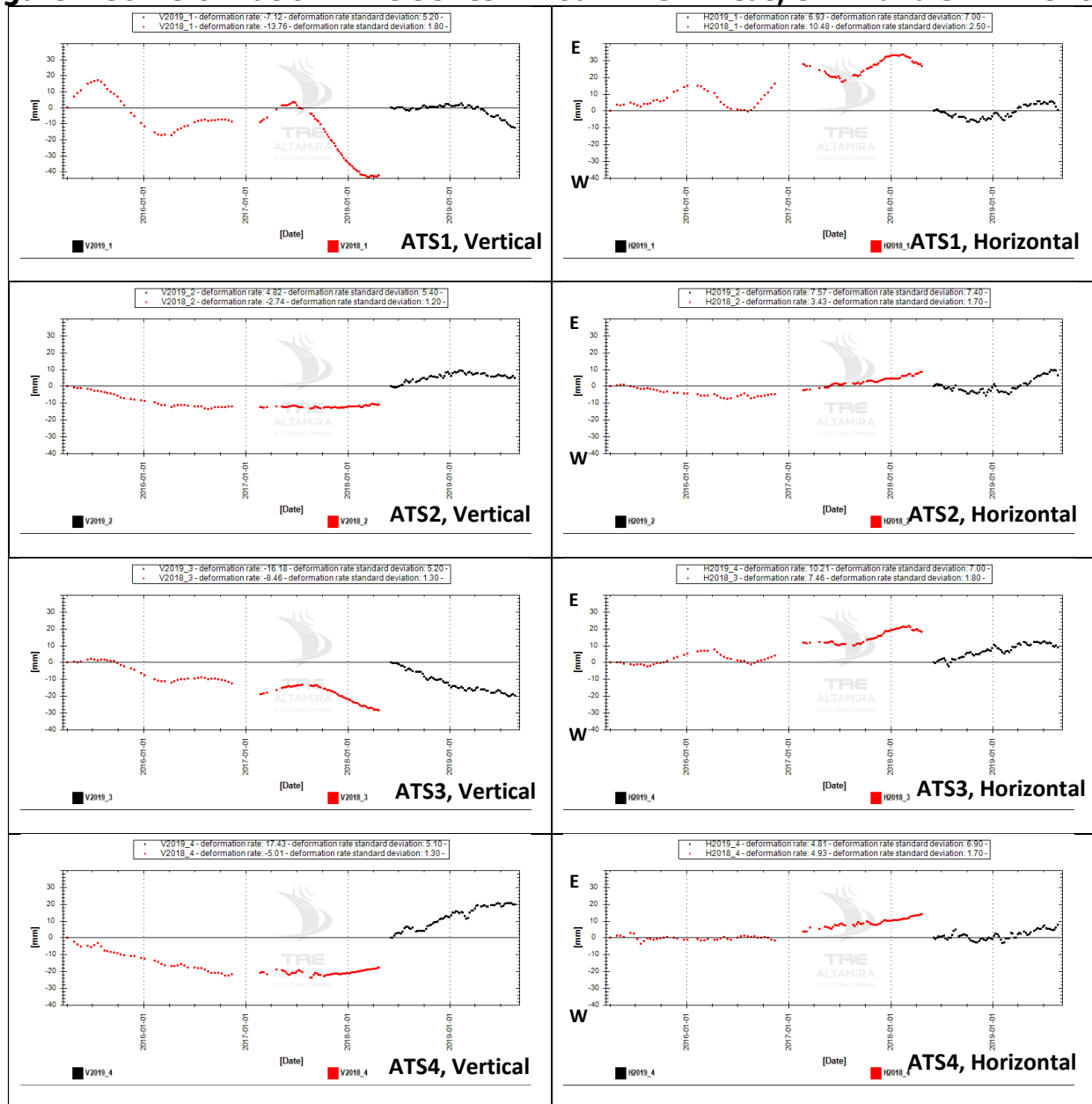
Red and black symbols mark the SNT1 and SNT2 periods, respectively. Numbers in titles show deformation rates calculated from the slopes of straight lines through the time series. However, their non-linearity renders these estimates unreliable.

Source: TRE Altamira

Figure 2.81 Seismicity and deformation from GPS at the NBGF
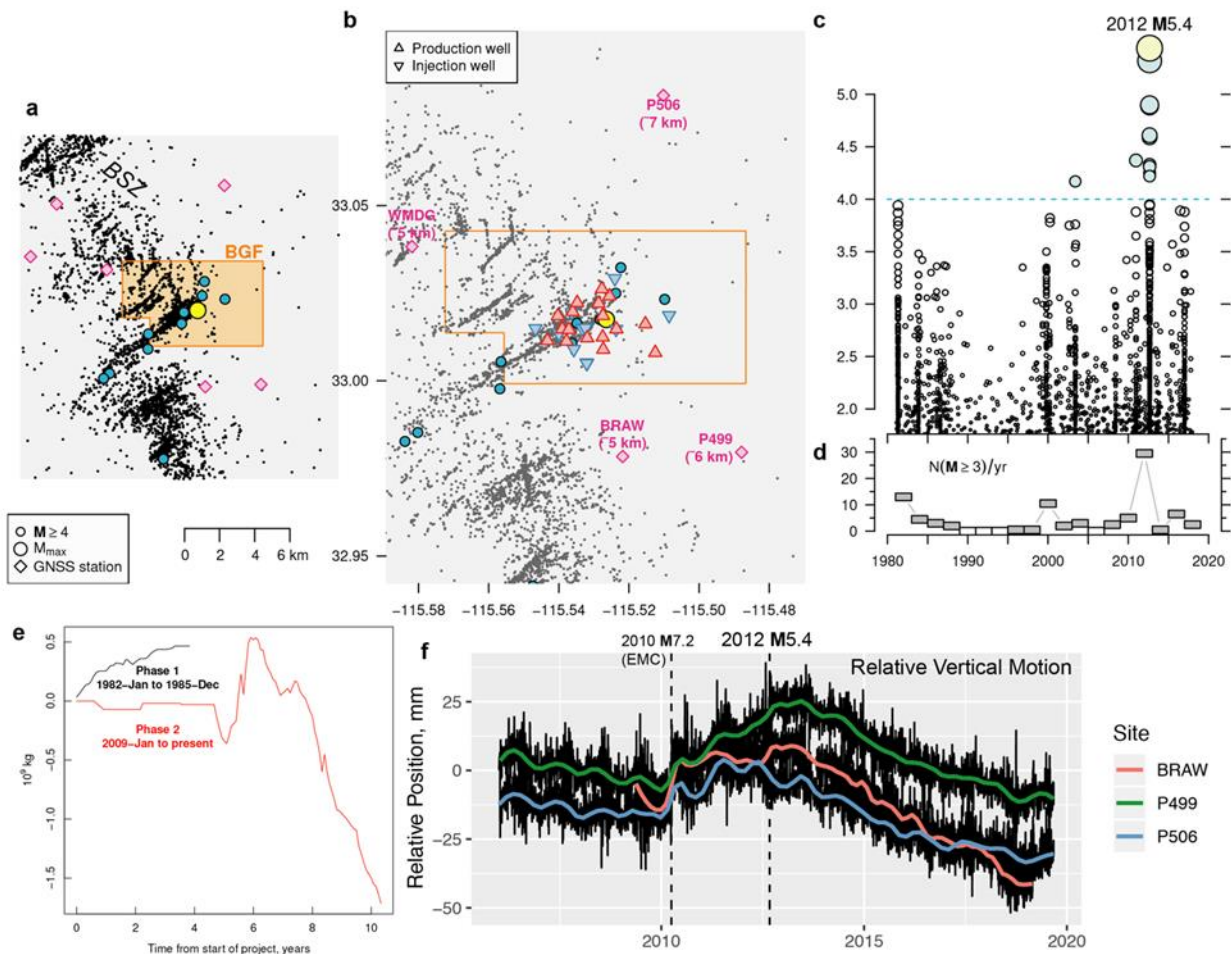
(a) Regional seismicity in the Brawley Seismic Zone (BSZ), with locations of M≥4 earthquakes and continuous GNSS GPS stations (diamonds). **(b)** Zoom in on the NBGF wells and associated seismicity. The 2012 M5.4 epicenter is the large circle around the centroid of the geothermal wells. **(c)** Time evolution of seismicity magnitudes, showing the M5.4 sequence. **(d)** Rates of M≥3 seismicity in two-year intervals (unfilled boxes indicate no earthquakes). **(e)** Cumulative net produced fluid (positive indicates fluid-mass loss). These curves should be zero, or very nearly zero because this field uses binary technology; however, in the last five years more fluid has been injected than produced. **(f)** GPS observations of transient, vertical ground deformation associated with the Apr 2010 M7.2 El Mayor Cucapah earthquake in Mexico, followed by deformation associated with the 2012 M5.4 Brawley swarm (Hauksson et al., 2013). Solid lines show local regression smoothing applied to daily relative positions (in mm).

Source: A. Barbour (USGS)

Finally, preliminary results are shown here, from work at USGS using DInSAR applied to data from the L-band airborne UAVSAR (Uninhabited Aerial Vehicle Synthetic Aperture Radar) - https://uavsar.jpl.nasa.gov. This was not planned as part of this project but happens to be relevant to the results from the NBGF. Scenes from one of the UAVSAR tracks (26509) showed several deformation signals, including around the time of the Aug 2012 M5.4 swarm. There were 11 acquisitions from this track, from which 55 pairs of scenes were formed to obtain interferograms, and the processing continues. Figure 2.82 summarizes some of the preliminary findings.

Figure 2.82 Preliminary Observations at NBGF from UAVSAR
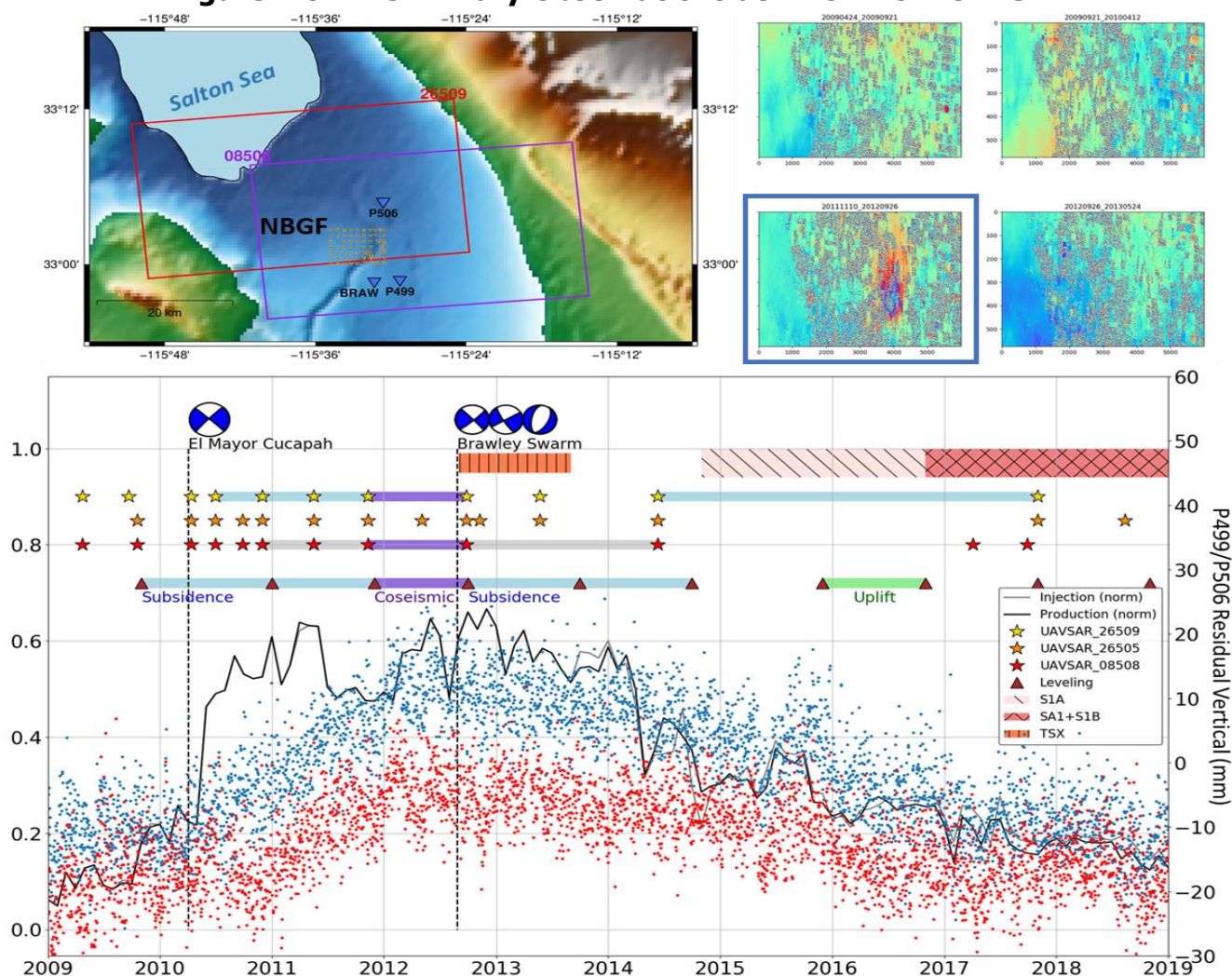
Top left — map showing the footprints of two UAVSAR scenes covering the NBGF. Small yellow triangles show locations of the leveling benchmarks. Inverted triangles show GPS stations in the neighborhood. Top right — examples of unwrapped differential interferograms from DInSAR. The titles show the dates of the scenes paired to form the interferograms. The largest signal is seen for the pair outlined with a blue rectangle, formed from Nov 10, 2011, and Dec 26, 2012 UAVSAR scenes (track 26509), which enclose the Aug 2012 M5.4 swarm. Bottom — normalized monthly production and injection fluid masses are shown together with vertical measurements from two GPS stations (blue and red dots). Stars show the times of the various UAVSAR acquisitions, with different colors for different tracks (see legend). Triangles mark the times of leveling surveys. "Beachball" symbols on top show fault-plane solutions for the Apr 2010 M7.2 earthquake south of the U.S.-Mexico border and the Aug 2012 M5.4 swarm on the territory of the NBGF.

Source: Individual plots by K. Materna (USGS), assembled and slightly modified by M. Eneva.

2.2.5 Heber Geothermal Field

2.2.5.1 General Description of the HBGF

Heber represents a blind geothermal system (e.g., Lippmann and Bodvarsson, 1985) located just north of the border with Mexico, and south-southeast of the town of El Centro (see Fig. 2.48 above). The field was first developed in the early 1980's by Chevron, starting with a double flashed plant. Initial output was lower than expected, so a modular binary power plant was added, making the geothermal operations successful since the mid-1993 (Sones and Krieger, 2000). At present, the field has one double flash and three binary plants (Figure 2.83). Their average power production in 2018 was 16.5 percent gross and 13 percent net of the total Imperial Valley geothermal production (see Table 2.11 above). The installed capacity at the HBGF is 161.5 MW. The reservoir volume is estimated at 23 km^3 (Gawell, 2014) to 28 km^3 (Geothermex, 2004). The depths to the top and bottom of the reservoir are 1,200 m and 1,800 m, respectively (Sones and Schochet (1999). The mean temperature at depth has been reported at 375°C (USGS, 2008), but the lower average temperature of the geofluids (174°C) necessitated the construction of binary plants.

Figure 2.83 A Power Plant at the HBGF

Source: Ormat (http://www.ormat.com)

There are some reports for the existence of right strike-slip and normal faults at the HBGF (James et al., 1987; Allison, 1990) at Heber, shown in Figure 2.84. Their locations are approximate, because the sketches in the cited papers that were used to trace these faults did not show geographic coordinates. James et al. (1987) also showed temperature maps and cross-sections, indicating that the maximum of the temperature anomaly, 380^0 F (193^0 C) at 6000 ft (~1,830 m) is located just west of the normal fault, while Allison (1990) reported on the location of the maximum temperature gradient, 58^0 F/100 ft (46^0 C/100 m), further northwest. Therefore, it is assumed that the controlling structure at the HBGF is pull-apart, in a strike-slip fault zone, with a reservoir model including three major permeability units (James et al., 1987) – "capping" clays at depth of 150-150 m, high matrix permeability sandstone "outflow" reservoir at 150-1,680 m, and high permeability "feeder" faults and fractures in indurated sediments below 1,680 m. These were deduced from seismic lines, and maps and cross-sections of lost

118

Figure 2.84 Map of the HBGF
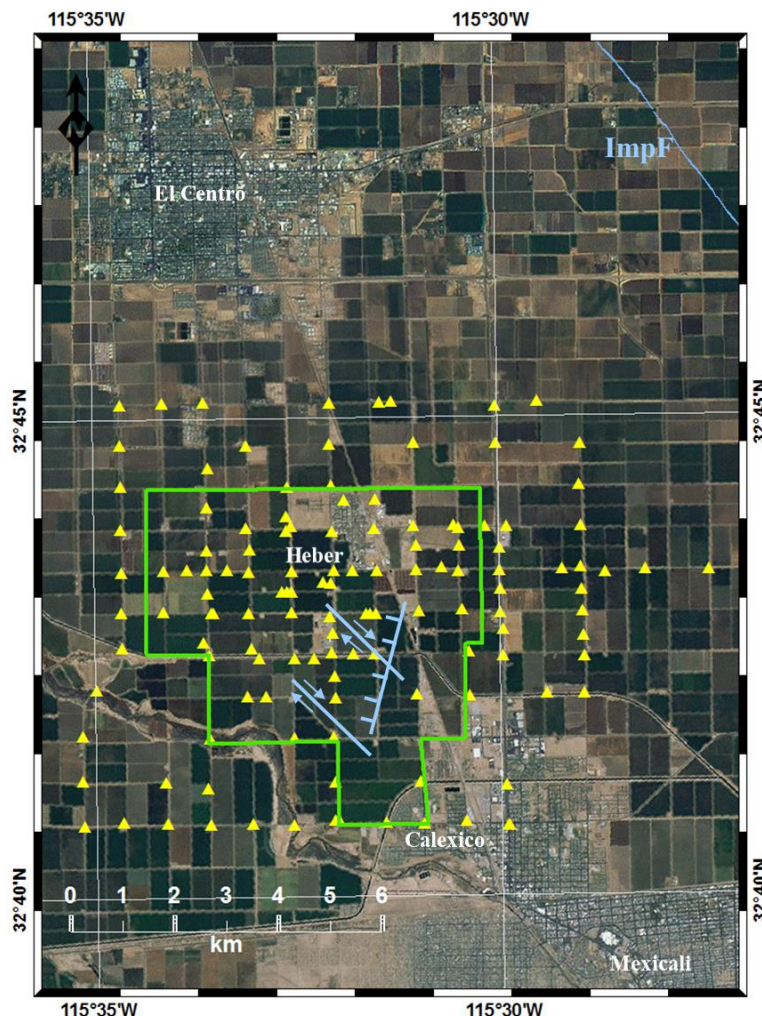
Green polygon outlines the Heber KGRA. Light blue lines mark the approximate locations of faults according to James et al. (1987) – movement on two strike-slip faults is marked with arrows, and on a normal fault - with a comb-like pattern. Blue line to the northeast marks the Imperial fault. Yellow triangles show leveling benchmarks.

Source: M. Eneva

circulation and temperature distribution. James et al. (1987) also commented on a steep pressure decline under initial production, but subsequent rapid stabilization due to regional aquifer support. These authors concluded that the reservoir is very permeable and that there is a significant opportunity for additional development of the field. Allison (1990) used borehole breakout orientations to confirm these findings, particularly the right strike-slip and normal faults suggested by James et al. (1987).

2.2.5.2 Data Used at the HBGF

Similar to the two other geothermal fields, the satellite data used for the HBGF in this project were from the SNT1 and SNT2 periods, and also from the ENV period from a previous CEC project. Unlike the two other fields, there were no TSX data for the HBGF. One of the main early findings at Heber was the observation of adjacent areas of subsidence and uplift during

119

the ENV period (Eneva et al., 2013b); however, leveling surveys preceding the ENV period showed that the area of uplift was previously subsiding.

Figure 2.85 Wells and Leveling Benchmarks at the HBGF
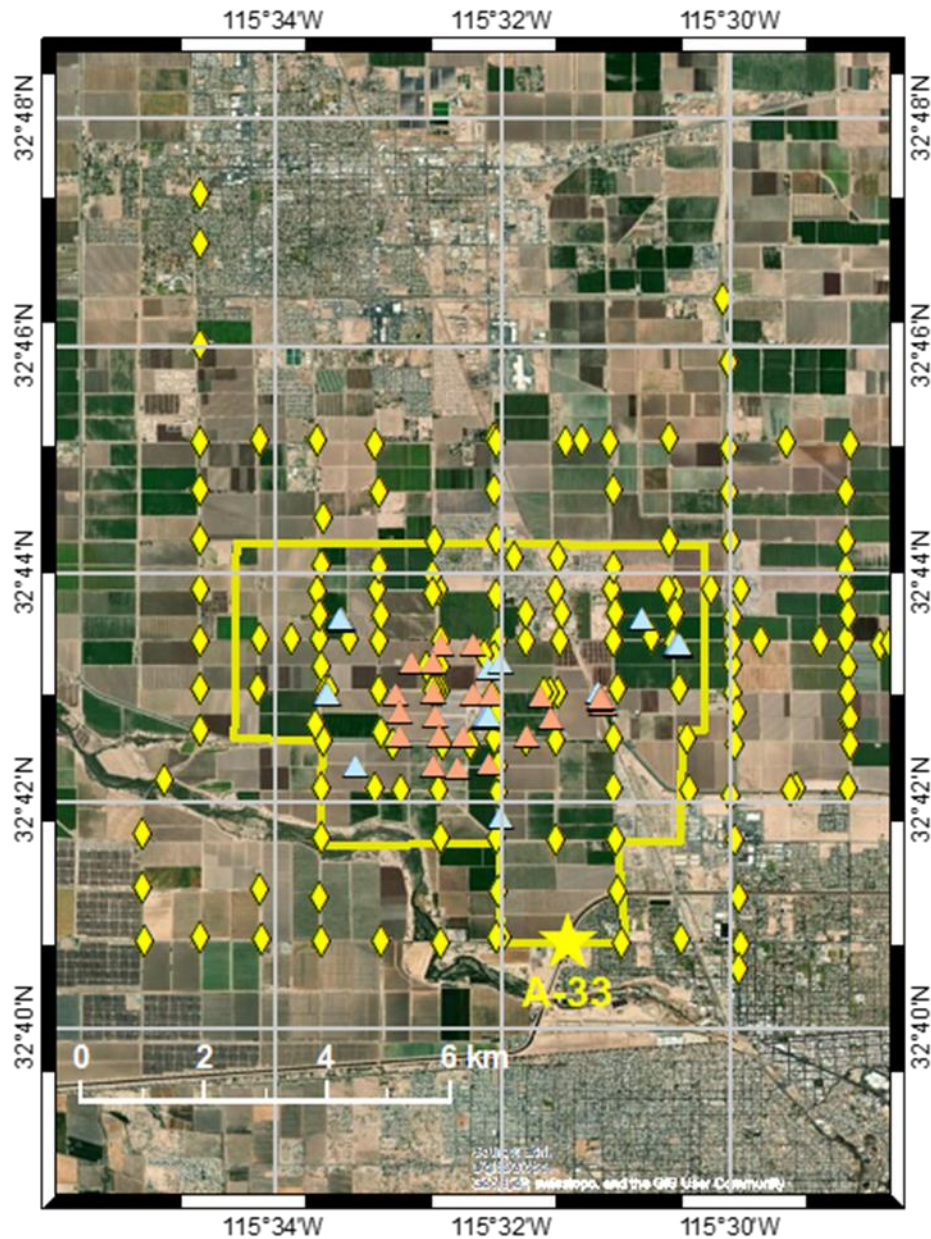
Yellow outline – Heber KGRA. Blue triangles – injection wells. Orange triangles – production wells. Yellow diamonds – leveling benchmark. Yellow star – benchmark A-33 that was used as datum in the leveling surveys, and for re-referencing of the InSAR results.

Source: M. Eneva

Figure 2.85 shows a map with the locations of wells and leveling benchmarks. Figure 2.86 illustrates the monthly well fluid masses. The well data, obtained from CalGEM, go back to 1985. The number of injection wells is 37. The number of production wells since 1985 is 41, of which 29 wells were active during the ENV and SNT periods, and three additional wells worked only in the gap between the two periods. The map displays fewer distinct well locations,

because some of the wells are closely clustered. Eight production wells operating in the period 1985-1988 were later turned into injection wells that were active during the study periods. One more production well in the period July 1993 - May 2015, stopped operating for 8 months

Figure 2.86 Monthly Production and Injection Fluid Mass at the HBGF
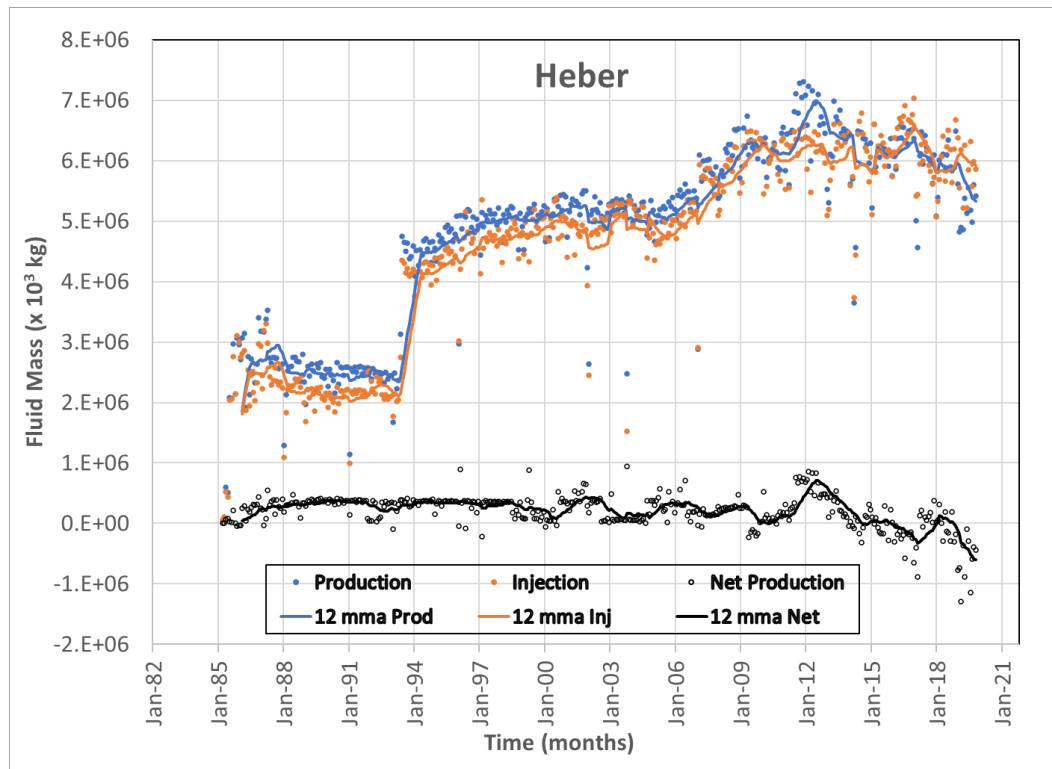
The lines are drawn through the monthly fluid mass values using 12-months moving average (mma).

Source: M. Eneva

and then continued as an injection well; this is the only well that switched type during one of the study periods. In 1993, there was a steep increase of production and injection when the first binary plant was added. Later on, when Ormat took over, another increase took place in 2005. As shown earlier (Eneva et al., 2013b) that this had a clear effect on surface deformation documented by the leveling surveys, which was a previously subsiding area in the northwestern part of the HBGF, turning into uplift.

ICDPW supplied data from 25 annual surveys at the HBGF, but only 10 of them were during the ENV and SNT periods (see Table 2.14 above). The number of surveyed benchmarks changed over the years – some started later than the earliest ones, and some stopped after several years. The last survey for which ICDPW provided data, was carried out in late 2018; it provided measurements at 106 benchmarks. Figure 2.87 shows time series for all HBGF benchmarks (left), as well as select time series from the area of persistent subsidence (right), and the area that has initially subsided, but experienced uplift for a while after 2005 (middle) (Eneva et al., 2013b). It is evident that for some of the benchmarks, the temporarily uplifting area resumed subsiding after about 2010.

While Fig. 2.86 showed the total monthly well time series from all wells, Figure 2.88 illustrates time series for select individual injection and production wells that are located in the same parts of the HBGF as the leveling data in the middle and right plots in Fig. 2.87. That is, some injection time series (Fig. 2.88, left) showing significant increase in 2005 (when Ormat took

Figure 2.87 Leveling Time Series at the HBGF
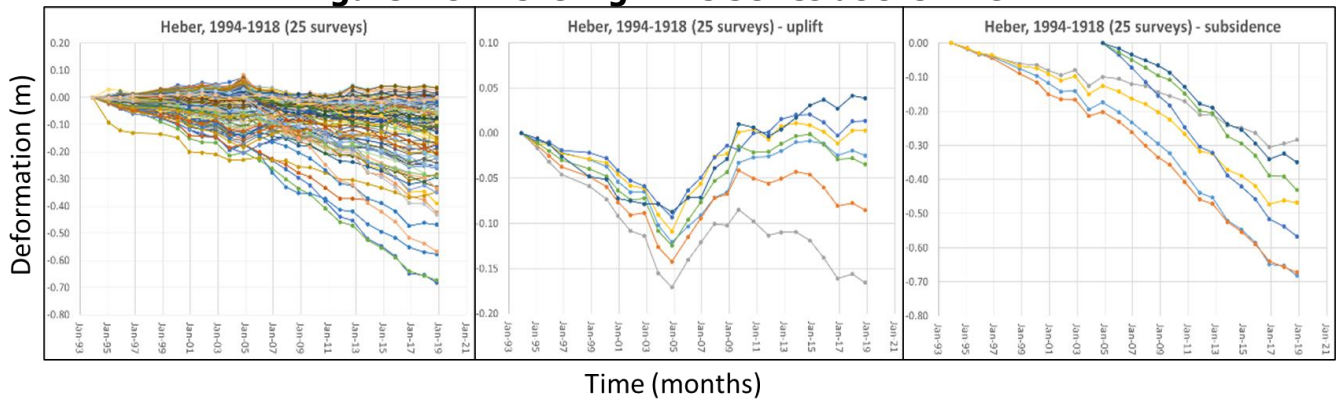
Source: M. Eneva

over) are likely associated with the subsidence turning to uplift at the same time (Fig. 2.87, middle). However, as the InSAR data show below, the uplift area during the ENV period was subsiding in the SNT1 period, while in the SNT2 period, another area of uplift appeared to the south of the ENV uplift. The plot to the right in Fig. 2.88 shows fluid time series for several production wells from around the center of the field, where the ongoing subsidence takes place (Fig. 2.87, right). It is evident that the production from some of those wells started increasing after about 2006, but this increase slowed down for some wells, or leveled out, after 2010. Although the subsidence in this area is persistent, its rate increased at some benchmarks after 2005, and started decreasing again in 2017.

Figure 2.88 Time Series of Fluid Mass Jan 1993 – Apr 2018
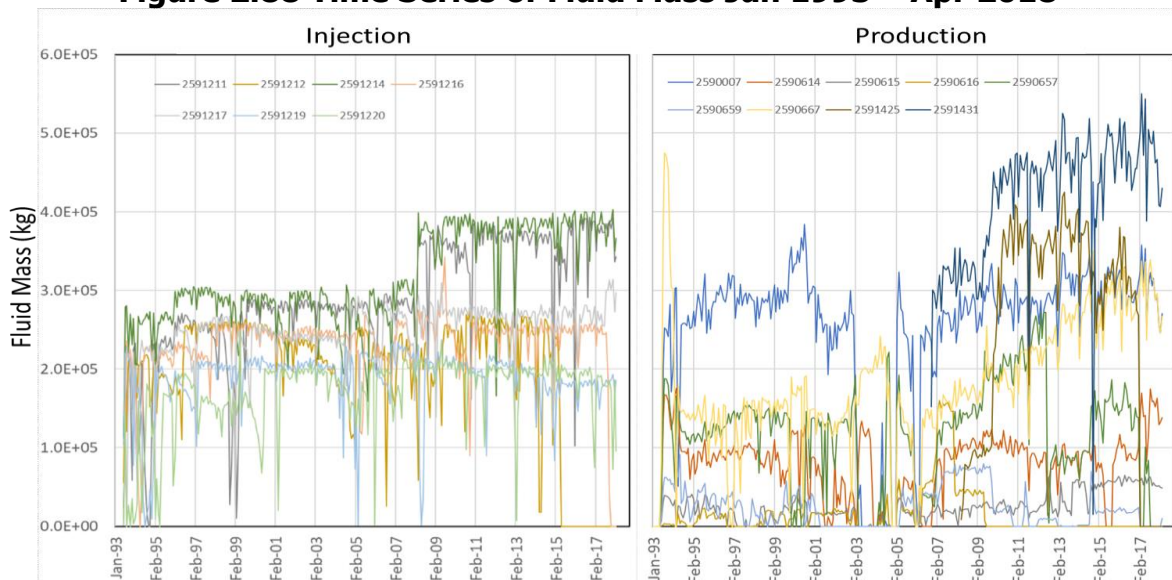
Source: M. Eneva

Figure 2.89 Seismicity at the HBGF and Surroundings
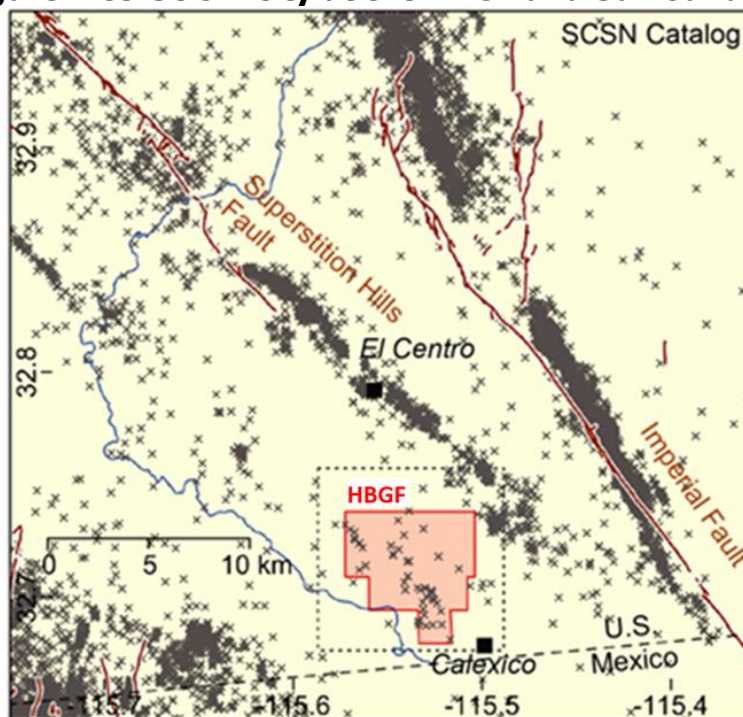
Source: A. Barbour (USGS), data from SCSN catalog.

Furthermore, earthquake data at the HBGF were compared with the fluid time series and leveling data. Seismic activity at the HBGF is lower than elsewhere in Imperial Valley (Figure 2.89), especially when compared with the SSGF and NBGF, however it was still possible to identify some correlations. Low levels of seismicity at the HBGF were first detected around 1993, when the first binary plant was installed and production was ramped up. Enough events have been detected by the regional seismic network (SCSN) that a series of rapid increases in seismicity rate have been observed from the initiation of a transient deformation in 2004 through 2007 on structures flanking the geothermal wells (Figure 2.90). Barbour et al. (2019) used a match-filter detection algorithm to improve and enhance that catalog. This yielded a nearly tenfold increase in detected events, with similar temporal patterns (Fig. 2.90-c). This was also compared with data from the local seismic network that Ormat has installed at the HBGF, which showed similar variations in the seismicity rates with time (Fig. 2.90-d). It was found that changes in seismicity rate are nearly instantaneous and correspond to significant changes in injection and production. On the other hand, ground deformation deduced from leveling surveys may be occurring slowly. This may suggest that reservoir bounding faults are critically loaded and thus small perturbations in stressing rates induced brittle failure (earthquakes). In contrast, the slow deformation opens up the possibility that the physical mechanisms responsible for these signals include triggered slow slip on reservoir bounding faults (e.g., Lohman and McGuire, 2007; Helmstetter and Shaw, 2009; Guglielmi et al., 2015), including a previously imaged "feeder fault" (the normal fault seen in Figs. 2.84 and 2.90-a), and a poroelastic step-response (e.g., Rudnicki, 1986) to systematic changes in fluid injection and production reported at the field (Figure 2.91).

123

Figure 2.90 Seismicity Rates at the HBGF
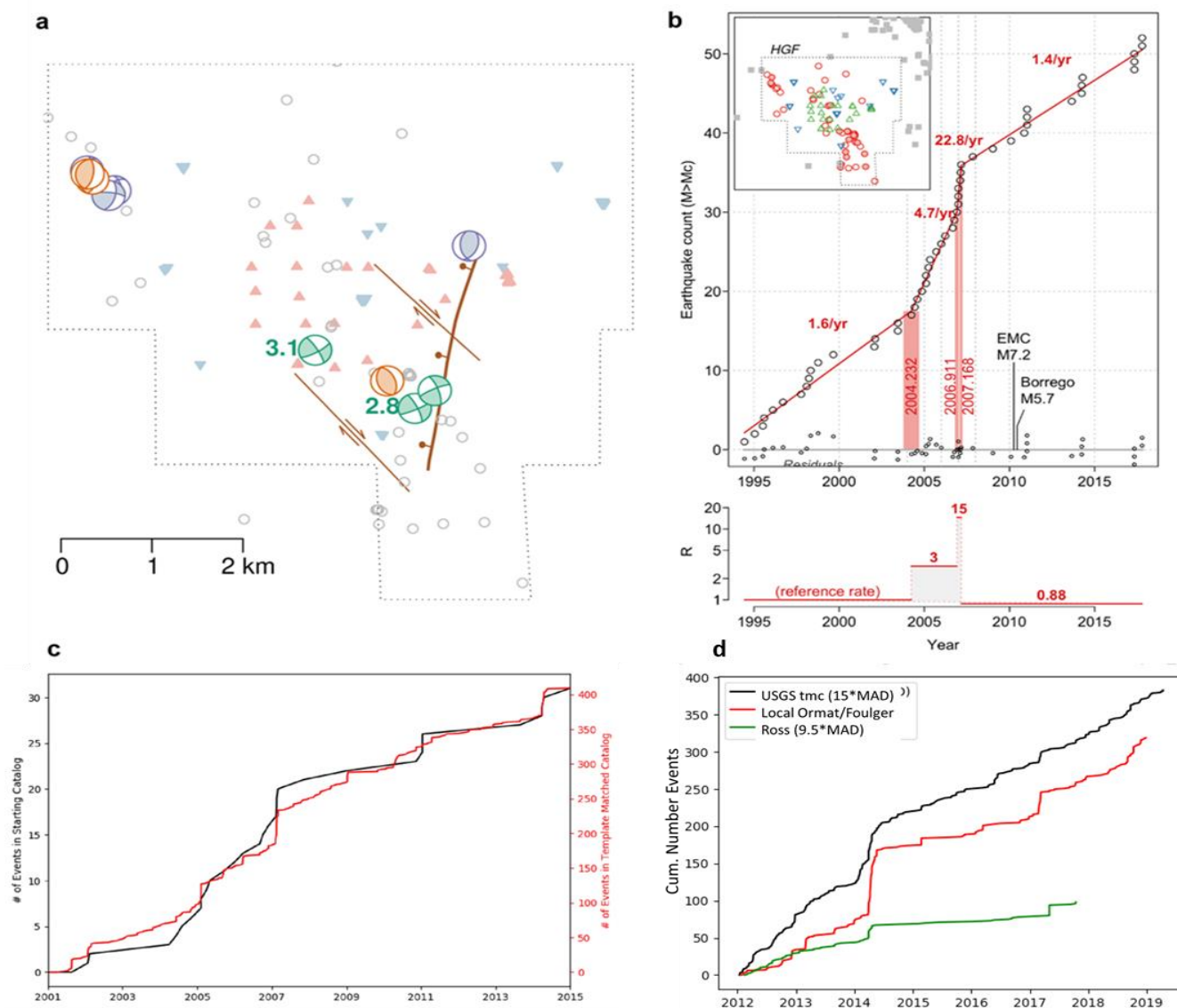
Map of seismicity with focal mechanisms, reservoir bounding faults, and geothermal wells in the HBGF. (b) Cumulative number of SCSN earthquakes within the Heber KGRA. Vertical red bars mark times of significant rate changes – late 2005, late 2006, early 2007 – with the relative rate shown below the cumulative plot. (c) Cumulative plot comparing the original seismic catalog (SCSN) and the improved catalog from template matching (Barbour et al., 2019). (d) Cumulative plot comparing template-matching catalog (tmc) with the catalog from the local Ormat network, and a catalog by Ross et al. (2019a).

- Source: A. Barbour (USGS). Catalog from template matching (match filtering) by Rob Skoumal (USGS). (a)-(c) From Barbour's WGC 2020 paper. (d) From an e-mail exchange between A. Barbour and M. Eneva. M. Eneva made modifications to above plots.

124

Figure 2.91 Seismicity, Injection and Production at the HBGF
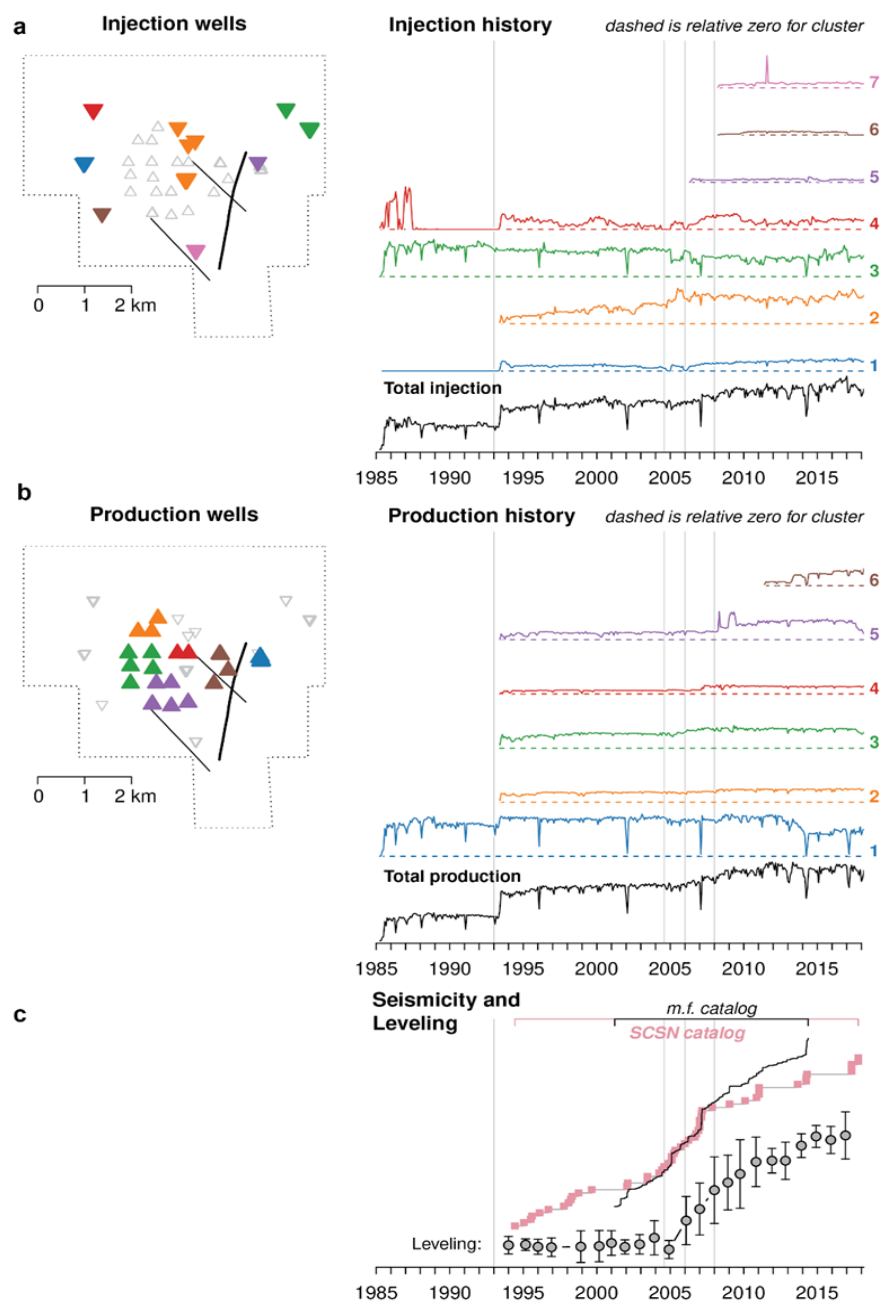
Injection (a) and production (b) records at the HBGF, compared to (c) seismicity rates and transient deformation measured by the leveling network. In (a) and (b), wells are grouped into spatial clusters (see maps on left) and the corresponding time series for total fluid mass in each cluster are shown to the right. The total injection and production time series are shown at the bottom, respectively. Vertical lines mark times of new power plants coming online. In (c), an earthquake catalog obtained by matched-filter detection (template matching) is compared to the starting SCSN catalog (Barbour et al., 2019), and to characteristic surface displacements from leveling surveys (amplitudes divided by their root-mean-square value) across the array of benchmarks.

Source: A. Barbour (USGS), from WGC 2020 paper.

125

2.2.5.3 Surface Deformation from InSAR at the HBGF

In the previous CEC project, both subsidence and uplift were identified at the HBGF from InSAR applied to ENV satellite data (Eneva et al., 2013b). At that time, many details of the data were shown, such as mean time series in subareas of interest, deformation rates along profiles, comparisons with leveling data, and comparisons with production and injection time series. Figure 2.92 shows an example of ENV (2005-2010) deformation rates along several profiles. The areas of subsidence (red area in the map) and uplift (blue area to the west and northwest of the subsidence area) are evident along the two profiles intersecting them (profiles 1 and 2 in Fig. 2.92). The ascending data (red crosses on the curves) likely probe the area of maximum subsidence; this is most noticeable along profiles 1 and 3. However, descending data are absent for the same area along these profiles - hence, there are only blue dots showing interpolated data, but no blue crosses for actual measurements. With one LOS missing, vertical rates are also absent in that area, so only pink dots are sown for the interpolated data, but no pink crosses for calculated vertical rates. Therefore, the maximum observed vertical rates are actually from the periphery of the subsidence area, and therefore, more attention should be paid to the ascending rates to evaluate the maximum subsidence.

Figure 2.92 ENV Deformation Rates along Profiles at the HBGF
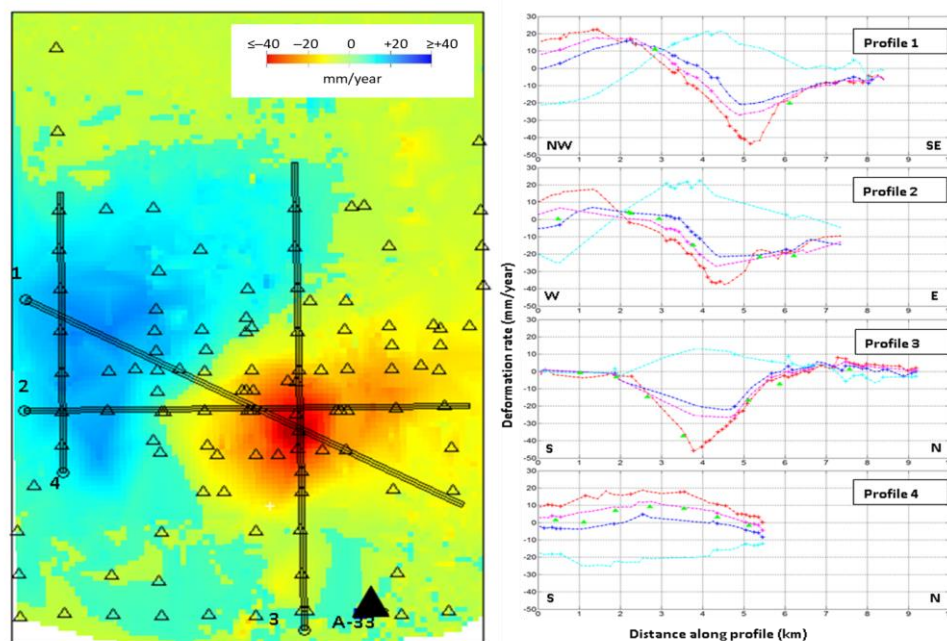
Left - Map shows ENV InSAR color-coded interpolated vertical deformation rates. Reference point is benchmark A-33 denoted with a solid black triangle. Empty triangles mark locations of the other leveling benchmarks. Lines 1 to 4 are profiles intersecting areas of interest. Right - Curves show deformation rates within 200 m along the profiles from the panel on the left: vertical (pink), east horizontal (light blue), descending (dark blue), and ascending (red) deformation rates. Crosses on the curves show measured mean values, dots are interpolated values. Green triangles show rates from leveling benchmarks.

Source: M. Eneva, using software by D. Adams.

Because of the ENV findings, it was of great interest what kind of deformation will be revealed after a four-year gap of satellite data, especially because the SNT data are expected to identify

larger numbers of PS/DS points. Table 2.20 shows the numbers of ascending and descending PS and DS points in a ~450 km^2 area covering the HBGF and its surroundings, for the ENV and SNT1 periods. The table also shows the number of 100-m pixels for which vertical and east horizontal rates could be calculated (i.e., pixels in which there were both ascending and descending LOS measurements). The table shows that the expectation for the SNT data to be significantly more numerous was justified.

Table 2.20 Numbers of PS/DS at the HBGF from ENV and SNT1

Satellite	Num Asc PS/DS	Num Desc PS/DS	Num 100-m pixels (Vert/East)
ENV	39,185	25,716	5,402 (of 44,460) – 12.2%
SNT1	94,215	104,483	16,772 (of 44,460) – 37.7%

Source: M. Eneva

Figure 2.93 shows maps of ascending and descending deformation rates (ref. A-33) that show that there are significant differences between the ENV and SNT1 periods. Another important observation is that, even though the number of PS and DS points is much larger than the number of leveling benchmarks (106 in 2018, the last year with available leveling survey data), and there are many such points where benchmarks are absent, the opposite is also observed - there are benchmarks in areas devoid of scatterers. This has already been noticed in the two other geothermal fields, and is not surprising in view of the agricultural land. Such problems can be overcome by installing corner reflectors (e.g., Garthwaite et al., 2015) in areas of interest, which are without PS/DS. In the case of the HBGF, this would definitely include the area of maximum subsidence, as expected from the leveling data and the ascending data, but not probed by descending measurements and hence lacking calculations of vertical rates from InSAR. Once installed, the corner reflectors would be identified in both the ascending and descending LOS in future satellite scenes, thus ensuring the capability of estimating the vertical and east horizontal rates where they are of most interest.

Figure 2.94 shows a complete set of maps of ENV and SNT1 linearly interpolated values from the LOS and Vertical/East rates (ref. A-33). This rendition of the data shows more clearly the major difference already gleaned from the point measurements in Fig. 2.93 – the SNT1 data lack the uplift during the ENV period, to the west and northwest in the study area. Otherwise, subsidence from the center of the Heber KGRA and extending to the northeast, is seen in both periods, covering an area of size ~ 5 km x 3 km. This confirms the observations from the benchmarks in the uplift (ENV only) and subsidence areas (Fig. 2.87). During the SNT1 period, the ENV uplift apparently turns into subsidence, extending also to the south and southeast of the previously uplifting area. Corresponding changes are also seen in the horizontal movements (plots on the bottom of Fig. 2.94). During the ENV period, there are eastward displacements to the west of the central subsidence area, and westward movements to the west and northwest of the uplift area. The pattern is different in the SNT1 period – there are several transitions between eastward and westward displacements, generally pointing toward the inner parts of the subsidence areas, i.e., the western flanks of subsidence areas tend to

Figure 2.93 Ascending and Descending LOS Rates from ENV and SNT1 at the HBGF
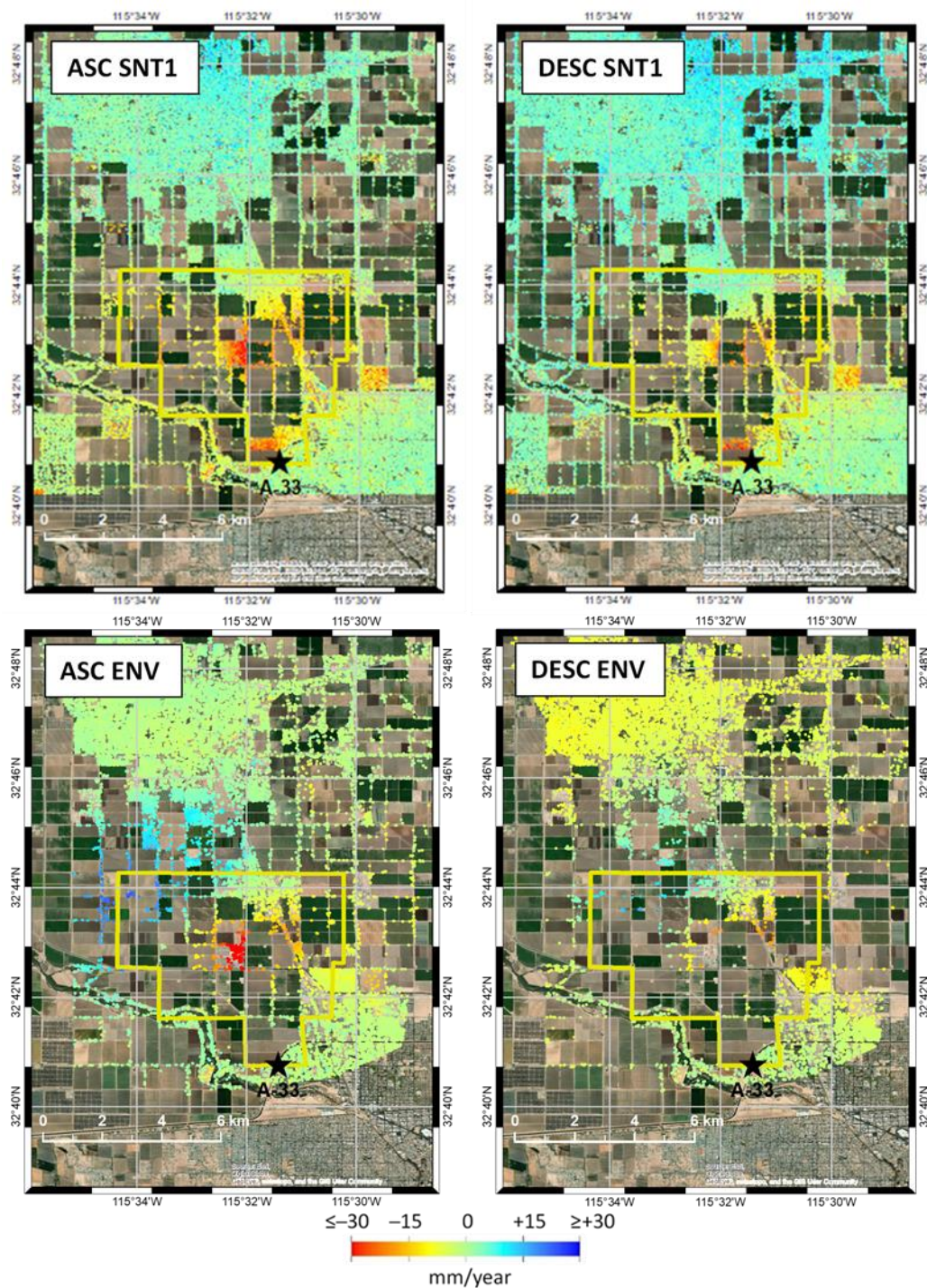
Source: M. Eneva

move eastward and the eastern flanks tend to move westward. Table 2.21 shows the maximum displacement rates measured from the two satellites. As a reminder, negative LOS values are away from the satellite, and positive LOS values are toward the satellite. Note that these measurements are not necessarily at the same points; for example, the maximum

128

Figure 2.94 Interpolated Deformation Rates from ENV and SNT1 at the HBGF
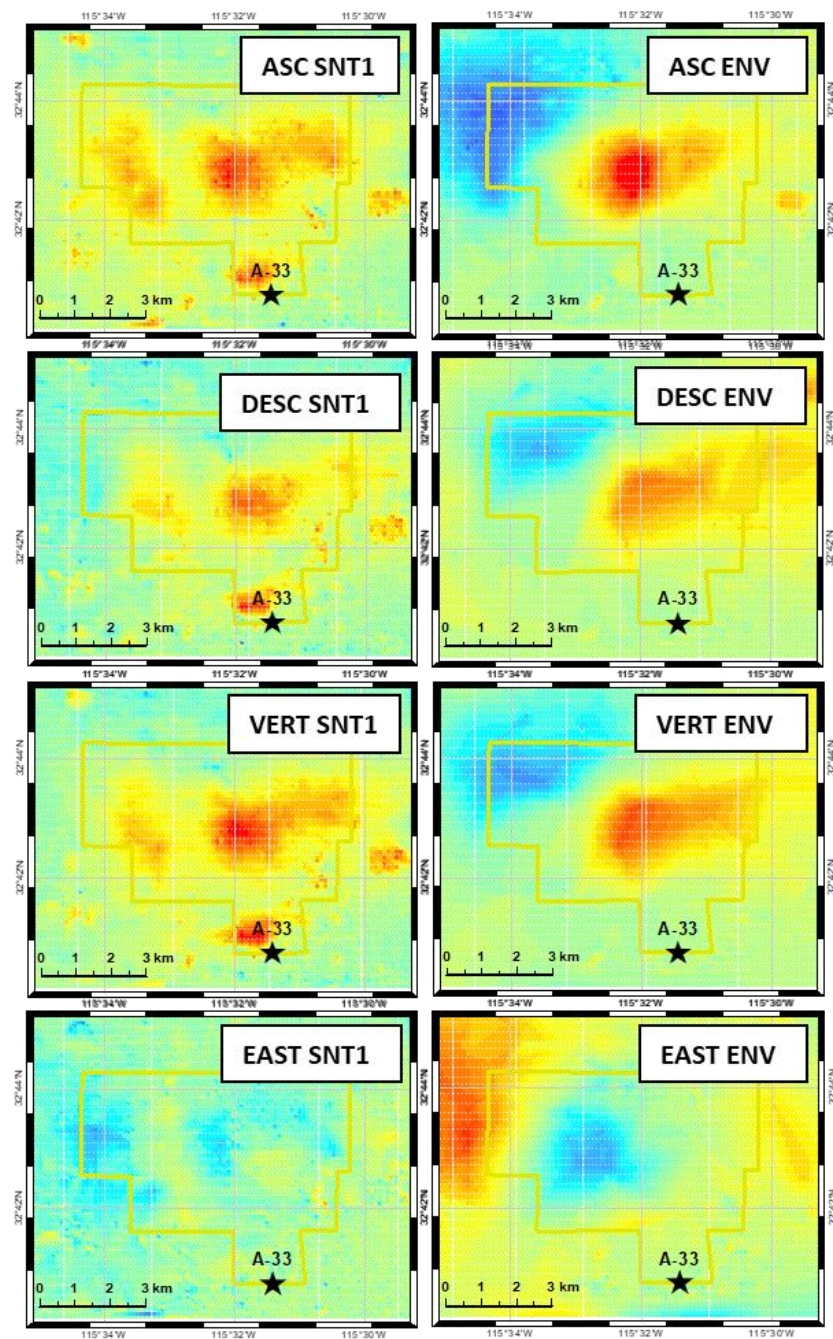
Source: M. Eneva

Table 2.21 Maximum Observed Rates at the HBGF in the ENV and SNT1 Periods

Satellite	Max Asc, mm/yr	Max Desc, mm/yr	Max Vert, mm/yr	Max East, mm/yr
ENV	-44.9; +24.3 (±4.1)	-30.7; +17.4 (±2.8)	-26.7; +18.8 (±3.1)	-29.6; +17.8 (±4.7)
SNT1	-44.1; +29.7 (±5.5)	-40.5; +4.3 (±5.5)	-38.1; +23.3 (±5.5)	-19.9; +25.9 (±3.4)

Source: M. Eneva

Figure 2.95 ENV and SNT1 Ascending Deformation Along a Profile at the HBGF
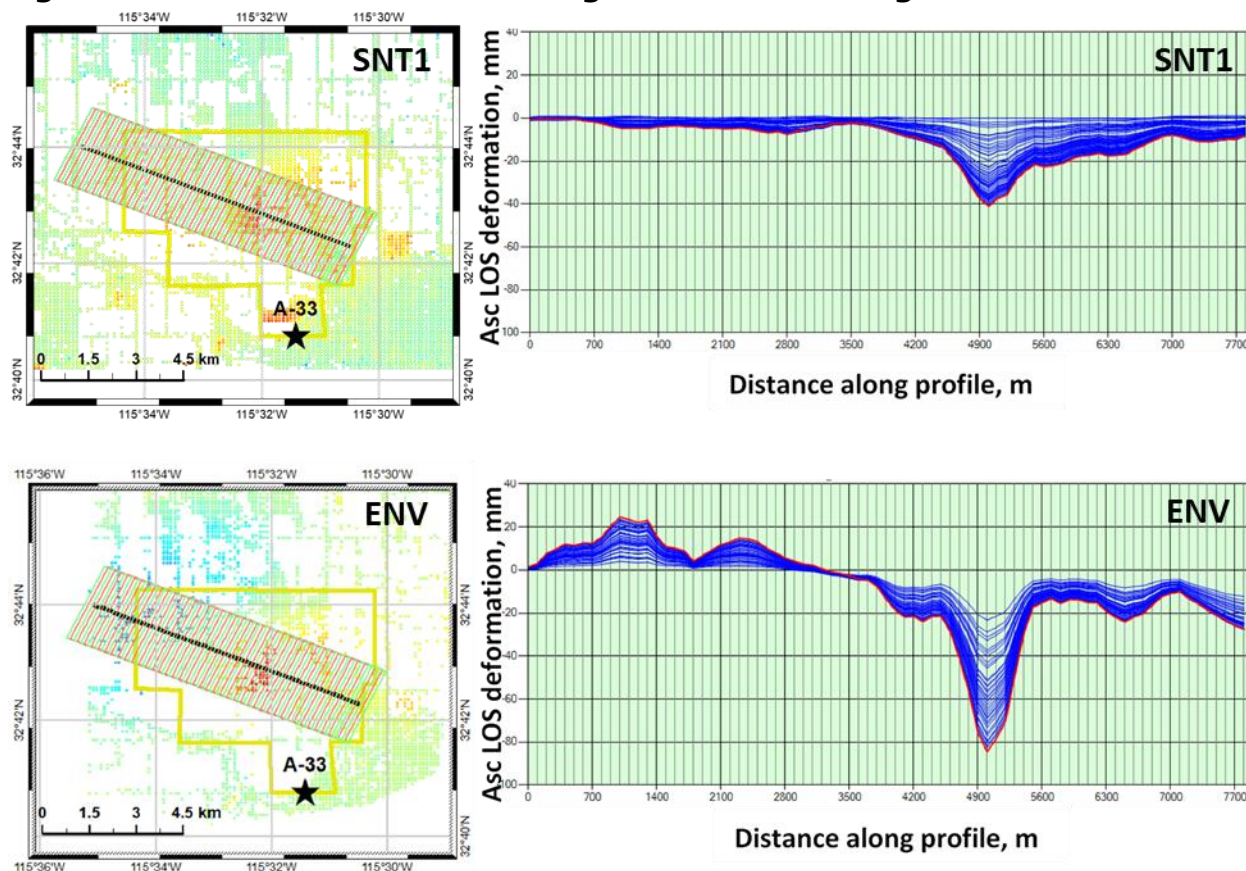
Source: M. Eneva

ascending value is not observed where the maximum vertical value is observed. In this connection, these maximum values do not always depict the true maximum values, as there may not be scatterers at the locations of the actual maximum displacements. That is, it is necessary to make a distinction between "observed" and true maximum rates. As already mentioned above, especially in the case of ENV, the maximum ascending rates are more representative of the true maximum subsidence, which can be assumed to be around −45 mm/year. Similarly, the true maximum uplift was likely around 20-25 mm/year.

Figure 2.95 shows the progression of deformation (ref. A-33) along a profile that intersects the uplift area to the northwest seen in the ENV period and the subsidence area present in both the ENV and SNT1 periods. The thickness of the profile, 2.5 km, captures more clearly the uplift and subsidence, compared with a thinner profile passing through the maximum that would enclose very few data points. This leads to smaller cumulative subsidence and uplift, as

compared with the maximum rates. Comparing the ENV and SNT1 periods, Fig. 2.95 demonstrates the absence of uplift to the northwest, as well as continuing, but reduced subsidence at the center of the field.

Another way to compare the two periods is on a pixel-to-pixel basis. Figure 2.96 displays the ENV vertical rates versus the SNT1 ones (ref. A-33), for pixels that have measurements from

Figure 2.96 Comparison of ENV and SNT1 Vertical Rates at the HBGF
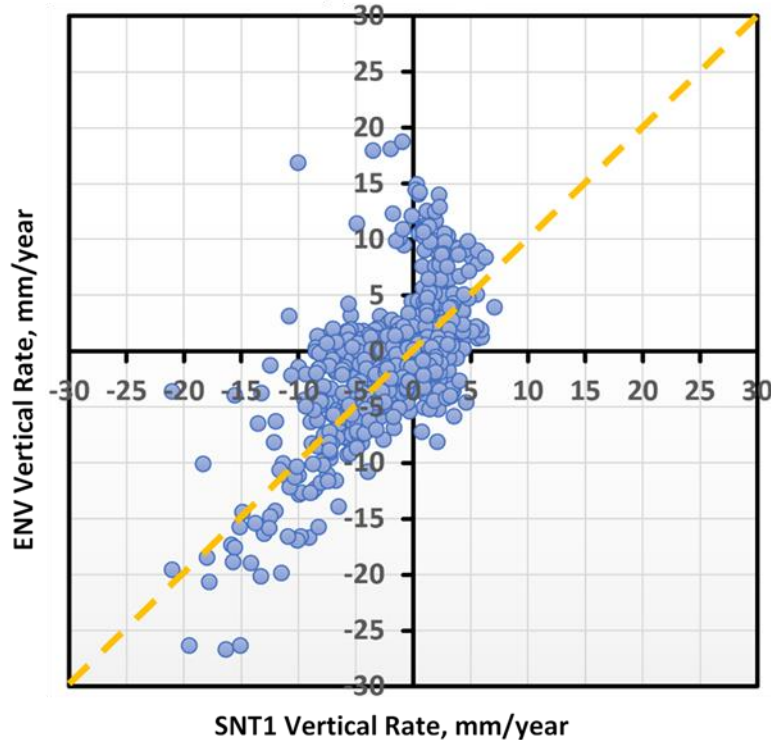
Source: M. Eneva

both periods. In this case, the comparison is from a much smaller area, of size ~45 km^2, that encloses the Heber KGRA (i.e., without extending to El Centro to the north). In that area, 734 100-m pixels have both measurements. If the measurements spanning both periods are similar, the points in Fig. 2.96 would cluster around the yellow dashed line in the plot. Some of this tendency is evident in the lower left quadrant, where the pixels with subsidence in both periods are clustered. These pixels are from the subsidence bowl in the center of the field. Still, more points are below the yellow line than above it, indicating larger subsidence in the earlier ENV period for the same pixels. In contrast, points above the horizontal axis are related to the pixels with uplift in the ENV period. Several of the points with the largest uplift in the ENV data exhibit subsidence in the SNT1 period (upper left quadrant). Other pixels that experienced uplift in the ENV period, still show uplift in the SNT1 period, but at a much lower rate (upper right quadrant); once the rates fall below +5 mm/year, they are comparable with the standard deviation (see Table 2.18).

The satellite data following the SNT1 period show yet another change in the spatial patterns of deformation at the HBGF. Figure 2.97 shows the ENV and SNT1 maps of ascending deformation rates (similar to the panels on the left in Fig. 2.93), along with the corresponding SNT2 map (ref. A-33). It is evident that uplift (blue) has reappeared in the SNT2 period,

however its location is south of the former ENV uplift, while the subsidence (red) continues more or less where it was earlier.

Figure 2.97 Ascending Deformation Rates at the HBGF (ENV, SNT1, SNT2)
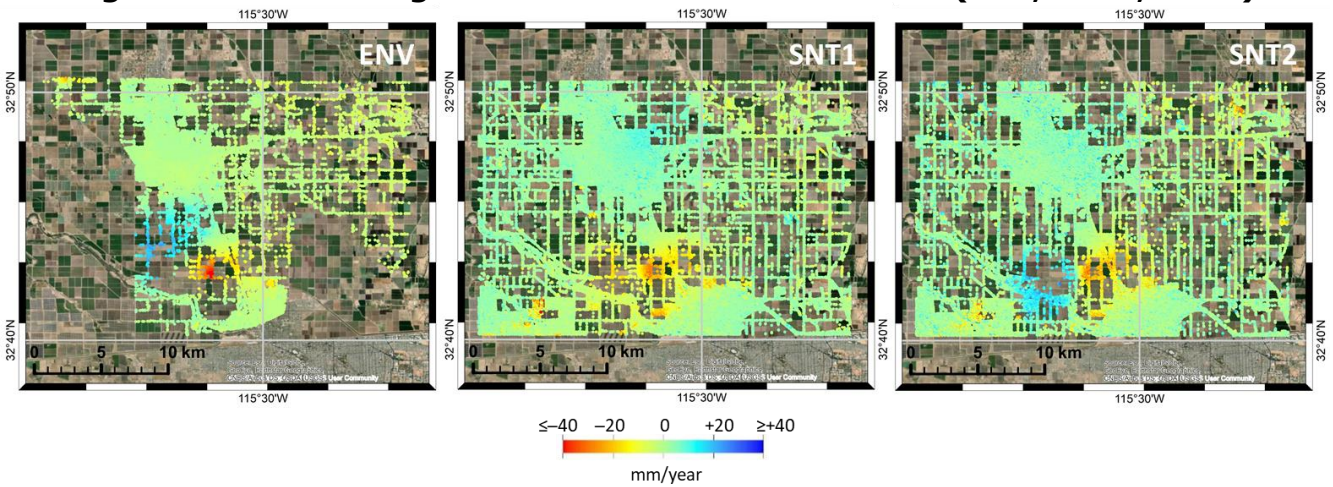
Source: M. Eneva

Furthermore, some examples of deformation time series from areas of interest (Figures 2.98 and 2.99) are shown, as well as deformation progression along profiles (Figures 2.100 and 2.101). These figures are from TRE Altamira, so the original reference point was used (see Figs. 2.51-2.53), which is to the northeast of Imperial Valley. The deformation maps so far all showed re-referenced data, using the leveling datum benchmark A-33. However, the difference is not large, as A-33's vertical rate compared with the original reference point is rather small.

Figure 2.98 Three HBGF Areas Where SNT1 Average Time Series are Calculated.

Source: TRE Altamira

132
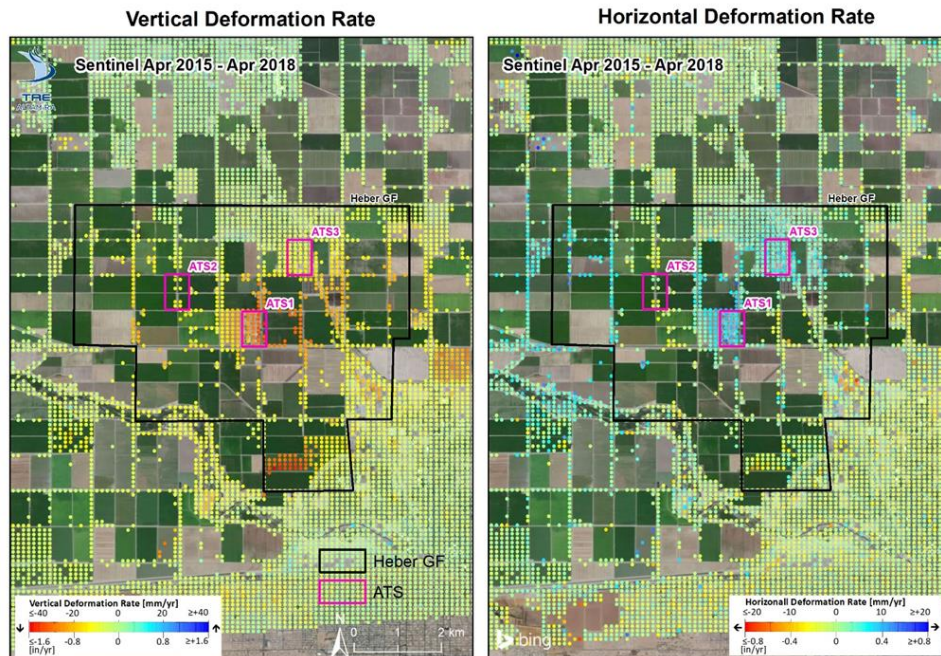
Figure 2.99 Average SNT1 Vertical and East Time Series in Three Areas at the HBGF
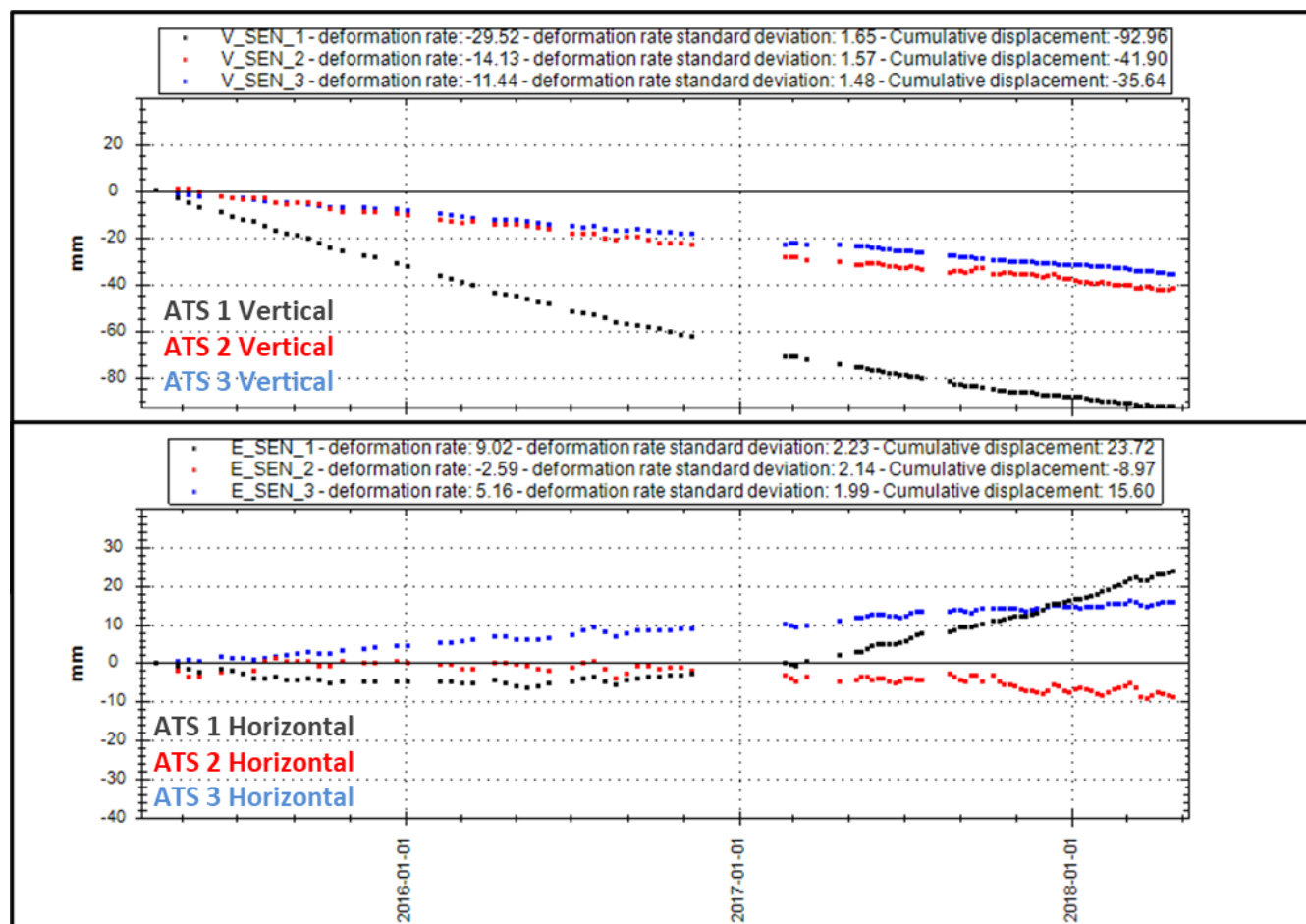
Source: TRE Altamira, modified by M. Eneva

On top of the plots in Fig. 2.99, shown are the deformation rates and their standard deviations in mm/year, as well as the cumulative displacements in mm. All rates are calculated from the slopes of lines through the points, but it is evident that not all deformation curves are linear. The area of largest subsidence (ATS1) shows decreasing rate after about Feb 2017. The east horizontal components also change around the same time. In particular, this is when significant eastward movement started in ATS1. So, the rate shown in the title, which is derived for the whole SNT1 period, actually underestimates the east deformation rate for the last year of this period (Feb 2017 – Apr 2018).

Figure 2.100 shows maps of vertical and east horizontal deformation in the SNT1 and SNT2 periods, with a profile (A-A') along which the progression of displacement is shown in Figure 2.101. The top portion of the figure indicates that the SNT1 period was characterized only by subsidence along this profile (green curves). Subsidence was also present in the SNT2 period (blue curves), but it was significantly smaller and occupied a smaller area, about 2/3 of the extent of the SNT1 subsidence. Meanwhile, the SNT1 subsidence in the western 1/3 of the profile turned into SNT2 uplift. There are corresponding changes in the east horizontal

133

Figure 2.100 Vertical and East Rates at the HBGF for the SNT1 and SNT2 Periods
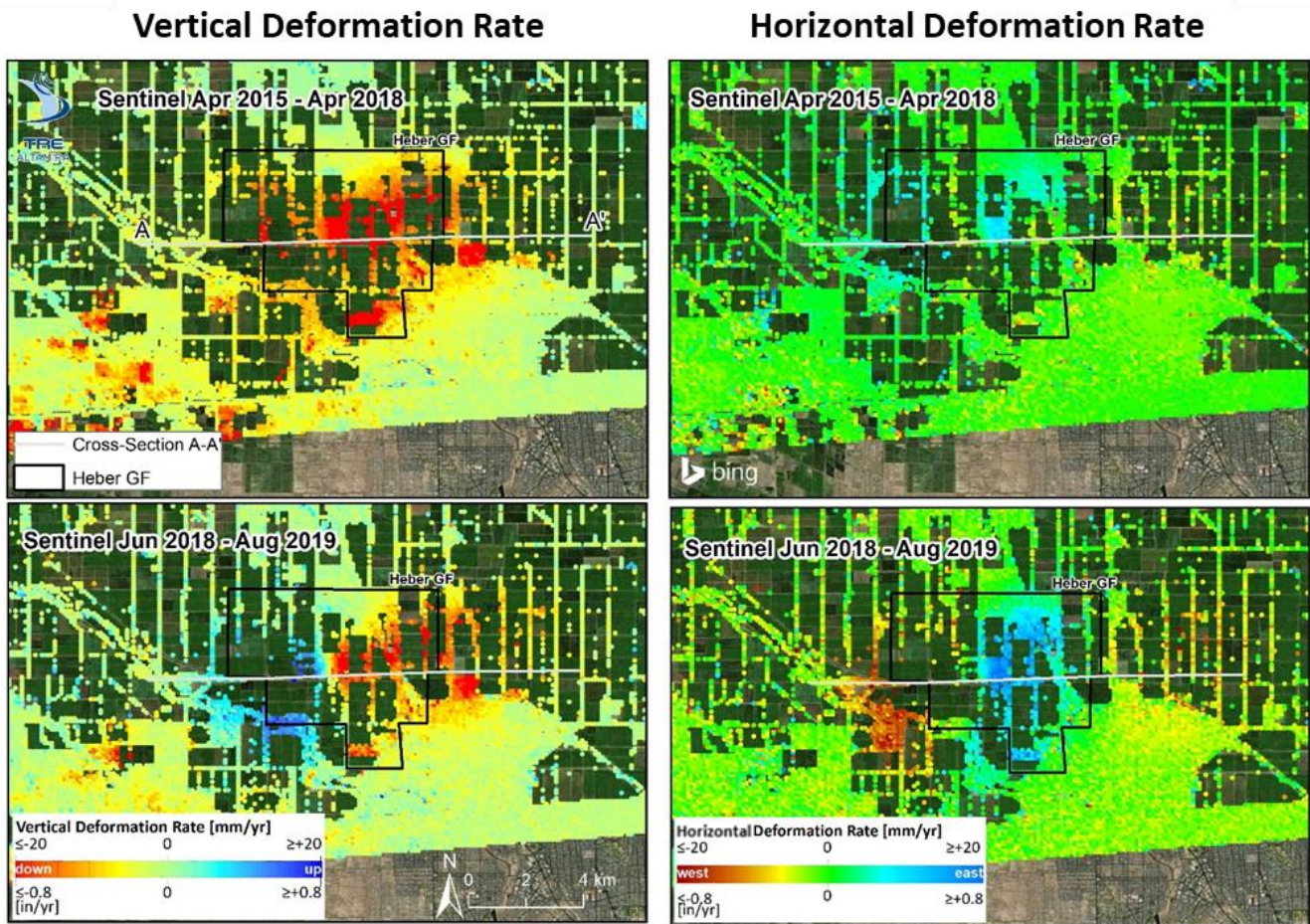
Source: TRE Altamira

component as well (bottom plot in Fig. 2.101). In the SNT1 period (green curves), eastward movement took place in the western half of the subsidence bowl, while westward displacement was observed in the eastern half; this is the normal interplay between vertical and east horizontal deformation in the opposing sides of a subsidence area. In the SNT2 period, the changes in the pattern of vertical deformation led to westward displacement on the western flank of the uplift, and to eastward movements on the western edge of the SNT2 subsidence. Unlike the significant difference in the magnitude of vertical SNT1 and SNT2 movements (top panel), the horizontal displacements in the two periods are more comparable in size.

Another confirmation of the above is that the SNT1 and SNT2 maximum observed deformation rates (re. the original ref. point) are as follows: subsidence −47.2 mm/year (SNT1) vs. −31.5 mm/year (SNT2); uplift 4.1 mm/year (SNT1) vs. 20.5 mm/year (SNT2); eastward 17.8 mm/year (SNT1) vs. 23.5 mm/year (SNT2); and −19.4 mm/year (SNT1) vs. −16.8 mm/year (SNT2).

Figure 2.101 Deformation Progression at the HBGF in the SNT1 and SNT2 Periods
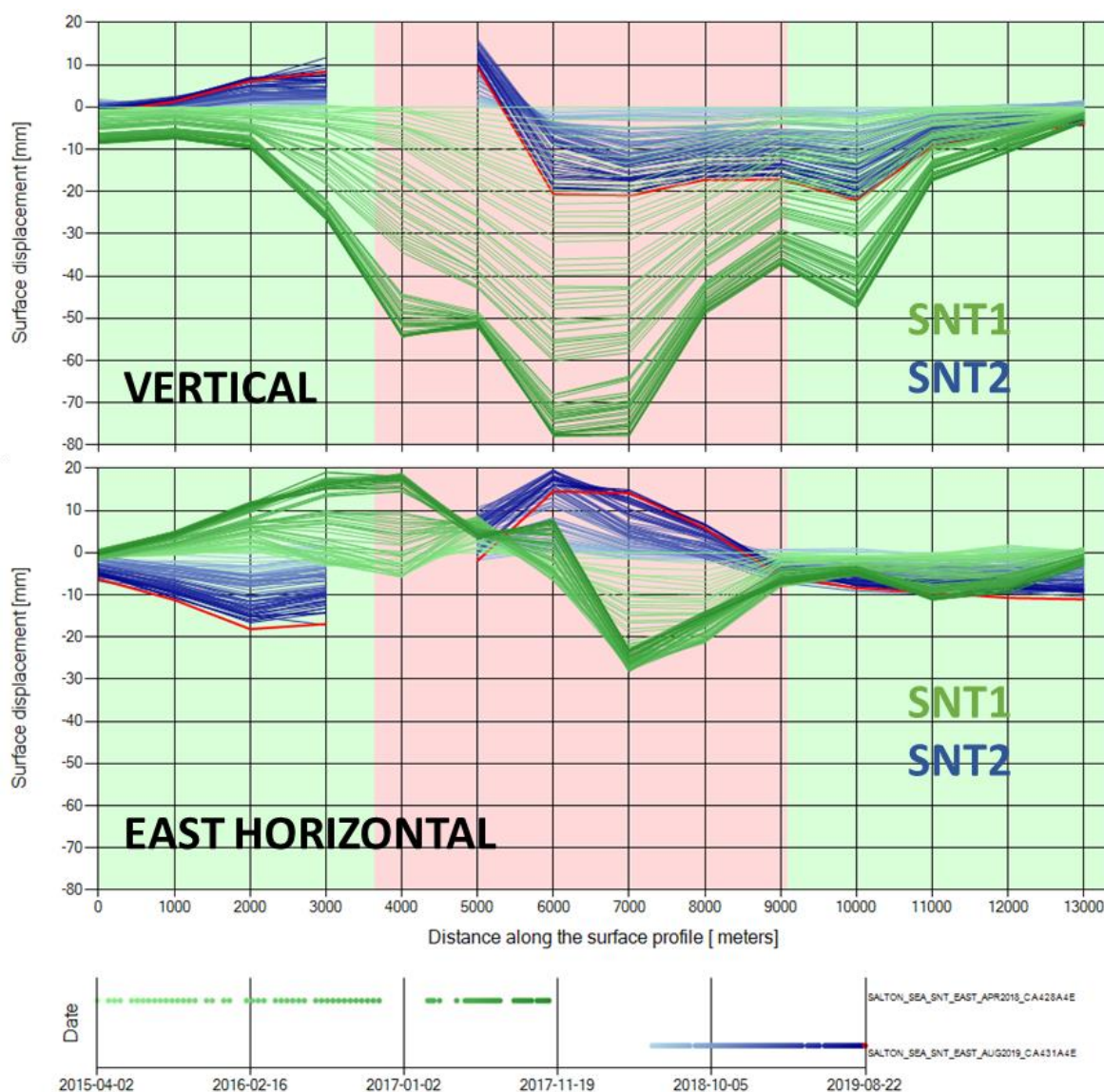
Source: TRE Altamira, modified by M. Eneva

As previously noted for the NBGF, it is usually assumed that surface deformation should not be observed around binary plants, because of the almost 100-percent reinjection of the produced fluids. The results for the HBGF show once again that this is not the case. Instead, both subsidence and uplift were observed that change dynamically with changes in production and injection. The maximum subsidence rate is comparable with that from the SSGF (Eneva et al., 2014 and Section 2.2.3), where only flash plants are installed. Even in that case, the reinjection is pretty high, at 82 percent on average. While such rates of surface deformation may appear high, the displacements would have been significantly larger without such significant levels of reinjection. This is exemplified by the Cerro Prieto geothermal field, to the south in Mexico, where a reinjection strategy is either absent or insufficient, and the maximum subsidence is much larger, at −170 mm/year in a recharge area next to the field, and −110 mm/year in the producing area (Sarychikhina et al., 2011, 2018).

2.2.6 Comparison of Surface Deformation Rates Derived from InSAR and Leveling Surveys in Imperial Valley

In the previous sections, some comparisons were already illustrated between leveling survey measurements and InSAR observations in the vicinities of benchmarks. s is shown here. Table 2.22 shows a systematic comparison for all possible paired measurements, in terms of mean differences between the two types of rates and their standard deviations.

Table 2.22 Differences Between Vertical InSAR and Leveling Rates in Imperial Valley

Location	Surv /Sat	Time intervals	Mean difference, mm/year	95% conf. accuracy, mm/year	Number of surveys	Number of benchmarks	Number of InSAR points in time series
Salton Sea-CalEnergy	S ENV	Jun 2004 – Feb 2011 Aug 2005 – Sep 2010	0.9 ±0.7	7.2	7	49 of 81	23 (30 A, 40 D)
Salton Sea-CalEnergy	S ENV	Jun 2004 – Mar 2010 Aug 2005 – Nov 2009	1.0 ± 0.8	8.7	6	48 of 80	18 (25 A, 34D)
Salton Sea-CalEnergy	S SNT 1	Mar 2015 – Nov 2018 Apr 2015 – Apr 2018	6.7 ± 1.2	18.5	4	44 of 113	48 (60 A, 51 D)
Salton Sea-CalEnergy	SNT 2	Nov 2017 – Sep 2019 Jun 2018 – Aug 2019	2.8 ± 0.7	14.0	2	82 of 110	36 (37 A, 40 D)
Salton Sea-CalEnergy	S TSX	Mar 2012 – Mar 2014 Sep 2012 – Sep 2013	-2.1 ±0.4	7.4	3	104 of 108	9 (17 A, 15 D)
Salton Sea-Energy Source	S SNT 1	Nov 2014 – Nov 2018 Apr 2015 – Apr 2018	1.8 ± 0.6	11.8	5	65 of 93	48 (60 A, 51D)
Heber	S ENV	Feb 2006 – Nov 2010 May 2006 – Sep 2010	2.2 ± 0.5	7.3	5	74 of 137	25 (34 A, 30D)
Heber	S SNT 1	Dec 2014 – Jan 2018 Apr 2015 – Dec 2017	1.6 ± 0.3	8.3	4	126 of 129	38 (50 A, 41D)

136

Location	Surv /Sat	Time intervals	Mean difference, mm/year	95% conf. accuracy, mm/year	Number of surveys	Number of benchmarks	Number of InSAR points in time series
Heber	S SNT 2	Dec 2016 – Aug 2019 Jun 2018 – Aug 2019	2.4 ± 0.5	10.4	3	115 of 127	36 (37 A, 39 D)
North Brawley	S TSX	Oct 2012 – Oct 2013 Oct 2012 – Sep 2013	-3.3 ± 1.1	14.5	2	75 of 75	8 (15 A, 12 D)

Columns from left to right: "S" marks surveys; ENV, TSX, SNT1, SNT2 mark the various satellite periods; time intervals compared from the surveys and the satellites; mean differences between subsidence rates derived from InSAR and the leveling surveys; 95th percentile of the absolute values of the differences; number of surveys used to calculate rates within the survey periods shown in the second column; number of stations, for which InSAR vertical measurements within 200 m were observed, out of all stations for which leveling rates could be calculated in that period; and number of points in the InSAR time series, from which the vertical rates are calculated, followed by the numbers of ascending (A) and descending (D) scenes in parentheses. Rows highlighted in gray are for periods shown in subsequent figures.

Source: M. Eneva

Figure 2.102 Vertical InSAR vs. Leveling Rates at the SSGF, CalEnergy Units
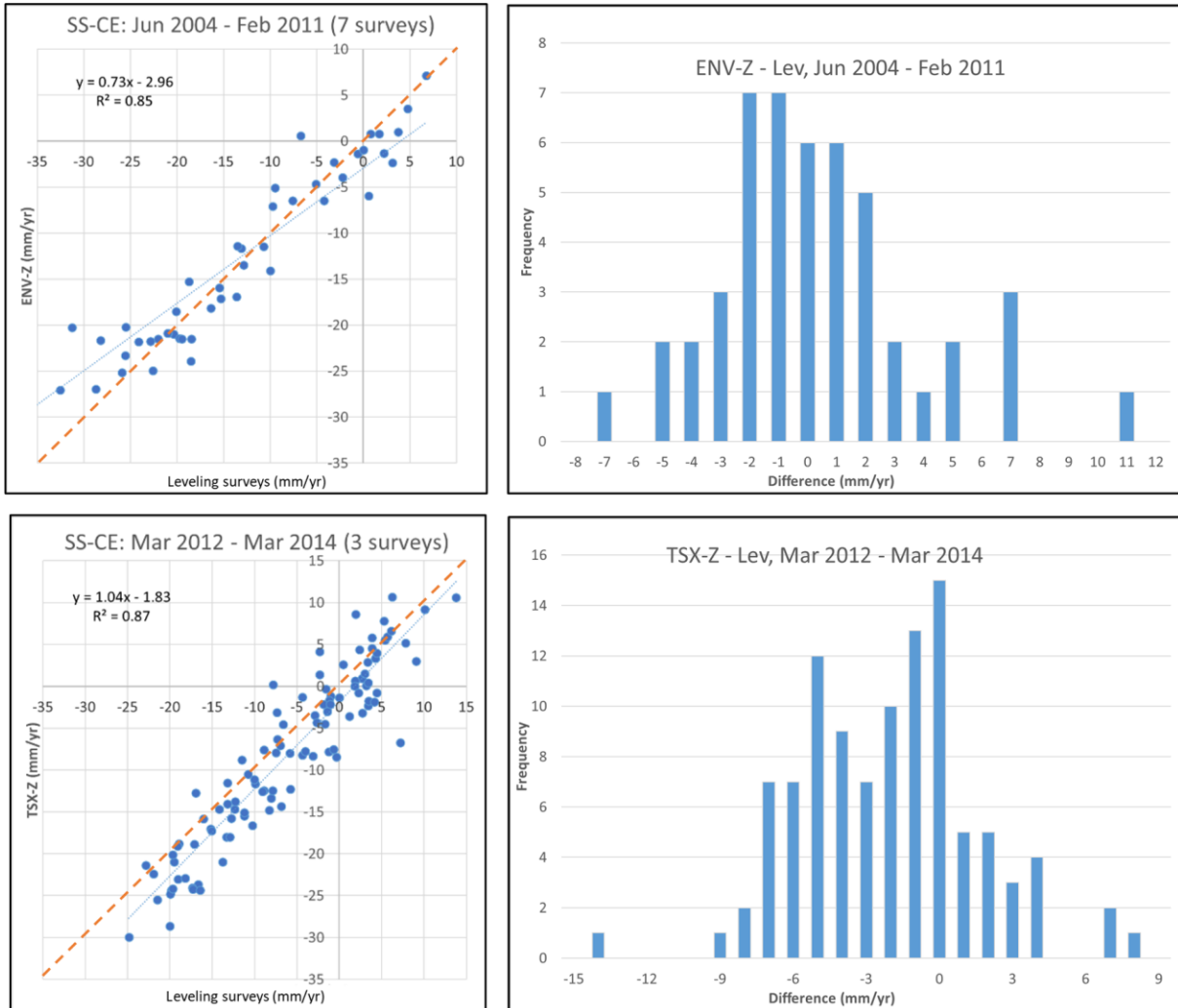
Left – examples of scatter plots for two periods, as indicated: right – corresponding histograms. The dotted blue lines indicate the best linear fit to the data, with corresponding equations shown in the scatter plots. The dashed red lines show where the points in the scatter plots would be positioned if the survey and InSAR rates were identical.

Source: M. Eneva

The InSAR results are re-referenced in each case to the locations of the individual datum benchmarks used in the surveys (S-1246 for the SSGF-CE and SSGF-SE; Y-1225 for the NBGF, and A-33 for the HBGF). The InSAR rates are calculated as averages from the vertical measurements within 200 m from the benchmarks. This distance does not have a special meaning – it is a compromise between being close enough to the benchmarks, yet including a representative number of InSAR vertical measurements. The highlighted rows in Table 2.22 are for differences shown in scatter plots and histograms in Figures 2.102-2.104. The scatter plots also show lines and their equations from the application of a least-squares linear fit. Some satellite periods are with very few, or even no surveys at the same time, so comparisons either cannot be made, or rates are calculated from only two or three surveys, with the understanding that such rates are less reliable. Therefore, in order to use data from a few

more surveys, the survey periods are sometimes quite longer than the satellite periods. Also, in Imperial Valley, not all benchmarks have InSAR measurements within 200 m, despite of

Figure 2.103 Vertical InSAR vs. Leveling Rates at the SSGF-ES and NBGF
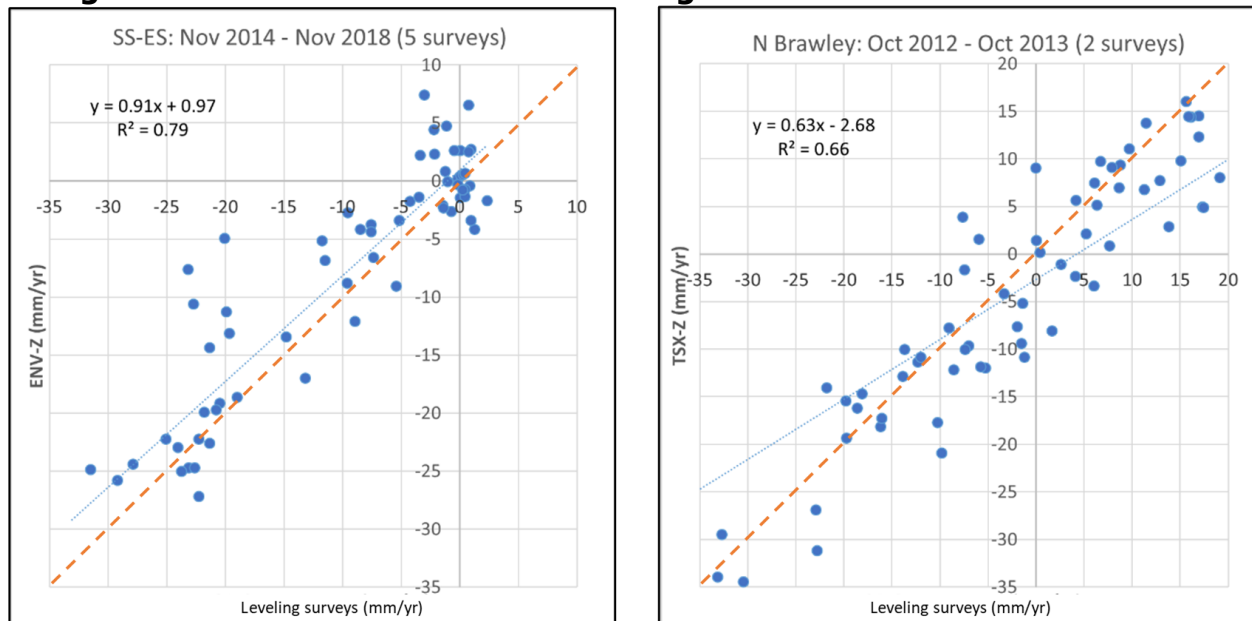
Source: M. Eneva

identifying thousands of PS/DS points, because there are gaps in coverage in the agricultural areas. If corner reflectors are strategically installed in the future, most, or even all, benchmarks could have InSAR measurements in their vicinities.

Compared with the Coso geothermal field (Table 2.8 and Fig. 2.25 in Section 2.1.3.2), the results for the Imperial Valley are more variable and scattered, which is not surprising in view of the agricultural environment and lack of LOS measurements near benchmarks. Figure 2.102 shows examples of comparisons of survey rates with ENV and TSX vertical rates for the SSGF-CE (CalEnergy units of the SSGF). Table 2.22 shows that in those cases 95 percent of the absolute differences are below 7.2 and 7.4 mm/year, respectively, with a tendency for the TSX rates to show larger subsidence, by about −2.1 mm/year on average, than the rates from three leveling surveys encompassing the TSX period. The mean difference of 6.7 mm/year is significantly larger for the SNT1 period (Table 2.22), which cannot be explained at this time, other than with the smaller number of surveys compared with the ENV period. It is worse even than the mean difference in the SNT2 period (2.8 mm/year), but the scatter, as measured with the 95-percent limit, is significantly larger in both SNT periods (18.5 mm/year for SNT1 and 14.0 for SNT2). Figure 2.103 displays examples of scatter plots for the SSGF-ES (EnergySource part of the SSGF) and the NBGF, in the ENV and TSX periods, respectively. The mean differences are rather small, 1.8 mm/year and −3.3 mm/year, respectively, but the scatter is significant (11.8 mm/year and 14.5 mm/year for 95 percent of the absolute differences). Figure 2.104 shows results from the HBGF for the ENV, SNT1 and SNT2 periods. The InSAR vertical rates are by 1.6 to 2.4 mm/year larger than the survey rates (i.e., showing smaller subsidence), and 95 percent of the absolute values of the differences fall within 7.3 to 10.4 mm/year (Table 2.22).

Figure 2.104 Vertical InSAR vs. Leveling Rates at the HBGF
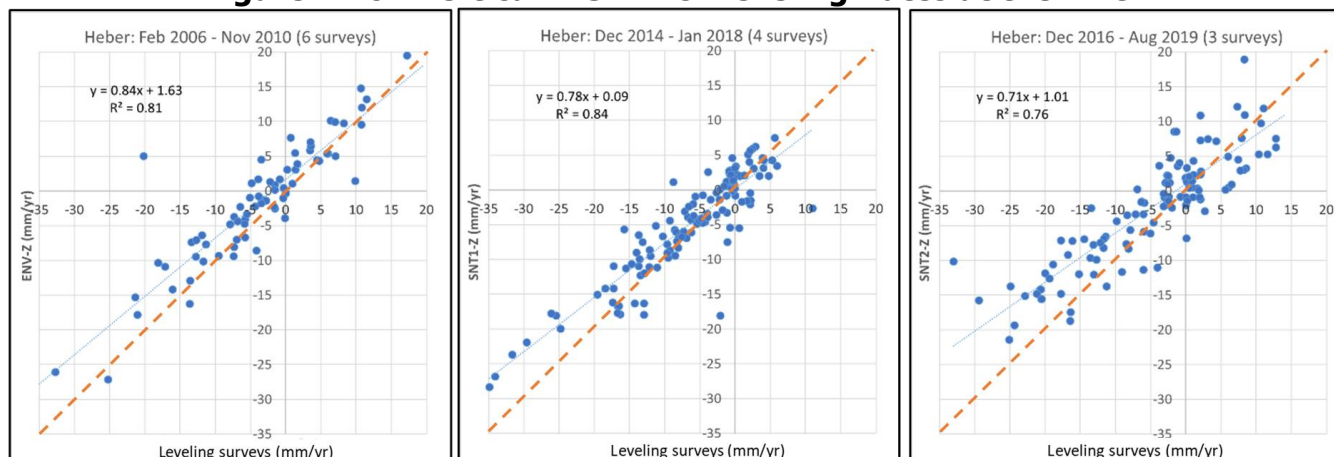
Source: M. Eneva

The results of these comparisons indicate that for the most part, the two types of measurements agree reasonably well with each other. However, there are some systematic biases, and the scatter is sometimes substantial, limiting the conclusions for individual benchmarks, especially for the SNT1 period at the SSGF-CE. Still, on average, the differences are small enough that the overall spatial patterns of surface deformation derived from InSAR and the ground-based surveys should be similar.

As a reminder, because vertical decomposition is only possible when both types of PS/DS points are identified (descending and ascending), there is loss of information due to ignoring all the numerous LOS measurements when they are of only one type. In particular, in Imperial Valley there are many areas where ascending PS/DS are more abundant than the descending ones, so in the future, it may be better in such cases to stay with the LOS measurements and convert the leveling measurements to that LOS direction for comparison purposes. This would identify much more InSAR rates (e.g., ascending LOS rates) within 200 m of the benchmarks, providing a more complete basis for comparison.

A study from the Department of Water Resources/California Natural Resources Agency, for which TRE Altamira Inc. provided InSAR measurements, compared InSAR deformation with measurements from continuous GPS in more than 200 groundwater basins in California (*InSAR Data Accuracy for California Groundwater Basins*, 2019). The conclusion was that InSAR using Sentinel data in the period Jan 2015 – Jun 2018 measured vertical displacement in California within 16-mm accuracy, at the 95-percent confidence level. The report stated that this is valid for the state-wide data set, and results may be different for regional and localized area data subsets. Obviously, the annual surveys here are very different in collection frequency compared with the continuous GPS used in that study. However, the accuracy stated is comparable with the numbers listed in the fourth column of Table 2.22 above (95th percentile of the absolute differences). Comparisons with continuous GPS stations were not made, because they are outside the geothermal fields studied here.

2.2.7 Financial Considerations

The main advantages of InSAR are that it is cost-effective (covering large areas at a time), provides deformation time series and deformation rates at tens of thousands to hundreds of thousands of locations, and current satellite revisits are every 6 days leading to tens of

measurements per year at each point. In contrast, four traditional leveling surveys are done once per year at each of the geothermal fields in Imperial Valley, with two separate surveys at the SSGF (for CalEnergy and EnergySource). The surveys use several tens of benchmarks per field, occasionally more than 100 (see Table 2.22). In terms of temporal coverage, the continuous GPS technology is superior to InSAR, but there is only one such station (P507) in proximity to SSGF.

Table 2.23 compares costs associated with InSAR and the leveling surveys in Imperial Valley. The available information about the cost of the annual leveling survey covering the CalEnergy units of SSGF is $55,000. This cost was cited during a personal communication in the period 2011-2014, in connection to a previous project of Imageair Inc. with the California Energy Commission. Admittedly, this citation is old, but a current one is not available. In the absence of information about the annual leveling costs of Energy Source for the northeastern part of SSGF, and of Ormat for NBGF and HGF, the above annual cost estimate is used for each of the four surveys.

TRE Altamira cited the InSAR costs in 2020. They include the processing of satellite data that TRE Altamira would do, which can be accompanied by a report. These costs do not include the additional data analysis by Imageair Inc. as reported in Sections 2.2.1 – 2.2.6.

Table 2.23 Comparison of InSAR and Leveling Surveys Costs in Imperial Valley

Attribute	InSAR	Leveling Surveys
Number of surveyed points	Tens to hundreds of thousands per geothermal field	Tens of points, up to less than 150, per geothermal field
Number of times measured per year	Every 6 days (~ 60 times per year)	Once per year
Cost to cover all three fields, one-time measurement	$45,000	Estimated $220,000 = $55k per annual survey, for four surveys
Annual cost for all three fields, if measurements are done once per year	$36,000 (=$45k – 20% discount)	Same as above
Annual cost for all three fields, if measurements are done twice per year	$57,600 (=2 x $36k – additional 20% discount)	Not done; maybe double the above, with some discount

As Table 2.23 shows, InSAR is significantly more cost-effective than the leveling surveys, but this does not mean that surveys should not be performed. Such decisions are left to the geothermal operators, given the results presented in this report.

As previously explained, although the number of locations for which InSAR provides deformation time series is many orders of magnitude larger than the number of benchmarks used in the leveling surveys, there are locations with benchmarks where InSAR observations

are missing. This is especially valid in agricultural areas like Imperial Valley. The remedy is to install corner reflectors in strategic locations of interest. As an example of one-time cost, in 2020 the project team received a quote from TRE Altamira for $37,000 for 20 corner reflectors, including materials, shipment, travel to the site, and installation labor. Again, geothermal operators are the ones who would determine the best locations for corner reflectors, as well as their optimal number.

CHAPTER 3: Professional Presentations and Outreach Activities

3.1 Presentations at Professional Meetings and Papers in Meeting Proceedings

The results of this project were presented by M. Eneva (Imageair Inc.) at the annual meetings of the Geothermal Resources Council (GRC) and the annual Stanford Geothermal Workshops (SGW), as follows: for Coso at GRC 2018, North Brawley at GRC 2019, Heber at SGW 2019, and comparisons of vertical rates from InSAR and ground-based surveys in all studied fields at SGW 2020. The following papers were published in the proceedings of these meetings:

- Eneva, M., A. Barbour, D. Adams, V. Hsiao, K. Blake, G. Falorni, and R. Locatelli. 2018. Satellite observations of surface deformation at the Coso geothermal field, California. Geothermal Resources Council Transactions 42, 1383-1401.

- Eneva, M., D. Adams, V. Hsiao, G. Falorni, and R. Locatelli. 2019. Surface deformation at the Heber geothermal field in southern California. Proceedings of the 44th Workshop on Geothermal Reservoir Engineering, Stanford University, Stanford, California, February 11-13, 2019, SGP-TR-214.

- Eneva, M., D. Adams, G. Falorni, and M. Shumski. 2019. Surface deformation and seismicity at the North Brawley geothermal field in southern California. Geothermal Resources Council Transactions 43, 767-783.

- Eneva, M., D. Adams, K. Blake, V. Hsiao, and G. Falorni. 2020, Comparison of surface deformation rates from InSAR and ground-based surveys in geothermal fields of California. Proceedings of the 45h Workshop on Geothermal Reservoir Engineering, Stanford University, Stanford, California, February 10-12, 2020, SGP-TR-216.

Furthermore, A. Barbour (USGS) and K. Blake (U.S. Navy GPO) submitted two papers for the proceedings of the World Geothermal Congress that featured results from this project. The congress was going to be held in April 2020, but due to the pandemic was postponed. The papers are as follows:

- Barbour, A. 2021. Induced seismicity and deformation at geothermal fields in California, USA. *Proceedings World Geothermal Congress 2020+1, Reykjavik, Iceland, April-October 2021* (submitted October 2019). Available online at: http://www.geothermal-energy.org/pdf/IGAstandard/WGC/2020/06005.pdf

- Blake, K., A. Sabin, M. Eneva, S. Nale, M. Lazaro, A. Tiedeman, D. Meade, W.-C. Huang, D. Fujii, and J. Zimmerman. 2021. Updated shallow temperature survey, resource evolution and preliminary conceptual geologic model for the Coso geothermal field. *Proceedings World Geothermal Congress 2020+1, Reykjavik, Iceland, April-October 2021* (submitted October 2019). Available online at: http://www.geothermal-energy.org/pdf/IGAstandard/WGC/2020/12197.pdf

In addition, A. Barbour (USGS) delivered talks at several professional meetings. Two of his PowerPoint presentations can be found at the following links:

- Barbour, A. J., R. Skoumal, and A. Crandall-Bear. 2019. Slow deformation and rapid seismicity-rate changes triggered by geothermal fluid redistribution. Proceedings of the Third Schatzalp Workshop on Induced Seismicity, Davos, Switzerland, 5-8 Match, 2019. Available online at http://www.seismo.ethz.ch/export/sites/sedsite/research-and-teaching/.galleries/pdf_schatzalp/Schatzalp_2019_Talk46_Barbour.pdf .
- Barbour, A. 2019. Preliminary analysis of the seismicity development at the Heber geothermal field, https://onedrive.live.com/view.aspx?resid=A98D6DD5A47E43C7!324&ithint=file%2cpptx&authkey=!AKhTFDSHr_PvPX4.

Finally, M. Eneva gave two professional presentations early in the project (March 2018) at the:

- U.S. Navy GPO office in China Lake, CA
- Coso Operating Company (COC) located in the Coso geothermal field.

3.2 Outreach Activities to Non-Professional Audiences

In addition to the professional papers and presentations, the project team either gave talks, or provided material for the talks of others, aimed at reaching non-professional audience.

1. In March 2018, M. Eneva and D. Adams joined the U.S. Navy GPO in several presentations in front of high-school students at the Burroughs High School, in Ridgecrest, CA, during the school STEM Day (Science Day). The GPO had routinely participated in such activities as part of their outreach to the community. Kelly Blake was in charge of GPO's involvement. M. Eneva provided slides featuring early project results for the Coso geothermal field to complement K. Blake's PowerPoint presentation. The STEM Day was organized in such a way that different groups of students went from one classroom to another, and heard different scientific presentations. There were nine consecutive groups throughout the day. In eight of the presentations, M. Eneva pitched in to talk about the InSAR results, and D. Adams did it in one of the presentations. The students showed a lot of interest and asked questions. This was a good practice for other outreach activities planned later in the project.

2. In the fall of 2018, the GPO participated in another STEM Day at the same school. Kelly Blake included results from the project in her presentation.

3. In March 2019, M. Eneva prepared and gave a presentation in front of students and professors at Mesa College, San Diego (CA). The talk started with information on renewable energy in general, then provided more details about geothermal energy in particular. After this introductory part, some results from the project were illustrated and discussed.

4. In October 2019, D. Adams delivered the same presentation as in (3) in front of students at Cuyamaca College in San Diego (CA).

5. In November 2019, M. Eneva prepared and delivered a presentation at San Diego State University – Imperial Valley campus, in Calexico (CA). This talk was similar to the talks in (3) and (4) above, but was tailored more to the interests of the local students that were not with technical background. Also, the talk included more substantial information on Imperial Valley in particular, where these students live and study.

6. Finally, M. Eneva had the idea to distribute geothermal posters in English and Spanish to high schools in Imperial County, CA. She saw these posters for the first time at the

Geothermal Resources Council (GRC) meeting in the fall of 2019. The posters were created by Dewhurst Group LLC (Figure 3.1) and were supplied by the GRC. Even though these posters feature geothermal energy in general, it was deemed beneficial to distribute them as a contribution to the STEM education in Imperial County. For this purpose, M. Eneva identified the names of high school science teachers and their addresses. However, students started home schooling due to the pandemic, so the mailing of the posters remained to be done after the end of the project.

Figure 3.1 Geothermal Poster in English and Spanish

Source: Dewhurst Group LLC
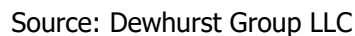
CHAPTER 4: Conclusions and Recommendations

A state-of-the art InSAR technique, SqueeSAR, was applied to process satellite radar scenes collected over four geothermal fields in California – Coso in the eastern part of central California, and three fields in the Imperial Valley of southern California (Salton Sea, North Brawley, and Heber). This type of satellite data processing makes it possible to detect surface deformation at numerous locations, even in agricultural areas like those in Imperial Valley where earlier InSAR techniques had not work. The processing results consist of deformation time series and rates (in mm/year) in each individual location. They make it possible to examine average time series within areas and along profiles of interest, as well as progression of deformation in time along profiles. For the most part, the SqueeSAR results agreed well with ground-based measurements at the geothermal fields. However, any InSAR technique, when it works, has several advantages over ground-based measurements, such as: (1) large-area coverage at once (which makes it more cost-effective than the surveys); (2) observations multiple times per year (as opposed to only annually or less frequently for the surveys); and (3) dense spatial coverage (deformation measurements at thousands of locations compared with only tens of ground stations or benchmarks). Details in space and time like these made it possible to better identify and characterize dynamic variations in surface deformation associated with changes in production and injection. For example, decreasing subsidence was observed as production decreased at Coso and North Brawley, subsidence transforming into uplift with increasing injection and subsequent redistribution of subsidence and uplift areas at Heber, and relatively steady subsidence at Salton Sea due to stable ongoing production.

Seismicity was also examined in these geothermal fields and association was observed between the locations of maximum subsidence and microearthquake clusters, some connections with production and injection, and changes in surface deformation caused by moderate earthquakes on the territories of two Imperial Valley geothermal fields and a large earthquake outside the Coso geothermal field.

The study area in Imperial Valley in particular, is very complicated, with interplay of numerous factors, such as significant regional and local tectonic movements, earthquakes, aseismic events, anthropological changes due to the operating geothermal facilities, and substantial agriculture. Therefore, despite some limitations encountered in this work, the project results are the best that have ever been obtained in this region, and in such a complex environment.

In summary, the project findings indicate the need for further monitoring of surface deformation so that geothermal operators and regulators may better understand and prepare for subsidence and uplift likely to occur at new developments over time. It is worth noting that the rates of subsidence in the fields studied here are significantly lower than those at a neighboring geothermal field, Cerro Prieto, in Mexico, where reinjection is not performed to the extent it occurs in the California facilities. As a consequence, the maximum rates of subsidence at Cerro Prieto are up to six times higher than those at the California's KGRAs. The project observations also indicate the presence of some induced seismicity from geothermal operations that also needs continued monitoring.

Based on the results of this work, the project team has the following recommendations:

- *Reservoir management and mitigation of environmental impact.* It is imperative that geothermal operators and regulators get acquainted with the capabilities of InSAR and incorporate such types of measurements, along with attention to induced seismicity, in reservoir management and field operations. For example, compared with annual (or rarer) ground-based surveys, InSAR is capable of identifying changes in surface deformation much faster, and possibly with more spatial details, which may signal undesirable effects of particular locations and amounts of production and injection. While this can help with the field operations, mitigation of environmental impact is also facilitated with InSAR, as it may be particularly important in some areas, such as agricultural fields. In addition, the measurements that this project provided for four geothermal fields can be used as a reference point for future monitoring activities.

- *Attention to the results of this project in view of future geothermal developments.* It would be prudent to view the maximum subsidence (up to 50 mm/year) observed in the currently operating fields, with an eye to the future. If 1,700 MW additional geothermal capacity gets developed in the extended Salton Sea area, as previously proclaimed, it is important to keep in mind that the current power production in Imperial Valley that is three times lower, is already associated with substantial surface deformation and induced seismicity.

- *Enhancement of InSAR capabilities.* For all its advantages, the technique applied did show some limitations in the agricultural areas of Imperial Valley. Although the density of locations at which deformation measurements are possible is by orders of magnitude larger than the number of leveling benchmarks, there were some areas, where deformation could not be measured. This limitation could be improved on, or eliminated, if corner reflectors are installed in known areas of interest where previous satellite observations could not identify deformation. Corner reflectors are relatively small structures that once installed, would always reflect radar signals back to the satellites, playing the role of artificial PS points in all future satellite data acquisitions. They do not require a power source or any maintenance after installation, and the only way for them to cease functioning are acts of vandalism, or any other deliberate removal. Areas suitable for installation of corner reflectors may be around specific wells, locations of benchmarks and GPS stations, bridges, within agricultural fields, or areas prone to snow in the winter.

REFERENCES

Allison, M. L. 1990. Remote detection of active faults using borehole breakouts in the Heber geothermal field, Imperial Valley, California. Geothermal Research Council Transactions, 14, 1359-1364.

Ayling, B. and the Fallon FORGE team (36 co-authors). 2018. Phase 2 update for the Fallon FORGE site, Nevada, USA. Proceedings: 43rd Workshop on Geothermal Reservoir Engineering, Stanford University, Stanford, CA, February 2018, SGP-TR-213.

Barbour, A. J., E. L. Evans, S. H. Hickman, and M. Eneva. 2016. Subsidence sates at the southern Salton Sea consistent with reservoir depletion. Journal of Geophysical Research, Solid Earth, 121(7), 5308–5327, doi: 10.1002/2016JB012903

Barbour, A. J., R. Skoumal, and A. Crandall-Bear. 2019. Slow deformation and rapid seismicity-rate changes triggered by geothermal fluid redistribution. Proceedings: 3rd Schatzalp Workshop on Induced Seismicity, Davos, Switzerland, 5-8 Match, 2019; available online at http://www.seismo.ethz.ch/en/research-and-teaching/schatzalp-workshop/download-2019/ (last accessed Oct 2019).

Barbour, A. 2021. Induced seismicity and deformation at geothermal fields in California, USA. *Proceedings World Geothermal Congress 2020+1, Reykjavik, Iceland, April-October 2021* (submitted October 2019).

Belisle, C. J. P. 1992. Convergence theorems for a class of simulated annealing algorithms on Rd. Journal of Applied Probability, 29(4), 885-895, doi: 10.2307/3214721.

Ben-Zion, Y., and V. Lyakhovsky. 2006. Analysis of aftershocks in a lithospheric model with seismogenic zone governed by damage rheology. Geophysical Journal International, 165, 197– 210.

Blake, K., A. Sabin, M. Eneva, S. Nale, M. Lazaro, A. Tiedeman, D. Meade, W.-C. Huang, D. Fujii, and J. Zimmerman. 2021. Updated shallow temperature survey, resource evolution and preliminary conceptual geologic model for the Coso geothermal field. *Proceedings World Geothermal Congress 2020+1, Reykjavik, Iceland, April-October 2021* (submitted October 2019).

Blake, K., A. Sabin, M. Lazaro, A. Tiedeman, D. Meade, and W.-C. Huang. 2018. LiDAR analysis over the Coso volcanic field, CA. Geothermal Resources Council Transactions, 42.

Brodsky, E. E., and L. J. Lajoie. 2013. Anthropogenic seismicity rates and operational parameters at the Salton Sea geothermal field. Science, 341(6145), 543–546, doi:10.1126/science.1239213.

Brothers, D. S., N. W. Driscoll, G. M. Kent, A. J. Harding, J. M. Babcock, and R. L. Baskin. 2009. Tectonic evolution of the Salton Sea inferred from seismic reflection data. Nature Geosciences, 2, 581-584, doi:10.1038/NGEO590.

California Energy Commission (CEC). 2019. *Power Plant Owner Reporting Database, Technical Report*, QFER CEC-1304, https://ww2.energy.ca.gov/almanac/electricity_data/web_qfer/index_cms.php.

California Geologic Energy Management Division (CalGEM)/California Department of Conservation, https://www.conservation.ca.gov/calgem.

Chen, X., P. M. Shearer, and R. E. Abercrombie. 2012. Spatial migration of earthquakes within seismic clusters in southern California: Evidence for fluid diffusion. Journal of Geophysical Research, 117(B4), doi: 10.1029/2011JB008973.

Combs, J. 1980. Heat flow in the Coso geothermal area, Inyo County, California. Journal of Geophysical Research, https://doi.org/10.1029/JB085iB05p02411.

Crandall-Bear, A. T., A. J. Barbour, and M. Schoenball. 2018. Irregular focal mechanisms observed at Salton Sea geothermal field: Possible influences of anthropogenic stress perturbations. Proceedings: 43rd Workshop on Geothermal Reservoir Engineering, Stanford University, Stanford, California, February 2018, SGP-TR-213.

Crow, N. B., and P. W. Kasamayer. 1978. Monitoring natural subsidence and seismicity in the Imperial Valley as a basis for evaluating potential impacts of geothermal production. Geothermal Resources Council Transactions, 2, 125–128.

Crowell, B. W., Y. Bock, D. T. Sandwell, and Y. Fialko. 2013. Geodetic investigation into the deformation of the Salton Trough. Journal of Geophysical Research, 118, 5030-5039.

Eneva, M., M. Coolbaugh, S. Bjornstad, and J. Combs. 2007. In search for thermal anomalies in the Coso geothermal field (California) using remote sensing and field data. Proceedings: 32nd Stanford Geothermal Workshop.

Eneva, M., and M. Coolbaugh. 2009. Importance of elevation and temperature inversions for the interpretation of thermal infrared satellite images used in geothermal exploration, Geothermal Resources Council Transactions, 33, 467-470.

Eneva, M., G. Falorni, D. Adams, J. Allievi, and F. Novali. 2009. Application of satellite interferometry to the detection of surface deformation in the Salton Sea geothermal field, California. Geothermal Resources Council Transactions, 33, 315-319.

Eneva, M. 2010a. *Application of InSAR to the Detection of Surface Deformation in the Geothermal Fields of Imperial Valley, California*, California Energy Commission, PIER Program, CEC-500-2010-019, 2010. Available online at: http://web.archive.org/web/20190228002056/https://www.energy.ca.gov/2010publications/CEC-500-2010-019/CEC-500-2010-019.pdf

Eneva, M. 2010b. Detection of surface deformation at mining and geothermal sites using satellite radar interferometry (InSAR). Proceedings: 44th U.S. Rock Mechanics Symposium and 5th U.S. – Canada Rock Mechanics Symposium, Salt Lake City, UT.

Eneva, M., and D. Adams. 2010. Modeling of surface deformation from satellite radar interferometry in the Salton Sea geothermal field, California. Geothermal Resources Council Transactions, 34, 527-534.

Eneva, M., G. Falorni, W. Teplow, J. Morgan, G. Rhodes, and D. Adams. 2011. Surface deformation at the San Emidio geothermal field, Nevada, from satellite radar interferometry. Geothermal Resources Council Transactions, 35, 1647-1653.

Eneva, M. 2012. *Geothermal Exploration in Eastern California Using ASTER Thermal Infrared Data*, California Energy Commission, PIER Program, CEC-500-2012-005, 2010. Available online at: http://web.archive.org/web/20190228020830/https://www.energy.ca.gov/2012publications/CEC-500-2012-005/CEC-500-2012-005.pdf

Eneva, M., D. Adams, G. Falorni, and J. Morgan. 2012. Surface deformation in Imperial Valley, CA, from satellite radar interferometry. Geothermal Resources Council Transactions, 36, 1339-1344.

Eneva, M., D. Adams, D., G. Falorni, and J. Morgan. 2013a. Applications of radar interferometry to detect surface deformation in geothermal areas of Imperial Valley in southern California. Proceedings: 38th Workshop on Geothermal Reservoir Engineering, Stanford University, Stanford, CA, February 2013, SGP-TR-198.

Eneva, M., D. Adams, G. Falorni, and J. Morgan. 2013b. Application of radar interferometry to detect subsidence and uplift at the Heber geothermal field, southern California. Geothermal Resources Council Transactions, 37, 491-499.

Eneva, M., D. Adams, G. Falorni, F. Novali, and V. Hsiao. 2014. Surface deformation at the Salton Sea geothermal field from high-precision radar interferometry. Geothermal Resources Council Transactions, 38, 991-999.

Eneva, M., A. J. Barbour, D. Adams, V. Hsiao, K. Blake, G. Falorni, and R. Locatelli. 2018. Satellite observations of surface deformation at the Coso geothermal field, California. Geothermal Resources Council Transactions, 42, 1383-1401.

Eneva, M., D. Adams, V. Hsiao, G. Falorni, and R. Locatelli. 2019a. Surface deformation at the Heber geothermal field in southern California. Proceedings: 44th Workshop on Geothermal Reservoir Engineering, Stanford University, Stanford, California, February 2019, SGP-TR-214.

Eneva, M., D. Adams, G. Falorni, and M. Shumski. 2019b. Surface deformation and seismicity at the North Brawley geothermal field in southern California. Geothermal Resources Council Transactions, 43, 767-783.

Eneva, M., D. Adams, K. Blake, V. Hsiao, G. Falorni, 2020. Comparison of surface deformation rates from InSAR and ground-based surveys in geothermal fields of California. Proceedings: 45h Workshop on Geothermal Reservoir Engineering, Stanford University, Stanford, California, February 2020, SGP-TR-216.

Fay, N. P., and E. D. Humphreys. 2005. Fault slip rates, effects of elastic heterogeneity on geodetic data, and the strength of the lower crust in the Salton Trough. Journal of Geophysical Research, 110, 1-14, doi:10.1029/2004JB003548.

Ferretti, A., C. Prati, and F. Rocca. 2000. Nonlinear subsidence rate estimation using permanent scatterers in differential SAR Interferometry. IEEE Transactions on Geoscience and Remote Sensing, 38, 2202-2212.

Ferretti, A., G. Savio, R. Barzaghi, A. Borghi, S. Musazzi, F. Novali, C. Prati, and F. Rocca. 2007, Submillimeter accuracy of InSAR time series: Experimental validation. IEEE Transactions on Geoscience and Remote Sensing, 45, 1142-1153.

Ferretti, A., A. Fumagalli, F. Novali, C. Prati, F. Rocca, and A. Rucci, A. 2011. A new algorithm for processing interferometric data-stacks: SqueeSAR. IEEE Transactions on Geoscience and Remote Sensing, 49(9), 3460-3470.

Fialko, Y., and M. Simons. 2000. Deformation and seismicity in the Coso geothermal area, Inyo County, California: Observations and modeling using satellite radar interferometry. Journal of Geophysical Research, Solid Earth, 105, 21781–21793, doi: 10.1029/2000JB900169.

Fialko, Y. 2006. Interseismic strain accumulation and the earthquake potential on the southern San Andreas fault system. Nature, 441, 968-971, https://doi.org/10.1038/nature04797.

Garthwaite, M., S. Lawrie, J. Dawson, and M. Thankappan. 2015. Corner reflectors as tie between InSAR and GNSS measurements: Case study of resource extraction in Australia. Proceedings: Fringe Workshop, Frascati, Italy, ESA SP-731.

Gawell, K. 2014. Statement before the Senate Select Committee on California's Energy Independence & Assembly Select Committee on Renewable Energy Economy in Rural California.

Genrich, J. F., Y. Bock, and R. G. Mason. 1997. Crustal deformation across the Imperial Fault: Results from kinematic GPS surveys and trilateration of a densely spaced, small-aperture network. Journal of Geophysical Research, 102, 4985-5004.

Geothermex Inc. 2004. *New Geothermal Site Identification and Qualification*, Richmond, CA, California Energy Commission. Report No.: P500-04-051, Contract No.: 500-04-051.

Guglielmi, Y., F. Cappa, J.-P. Avouac, P. Henry, and D. Elsworth. 2015. Seismicity triggered by fluid injection-induced aseismic slip. Science, 348, 1224–1226, doi: 10.1126/science.aab0476.

Hauksson, E., W. Yang, and P. M. Shearer. 2012. Waveform relocated earthquake catalog for southern California (1981 to 2011). Bulletin of the Seismological Society of America, 102(5), 2239-2244, doi:10.1785/0120120010.

Hauksson, E., J. M. Stock, R. Bilham, M. Boese, X. Chen, E. J. Fielding, J. E. Galetzka, K. W. Hudnut, K. Hutton, L. M. Jones, H. Kanamori, P. M. Shearer, J. H. Steidl, J. A. Treiman, S. Wei, and W. Yang. 2013. Report on the August 2012 Brawley earthquake swarm in Imperial Valley, southern California. Seismological Research Letters, 84(2), 177-189, doi: 10.1785/0220120169.

Helmstetter, A. and B. E. Shaw. 2009. Afterslip and aftershocks in the rate-and-state friction law. Journal of Geophysical Research, Solid Earth, 114, doi: 10.1029/2007JB005077.

InSAR Data Accuracy for California Groundwater Basins: CGPS Data Comparative Analysis, January 2015 to June 2018. 2019. California Department of Water Resources, Prepared by Towill Inc., with the participation of TRE Altamira Inc., pp. 159.

Hill, D. P. 1977. A model for earthquake swarms. Journal of Geophysical Research, 82, 1347-1352.

Inyo County Water Department - http://www.inyowater.org/projects/groundwater/coso-hay-ranch-project/; Coso-Hay Ranch Project; website accessed on June 1, 2018.

James, E. D., V. T. Hoang, and I. J. Epperson. 1987. Structure, permeability and production characteristics of the Heber, California geothermal field. Proceedings: 12th Workshop on Geothermal Reservoir Engineering, Stanford University, Stanford, California, 267-271.

Johnson, C. E., and D. P. Hill. 1982. Seismicity in the Imperial Valley. In *The Imperial Valley Earthquake, California of October 15, 1979*. U. S. Geological Survey Professional Paper, 1254, 15-24.

Kagel, A., B. Bates, and K. Gawel. 2007. *A Guide to Geothermal Energy and the Environment*. Geothermal Energy Association, 75 pp.

Kaven, J. O., S. H. Hickman, and N. C. Davatzes. 2011. Micro seismicity, fault structure and hydraulic compartmentalization within the Coso geothermal field, California. Proceedings: 36th Workshop on Geothermal Reservoir Engineering, Stanford University, Stanford, CA, SGP-TR-191.

Kaven, J. O., S. H. Hickman, and N. C. Davatzes. 2012. Mapping of fluid compartments with microseismicity and seismic velocities within the Coso geothermal field, California. Proceedings: 37th Workshop on Geothermal Reservoir Engineering, Stanford University, Stanford University, Stanford, CA, SGP-TR-194.

Kaven, J. O., S. H. Hickman, and N. C. Davatzes. 2014. Micro-seismicity and seismic moment release within the Coso geothermal field, California. Proceedings: 39th Workshop on Geothermal Reservoir Engineering, Stanford University, Stanford, CA, SGP-TR-202.

Kaven, J. O., S. H. Hickman, and N. C. Davatzes. 2015. Seismicity and deformation in the Coso Geothermal Field from 2000 to 2012. Geophysical Research Abstracts, 17, EGU2015-14466.

Lachenbruch, A. H., J. H. Sass, and S. P. Galanis. 1985. Heat flow in southernmost California and the origin of the Salton Trough. Journal of Geophysical Research, 90, 6709-6736.

LeSchack, A. and J. E. Lewis, 1983. Geothermal prospecting with Shallo-Temp surveys. Geophysics, 48, 975-996.

Lin, G., P. M. Shearer, and E. Hauksson. 2007. Applying a three-dimensional velocity model, waveform cross correlation, and cluster analysis to locate southern California seismicity from 1981 to 2005. Journal of Geophysical Research, 112, B12309, doi:10.1029/2007JB004986.

Lippmann, M. J., and G. S. Bodvarsson. 1985. The Heber geothermal field, California: Natural state and exploitation modeling studies. Journal of Geophysical Research, 90(B1).

Llenos, A. L., and A. J. Michael. 2016. Characterizing potentially induced earthquake rate changes in the Brawley Seismic Zone, southern California. Bulletin of the Seismological Society of America, 106 (5), 2045-2062, doi: 10.1785/0120150053.

Lohman, R. B., and J. J. McGuire. 2007. Earthquake swarms driven by aseismic creep in the Salton Trough, California. Journal of Geophysical Research, 112, B04405, doi:10.1029/2006JB004596.

Lyons, S. N., Y. Bock, and D. T. Sandwell. 2002. Creep along the Imperial Fault, southern California, from GPS measurements. Journal of Geophysical Research 107(B10), 2249, doi:10.1029/2001JB000763.

Matek, B. 2014. *2014 Annual US & Global Geothermal Power Production Report*, Geothermal Energy Association, pp. 25, https://geothermal.org/Policy_Committee/Documents/2014_Annual_US_&_Global_Geot hermal%20Power%20Production_Report.pdf

Matlick, S., T. and Jayne. 2008. Brawley resurrection of a previously developed geothermal field. Geothermal Resources Council Transactions, 32, 159-162.

Meltzner, A. J., T. K. Rockwell, and L. A. Owen. 2006. Recent and long-term behavior of the Brawley Fault Zone, Imperial Valley, California: An escalation in slip rate. Bulletin of the Seismological Society of America, 96, 2304-2328.

Monastero, F. C., 2002. An overview of industry-military cooperation in the development of power operations at the Coso geothermal field in southern California. Geothermal Research Council Bulletin, 31(5), 188-195.

Monastero, F. C., A. M. Katzenstein, J. S. Miller, J. R. Unruh, and K. Richards-Dinger. 2005. The Coso geothermal field: A nascent metamorphic core complex. Geological Society of America Bulletin, 117(11-12), 1534-1553.

Newman, G. A., E. Gasperikova, G. M. Hoversten, and P. E. Wannamaker. 2008. Three-dimensional magnetotelluric characterization of the Coso geothermal field. Geothermics, 37, 369-399.

Nice, T. 2016. The most mysterious fault in California. Forbes, October 9, 2016; https://www.forbes.com/sites/trevornace/2016/10/09/most-mysterious-fault-california/#2066807f41ea.

Reinisch, E. C., S. T. Ali, M. Cardiff, J. O. Kaven, K. L. Feigl. 2020. Geodetic measurements and numerical models of deformation at Coso Geothermal Field, California, USA, 2004-2016. Remote Sensing, 12, 225.

Ross, Z. E., D. T. Trugman, E. Hauksson, and P. M. Shearer. 2019a. Searching for hidden earthquakes in southern California. Science, 364 (6442), 767-771, doi: 10.1126/science.aaw6888.

Ross, Z. E., B. Idini, Z. Jia, O. L. Stephenson, M. Zhong, X. Wang, Z. Zhan, M. Simons, E. J. Fielding, S.-H. Yun, E. Hauksson, A. W. Moore, Z. Liu, and J. Jung. 2019b. Hierarchical interlocked orthogonal faulting in the 2019 Ridgecrest earthquake sequence. Science, 366 (6463), 346-351, doi: 10.1126/science.aaz0109.

Roth, S. 2020. California needs clean energy after sundown. Is the answer under our feet? Los Angeles Times, January 22, 2020, https://www.latimes.com/environment/story/2020-01-22/california-needs-clean-energy-after-sundown-geothermal-could-be-the-answer.

Rudnicki, J. W. 1986. Fluid mass sources and point forces in linear elastic diffusive solids. Mechanics of Materials, 5, 383–393, doi:10.1016/0167-6636(86)90042-6.

Rymer, M. J., J. Boatwright, L. C. Seekins, J. D. Yule, and J. Liu. 2002. Triggered surface slips in the Salton Trough associated with the 1999 Hector Mine, California earthquake. Bulletin of the Seismological Society of America, 92, 1300-1317.

Rymer, M. J., J. A. Treiman, K. J. Kendrick, J. J. Lienkaemper, R. J. Weldon, R. Bilham, M. Wei, E. J. Fielding, J. L. Hernandez, B. P. E. Olson, P. J. Irvine, N. Knepprath, R. R. Sickler, X. Tong, and M. E. Siem. 2011. Triggered surface slips in southern California associated with the 2010 El Mayor-Cucapah, Baja California, Mexico, earthquake. U.S. Geological Survey Open-File Report 2010–1333 and California Geological Survey Special Report 221, pp. 62 (https://pubs.usgs.gov/of/2010/1333/).

Sarychikhina, O., E. Glowacka, R. Mellors, and V. F. Suarez. 2011. Land subsidence in the Cerro Prieto geothermal field, Baja California, Mexico, from 1994 to 2005: An integrated analysis of DInSAR, leveling, and geological data. Journal of Volcanology and Geothermal Research, 204, (1-4), 76-90, doi: 10.1016/j.jvolgeores.2011.03.004.

Sarychikhina, O., E. Glowacka, and B. Robles. 2018. Multi-sensor DInSAR applied to the spatiotemporal evolution analysis of ground surface deformation in Cerro Prieto basin, Baja California, Mexico, for the 1993-2014 period. Natural Hazards, 92(1), 225-255. doi: 10.1007/s11069-018-3206-2.

Schoenball, M., N. C. Davatzes, and J. M. G. Glen. 2015. Differentiating induced and natural seismicity using space-time-magnitude statistics applied to the Coso geothermal field. Geophysical Research Letters, 42, 6221-6228, doi:10.1002/2015GL064772.

Scripps Orbit and Permanent Array Center (SOPAC) – http://sopac.ucsd.edu/.

Segall, P. 1985. Stress and subsidence resulting from subsurface fluid withdrawal in the epicentral region of the 1983 Coalinga earthquake. Journal of Geophysical Research, 90(B8), 6801-6816, doi: 10.1029/JB090iB08p06801.

Segall, P. 1989. Earthquakes triggered by fluid extraction. Geology, 17(10), 942-946, doi: 10.1130/0091-7613.

Seher, T., H. Zhang, M. Fehler, H. Yu, V. Soukhovitskaya, M. Commer, and G. Newman. 2011. Temporal velocity variation beneath the Coso geothermal field observed using seismic double difference tomography of compressional and shear wave arrival times. Geothermal Resources Council Transactions, 90, 1743-1747.

Sones, R., and Z. Krieger. 2000. Case history of the binary power plant development at the Heber, California geothermal resource. Proceedings: World Geothermal Congress 2000, Kyushu – Tohoku, Japan, 2217-2219.

Sones, R., and D. N. Schochet. 1999. Binary geothermal power plant development at the Heber, California geothermal resource area, Geothermal Resources Council Transactions, 23, 93-97.

Thomas, A. P., and T. K. Rockwell. 1996. A 300- to 500-year history of slip on the Imperial Fault near the U.S.-Mexico border: Missing slip at the Imperial fault bottleneck. Journal of Geophysical Research, 101, 5987-5997.

Trugman, D. T., P. M. Shearer, A. A. Borsa, and Y. Fialko. 2016. A comparison of long-term changes in seismicity at The Geysers, Salton Sea, and Coso geothermal fields. Journal of Geophysical Research, Solid Earth, 121, 225-247, doi: 10.1002/2015JB012510.

U.S. Geological Survey. 2008. *Assessment of Moderate- and High-Temperature Geothermal Resources of the United States*. U.S. Geological Survey Fact Sheet 2008-3082.

Vasco, D. W., C. Wicks, K. Karasaki, and O. Marques. 2002. Geodetic imaging: Reservoir monitoring using satellite interferometry. Geophysical Journal International, 149, 555-571.

Wang, H. F. 2000. *Theory of Linear Poroelasticity with Applications to Geomechanics and Hydrogeology*. Princeton University Press, Princeton, N. J., pp. 304.

Wei, M., D. Sandwell, and Y. Fialko. 2009. A silent Mw 4.7 slip event of October 2006 on the Superstition Hills Fault, southern California. Journal of Geophysical Research, 114, B07402, doi:10.1029/2008JB006135.

Wei, M., D. Sandwell, Y. Fialko, and R. Bilham. 2011. Slip on faults in the Imperial Valley triggered by the 4 April 2010 Mw 7.2 El Mayor-Cucapah earthquake revealed by InSAR. Geophysical Research Letters, 38, L01308.

Wei, S., J. P. Avouac, K. W. Hudnut, A. Donnellan, J. W. Parker, R. W. Graves, D., Helmberger, E. Fielding, Z. Liu, F. Cappa, and M. Eneva. 2015. The 2012 Brawley swarm triggered by injection-induced aseismic slip. Earth and Planetary Science Letters, 422, 115-125.

Wicks, C., W. Tatcher, F. Monastero, and M. Hasting. 2001. Steady-state deformation of the Coso Range, East Central California, inferred from satellite radar interferometry. Journal of Geophysical Research, 106, 13769-13780.

Xu, X., D. T. Sandwell, and B. Smith-Konter. 2020. Displacements and Surface fractures from Sentinel-1 InSAR: 2019 Ridgecrest earthquakes. Seismological Research Letters. https://doi.org/10.1785/0220190275

Yang, W., E. Hauksson, and P. M. Shearer. 2012. Computing a large refined catalog of focal mechanisms for southern California (1981 - 2010): Temporal stability of the style of faulting. Bulletin of the Seismological Society of America, 102, 1179-1194, doi: 10.1785/0120110311.

GLOSSARY

Abbreviation, Acronym, or Term	Definition
CalGEM	California Geologic Energy Management Division/California Department of Conservation (formerly DOGGR – Division of Oil, Gas and Geothermal Resources). CalGEM oversees the drilling, operation, maintenance, and plugging and abandonment of oil, natural gas, and geothermal energy wells. In this project, source of data for geothermal wells. Website: https://www.conservation.ca.gov/calgem.
CEC	California Energy Commission
Deformation	Specific land changes, or ground surface displacements, where the ground surface moves up or down (i.e., in the vertical direction), as well as sideways (i.e., horizontally).
DInSAR	Differential InSAR – an InSAR technique where interferograms from two different passages are compared to obtain surface deformation.
DS	Distributed scatterers. These are areas, which emit signals that are lower than those from the PS (see below), but still above the noise. DS are bare land, fallow fields, etc. Used in the SqueeSAR technique developed at TRE Altamira, Italy.
ENV, or Envisat	A European satellite, which carried a SAR instrument on board, and collected data suitable for InSAR processing between February 2003 and October 2010. The SAR instrument was C-band (wavelength 56 mm). The minimum revisit time period was 35 days. Archived data are available from the European Space Agency (ESA) at no cost.
ESA	European Space Agency: Envisat and Sentinel are ESA satellites.
GRC	Geothermal Resources Council. Annual meetings take place in the fall.
GPO	United States Navy Geothermal Program Office. Manages the Coso geothermal field. Provided data from Coso for this project.
GPS	Global Positioning System – GPS stations measure time series of three components of surface deformation. The three components are: vertical (Up), horizontal east-west (East), and horizontal south-north (North).
HBGF	Heber geothermal field in Imperial Valley, southern California; operated by Ormat.
Horizontal deformation,	The ground surface moves sideways, in a direction perpendicular to the vertical. Two horizontal components are commonly considered – in the west-east and south-north directions. InSAR can detect

156

Abbreviation, Acronym, or Term	Definition
displacement, movement	westward and eastward movements, but cannot "see" southward and northward displacements.
ICDPW	Imperial County Department of Public Works. Geothermal companies operating in Imperial Valley provide leveling and seismic data to ICDPW.
IID	Imperial Irrigation District
InSAR	Interferometric Synthetic Aperture Radar – a method to process SAR data to obtain interferograms.
KGRA	Known Geothermal Resource Area
LOS	Line-of-Sight – direction to the satellite, in which movements are measured. Could be toward the satellite or away from the satellite.
Magnitude of completeness	Earthquake magnitude above which all seismic events are assumed to be recorded (i.e., none is missed because it is too weak to be recorded). Earthquakes with lower magnitudes are also recorded, but not all of them (depending on distance to seismic stations).
MFR	Magnitude-frequency relationship – the logarithm of the number of events with a given magnitude versus the magnitude.
NBGF	North Brawley geothermal field in Imperial Valley, southern California; operated by Ormat.
PBO	Plate Boundary Observatory – a network of 1,100 permanent, continuously recording GPS stations, and other instruments.
PS	Permanent Scatterers – these are building, boulders, roads, canals, etc., identified in all SAR scenes, from which the time series are extracted in the PSInSAR and SqueeSAR techniques developed at TRE Altamira, Italy.
PSInSAR™	Permanent Scatterers InSAR – an InSAR technique using permanent scatterers (PS), to obtain deformation time series at individual PS locations. Developed at TRE Altamira, Italy.
Rate of deformation (or, deformation rate)	Amount of displacement per unit time. Can be also referred to as "velocity." In this project, deformation rates are measured in millimeters per year (mm/year). They are shown as positive numbers for uplift, or movements toward a satellite, or eastward displacements. Conversely, negative numbers mark subsidence, or movements away from a satellite, or westward displacements.
Rate of seismicity (or, seismicity rate)	Number of earthquakes per unit time – for example, could be per month, or per year.

Abbreviation, Acronym, or Term	Definition
SAR	Synthetic Aperture Radar – a type of satellite radar data used in this project.
Scatterer	A point that can be identified in all satellite images used in the InSAR processing. See PS and DS above.
SCSN	Southern California Seismic Network
SGW	Stanford Geothermal Workshop. Held annually, usually in February.
SNT, or Sentinel	European satellites that are successors of Envisat and with similar characteristics. There are two such satellites – Sentinel-1A and Sentinel-1B. For the study areas in this project, such data were available from November 2015 on. Minimum revisit time was at first 24 days, then 12 days, and is now 6 days. Data are available from the European Space Agency (ESA) at no cost.
SNT1 and SNT2	Two sets of data covering two adjacent periods, for which Sentinel satellite data were processed in this project.
SqueeSAR™	The latest development of PSInSAR, in which uses both PS and DS. Developed at TRE Altamira, Italy.
SSGF	Salton Sea geothermal field in Imperial Valley, southern California; operated by CalEnergy and EnergySource.
SSGF-CE	CalEnergy units of the SSGF.
SSGF-ES	The northeastern part of the SSGF operated by EnergySource LLC.
Subsidence	Sinking of the ground surface, downward displacement (movement).
TRE Altamira, or simply TRE	Tele-Rilevamento Europa, Altamira (TRE Altamira) – a company with headquarters in Milan, Italy, and a branch in Vancouver, British Columbia (Canada). TRE Altamira provided SqueeSAR processing for this project.
TSX, or TerraSAR	A German satellite with a SAR instrument on board, using X-band (wavelength 31 mm). Minimum revisit time is 11 days. Data are available from the German Space Agency (DRL), at a reduced cost for research projects, and sometimes at no cost for older data. However, such data can be expensive for commercial projects.
Uplift	Rising of the ground surface, upward displacement (movement).
USGS	United States Geological Survey
Vertical deformation, displacement, movement	The ground surface moves down (sinks, subsides) or up (rises, uplifts).

Abbreviation, Acronym, or Term	Definition
WGC	World Geothermal Congress. In this report, there are references to the intended 2020 WGC that was postponed to 2021, due to the ongoing Covid-19 pandemic.